Higher-Order QCD Corrections and Threshold Resummation for Processes in the Standard Model and Beyond at hadron colliders.

A
Thesis Submitted
in Partial Fulfillment of the Requirements
for the Degree of
DOCTOR OF PHILOSOPHY
By

CHINMOY DEY
Roll No - 196121103
Supervisor : Dr. M C KUMAR

Department of Physics
Indian Institute of Technology Guwahati
Guwahati-781039, Assam, India

March, 2025

Declaration

This is to certify that the thesis entitled " **Higher-Order QCD Corrections and Threshold Resummation for Processes in the Standard Model and Beyond at hadron colliders.**", submitted by me to the *Indian Institute of Technology Guwahati*, for the award of the degree of Doctor of Philosophy, is a bonafide work carried out by me under the supervision of Dr. M C Kumar. The content of this thesis, in full or in parts, have not been submitted to any other University or Institute for the award of any degree or diploma. I also wish to state that to the best of my knowledge and understanding nothing in this report amounts to plagiarism.

Signed: ______________________________

Chinmoy Dey
Department of Physics,
Indian Institute of Technology Guwahati,
Guwahati-781039, Assam, India.

Date: 21/05/2025

Certificate

This is to certify that the thesis entitled " **Higher-Order QCD Corrections and Threshold Resummation for Processes in the Standard Model and Beyond at hadron colliders.**", submitted by Chinmoy Dey (196121103), a Research scholar in the *Department of Physics*, *Indian Institute of Technology Guwahati*, for the award of the degree of Doctor of Philosophy, is a record of an original research work carried out by him under my supervision and guidance. The thesis has fulfilled all requirements as per the regulations of the institute and in my opinion has reached the standard needed for submission. The results embodied in this thesis have not been submitted to any other University or Institute for the award of any degree or diploma.

Signed: ____

Supervisor: Dr. M C Kumar
Department of Physics,
Indian Institute of Technology Guwahati,
Guwahati-781039, Assam, India.

Date: 21/05/2025

Acknowledgements

This thesis would not have been possible without the valuable support, guidance, and encouragement I received from many individuals during this journey. While it is difficult to name everyone, I would like to express my gratitude to some of them here.

First and foremost, I would like to express my deepest gratitude to my supervisor, **Dr. Meduri C Kumar**, for their invaluable guidance, constant support, and encouragement throughout the course of my Ph.D. Their insights, patience, and mentorship have played a crucial role in shaping my academic journey.

I would like to acknowledge all the **course instructors during my Ph.D. coursework** for laying a strong academic foundation and deepening my understanding of the core subjects. I would also like to sincerely thank the members of my Ph.D. Doctoral Committee: **Dr. Udit Raha**, **Prof. Soumitra Nandi**, **Prof. Poulose Poulose**, and **Prof. Subhaditya Bhattacharya** for their valuable feedback, constructive suggestions, and continuous encouragement during my research.

I am also thankful to the current Head of the Department, **Prof. Basanta R Boruah**, and the former Head of the Department, **Prof. Perumal Alagarsamy and Prof. Subhradip Ghosh**, for providing a supportive academic environment and necessary resources during my research. My sincere thanks to all the **faculty and staff members of the Department of Physics** at IIT Guwahati for their assistance, cooperation, and for maintaining a smooth and efficient research ecosystem.

I deeply appreciate the support and collaboration of my research collaborators: **Dr. Kajal Samanta**, **Dr. Goutam Das**, **Dr. Pulak Banerjee**, **Prof. V. Ravindran**, **Vaibhav Pandey**, whose insights and teamwork significantly enriched the quality of my research. I am also thankful to my **juniors**, especially **Niraj Koiral**, for their help, discussions, and camaraderie. I would like to thank **Vaibhav** and **Niraj** once again for their kind help in preparing the diagrams presented in this thesis.

I also gratefully acknowledge the computational support provided by the **Param Ishan and Param Kamrupa supercomputing facilities** at IIT Guwahati, which played an essential role in completing my research.

I would like to acknowledge the support of all the members of **RS-3 and RS-4 Labs**, who contributed to creating a vibrant and collaborative research environment. Their presence made working in the lab both productive and enjoyable.

A special mention goes to the ever-smiling **tea vendors in Core-3 and Core-4**—your tea and warm presence provided countless moments of comfort during long working days.

To my dear friends **Shantanu, Dipankar, Sunil, Mijanur, Debu, Sumana Di, Lipika, Gargi, Banashree, Seshadri, Himangshu, Samik, Swarup, Soumen, Anupam, Didwamsa, Dev, Sujit, Arkodip, Sagar, Soumalya** and many others, thank you for your companionship, motivation, and the countless memories we've shared. I also thank my **cricket, football, and badminton friends**, especially **Niloy**, **Nihar, Himanshu, Ankan, Swargiary, Dipendu Halder**, **Subrata Da**, **Shantanu Dolai**, **Arin Da**, **Sukanta Da** and **Bivakar**, for the much-needed breaks and joyful moments beyond academics.

I am sincerely grateful to my seniors in the department, especially **Arghya Da, Surojit Da, Sayan Da**, **Golam Da**, **Roni Da**, **Mrinal Da**, **Sudeshna Di**, **Lopa Di**, and **Sahabub Da**, for their guidance, encouragement, and helpful advice throughout the years.

I am also thankful to my juniors in the department, including **Abhik**, **Dipendu Bhandari**, **Nayan**, **Sourav**, **Utsab**, **Likun**, **Disha**, and **Hemant**, for their energetic presence, assistance, and engaging discussions which made the research journey more dynamic and enjoyable.

Lastly, I owe everything to my **parents and family**. Their unconditional love, sacrifices, and belief in me have been the foundation of my strength. Without their support, this achievement would not have been possible.

Thank you all.

Sincerely
Chinmoy Dey

Abstract

Quantum Chromodynamics (QCD), the theory of the strong interaction, is an essential component of the Standard Model (SM) of particle physics. Precision predictions within QCD are necessary for interpreting collider data and for testing the SM against experimental observations. In recent years, the demands for theoretical precision has grown due to the increasing accuracy of measurements at the Large Hadron Collider (LHC). In this thesis, we address this challenge by performing higher-order perturbative QCD calculations and threshold resummation for a class of processes at the LHC. These include both Standard Model processes and those sensitive to potential extensions beyond it.

A central focus of this work is on soft-gluon threshold resummation—a technique used to account for the dominant logarithmic corrections that arise when partonic processes are near threshold. Such logarithms, if left untreated, can spoil the convergence of the perturbative expansion. We perform the threshold resummation in the Mellin-space to systematically resum these logarithms to next-to-next-to-next-to-leading logarithmic (N^3LL) accuracy, matched with the available next-to-next-to-next-to-leading order (N^3LO) fixed-order results. This provides the state-of-the-art precision for hadronic cross-section predictions.

In Chapter 3, we study the threshold resummation of Drell-Yan-like processes at N^3LO + N^3LL accuracy. Drell-Yan processes serve as clean probes of QCD dynamics due to their relatively simple final states and have played a critical role in precision studies at hadron colliders. We perform the resummation for neutral and charged Drell-Yan, VH production and Higgs production through bottom quark annihilation and present phenomenological results relevant to current LHC energies.

In Chapter 4, we extend threshold resummation to the associated production of a Higgs boson with a Z boson (ZH production) through gluon fusion. This is a loop-induced process in the Standard Model and sensitive to new physics effects. We perform soft-virtual (SV) and next-to-soft-virtual (NSV) resummation for this process in born-improved theory at the LHC, achieving improved theoretical control over uncertainties from unknown higher-order corrections.

In Chapter 5, we investigate the threshold resummation of ZZ production at the LHC up to NNLO + NNLL accuracy. Diboson production processes like ZZ are crucial both as precision SM measurements and as backgrounds to Higgs and new physics searches. We make use of the resummation formalism developed for $2 \to n$ type processes involving colorless final states and tailor it to the ZZ production process for performing the resummation. We notice that these improved predictions reduce the scale uncertainties, particularly in the high invariant mass region.

In Chapter 6, we shift focus to the computation of two-loop virtual amplitudes for the decay of a pseudo-scalar Higgs boson to three partons, within an effective theory approach. These amplitudes are relevant for understanding pseudo-scalar Higgs production in association with a jet at hadron colliders, especially in scenarios beyond the Standard Model such as the Minimal Supersymmetric Standard Model (MSSM). We compute the amplitudes to NNLO accuracy, including the terms beyond the positive power in the dimensional regulator ϵ, which are essential for the computation of three-loop pseudo-scalar production cross sections.

Finally, the results presented in this thesis represent significant advances in precision QCD calculations, enhancing our ability to interpret LHC data and to test the boundaries of the Standard Model. The resummation techniques and multi-loop calculations studied herein are not only relevant for the processes studied but also provide a framework that can be extended to a broad class of observables in collider physics.

Contents

List of Figures

List of Tables

Chapter 1

Introduction

The known interactions among all forms of matter in the universe are governed by four fundamental forces: gravity, electromagnetism, the weak force, and the strong force. Over the decades, there has been a sustained effort to unify our understanding of these interactions within a common theoretical framework. However, classical physics falls short of accurately capturing the dynamics of these forces, especially at very small or very high-energy scales. The advent of quantum mechanics combined with the theory of special relativity laid the foundation for a more complete formulation, known today as quantum field theory (QFT). This framework interprets particles as excitations of underlying quantum fields and incorporates the principle of local gauge invariance. Enforcing such local symmetries naturally requires the introduction of gauge fields, which mediate interactions between matter particles. The strength of each interaction is characterized by a corresponding coupling constant.

The Standard Model (SM) of particle physics provides a unified theoretical framework for describing three of the four fundamental interactions in nature—electromagnetic, weak, and strong forces—excluding gravity. It integrates the electromagnetic and weak forces into a single electroweak theory and combines this with quantum chromodynamics (QCD) to account for the strong interaction. The incorporation of the Higgs mechanism allows the SM to explain the origin of particle masses in a gauge-invariant manner. Structurally, the SM is built upon the local gauge symmetry group $\mathrm{SU}(3)_C \times \mathrm{SU}(2)_L \times \mathrm{U}(1)_Y$. Each of these gauge groups governs a fundamental interaction: $\mathrm{SU}(3)_c$ corresponds to the strong

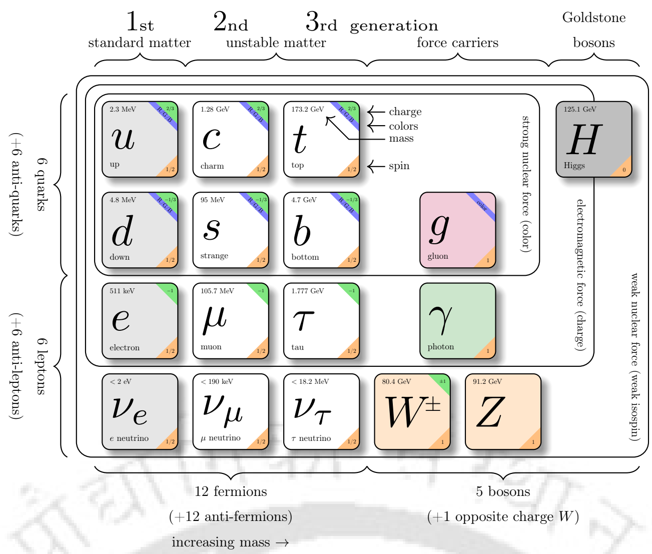

FIGURE 1.1: The particle spectrum of the Standard Model (SM)

force, responsible for the interactions between color-charged particles; $SU(2)_L$ is associated with the weak interaction, which acts on left-handed particles; and $U(1)_Y$ describes the hypercharge interaction, leading to electromagnetism after electroweak symmetry breaking. The foundational step towards this theory was taken by Glashow [5], who proposed a unified framework for the weak and electromagnetic interactions. This was later extended by Weinberg [6] and Salam [7], who introduced the Higgs mechanism [8–12] into the electroweak theory, enabling a consistent explanation for the masses of gauge bosons and fermions. In the current formulation, the electroweak interaction is described by a spontaneously broken $SU(2)_L \times U(1)_Y$ gauge symmetry, while the strong interaction remains governed by an unbroken $SU(3)_C$ color gauge symmetry.

The SM particle content includes six quark flavors—up (u), down (d), charm (c), strange (s), top (t), and bottom (b)—each appearing in three color charges: red, green, and blue. These quarks interact via eight gluons, the gauge bosons of the strong force. The leptonic sector comprises three charged leptons—electron ($e^\pm$), muon ($\mu^\pm$), and tau ($\tau^\pm$)—along with their corresponding neutrinos (ν_e, ν_μ, and ν_τ). The mediators of the weak interaction are the $W^\pm$ and Z bosons, while the electromagnetic interaction is mediated by the photon (γ). Additionally, the model includes a scalar Higgs boson (H), which is responsible for the mass generation of fundamental particles via the Higgs mechanism. The spectrum of particles are given in Fig. 1.1.

The validation of the SM which is based on elegant gauge symmetries and quantum field theory requires precise experimental verification. High-energy particle colliders have been instrumental in this effort, enabling the discovery of predicted particles, the measurement

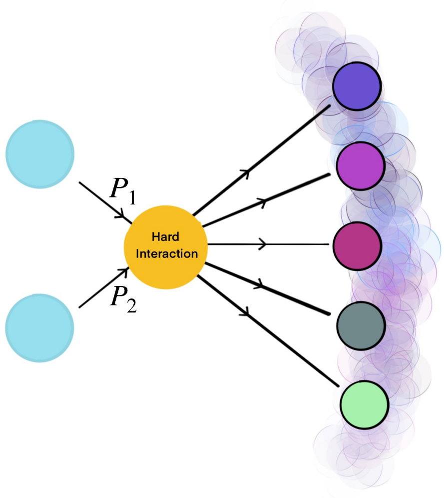

FIGURE 1.2: A schematic representation of Collider.

of fundamental parameters, and the testing of quantum corrections in QFT. The interplay between theoretical predictions—often involving perturbative quantum chromodynamics (QCD)—and collider measurements has allowed for stringent tests of the SM and has constrained possible extensions. Different types of colliders contribute uniquely to this program by providing complementary experimental conditions and energy regimes [13, 14].

Lepton colliders, such as LEP and future proposed machines like the ILC [15, 16] or FCC-ee [17], provide a clean environment for precision studies of the Standard Model. Since the initial states in these colliders are fundamental particles with no internal structure, the associated background and non-perturbative effects are minimal. This simplicity allows for highly accurate theoretical predictions using perturbative quantum field theory, including QCD corrections to final states such as hadronic jets. Precision measurements of electroweak parameters and strong coupling constants at lepton colliders have played a vital role in validating the Standard Model and probing for indirect signals of new physics.

In contrast, hadron colliders like the Tevatron and the Large Hadron Collider (LHC) offer access to a much wider energy range and allow direct production of heavy particles such as the Higgs boson and top quark. However, because protons are composite particles, hadronic collisions involve a mixture of partonic subprocesses and initial-state QCD radiation, making theoretical predictions more complex. Despite these challenges, advances in perturbative QCD, including high-order corrections and resummation techniques, have enabled precise cross-section calculations and differential predictions. These developments are crucial for testing the Standard Model in the high-energy regime and for extracting parton distribution functions (PDFs) with improved accuracy.

The SM of particle physics stands as a remarkable theoretical framework, not only due to its mathematical consistency—being a renormalizable quantum field theory—but also because of its striking agreement with experimental observations. Its predictive power has been validated through numerous key discoveries over the decades. One of the earliest confirmations was a phenomenon anticipated by the electroweak theory came in 1973, with the observation of neutral currents by the Gargamelle collaboration [18]. This was followed a decade later, in 1983, by the direct detection of the massive gauge bosons W and Z at CERN by the UA1 [19] and UA2 [20] collaborations, respectively in the Super Proton Synchrotron collider, cementing the electroweak component of the SM.

The strong interaction sector also saw major breakthroughs by the discovery of the J/ψ meson in 1974 by experiments at SLAC [21] and BNL [22] provided compelling evidence for the charm quark, offering a cornerstone for the development of QCD. In 1977, the bottom quark was discovered through the observation of bottomonium states at Fermilab [23, 24], and nearly two decades later, the top quark was discovered in 1995 by the CDF [25] and DØ [26] collaborations at the Tevatron, completing the third generation of quarks. The discovery of the Higgs boson by the ATLAS [27] and CMS [28] experiments in 2012 marked the final piece of the SM puzzle, bringing the model to its current completeness.

The remarkable success of modern high-energy physics experiments is rooted in the tireless efforts of both experimental and theoretical communities. On the one hand, experimentalists have extracted highly accurate measurements from vast datasets; on the other hand, theorists have strived to match this level of precision by accounting for contributions from all relevant interaction channels and computing them to sufficiently high orders in the perturbative expansion. As experimental accuracy improved, it became increasingly evident that theoretical predictions needed to incorporate higher-order effects to maintain consistency and predictive power. For instance, early observations of W and Z production rates by UA1 and UA2 [29, 30] were found to be consistent with then-recent QCD corrections computed at next-to-leading order (NLO) [31–35]. Simultaneous progress was made in computing NLO corrections for processes such as Drell–Yan (DY) and Deep Inelastic Scattering (DIS) [36, 37].

Furthermore, searches for the Higgs boson at earlier colliders such as the Large Electron–Positron Collider (LEP) [38] and the Tevatron [39] were instrumental in narrowing down the allowed mass range of Higgs boson. LEP set a lower bound of 114.4 GeV on the Higgs boson mass, while global fits to electroweak precision data constrained the upper bound of Higgs boson mass to 152 GeV at 95% confidence level [40].

As colliders reached multi-TeV energy scales at the Large Hadron Collider (LHC) at CERN, the requirement for highly precise theoretical predictions became ever more critical—particularly for hadron-initiated processes where strong interactions dominate. With increasing luminosity and energy at the LHC—from 196 fb^{-1} at 13 TeV to 500 fb^{-1} at 14 TeV after Run 3—and the eventual goal of reaching 100 TeV at future hadron colliders, one can probe a much higher energy frontier. With the prospects of achieving the integrated luminosity of 1 ab^{-1} in future colliders, the properties of SM particles are expected to be probed to unprecedented accuracy. Due to the asymptotic freedom of QCD, the strong coupling becomes small at high energies and in this energy regime one can use it as an expansion parameter and consequently the perturbation theory can be used to compute higher-order QCD corrections to physical observable that can well be measured at collider experiments. In this context, next-to-next-to-leading order (NNLO) calculations for processes like DY [41–43] and DIS [44], have been vital for refining parton distribution functions (PDFs). Similarly, the discovery of the Higgs boson have heavily relied on the advanced theoretical predictions up to NNLO results [45–53]. Other than DY and Higgs production, NNLO QCD corrections have been computed for several important processes within the SM at the LHC, including top quark pair production [54–59], dijet production [60–63], di-photon [64], di-boson [65–67] and tri-photon [68] final states. More recently, next-to-next-to-next-to-leading order (N^3LO) QCD corrections have been achieved for benchmark processes such as Higgs boson production [69, 70], Drell-Yan [71–73]. In addition, mixed QCD–electroweak (EW) corrections to the Drell–Yan process have also been computed up to NNLO accuracy. These developments mark a substantial enhancement in precision. However, further improvements are essential to match the increasing accuracy of experimental measurements at the LHC and future colliders. Achieving even higher-order corrections will help reduce theoretical uncertainties, refine the extraction of fundamental parameters, and improve our sensitivity to possible signals of new physics beyond the Standard Model.

Despite the remarkable success of the Standard Model (SM) in explaining a wide range of phenomena, it leaves several fundamental questions unanswered. One major gap is the absence of a consistent quantum field theoretical formulation of gravity. Although gravity is well described classically by general relativity, the quantum mediator of the gravitational interaction—the graviton—has not yet been observed. Additionally, the SM fails to account for dark matter and dark energy, which together constitute about 95% of the energy content of the universe, leaving only a small fraction ($\sim 5\%$) that is described by known SM particles.

The search for physics beyond the SM is also driven by the idea of unifying all the fundamental forces under a common theoretical framework. Grand Unified Theories (GUTs), which attempt to combine the strong, weak, and electromagnetic interactions into a single gauge group, provide a promising path in this direction. These theories predict new particles and interactions, some of which could be tested at current or future colliders. Another notable shortcoming is related to the mass of neutrinos. Within the SM framework, neutrinos are massless, yet experimental evidence, such as neutrino oscillations, clearly demonstrates that they possess finite masses. Moreover, the SM does not provide a natural explanation for the large difference between the electroweak scale and the Planck scale, known as the hierarchy problem. In particular, keeping the Higgs boson mass stable at the electroweak scale requires fine-tuning unless new physics is introduced. Furthermore, recent results from the ATLAS [74] and CMS [75] collaborations at the LHC have shown an excess in the di-photon production channel relative to SM expectations at the 2σ level. These observations may suggest the presence of new physics phenomena beyond the SM.

To identify such potential signals of physics beyond the Standard Model (BSM), it is essential to have highly accurate theoretical predictions within the SM. Only with such precision can any deviations be confidently attributed to new physics. This thesis focuses on achieving precise theoretical predictions for important processes within the SM at the LHC: Drell–Yan production, associated production of Higgs boson with a massive vector boson, bottom quark annihilation to Higgs boson production and Z-boson pair production. Apart from these, we have computed the amplitudes for the decay of pseudo-scalar Higgs boson to three partons at the two-loop level to the higher power of the dimensional regulator in the context of BSM.

The fixed-order correction is important to achieve the desired accuracy of the theoretical predictions. However, the behavior of certain observables is very poor in certain kinematic region for fixed order correction. In particular, the fixed order correction introduces finite logarithmic terms originating from the soft and collinear parton radiation in the final states. These logarithms contribute significantly to the partonic cross section near the kinematic threshold region and can spoil the convergence of the perturbative expansion. To obtain reliable theoretical results, one has to resum all these large logarithms to all orders in the perturbation theory. We have focused extensively on the threshold resummation of QCD processes, particularly for the production of neutral and charged Drell-Yan, associated production of a Higgs boson with a vector boson, and Higgs production in bottom quark annihilation at the LHC.

The production of massive lepton pairs in hadronic collisions—commonly known as the Drell–Yan (DY) process—has been a topic of great interest for over five decades. It was first observed by Christenson *et al.* in 1970 [76] through proton–nucleus collisions. Since then, the process has been studied in numerous experiments at increasingly higher energies and improved precision. Initially motivated by the search for new vector mesons, the Drell–Yan process has become a crucial probe of hadron structure. In particular, parton distribution functions (PDFs) are extracted by fitting large datasets of cross-section measurements from channels like deep inelastic scattering (DIS) and Drell–Yan processes.

The large next-to-leading order (NLO) corrections [31–35] to the DY cross section cast doubts on the validity of perturbative QCD (pQCD), highlighting the necessity for next-to-next-to-leading order (NNLO) predictions [41–43]. Recently, complete next-to-next-to-next-to-leading order (N^{3}LO) results are available for DY [71–73]. Although N^{3}LO corrections are smaller in magnitude, they play a critical role in verifying the convergence of the perturbative expansion. Moreover, the process of mass factorization and ultraviolet (UV) renormalization introduces two arbitrary scales—the factorization scale and the renormalization scale. At each perturbative order, residual dependence on these scales manifests through logarithmic terms. However, such dependence systematically reduces as higher-order corrections are included, ideally vanishing in the all-orders limit. These theoretical considerations provide a strong motivation to pursue Drell–Yan cross section calculations beyond N^{3}LO by resumming the all order logarithms in the threshold limit, as done in this thesis.

The pursuit of precision in Higgs boson production predictions has necessitated the inclusion of higher-order QCD corrections. Initial next-to-leading order (NLO) corrections [45–48] were found to be large around 128% of LO, and subsequent next-to-next-to-leading order (NNLO) corrections [49–53] are significant around 44% of LO and the correction showed significant reduction in the scale uncertainties from 16.6% to 8.8% . Unlike in the Drell-Yan process, the convergence of the perturbative expansion for Higgs production is slower, prompting extensive studies beyond NNLO [77–89]. This ultimately led to the computation of next-to-next-to-next-to-leading order (N^{3}LO) corrections [69] in the heavy-top effective theory, where the top quark is integrated out, resulting in an effective interaction between the Higgs boson and gluons. The level of precision achieved at this order is remarkable and has opened the door to exploring contributions from less dominant but phenomenologically relevant production modes. Among these is the Higgs production through bottom quark annihilation, where the bottom quark is considered massless except in the Yukawa coupling. Though its contribution is smaller than that from gluon fusion, NNLO corrections have been computed for this channel [90], showing that its size can become competitive with higher-order corrections in other channels, highlighting its importance in precision Higgs physics. Recently, N^{3}LO cross sections are available for this process [91], and for 13 TeV LHC case they are found to be about $5.42 \pm 4.8\%$ pb.

Although gluon fusion is the dominant contribution for Higgs boson production at hadron colliders, the associated process of bottom quark annihilation ($b\bar{b} \to H$) provides a compelling complementary production channel, particularly in scenarios where the Higgs coupling to bottom quarks is enhanced. In the Standard Model (SM), the bottom Yukawa coupling is relatively small, and the $b\bar{b} \to H$ contribution is subleading. However, in several Beyond the Standard Model (BSM) frameworks, including the Minimal Supersymmetric Standard Model (MSSM) and two-Higgs-doublet models (2HDMs), this coupling can be significantly amplified, making $b\bar{b}$-initiated processes especially relevant [92, 93]. Moreover, from a phenomenological standpoint, studying Higgs production in bottom quark annihilation is crucial to validate and constrain models with extended Higgs sectors, where scalar or pseudoscalar Higgs bosons may couple more strongly to down-type quarks. Experimentally, this channel contributes to inclusive Higgs production and has been examined through its impact on the $H \to \tau^+\tau^-$ decay channel, where an excess in the bottom fusion mode was observed in the Run II analyses of the ATLAS and CMS collaborations [94, 95]. On the theoretical side, calculations for $b\bar{b} \to H$ were initially performed at leading order (LO) and improved to next-to-leading order (NLO) using the five-flavor scheme (5FS), where bottom quarks are treated as massless partons in the proton [96, 97]. The full NNLO QCD corrections in the 5FS were later computed [90], showing significant improvements in perturbative stability and reduced dependence on the renormalization and factorization scales. In parallel, the four-flavor scheme (4FS), where bottom quarks appear only in the final state and are treated as massive, has also been developed to NLO [98, 99], offering a complementary approach. The two schemes were reconciled through matching procedures such as Santander matching [100]. Furthermore, differential distributions and resummation techniques have been explored to account for logarithmically enhanced terms arising from initial-state radiation [101]. As precision Higgs physics advances, the $b\bar{b} \to H$ channel remains important for accurate determinations of the Higgs coupling to bottom quarks and plays a key role in constraining new physics scenarios at the LHC and future hadron colliders.

The production of the Higgs boson in association with a massive vector boson ($W^{\pm}$ or Z), known as VH production, serves as a key channel for testing the electroweak sector of the Standard Model (SM). This process is particularly valuable due to its distinctive experimental signatures, especially when the accompanying vector boson undergoes leptonic decay, allowing for efficient signal reconstruction. Among these channels, ZH production plays a central role owing to the strength of the Higgs-Z boson interaction, which contributes significantly to the overall cross section and provides a sensitive probe of potential deviations from SM expectations. The significance of VH production became prominent with the observation of the Higgs boson at the LHC in 2012 by the ATLAS and CMS collaborations [27, 28], where evidence from multiple channels—including VH with $H \to b\bar{b}$—contributed to the discovery. Notably, the direct observation of $VH(b\bar{b})$ was achieved during Run 2 of the LHC at $\sqrt{s} = 13$ TeV [102, 103], marking a key milestone in confirming the Yukawa coupling of the Higgs to bottom quarks. From a theoretical standpoint, the VH channel was initially calculated at leading order (LO) using electroweak theory. With the need for precision matching the experimental capabilities, next-to-leading order (NLO) QCD corrections were computed decades ago [104, 105], reducing uncertainties and enhancing cross section predictions. Subsequent developments led to the full computation of NNLO QCD corrections in the narrow-width approximation [106–110], which provided more accurate predictions, particularly for total and differential distributions. In parallel, next-to-leading order electroweak (NLO EW) corrections were also derived [111, 112], showing notable effects in high transverse momentum regimes due to Sudakov logarithms.

In the pursuit of precision predictions for associated Higgs production, significant progress has been made by incorporating soft-gluon resummation at next-to-next-to-leading logarithmic (NNLL) accuracy, consistently matched to next-to-next-to-leading order (NNLO) fixed-order results [113]. Additionally, threshold-enhanced approximations have been explored at next-to-next-to-next-to-leading order (N^{3}LO) within the Drell-Yan–like channel through soft-virtual techniques [114]. More recently, complete N^{3}LO corrections for the DY-type contributions have become available using the `n3loxs` package [73]. These developments underscore the importance of resumming large logarithmic corrections in the threshold limit to all orders in perturbation theory. Motivated by this, the present thesis focuses on advancing precision studies of the VH production cross section by implementing threshold resummation techniques beyond the N^{3}LO fixed-order level.

In addition to the dominant Drell-Yan–like mechanism, the associated production of a Higgs boson with a Z-boson receives notable contributions from the loop-induced gluon fusion channel, $gg \to ZH$. These processes, although formally higher order in QCD, can be numerically significant due to the large gluon luminosity at the LHC. Leading-order studies [115–118] and next-to-leading order corrections [119–126] have revealed that this channel can substantially enhance the total cross section, particularly in specific regions of phase space such as the boosted regime. Moreover, soft-gluon effects for this process have been addressed through inclusive resummation techniques in the so-called Born-improved framework [127]. Given that the theoretical uncertainties remain relatively large for this channel, a precise prediction of differential observables is essential. In this thesis, we aim to perform the resummation of the invariant mass distribution for the ZH final state in the gluon fusion channel. This analysis is crucial for improving theoretical control and reducing uncertainties in the modeling of this subdominant but phenomenologically important production mode.

The production of a pair of on-shell Z bosons at the Large Hadron Collider (LHC) plays a pivotal role in testing the Standard Model (SM) and in exploring possible deviations arising from new physics. As a clean final state, the ZZ channel provides an essential background to Higgs boson measurements, particularly in the decay mode $H \to ZZ^* \to 4\ell$, and contributes significantly to precision electroweak studies. The process was first observed at the Tevatron [128, 129] and later studied extensively at the LHC, where the increased center-of-mass energy and luminosity allowed for detailed measurements of total and differential cross sections [130, 131]. From a theoretical standpoint, ZZ production is particularly attractive as it allows for precision calculations in QCD due to its color-singlet final state. Fixed-order predictions have advanced to next-to-next-to-leading order (NNLO) in QCD [132, 133], significantly reducing the renormalization and factorization scale uncertainties. However, in regions where the partonic center-of-mass energy approaches the production threshold, soft-gluon emissions introduce large logarithmic corrections that can compromise the convergence of the perturbative series. To address this, threshold resummation techniques are employed. The resummation of next-to-next-to-leading logarithmic (NNLL) terms matched to NLO fixed-order results [134] has shown to improve theoretical predictions, especially for observables such as the invariant mass distribution of the ZZ system and the rapidity separation between the bosons. These improvements are crucial for high-precision comparisons with experimental data and for constraining anomalous gauge couplings and other beyond-the-SM scenarios. The present thesis contributes to this program by providing NNLO+NNLL accurate predictions for the total and differential cross sections of ZZ production at the LHC.

The pursuit of physics beyond the Standard Model (BSM) is driven by several compelling theoretical ideas, each aiming to address the unresolved issues within the Standard Model (SM). Among the prominent approaches are models involving extra spatial dimensions, proposed as a potential solution to the hierarchy problem—namely, the vast disparity between the electroweak and Planck scales, which remains unexplained in the SM framework. In these scenarios, SM particles are restricted to a 3+1 dimensional hypersurface (brane), while gravity propagates in the higher-dimensional bulk. The graviton in such theories, originating from a $(4+n)$-dimensional spacetime, appears in four dimensions as a tower of massive spin-2 states. Depending on the specific construction, this spectrum can be continuous, as in the Arkani-Hamed–Dimopoulos–Dvali (ADD) model, or consist of discrete resonances, as in the Randall–Sundrum (RS) model.

Supersymmetric theories form another robust category of BSM models, offering solutions to multiple theoretical shortcomings of the SM. In the MSSM, for instance, the Higgs sector comprises five physical states: two CP-even scalars, one CP-odd pseudo-scalar, and a pair of charged Higgs bosons. Beyond the MSSM, many BSM scenarios such as the two-Higgs-doublet models (2HDMs) also predict additional bosons that couple to SM fermions. The discovery of such particles at the LHC would provide strong evidence for new physics and requires both extensive experimental searches [135–138] and highly accurate theoretical predictions.

Among them, the Minimal Supersymmetric Standard Model (MSSM) and the Two Higgs Doublet Model (2HDM) [139–147] are well-studied examples that extend the scalar sector by introducing additional Higgs bosons. These extended models predict both CP-even and CP-odd scalar particles, including a pseudo-scalar Higgs boson A, whose discovery has been a focus of experimental efforts at the LHC.

Theoretical studies have been crucial in characterizing the production mechanisms and decay modes of such CP-odd Higgs bosons. Next-to-leading order (NLO) QCD corrections to the inclusive production cross section of A have been calculated [48, 148–151], and the enhancements over the leading-order (LO) predictions are found to be substantial—reaching up to 67% in some scenarios. Further progress has been made by computing the next-to-next-to-leading order (NNLO) cross section within an effective field theory approach [53, 152, 153], enabling more precise rate predictions.

While inclusive rates are essential, differential observables provide deeper insight into the nature of A and its interactions with Standard Model particles. In particular, studying A in association with hard jets or under jet veto conditions can significantly improve signal-to-background discrimination. It has been shown [154, 155] that such strategies enhance the sensitivity to Higgs signals and allow for a better understanding of the underlying dynamics. Recent work has produced NNLO predictions for Higgs-plus-jet final states, including fiducial cross sections defined by realistic detector acceptance criteria [156]. These developments build upon earlier NNLO calculations for Higgs-plus-jet observables [157–161] and rely on two-loop amplitudes that have been computed for scalar Higgs-plus-jet production [162–168]. The production of a pseudo-scalar Higgs boson (A) at hadron colliders is a key avenue for exploring the structure of extended Higgs sectors and CP-odd couplings in theories beyond the Standard Model (SM). Unlike the CP-even SM Higgs boson, the pseudo-scalar arises naturally in models like the Minimal Supersymmetric Standard Model (MSSM) and other two-Higgs doublet frameworks [169]. In such scenarios, the discovery of a CP-odd scalar would provide compelling evidence for extended scalar sectors. Although the SM does not contain a pseudo-scalar Higgs, its presence has been actively searched for at the LHC, primarily in the $\tau^+\tau^-$ decay channel. Limits on the pseudo-scalar mass and couplings have been reported by both ATLAS and CMS [138, 170], prompting precise theoretical predictions. Since the pseudo-scalar does not couple directly to vector bosons at tree-level, its dominant production at hadron colliders proceeds via gluon fusion through a top-quark loop. In the heavy top-quark limit, the interaction can be modeled effectively via an operator coupling the pseudo-scalar to gluons and quarks, allowing for higher-order QCD corrections to be computed analytically. The leading-order (LO) [48, 171] and next-to-leading order (NLO) [172, 173] corrections were derived early on using this effective field theory (EFT) approach, which showed large K-factors and reduced scale dependence. However, differential distributions for A, such as transverse momentum and rapidity distribution, are currently only available up to NNLO accuracy [174, 175]. As precision goals rise, going beyond NNLO becomes essential, especially for distinguishing pseudo-scalar signals from SM-like Higgs backgrounds. Therefore, extending these predictions to N^{3}LO, particularly for exclusive processes like pseudo scalar Higgs and a jet production, is highly desirable. Such precision would not only reduce theoretical uncertainties but also improve the reliability of experimental analyses incorporating selection cuts and fiducial constraints. In this thesis, we computed the two-loop amplitude with higher powers of the dimension regulator, which are important ingredients of the three-loop computation. These amplitudes form a vital ingredient in extending the total cross section to N^{3}LO using threshold approximation or soft-virtual techniques. Moreover, understanding the ultraviolet (UV) renormalization of pseudo-scalar form factors is subtle due to the axial anomaly and operator mixing in the effective Lagrangian [176, 177]. The interplay between these theoretical challenges and the increasing accuracy of experimental data reinforces the importance of precise predictions for pseudo-scalar production processes at current and future colliders.

The next section outlines the structure and objectives of this thesis.

Outline

This thesis presents a collection of research works aimed at a comprehensive understanding of higher-order contributions in perturbative QCD for important color-singlet processes at the LHC in SM and higher order correction at beyond NNLO for pseudo saclar Higgs boson decay to three partons in BSM.

Chapter 2 offers a concise review of the fundamentals of pQCD and then we describe the formalism for deriving threshold-resummed partonic cross sections based on the approaches discussed in [81, 82, 178, 179]. A general expression for the threshold-enhanced terms in partonic processes is provided. By employing the factorization properties and the universal infrared (IR) and ultraviolet (UV) behavior of QCD amplitudes, we explore the structure of these corrections. A detailed investigation reveals a Casimir scaling property between quark- and gluon-initiated processes for the soft distribution functions [77, 180]. This is already observed more than 15 years ago.

In Chapter 3, we will utilize the maximally non-Abelian nature of the soft functions as discussed in Chapter 2 to derive the threshold resummed contributions to Drell-Yan (DY) production at N^{3}LO+N^{3}LL accuracy [181]. Numerical studies are performed to assess the impact of these corrections. It is found that the the resummed contributions are relatively small, affirming the convergence of the perturbative expansion, and a notable reduction in scale uncertainties is observed. These results were subsequently extended to compute N^{3}LO+N^{3}LL threshold contributions for Higgs boson production via bottom quark annihilation [181] and associated Higgs production with a vector boson [181] for other DY-type color neutral production at N^{3}LO+N^{3}LL in QCD.

In Chapter 4, we focus on gluon fusion ZH production at the LHC. Although the Drell-Yan-like $q\bar{q} \to ZH$ channel is dominant as discussed in chapter 3, the gluon-initiated loop-induced process $gg \to ZH$ contributes significantly, particularly at high invariant masses. We carry out the soft-gluon resummation at next-to-leading logarithmic (NLL) accuracy, matched to the fixed-order NLO results and extended to next-to-soft-virtual resummation [182]. The computation is performed in the Born-improved effective theory framework, where exact Born-level matrix elements are retained, and higher-order corrections are resummed based on the soft limit behavior. The importance of this channel stems from its relatively large theoretical uncertainties compared to the Drell-Yan type process, making soft-gluon resummation crucial for reducing scale dependence and improving precision. Phenomenological studies at different center-of-mass energies are presented, showing how the resummation impacts the invariant mass distributions and total cross sections.

In Chapter 5, we turn to the production of on-shell ZZ pairs at the LHC. This process plays a vital role both as a background to Higgs boson studies and as a probe of the electroweak sector. The fixed-order NNLO QCD corrections have been available for some time; however, sizeable threshold logarithms at partonic energies close to the production threshold can spoil the convergence of perturbation theory. To address this, we perform threshold resummation up to next-to-next-to-leading logarithmic (NNLL) accuracy and match the resummed results with the fixed-order NNLO computations for ZZ production [183]. The soft-collinear factorization framework is employed, taking advantage of the known universal infrared structure of QCD amplitudes. We provide numerical predictions for total and differential cross sections at various collider energies and analyze the reduction in theoretical uncertainties due to the resummation.

In Chapter 6, we represented the first step toward beyond-NNLO precision for pseudo scalar decay to three partons in higher powers of the dimension regulator. Here, the three-loop quark and gluon form factors are computed [184]. The computation involves generating Feynman diagrams using QGRAF [185], simplifying the algebra with FORM [186, 187], and performing integral reduction through IBP identities using LiteRed [188] and Reduze2 [189]. Dimensional regularization in $d = 4+\epsilon$ dimensions is employed to systematically handle divergences. The ultraviolet (UV) singularities arising from loop integrals are removed through the standard renormalization procedure, which includes both the renormalization of the coupling constant and the operator renormalization. This ensures that the resulting amplitudes is UV finite. The universal behavior of IR singularities provides a non-trivial check of the results and the finite amplitudes are expressed in terms of Generalised polylogarithms (GPLs). The amplitudes for decay to three partons are then simplified in mathematical routine and then optimized in FORM then implemented in FORTRAN-95 routine for use in any Monte-carlo generator, and make the code public.

Finally, in Chapter 7, we summarize the main findings of the thesis and discuss possible future extensions of this work toward even higher accuracies and applications to other important LHC processes.

Chapter 2

Perturbative QCD

THE STANDARD MODEL (SM) of particle physics provides a successful framework for understanding the fundamental particles and their interactions. Over the decades, it has been tested extensively through a wide range of experiments, particularly at high-energy colliders such as the Large Hadron Collider (LHC). Among the three fundamental forces described by the SM—electromagnetic, weak, and strong—the strong interaction, governed by Quantum Chromodynamics (QCD), plays a central role in hadron collider physics.

At hadron colliders like the LHC, protons are collided at very high energies, and since protons are made of quarks and gluons, it is these partons that interact in high-energy collisions. Describing these interactions accurately requires a deep understanding of QCD, which is a non-Abelian gauge theory. One of the challenges in QCD is that the strong coupling becomes large at low energies, making non-perturbative effects important. However, at high energies, the coupling becomes small, and the perturbative approach becomes applicable.

Precise theoretical predictions are essential for comparing experimental results with the Standard Model and for uncovering any possible hints of new physics. This demands computations beyond the leading-order approximation. Higher-order corrections in QCD, such as next-to-leading order (NLO) and next-to-next-to-leading order (NNLO), significantly improve the reliability of theoretical predictions. These corrections help reduce the uncertainties related to scale choices and improve the stability of the predictions.

In addition to fixed-order calculations, there are specific kinematic regions—such as those near the threshold of partonic reactions—where fixed-order expansions fail to converge well due to the presence of large logarithmic terms. In such cases, resummation techniques become necessary. These methods allow us to systematically sum over all orders of such dominant contributions, thereby improving the accuracy and reliability of theoretical predictions.

In this context, the study of higher-order corrections and resummation techniques is essential for precision collider physics. In the following sections, we will introduce the basics of QCD and explain how higher-order computations and resummation methods are implemented to enhance theoretical predictions for processes of interest at the LHC.

2.1 Basics of QCD

Quantum Chromodynamics (QCD) is the quantum field theory that describes the fundamental interactions of strong forces. QCD is a non-Abelian gauge theory based on the $SU(3)$ symmetry group. While the theoretical framework is straightforward to construct, the physical implications of this theory are highly complex. The strong interaction was understood in terms of general scattering principles without any knowledge of its elementary constituents in the beginning. The theories were developed based on the analytical computation of the S-Matrix and Regge theory. This was initially followed by the development of current algebra, which was later succeeded by the introduction of quarks and partons in the quark model. Murray Gell-Mann and George Zweig independently proposed the quark model to describe the observed patterns in hadron spectroscopy. Quarks were introduced as the fundamental building blocks of protons, neutrons, and other hadrons, though they were initially considered abstract mathematical constructs rather than physical particles. Experiments at SLAC (Stanford Linear Accelerator Center) revealed that protons are made up of tiny point-like particles, confirming that quarks are real. These findings matched Richard Feynman's parton model, which described quarks as almost free particles at high energies. These quarks follow Fermi-Dirac statistics, but the way hadrons were arranged suggested that something was missing to follow the Pauli exclusion principle. To explain how three identical quarks could exist together inside a baryon, physicists introduced the idea of "color charge". This led to the understanding that quarks carry a special type of charge, governed by $SU(3)$ symmetry. David Gross, Frank Wilczek, and David Politzer discovered asymptotic freedom, showing that the strong interaction weakens at short distances. This means that quarks act almost like free particles at high energy. To describe this, the QCD Lagrangian was formulated as a non-Abelian $SU(3)$ gauge theory, incorporating quark fields, gluon fields, and their interactions. Unlike electromagnetism, gluons themselves carry color charge, allowing them to interact with each other. This leads to confinement, which means quarks can never exist alone and are always bound inside larger particles like protons and neutrons. Finally, the success of QCD in describing the strong interaction is defined by two key concepts: asymptotic freedom and confinement. Asymptotic freedom signifies the weakening of the interaction at short distances, while confinement arises from its increasing strength at long distances. However, many theoretical predictions—primarily, but not exclusively, related to inclusive processes—are independent of QCD's long-distance behavior. These predictions fall within the domain of perturbative QCD (pQCD).

In the following, we briefly outline the corresponding QCD Lagrangian and discuss the evolution of the strong coupling constant. We then introduce the parton model and mass factorization.

2.1.1 QCD Lagrangian

QCD is an $SU(3)$ gauge theory that describes the strong interaction. It consists of eight gauge bosons, known as gluons, which interact exclusively with colored particles such as quarks and with themselves. This self-interaction among gluons distinguishes QCD from Quantum Electrodynamics (QED) because of non-abelian theory. The interaction Lagrangian of QCD is expressed as

$$\mathcal{L}_{QCD} = -\frac{1}{4}F^a_{\mu\nu}F^{a\mu\nu} + \bar{\psi}_i\left(i\gamma^\mu\mathcal{D}^{ij}_\mu - m\delta^{ij}\right)\psi_j - \frac{1}{2\zeta_0}(\partial_\mu A^{a\mu})^2 - \bar{c}^a\left(-\partial^\mu\mathcal{D}^{ac}_\mu\right)c^c \tag{2.1}$$

where $F^a_{\mu\nu}$ is the field strength tensor,

$$F^a_{\mu\nu} = \partial_\mu A^a_\nu - \partial_\nu A^a_\mu + \hat{g}_s f^{abc}A^b_\mu A^c_\nu. \tag{2.2}$$

$\mathcal{D}^{ab}_\mu$ and $\mathcal{D}^{ij}_\mu$ are the covariant derivatives for quark and gluon fields, respectively:

$$\mathcal{D}_\mu^{ab} = \delta^{ab}\partial_\mu - \hat{g}_s f^{abc} A_\mu^c. \tag{2.3}$$

$$\mathcal{D}_\mu^{ij} = \delta^{ij}\partial_\mu - i\hat{g}_s T_{ij}^a A_\mu^a, \tag{2.4}$$

Where the following definitions are,

ψ_i : the fermionic field (quarks)
A_μ^a : the gauge field (gluons)
c^a : the ghost fields
T_{ij}^a : generators of $SU(3)$ group
f^{abc} : the structure constant of $SU(3)$ group
i, j : color indices in the fundamental representation
a, b, c : color indices in the adjoint representation
m : mass of quark field
ζ_0 : the gauge parameter
$\hat{g}_s$: the bare strong coupling constant

The first two terms in Eq. (2.1) represent the kinetic terms for the gauge and fermionic fields, respectively. The third term corresponds to the gauge-fixing component of the Lagrangian in the covariant gauge, which is introduced to properly define the gluon propagator during quantization, ensuring a consistent quantum field theory. This arises because the gluon propagator contains additional degrees of freedom that must be eliminated through constrained gauge fields. Ghost fields play a crucial role in canceling the unphysical polarization states of gluons that would otherwise contribute to physically measurable quantities. Therefore, the gauge-fixing term is complemented by the fourth term in Eq. (2.1), which represents the kinetic term for the ghost fields.

A common framework employed in collider physics is perturbative Quantum Chromodynamics (pQCD), which relies on expanding physical observables as a series in the strong coupling constant $\alpha_s = \hat{g}_s^2/(4\pi)$. Under the assumption that α_s is sufficiently small at high energies, physical quantities can be systematically computed order-by-order. For an observable σ, the perturbative expansion can be expressed as:

$$\sigma = \sigma_0 + \alpha_s\sigma_1 + \alpha_s^2\sigma_2 + \cdots , \tag{2.5}$$

where σ_0 denotes the leading-order (LO) contribution, σ_1 the next-to-leading order (NLO) correction, and so on. Each term σ_i corresponds to a correction calculated using Feynman diagrammatic methods within the perturbative framework. In this thesis, our primary focus lies on the perturbative techniques in QCD and their applications to high-energy collider processes.

2.1.2 Ultraviolet divergences and renormalization

Quantum field theories typically suffer from divergences at high energies. In QCD, these divergences are handled through renormalization, where physical quantities are redefined to absorb infinities.

While an exact analytical solution for the QCD Lagrangian remains elusive, the property of asymptotic freedom—where the strong coupling constant decreases at high energies—allows for the use of perturbative techniques by expanding around the free field limit. In this expansion, the strong coupling constant $\hat{g}_s$ serves as the perturbative parameter. The typical approach begins by deriving Feynman rules and proceeds toward calculating physical observables. Leading-order (LO) calculations are usually manageable; however, incorporating higher-order corrections introduces complexities, especially due to phase-space integrations and loop diagrams, which often result in divergences.

To handle these divergences systematically, a regularization method must be applied. Here, we employ dimensional regularization [190], in which the number of space-time dimensions is shifted to $d = 4 + \epsilon$. Within this framework, divergences manifest as poles in $1/\epsilon$, where ϵ is an infinitesimally small quantity.

Divergences encountered in calculations can be broadly classified based on their origin. Ultraviolet (UV) divergences arise when loop momenta become arbitrarily large, while infrared (IR) divergences occur when a parton's momentum becomes soft or collinear to another. In this section, our primary focus is on addressing UV divergences.

Using dimensional regularization, UV divergences appear explicitly as $1/\epsilon$ poles. To systematically eliminate these divergences, the concept of renormalization is introduced. The essence of renormalization lies in redefining the bare fields and coupling constants so that physical quantities remain finite in the limit $\epsilon \to 0$. We denote bare quantities with a hat, for instance, $\hat{g}_s$ for the strong coupling constant, and $\hat{\phi}$ for generic fields $\phi \in \{A, \Psi, c\}$, representing gluon, quark, and ghost fields, respectively. Since $\hat{g}_s$ acquires mass dimension in d dimensions, we introduce an auxiliary mass scale μ_0 to restore dimensionlessness.

The UV divergences are absorbed into renormalization constants Z, leading to the relations:

$$\hat{\phi} = Z_\phi(\mu_R)\,\phi(\mu_R), \quad \hat{g}_s = Z_g(\mu_R)\,g_s(\mu_R), \tag{2.6}$$

where μ_R is the renormalization scale introduced during the redefinition. The renormalized Lagrangian thus includes counterterms that cancel UV divergences at every perturbative order.

The choice of how much finite contribution is absorbed into the renormalization constants is known as the renormalization scheme. In this thesis, we employ the modified minimal subtraction ($\overline{\text{MS}}$) scheme [191], where, in addition to the divergent $1/\epsilon$ terms, the finite parts involving $\ln 4\pi$ and the Euler-Mascheroni constant $\gamma_E \simeq 0.5772$ are also systematically absorbed.

2.1.3 Running of the strong coupling constant

The renormalized strong coupling constant is not constant but depends on the unphysical renormalization scale μ_R. We define $\hat{a}_s = \hat{\alpha}_s/4\pi = \hat{g}_s^2/16\pi^2$ and $a_s = \alpha_s/4\pi = g_s^2/16\pi^2$, then

$$S_\epsilon \frac{\hat{a}_s}{\mu_0^\epsilon} = Z(\mu_R^2)\frac{a_s(\mu_R^2)}{\mu_R^\epsilon} \tag{2.7}$$

where μ_0 is introduced to make the strong coupling constant dimensionless in $4+\epsilon$ dimensions. The scale μ_R refers to the renormalisation scale, at which the renormalised strong coupling constant $a_s(\mu_R)$ is defined. Where, $S_\epsilon = exp\left\{\frac{\epsilon}{2}[\gamma_E - \ln 4\pi]\right\}$ is the spherical factor characteristic of d-dimensional regularisation with γ_E is the Euler Mascheroni constant. The L.H.S of Eq. (2.7) is independent of μ_R, whereas the R.H.S is a function of μ_R. Therefore,

$$\mu_R^2 \frac{d\hat{a}_s}{d\mu_R^2} = 0 \tag{2.8}$$

This equation leads to the renormalized group equation (RGE) of a_s, and it reads as

$$\frac{d\ln a_s(\mu_R^2)}{d\ln\mu_R^2} = \frac{\epsilon}{2} - \frac{d\ln Z(\mu_R^2)}{d\ln\mu_R^2} \tag{2.9}$$

Now we define a new function called the β-function in $\overline{MS}$ scheme as

$$\frac{d\ln a_s(\mu_R^2)}{d\ln\mu_R^2} = \frac{\epsilon}{2} + \frac{1}{a_s(\mu_R^2)}\beta(a_s(\mu_R^2)) \tag{2.10}$$

This β-function can be written as a series of a_s as

$$\beta(a_s(\mu_R^2)) = -\sum_{n=0}^{\infty}\beta_n\left(a_s(\mu_R^2)\right)^{n+2} \tag{2.11}$$

Using Eq. (2.7) and Eq. (2.11), one can find the solution for $Z(\mu_R^2)$, and the solution is

$$\begin{aligned} Z(\mu_R^2) &= 1 + a_s(\mu_R^2)\frac{2\beta_0}{\epsilon} + a_s^2(\mu_R^2)\left(\frac{4\beta_0^2}{\epsilon^2} + \frac{\beta_1}{\epsilon}\right) + a_s^3(\mu_R^2)\left(\frac{8\beta_0^3}{\epsilon^3} + \frac{14\beta_0\beta_1}{3\epsilon^2} + \frac{2\beta_2}{3\epsilon}\right) \\ &+ a_s^4(\mu_R^2)\left(\frac{16\beta_0^4}{\epsilon^4} + \frac{46\beta_0^2\beta_1}{3\epsilon^3} + \frac{9\beta_1^2 + 20\beta_0\beta_2}{6\epsilon^2} + \frac{\beta_3}{2\epsilon}\right) + \mathcal{O}(a_s^5(\mu_R^2)) \end{aligned} \tag{2.12}$$

where the β's are given below [176, 192–198]:

$$\begin{aligned} \beta_0 &= \frac{11}{3}C_A - \frac{2}{3}n_f, \\ \beta_1 &= \frac{34}{3}C_A^2 - 4n_fT_FC_F - \frac{20}{3}n_fT_FC_A, \\ \beta_2 &= \frac{2857}{54}C_A^3 - \frac{1415}{27}C_A^2T_Fn_f + \frac{158}{27}C_AT_F^2n_f^2 + \frac{44}{9}C_FT_F^2n_f^2 - \frac{205}{9}C_FC_AT_Fn_f + 2C_F^2T_Fn_f, \\ \beta_3 &= \left(\frac{17152}{243} + \frac{448}{9}\zeta_3\right)C_AC_FT_F^2n_f^2 + \left(-\frac{4204}{27} + \frac{352}{9}\zeta_3\right)C_AC_F^2T_Fn_f \\ &+ \left(\frac{424}{243}C_AT_F^3n_f^3 + \left(\frac{7073}{243} - \frac{656}{9}\zeta_3\right)C_A^2C_FT_Fn_f\right) + \left(\frac{7930}{81} + \frac{224}{9}\zeta_3\right)C_A^2T_F^2n_f^2 \\ &+ \left(\frac{1232}{243}C_FT_F^3n_f^3 + \left(-\frac{39143}{81} + \frac{136}{3}\zeta_3\right)C_A^3T_Fn_f\right) + \left(\frac{150653}{486} - \frac{44}{9}\zeta_3\right)C_A^4 \\ &+ \left(\frac{1352}{27} - \frac{704}{9}\zeta_3\right)C_F^2T_F^2n_f^2 + 46C_F^3T_Fn_f + \left(\frac{512}{9} - \frac{1664}{3}\zeta_3\right)\frac{N(N^2+6)}{48}n_f \\ &+ \left(-\frac{704}{9} + \frac{512}{3}\zeta_3\right)\frac{(N^4 - 6N^2 + 18)}{96N^2}n_f^2 + \left(-\frac{80}{9} + \frac{704}{3}\zeta_3\right)\frac{N^2(N^2+36)}{24} \end{aligned} \tag{2.13}$$

where $C_A = N$, $C_F = \frac{N^2-1}{2N}$, n_f is the number of active quark flavors (equal to 5), $T_F = \frac{1}{2}$, and $N = 3$ for SU(3) gauge theory.

The running of the strong coupling constant $a_s(\mu_R)$ can be expressed using an approximate analytical solution incorporating the first three coefficients of the QCD β-function. The expression takes the following form:

$$a_s(\mu_R^2) = \frac{2\pi}{\beta_0 \ln(\mu_R^2/\Lambda^2)} \left\{ 1 - \frac{2\beta_1}{\beta_0^2} \frac{\ln\left(\ln(\mu_R^2/\Lambda^2)\right)}{\ln(\mu_R^2/\Lambda^2)} + \frac{4\beta_1^2}{\beta_0^4 \ln^2(\mu_R^2/\Lambda^2)} \left[\left(\ln\left(\ln(\mu_R^2/\Lambda^2)\right) - \frac{1}{2} \right)^2 - \frac{5}{4} + \frac{\beta_2\beta_0}{\beta_1^2} \right] \right\}, \tag{2.14}$$

where μ_R is the renormalization scale and Λ is the QCD scale parameter.

For fewer than 17 active quark flavors ($n_f < 17$), the first β-function coefficient β_0 remains positive, leading to a decrease in a_s with increasing μ_R, which is a manifestation of asymptotic freedom. However, this expression becomes unreliable at energy scales near Λ, where $\ln(\mu_R^2/\Lambda^2)$ approaches zero and a_s diverges — a behavior known as the Landau pole. Below this scale, the coupling becomes large and perturbative QCD (pQCD) is no longer valid. In contrast, for scales significantly above Λ, pQCD can be reliably applied. The precise value of Λ depends on the number of active quark flavors, the renormalization scheme, and the value of the strong coupling at a reference scale. For instance, using the $\overline{\text{MS}}$ scheme and four-loop evolution, the QCD scale Λ is approximately 210 ± 14 MeV for $n_f = 5$ and 292 ± 16 MeV for $n_f = 4$, consistent with the world average value $\alpha_s(M_Z) = 0.1181 \pm 0.0011$ [199].

2.2 The Parton model

Asymptotic freedom is one of the most profound results of Quantum Chromodynamics (QCD), providing a compelling explanation for the behavior of quark-gluon interactions at high energies. Despite this, free quarks and gluons are not observed in nature. Instead, it is protons (and other hadrons) that participate in high-energy collisions. However, describing proton interactions directly using perturbative QCD (pQCD) techniques is not feasible due to confinement effects.

To study high-energy hadronic processes, we rely on the Parton Model which is initially proposed by Feynman,. The parton model has been remarkably successful in describing the connection between low-energy confined hadronic states and high-energy free partons. In this framework, hadrons are composed of fundamental constituents known as *partons*. In the infinite momentum frame, each parton carries a fraction of the hadron's momentum. Specifically, if P is the proton momentum, the i-th parton carries momentum $p_i = x_i P$, where x_i is the momentum fraction $(0 \leq x_i \leq 1)$.

Within this framework, the hadronic cross section σ for a high-energy collision between two hadrons H_1 and H_2 with momenta P_1 and P_2 with centre-of-mass energy (S)can be written as a convolution of parton-level cross sections $\hat{\sigma}_{ab}$ with the PDFs:

$$\sigma_{H_1 H_2}(S) = \sum_{a,b} \int_0^1 dx_1\, dx_2\, \hat{f}_a^{H_1}(x_1)\, \hat{f}_b^{H_2}(x_2)\, \hat{\sigma}_{ab}(x_1 P_1, x_2 P_2), \tag{2.15}$$

where $\hat{\sigma}_{ab}$ partonic cross-section can be computed perturbatively, whereas the PDFs $\hat{f}_i^{H_i}(x)$ are non-perturbative inputs.

While the naive Parton Model captures many important features, it must be modified when QCD radiative corrections are included. Radiative processes introduce new phenomena, such as gluon emission and parton splitting, leading to an energy scale dependence in both the PDFs and the partonic cross sections.

Thus, the improved Parton Model incorporates the effects of these corrections, accounting for the evolution of the PDFs with energy scales. To understand these improvements, it is essential to study the divergence structures arising from radiative corrections, which will be discussed in subsequent sections.

Radiative corrections and factorization

In perturbative QCD (pQCD), the partonic cross section can be systematically expanded in powers of the strong coupling constant a_s:

$$\hat{\sigma}_{ab} = \sum_{k=0}^{\infty} a_s^k(\mu_R^2)\, \hat{\sigma}_{ab}^{(k)}(\mu_R^2), \tag{2.16}$$

where $\hat{\sigma}_{ab}^{(k)}$ represents the coefficient at order k in the expansion, computed using Feynman diagram techniques.

At leading order ($k = 0$), the computation is relatively straightforward. However, at higher orders ($k \geq 1$), contributions from both loop diagrams and real emission processes must be included. These contributions bring about divergences of two types: ultraviolet (UV) and infrared (IR). UV divergences, discussed earlier, are handled through renormalization procedures.

IR divergences, in contrast, arise due to soft gluon emissions and collinear configurations involving massless partons. Specifically, soft divergences emerge when the energy of emitted gluons tends to zero, while collinear divergences occur when massless partons become parallel. In physical observables, the soft and collinear divergences from virtual corrections are canceled by corresponding divergences from real emission processes, as guaranteed by the Kinoshita-Lee-Nauenberg (KLN) theorem [200, 201].

Although soft divergences cancel entirely, collinear divergences associated with initial state massless partons persist at the partonic level. To handle these, a technique known as mass factorization is employed. The approach resembles UV renormalization: collinear singularities are systematically factored out and absorbed into the bare parton distribution functions (PDFs), rendering them finite and universal quantities.

This procedure introduces a new energy scale, the factorization scale μ_F. Consequently, the renormalized partonic cross section can be written schematically as:

$$\hat{\sigma}_{ab}(x_1P_1, x_2P_2) = \sum_{i,j} \Gamma^T_{ai}(\mu_F^2)\, \hat{\sigma}_{ij}(x_1P_1, x_2P_2, \mu_F^2)\, \Gamma_{jb}(\mu_F^2), \tag{2.17}$$

where $\hat{\sigma}_{ij}(\mu_F^2)$ are finite partonic coefficient functions and $\Gamma_{ai}(\mu_F^2)$ and $\Gamma_{jb}(\mu_F^2)$ are the mass factorization kernels, often referred to as Altarelli-Parisi (AP) kernels [202].

Similarly, the singularities are absorbed inside bare PDF's and the finite PDFs are obtained:

$$f_i(x, \mu_F^2) = \sum_j \Gamma_{ij}(\mu_F^2)\hat{f}_j(x), \tag{2.18}$$

where Γ_{ij} encapsulates the collinear structure and give finite measurable quantity. The finite PDFs are universal and does not depend on the process.

Thus, including radiative correction ns and accounting for factorization scale dependence modifies the original naive parton model to the so-called *improved parton model*, which forms the backbone of QCD analyses at high-energy colliders.

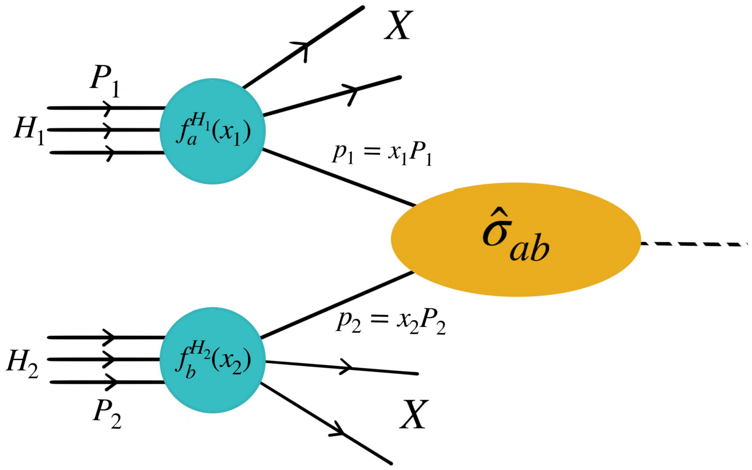

FIGURE 2.1: A schematic representation of parton model.

Partons are treated as if they exist in a frozen state within the hadron, meaning they do not interact with one another. Consequently, the scattering process is modeled as a weighted, incoherent sum of individual parton scattering processes. These subprocesses can be systematically calculated within a dynamical theory that describes parton interactions.

As an example, we consider the following hard-scattering process:

$$H_1(P_1) + H_2(P_2) \to F(\{q_i\}) + X. \tag{2.19}$$

where the collision of two hadrons H_1 and H_2 with momenta P_1 and P_2 with centre-of-mass-energy S produces the final state F, a system of colorless particles such as lepton pairs, Higgs boson, and so forth. For this process, the idea of the parton model is depicted in Figure 2.1, where the following notations are used generically. The variable x_i represents the fraction of the parent hadron's momentum, with $p_i = x_i P_i$, for $i = 1, 2$. The functions $f_a^{H_1}(x_1)$ and $f_b^{H_2}(x_2)$ denote the distribution functions of the partons a and b within the hadrons H_1 and H_2, respectively. The hadronic cross section $\sigma(S)$ is related to the partonic contributions through the following factorization formula

$$\sigma(S) = \sum_{a,b=q,\bar{q},g} \int_0^1 \mathrm{d}x_1 \int_0^1 \mathrm{d}x_2 \; f_a^{H_1}(x_1,\mu_F^2)\; f_b^{H_2}(x_2,\mu_F^2)\hat{\sigma}_{ab}(x_1P_1,x_2P_2,\mu_F^2) \tag{2.20}$$

In Eq. (2.19), the final state X can represent any inclusive collection of hadrons. The improved parton model refines the naive parton picture by incorporating radiative corrections in Eq. (2.20).

The initial hadronic beam is treated as an incoherent ensemble of its constituent partons. Each parton carries a fraction of the hadron's longitudinal momentum, governed by the parton distribution functions (PDFs). The short-distance hard scattering cross section between partons is perturbatively calculable. It can be expanded in the strong coupling constant a_s evaluated at the renormalization scale μ_R:

$$\hat{\sigma}_{ab}(x_1P_1,x_2P_2,\mu_F^2) = \sum_{k=0}^{\infty} a_s^k(\mu_R^2)\,\hat{\sigma}_{ab}^{(k)}(x_1P_1,x_2P_2,\mu_F^2,\mu_R^2). \tag{2.21}$$

Although the PDFs are non-perturbative in nature, which are universal and process-independent.

The scale evolution of the PDFs is described by the Dokshitzer-Gribov-Lipatov-Altarelli-Parisi (DGLAP) equations:

$$\mu_F^2 \frac{\partial}{\partial \mu_F^2} f_i(x,\mu_F^2) = \sum_j \int_x^1 \frac{dz}{z}\, P_{ij}(a_s(\mu_F^2),z)\, f_j\left(\frac{x}{z},\mu_F^2\right), \tag{2.22}$$

where P_{ij} are the splitting functions that encode the probability of parton j evolving into parton i with a momentum fraction z.

This combined framework, known as the collinear factorization theorem, ensures that the physical cross section remains finite and well-defined after mass factorization.

It is important to recognize that two unphysical scales now appear in the theory:

- The renormalization scale μ_R, where the strong coupling constant a_s is evaluated.
- The factorization scale μ_F, which separates short-distance physics from the collinear long-distance effects.

Typically, both μ_R and μ_F are chosen around the characteristic energy scale of the hard scattering to minimize large logarithmic corrections in the perturbative expansion.

The principal objective in this context is to improve the precision of short-distance partonic cross sections by including higher-order radiative corrections. In the next section, we will briefly introduce various methods employed for such higher-order computations.

2.3 Fixed order Computations

A widely adopted method for calculating higher-order QCD corrections is the fixed-order perturbative expansion. In this approach, observables are expanded systematically in powers of the strong coupling constant $a_s = \alpha_s/(4\pi)$, and only a finite number of terms are retained. Because a_s is relatively small at high energies, higher-order terms contribute diminishing corrections, and truncating the Taylor's series after a few orders often provides an excellent approximation to the full result.

The partonic cross section truncated at order n is given by

$$\hat{\sigma}_{ab}(x_1 P_1, x_2 P_2) = \sum_{k=0}^{n} a_s^k(\mu_R^2)\, \hat{\sigma}_{ab}^{(k)}(x_1 P_1, x_2 P_2, \mu_R^2) + \mathcal{O}(a_s^{n+1}). \tag{2.23}$$

Given that $a_s \ll 1$, contributions of order a_s^{n+1} are expected to be small and can typically be neglected (born type channel contribution), provided that the perturbative series exhibits good convergence behavior.

The first non-zero term defines the **leading order** (LO), with successive terms representing the **next-to-leading order** (NLO), **next-to-next-to-leading order** (NNLO), and so on. If the expansion is carried out to order n, we refer to it as an N^{n}LO calculation.

The order at which the perturbative series starts can vary by process. For example, in gluon-initiated Higgs boson production, the leading contribution appears at $\mathcal{O}(a_s^2)$, whereas in Drell-Yan process, it begins at $\mathcal{O}(a_s^0)$. Thus, a more general expression for the expansion is

$$\hat{\sigma}_{ab}(x_1 P_1, x_2 P_2) = a_s^{\lambda}(\mu_R^2) \sum_{k=0}^{n} a_s^k(\mu_R^2)\, \hat{\sigma}_{ab}^{(k)}(x_1 P_1, x_2 P_2, \mu_R) + \mathcal{O}(a_s^{n+\lambda+1}), \tag{2.24}$$

where λ denotes the starting order determined by the specific process under consideration.

Higher-order corrections stem from both virtual loop diagrams and real emissions. Considering a general partonic subprocess, two particles a and b into one particle F,

$$a(p_1) + b(p_2) \to F(q) + \sum_{i=1}^{m} R_i(k_i), \tag{2.25}$$

where F represents a colorless final state and R_i are the emitted partons with momentum k_i, the cross section can be written as

$$\hat{\sigma}_{ab} = \frac{1}{2\hat{s}} \int d\text{PS}_{1+m} \, |\mathcal{M}_{ab\to F}|^2. \tag{2.26}$$

Here, $\mathcal{M}_{ab\to F}$ is the matrix element, and $d\text{PS}_{1+m}$ denotes the $(1+m)$-particle phase space:

$$d\text{PS}_{1+m} = d\Phi(q) \prod_{i=1}^{m} d\Phi(k_i)(2\pi)^d \delta^{(d)} \left(p_a + p_b - q - \sum_{i=1}^{m} k_i \right), \tag{2.27}$$

where $d\Phi(p)$ represents the on-shell phase space measure for particle p. In this thesis, we mainly focus on presenting the invariant mass distributions of the final-state particles. In Appendix A, we have shown how to rewrite the two-body and three-body phase space expressions in terms of invariant mass variables.

At LO, only the Born-level matrix element squared contributes. At NLO, corrections consist of contributions from both:

- One-loop virtual diagrams, $\hat{\sigma}^V_{ab}$.
- Real emissions of an additional parton, $\hat{\sigma}^R_{ab}$.

Thus,

$$\hat{\sigma}^{(1)}_{ab} = \frac{1}{2\hat{s}} \left(\int d\text{PS}_1 \, \hat{\sigma}^V_{ab} + \int d\text{PS}_2 \, \hat{\sigma}^R_{ab} \right), \tag{2.28}$$

with

$$\hat{\sigma}^V_{ab} = 2\,\text{Re}\left(\mathcal{M}^{(0),\dagger}_{ab\to F} \mathcal{M}^{(1)}_{ab\to F} \right), \tag{2.29}$$

$$\hat{\sigma}^R_{ab} = |\mathcal{M}^{(0)}_{ab\to F+1}|^2. \tag{2.30}$$

At NNLO, three types of corrections arise:

- **Double real emissions (RR)**, involving two additional partons.

- **Real-virtual corrections (RV)**, combining one-loop corrections with one additional parton.
- **Double virtual corrections (VV)**, involving two-loop virtual contributions.

They contribute as:

$$\hat{\sigma}^{(2)}_{ab} = \frac{1}{2\hat{s}} \left(\int d\text{PS}_1\, \hat{\sigma}^{VV}_{ab} + \int d\text{PS}_2\, \hat{\sigma}^{RV}_{ab} + \int d\text{PS}_3\, \hat{\sigma}^{RR}_{ab} \right), \tag{2.31}$$

where

$$\hat{\sigma}^{RR}_{ab} = |\mathcal{M}^{(0)}_{ab\to F+2}|^2, \tag{2.32}$$

$$\hat{\sigma}^{RV}_{ab} = 2\,\text{Re}\left(\mathcal{M}^{(0),\dagger}_{ab\to F+1}\mathcal{M}^{(1)}_{ab\to F+1}\right), \tag{2.33}$$

$$\hat{\sigma}^{VV}_{ab} = 2\,\text{Re}\left(\mathcal{M}^{(0),\dagger}_{ab\to F}\mathcal{M}^{(2)}_{ab\to F}\right) + |\mathcal{M}^{(1)}_{ab\to F}|^2. \tag{2.34}$$

Throughout these calculations, both ultraviolet (UV) and infrared (IR) divergences arise. Renormalization is employed to remove UV divergences, while mass factorization is used to absorb initial-state collinear singularities into the PDFs. The resulting finite hard coefficient functions $\hat{\sigma}_{ab}$ are then convoluted with the PDFs to obtain physical cross sections.

Finally, for the fixed-order expansion to be reliable, it is necessary that each subsequent order yields increasingly smaller corrections:

$$\hat{\sigma}^{(n)}_{ab} \ll \hat{\sigma}^{(n-1)}_{ab}. \tag{2.35}$$

If instead $\hat{\sigma}^{(n)}_{ab} \sim \hat{\sigma}^{(n-1)}_{ab}$, the perturbative expansion becomes unreliable i.e. truncating series expansion is not reliable, then the need for alternative resummation techniques.

2.3.1 Scale Variations

In perturbative QCD calculations, the dependence on the unphysical renormalization (μ_R) and factorization (μ_F) scales is a primary source of theoretical uncertainty. A standard procedure to estimate this uncertainty is the 7-point scale variation method. In this approach, the two scales are varied independently around a central value μ_0 by factors of 2, but constrained such that their ratio does not become too large, typically requiring $|\ln(\mu_R/\mu_F)| \leq \ln 2$. This constraint defines seven distinct points in the (μ_R, μ_F)-plane:

the central point (μ_0, μ_0). The different choice of scales are $(\frac{\mu_0}{2}, \frac{\mu_0}{2})$, $(\frac{\mu_0}{2}, \mu_0)$, $(\mu_0, \frac{\mu_0}{2})$, (μ_0, μ_0), $(2\mu_0, \mu_0)$, $(\mu_0, 2\mu_0)$ and $(2\mu_0, 2\mu_0)$. The envelope of results from these seven calculations provides a conventional and widely adopted measure of the uncertainties in a theoretical prediction.

2.4 Thershold Resummation Framework

The fixed-order perturbative QCD predictions have achieved remarkable success, their applicability is often limited by the emergence of large logarithmic contributions. However, the behaviour of certain ovservables is very poor in certain kinematic region for fixed order correction. In particular, the fixed order correction introduces finite logarithmic terms originating from the soft and collinear parton radiation in the final states. These logarithm give very large contributions to the partonic cross section depending on the kinematic regions and break the convergence of the perturbation theory. To obtain reliable theoretical results, one has to resum all these large logarithms to all orders in perturbation theory. These enhanced logarithms primarily arise from three different origins: ultraviolet (UV) divergences, collinear divergences, and soft-gluon emissions.

As explained earlier, logarithms associated with UV divergences are systematically absorbed into the definition of the running coupling constant through renormalization. Similarly, collinear divergences are treated by absorbing the singularities into the parton distribution functions (PDFs) via the process of mass factorization. However, large logarithms stemming from soft emissions of gluons are not entirely canceled, even after the cancellation of divergences between real emissions and virtual corrections.

In specific kinematic regions, particularly where real and virtual contributions are imbalanced, soft-gluon effects remain substantial. In such cases, the reliability of the fixed-order expansion becomes questionable because the series convergence deteriorates. To properly account for these effects, it becomes essential to reorganize the perturbative expansion. This leads to a technique known as *resummation*, where classes of large logarithms are systematically summed to all orders in the coupling constant.

2.4.1 Soft-virtual correction

Moreover, at the hadronic level, the behavior of PDFs can also amplify the impact of soft emissions, especially in regions close to the partonic threshold. Consequently, soft corrections, when supplemented by the virtual contributions, form what are commonly referred to as *soft-virtual* or *threshold* corrections.

This section provides a concise overview of the formalism developed to capture these threshold contributions in inclusive processes, along with the framework for their all-order resummation based on [81, 82, 178, 179].

In the study of soft-gluon emissions, the *threshold limit* is of particular importance. This limit corresponds to the kinematic configuration where the produced final-state color-neutral system carries nearly the entire energy of the initial partonic center-of-mass system. The hadronic and partonic center-of-mass energy squared of incoming partons are define as $S \equiv (P_1 + P_2)^2$, and $\hat{s} \equiv (p_1 + p_2)^2$ respectively and Q is the invariant mass of the final-state particles. The partonic and hadronic threshold variables are define $z \equiv \frac{Q^2}{\hat{s}}$, and $\tau \equiv \frac{Q^2}{S}$ respectively. The approach to the threshold region can then be characterized using the dimensionless partonic thershold the limit $z \to 1$. Where the partonic threshold variable $z \to 1$ implies that very little energy is carried away by additional emissions, and the final state absorbs almost the entire initial energy and emitted radiation will be soft.

Now, hadronic cross-section parameterized in terms of threshold variables z and τ, can be written as

$$\begin{aligned}\sigma(S, Q) = &\sum_{a,b=q,\bar{q},g} \int_0^1 \mathrm{d}x_1 \int_0^1 \mathrm{d}x_2 \; f_a^{H_1}(x_1, \mu_F^2) \; f_b^{H_2}(x_2, \mu_F^2) \\ &\times \int_0^1 \mathrm{d}z \; \hat{\sigma}^{(0)} \Delta_{ab}^I(z, Q^2, \mu_F^2) \delta(\tau - z x_1 x_2)\,,\end{aligned} \tag{2.36}$$

The partonic coefficient function to any order n, can be written as

$$\begin{aligned}\Delta_{ab}^{I,(n)}(z, Q^2, \mu_F^2, \mu_R^2) =& C_{ab,\delta}(Q^2, \mu_F^2, \mu_R^2)\delta(1-z) + \sum_{i=0}^{2n-1} C_{ab,\mathcal{D}}^{(i)}(Q^2, \mu_F^2, \mu_R^2) f(\mathcal{D}_i(z)) \\ &+ C_{ab,reg}(Q^2, \mu_F^2, \mu_R^2) f_{\mathrm{reg}}(z)\end{aligned} \tag{2.37}$$

where the distribution function $\mathcal{D}_i(z)$ has the form

$$\mathcal{D}_i(z) = \left[\frac{\ln^i(1-z)}{1-z}\right]_+ \qquad i = 0, 1, 2, \cdots \tag{2.38}$$

The first term in Eq. (2.37) is coming from virtual correction and soft gluon radiation, the second term is the effect of soft and collinear gluon radiation and together these two terms is called soft-virtual (SV) partonic coefficient function. The third term is called regular part which is process dependent and also finite when $z \to 1$. The SV cross section constitutes a significant contribution to the partonic cross section in the limit $z \to 1$ and can be computed order by order in the strong coupling. Here, I represent the incoming partons like quark or gluon. Now, the threshold part can be separated from partonic coefficient as

$$\Delta_{ab}^{I,(n)}(z, Q^2, \mu_F^2, \mu_R^2) = \Delta_{ab,\mathrm{sv}}^{I,(n)}(z, Q^2, \mu_F^2, \mu_R^2) + \Delta_{ab,\mathrm{reg}}^{I,(n)}(z, Q^2, \mu_F^2, \mu_R^2) \tag{2.39}$$

The threshold partonic soft-virtual cross-section to all orders in perturbation theory in z space for the space-time dimensions $d = 4 + \epsilon$ can be written [81, 82] as,

$$\Delta_{\mathrm{sv}}^{I}(z, Q^2, \mu_F^2, \mu_R^2, \epsilon) = \mathcal{C} \exp\left(\Psi^I(z, Q^2, \mu_F^2, \mu_R^2, \epsilon)\right)\Big|_{\epsilon=0}, \qquad I = q, g \tag{2.40}$$

Where Ψ is the distribution function which is finite in the limit $\epsilon \to 0$. The symbol $\mathcal{C}$ represents the Mellin convolution operation (denoted by $\otimes$), and it acts according to the following expansion:

$$\mathcal{C} \exp\left(g(\epsilon)\right) = \delta(1-z) + \frac{1}{1!} g(\epsilon) + \frac{1}{2!} g(\epsilon) \otimes g(\epsilon) + \cdots, \tag{2.41}$$

where $g(\epsilon)$ is a function composed solely of $\delta(1-z)$ and plus distributions. In the threshold limit, the finite part of the exponent above can be re-organized and receives contributions from the form factor $\mathcal{F}^I(\hat{a}_s, q^2, \mu^2, \epsilon)$ (with $q^2 = -Q^2$), the soft-collinear function $\Phi^I(\hat{a}_s, Q^2, \mu_F^2, \epsilon)$ (referred to later as the soft function), and the mass factorization kernels $\Gamma_I(\hat{a}_s, \mu_F^2, \mu^2, \epsilon)$. In dimensional regularization, it can be expressed as:

$$\begin{aligned}\Psi^I(z, Q^2, \mu_F^2, \mu_R^2, \epsilon) = &\left(\ln\left[Z^I(\hat{a}_s, \mu_R^2, \mu_0^2, \epsilon)\right]^2 + \ln\left[\mathcal{F}^I(\hat{a}_s, Q^2, \mu_0^2, \epsilon)\right]\right)\delta(1-z) \\ &+ 2\Phi^I(\hat{a}_s, Q^2, \mu_F^2, \epsilon) - 2m\mathcal{C}\ln\Gamma_I(\hat{a}_s, \mu_F^2, \mu_0^2, \epsilon).\end{aligned} \tag{2.42}$$

In the above Eq. (2.42) $m = 1$ for Drell-Yan and Higgs productions cases and $m = 1/2$ for DIS case. Whereas $\hat{a}_s$ is the unrenormalised (bare) strong coupling constant is define as $\hat{a}_s = \frac{\hat{g}_s^2}{16\pi^2}$. Where $\hat{g}_s$ denotes the strong coupling constant, which remains dimensionless in $d = 4+\epsilon$ space-time dimensions. The parameter μ_0 is introduced through dimensional regularisation to ensure that the bare coupling $\hat{g}_s$ retains its dimensionless character in d dimensions.

The bare coupling constant $\hat{a}_s$ is connected to the renormalised coupling through the in Eq. (2.7).

Operator renormalization

The quantities $Z^I(\hat{a}_s, \mu_R^2, \mu_0^2, \epsilon)$ represent the overall renormalisation constants associated with the corresponding operators. In the case of the vector current, the renormalisation factor is trivial, i.e., $Z^q(\hat{a}_s, \mu_R^2, \mu_0^2) = 1$. However, for the gluonic operator is a non-trivial overall renormalisation factor is required, and the gluonic operator renormalisation factor [203] for the gluon fusion Higgs production case is

$$\begin{aligned} Z^g(\hat{a}_s, \mu_R^2, \mu_0^2, \epsilon) &= 1 + \hat{a}_s \left(\frac{\mu_R^2}{\mu_0^2}\right)^{\frac{\epsilon}{2}} S_\epsilon \left[\frac{2\beta_0}{\epsilon}\right] + \hat{a}_s^2 \left(\frac{\mu_R^2}{\mu_0^2}\right)^{\epsilon} S_\epsilon^2 \left[\frac{2\beta_1}{\epsilon}\right] \\ &\quad + \hat{a}_s^3 \left(\frac{\mu_R^2}{\mu_0^2}\right)^{3\frac{\epsilon}{2}} S_\epsilon^3 \left[\frac{1}{\epsilon^2}\Big(-2\beta_0\beta_1\Big) + \frac{2\beta_2}{\epsilon}\right] \end{aligned} \tag{2.43}$$

The form factor

The unrenormalised form factors $\hat{\mathcal{F}}^I(\hat{a}_s, Q^2, \mu_0^2)$ associated with both fermionic and gluonic operators follow an integro-differential equation. This equation emerges as a consequence of gauge invariance and the principles of the renormalisation group [204–207]. The form of the equation in dimensional regularization is,

$$Q^2 \frac{d}{dQ^2} \ln \hat{\mathcal{F}}^I\left(\hat{a}_s, Q^2, \mu_0^2, \epsilon\right) = \frac{1}{2}\left[\mathcal{K}^I\left(\hat{a}_s, \frac{\mu_R^2}{\mu_0^2}, \epsilon\right) + \mathcal{G}^I\left(\hat{a}_s, \frac{Q^2}{\mu_R^2}, \frac{\mu_R^2}{\mu_0^2}, \epsilon\right)\right] \tag{2.44}$$

where $\mathcal{K}^I$ contains all the negative powers of ϵ i.e. poles. On the other hand, $\mathcal{G}^I$ collects the rest of the terms that are finite when ϵ becomes zero. In other words, $\mathcal{G}^I$ contains only non-negative powers of ϵ. Since $\hat{\mathcal{F}}^I$ is follow the RG equation, we find that

$$\mu_R^2 \frac{d}{d\mu_R^2} \mathcal{K}^I \left(\hat{a}_s, \frac{\mu_R^2}{\mu_0^2}, \epsilon \right) = -A^I(a_s(\mu_R^2))$$

$$\mu_R^2 \frac{d}{d\mu_R^2} \mathcal{G}^I \left(\hat{a}_s, \frac{Q^2}{\mu_R^2}, \frac{\mu_R^2}{\mu_0^2}, \epsilon \right) = A^I(a_s(\mu_R^2)) \tag{2.45}$$

The functions A^I represent the conventional cusp anomalous dimensions and can be expressed as a perturbative series in the renormalized strong coupling constant $a_s(\mu_R^2)$:

$$A^I(\mu_R^2) = \sum_{k=1}^{\infty} a_s^k(\mu_R^2)\ A_k^I \tag{2.46}$$

The total derivative is given by

$$\mu_R^2 \frac{d}{d\mu_R^2} = \mu_R^2 \frac{\partial}{\partial \mu_R^2} + \frac{da_s(\mu_R^2)}{d\mu_R^2} \frac{\partial}{\partial a_s(\mu_R^2)} \tag{2.47}$$

The RG equations of $\mathcal{K}^I$ can be solved in powers of the bare coupling constant $\hat{a}_s$ as

$$\mathcal{K}^I \left(\hat{a}_s, \frac{\mu_R^2}{\mu_0^2}, \epsilon \right) = \sum_{k=1}^{\infty} \hat{a}_s^k \left(\frac{\mu_R^2}{\mu_0^2} \right)^{k\frac{\epsilon}{2}} S_\epsilon^k\ \mathcal{K}^{I,(k)}(\epsilon) \tag{2.48}$$

The explicit expression of the coefficients $\mathcal{K}^{I,(k)}$ are given in Appendix A.2.

Similarly, RG equations for $\mathcal{G}^I$ can also be solved, yielding the following solution:

$$\begin{aligned} \mathcal{G}^I \left(\hat{a}_s, \frac{Q^2}{\mu_R^2}, \frac{\mu_R^2}{\mu_0^2}, \epsilon \right) &= \mathcal{G}^I \left(a_s(\mu_R^2), \frac{Q^2}{\mu_R^2}, \epsilon \right) \\ &= \mathcal{G}^I \left(a_s(Q^2), 1, \epsilon \right) + \int_{\frac{Q^2}{\mu_R^2}}^{1} \frac{d\lambda^2}{\lambda^2} A^I \left(a_s(\lambda^2 \mu_R^2) \right) \end{aligned} \tag{2.49}$$

The integral in Eq. (2.49) can be performed, and solution to be

$$\int_{\frac{Q^2}{\mu_R^2}}^{1} \frac{d\lambda^2}{\lambda^2} A^I \left(a_s(\lambda^2 \mu_R^2) \right) = \sum_{i=1}^{\infty} \hat{a}_s^i \left(\frac{\mu_R^2}{(\mu_0)^2} \right)^{i\frac{\epsilon}{2}} \left[\left(\frac{Q^2}{\mu_R^2} \right)^{i\frac{\epsilon}{2}} - 1 \right] S_\epsilon^i\ \mathcal{K}^{I,(i)}(\epsilon) \tag{2.50}$$

The function $\mathcal{G}^I(a_s(Q^2), 1, \epsilon)$, this also admits a perturbative expansion in powers of $a_s(Q^2)$, given by

$$\mathcal{G}^I(a_s(Q^2), 1, \epsilon) = \sum_{k=1}^{\infty} a_s^k(Q^2)\ \mathcal{G}_k^I(\epsilon) \tag{2.51}$$

By inserting these solutions into Eq. (2.44) and carrying out the remaining integration, we arrive at the final expression:

$$\ln \hat{\mathcal{F}}^I(\hat{a}_s, Q^2, \mu_0^2, \epsilon) = \sum_{k=1}^{\infty} \hat{a}_s^k \left(\frac{Q^2}{\mu_0^2}\right)^{k\frac{\epsilon}{2}} S_\epsilon^k\ \hat{\mathcal{L}}_{\mathcal{F}}^{I,(k)}(\epsilon) \tag{2.52}$$

The explicit expressions of the coefficients $\hat{\mathcal{L}}_{\mathcal{F}}^{I,(k)}$ are given in Appendix A.2 in Eq. (A.12).

The result presented above is consistent with the findings of [208], where various algorithms for evaluating nested sums were employed. The cusp anomalous dimensions, A_k^I and $\mathcal{G}_k^I(\epsilon)$, are known up to the third order in the strong coupling constant a_s. Notably, the cusp anomalous dimensions exhibit a maximally non-Abelian structure and leading to the following relation:

$$A^q = \frac{C_F}{C_A}\ A^g \tag{2.53}$$

The expressions for the coefficients $\mathcal{G}_k^I(\epsilon)$, corresponding to both $I = q$ and $I = g$, are available in [209] with the necessary powers in the dimensional regulator ϵ. These coefficients follow

$$\begin{aligned}
\mathcal{G}_1^I(\epsilon) &= 2(B_1^I - \delta_{I,g}\beta_0) + f_1^I + \sum_{l=1}^{\infty} \epsilon^l {g_1}^{I,l} \\
\mathcal{G}_2^I(\epsilon) &= 2(B_2^I - 2\delta_{I,g}\beta_1) + f_2^I - 2\beta_0 {g_1}^{I,1} + \sum_{l=1}^{\infty} \epsilon^l {g_2}^{I,l} \\
\mathcal{G}_3^I(\epsilon) &= 2(B_3^I - 3\delta_{I,g}\beta_2) + f_3^I - 2\beta_1 {g_1}^{I,1} - 2\beta_0\Big({g_2}^{I,1} + 2\beta_0 {g_1}^{I,2}\Big) \\
&\quad + \sum_{l=1}^{\infty} \epsilon^l {g_3}^{I,l}
\end{aligned} \tag{2.54}$$

The coefficients B_k^I have been determined up to $\mathcal{O}(a_s^3)$, made possible by the advancement in the calculation of three-loop anomalous dimensions and splitting functions in [210, 211].

The constants f_k^I share similarities with the cusp anomalous dimensions A_k^I as in Eq. (2.53) that appear in the form factors. It was shown in [212] that the single pole (in ϵ) in the logarithm of form factors up to two loops (i.e., order a_s^2) can be traced back to these f_k^I constants. They exhibit a maximally non-Abelian structure, satisfying the relation

$$f_k^q = \frac{C_F}{C_A} f_k^g, \tag{2.55}$$

which mirrors the behavior of the A_k^I terms. This proportionality has been confirmed to persist even at the three-loop level, as demonstrated in [209].

Splitting function

The collinear divergences arise from massless partons, particularly when their emissions are parallel with the incoming partons. These collinear divergences are systematically removed by incorporating them into the bare parton distribution functions (PDFs). This yields renormalized PDFs, which are finite and physically observable. The process, known as mass factorization, is carried out at the factorization scale μ_F. As mentioned earlier in Eq. (2.17), this procedure introduces mass factorization kernels Γ_I, which effectively absorb the initial-state collinear divergences. Within the $\overline{MS}$ scheme, these kernels satisfy the following renormalization group (RG) equation:

$$\mu_F^2 \frac{d}{d\mu_F^2} \Gamma_{ab}(z, \mu_F^2, \epsilon) = \frac{1}{2} \sum_c P_{ac}\left(z, \mu_F^2\right) \otimes \Gamma_{cb}\left(z, \mu_F^2, \epsilon\right) \tag{2.56}$$

Where $P_{ab}(z, \mu_F^2)$ are known as Altarelli-Parisi splitting functions (matrix valued) and both are perturbatively expanded in powers of the strong coupling constant, $P_{ab}(z, \mu_F^2)$ known up to three loop level [210, 211]:

$$P_{ab}(z, \mu_F^2) = \sum_{i=1}^{\infty} a_s^i(\mu_F^2) P_{ab}^{(i-1)}(z) \tag{2.57}$$

Since we are focusing only on the SV part of the cross section. So, only the diagonal terms of splitting function contributes to our analysis, hence non-diagonal terms that arise beyond SV are neglected. The diagonal terms of splitting functions $P_I(z)$ $(a = b = I)$ have the following structure

$$P_I^{(i)}(z) = 2\left[B_{i+1}^I \delta(1-z) + A_{i+1}^I \mathcal{D}_0\right] + P_{reg,I}^{(i)}(z) \tag{2.58}$$

The functions $P^{(i)}_{reg,I}$ remain finite in the kinematic limit where $z \to 1$. The renormalization group equation (RGE) for the kernel can be addressed using dimensional regularization, with a perturbative expansion in the strong coupling constant. Since our focus lies on the soft and virtual components of the cross section, only the diagonal elements of the kernel are relevant. In the $\overline{MS}$ renormalization scheme, the kernel exclusively contains divergences in the form of ϵ-poles. The kernel can thus be expressed as a series in terms of the bare coupling $\hat{a}_s$,

$$\Gamma_I(z, \mu_F^2, \epsilon) = \delta(1-z) + \sum_{k=1}^{\infty} \hat{a}_s^k \left(\frac{\mu_F^2}{\mu_0^2}\right)^{k\frac{\epsilon}{2}} S_\epsilon^k \Gamma_I^{(k)}(z, \epsilon) \tag{2.59}$$

After solving the RG equation for the kernels, the solutions in the $\overline{MS}$ scheme are given in Appendix A.2 in Eq. (A.13). These parameters are universal in nature and remain unaffected by the choice of operator insertion.

Soft Distribution function

The IR structure of pure virtual amplitudes is known to be completely universal and does not depend on the number of external colorless particles. Consequently, in order to yield a finite cross section, the combined effects arising from real emission processes and mass factorization must also adhere to this universal behavior. By leveraging this universality and enforcing the requirement of cross-section finiteness, we can isolate the universal part of these contributions. This enables us to construct the soft-virtual (SV) cross section, which we discuss next.

The soft distribution functions $\Phi^I_{sv}(\hat{a}_s, Q^2, \mu_0^2, z)$ can be systematically derived using the known results up to three loops for the form factors $\hat{\mathcal{F}}^I$, the evolution kernels Γ_I, and the coefficient functions Δ^I_{sv}.

Since Δ^I_{sv} remains finite as $\epsilon \to 0$, it follows that Φ^I must exhibit a pole structure in ϵ analogous to that of $\hat{\mathcal{F}}^I$ and Γ_I. Furthermore, the soft functions $\Phi^I_{sv}(\hat{a}_s, Q^2, \mu_0^2, z)$ follow the renormalization group equation:

$$\mu_R^2 \frac{d}{d\mu_R^2} \Phi^I_{sv}(\hat{a}_s, Q^2, \mu_0^2, z, \epsilon) = 0 \tag{2.60}$$

Based on the preceding insights, it is reasonable to anticipate that the soft distribution functions also follow an integro-differential equation of the Sudakov type—similar to the one satisfied by the form factors $\hat{\mathcal{F}}^I(Q^2)$ (similar to Eq. (2.44)). Therefore,

$$Q^2\frac{d}{dQ^2}\Phi^I_{sv}(\hat{a}_s, Q^2, \mu_0^2, z, \epsilon) = \frac{1}{2}\left[\overline{K}^{\,I}\left(\hat{a}_s, \frac{\mu_R^2}{\mu_0^2}, z, \epsilon\right) + \overline{G}^{\,I}\left(\hat{a}_s, \frac{Q^2}{\mu_R^2}, \frac{\mu_R^2}{\mu_0^2}, z, \epsilon\right)\right] \tag{2.61}$$

where $\overline{K}^{\,I}$ contains all the poles terms i.e. negative powers of ϵ and $\overline{G}^{\,I}$ are contains the finite functions of ϵ. Then RG invariance leads to

$$-\mu_R^2\frac{d}{d\mu_R^2}\overline{K}^I\left(\hat{a}_s, \frac{\mu_R^2}{\mu_0^2}, z, \epsilon\right) = \mu_R^2\frac{d}{d\mu_R^2}\overline{G}^I\left(\hat{a}_s, \frac{Q^2}{\mu_R^2}, \frac{\mu_R^2}{\mu_0^2}, z, \epsilon\right) = \overline{A}^I(a_s(\mu_R^2))\delta(1-z) \tag{2.62}$$

In order for the soft distribution functions $\Phi^I_{sv}(\hat{a}_s, Q^2, \mu^2, z, \epsilon)$ to provide the necessary pole structure that cancels the divergences originating from the form factors $\hat{\mathcal{F}}^I$, the renormalization constants Z^I, and the mass factorization kernels Γ_I to ensuring the finiteness of Δ^I_{sv} in Eq. (2.40), then the functions $\overline{A}^{\,I}$ must satisfy the following condition:

$$\overline{A}^{\,I} = -A^I \tag{2.63}$$

In analogy with Eq. (2.48), we carry out an expansion of $\overline{K}^I$ in terms of $\hat{a}_s$ as follows:

$$\overline{K}^I\left(\hat{a}_s, \frac{\mu_R^2}{\mu_0^2}, z, \epsilon\right) = \delta(1-z) + \sum_{k=1}^{\infty}\hat{a}_s^k\left(\frac{\mu_R^2}{\mu_0^2}\right)^{k\epsilon}\overline{K}^{I,(k)}(\epsilon), \tag{2.64}$$

where each $\overline{K}^{I,(k)}(\epsilon)$ denotes the k-loop contribution. The structure of the solutions, as shown in [81] and it related to $\mathcal{K}^{I,(k)}$ in Eq. (A.11) as :

$$\overline{K}^{I,(k)}(\epsilon) = -\mathcal{K}^{I,(k)}(\epsilon) \tag{2.65}$$

Similarly, this approach is extended to solve the renormalization group equation (RGE) for $\overline{G}^I$.

$$\begin{aligned}\overline{G}^I\left(\hat{a}_s, \frac{Q^2}{\mu_R^2}, \frac{\mu_R^2}{\mu_0^2}, z, \epsilon\right) &= \overline{G}^I\left(a_s(\mu_R^2), \frac{Q^2}{\mu_R^2}, z, \epsilon\right) \\ &= \overline{G}^I\left(a_s(Q^2), 1, z, \epsilon\right) - \delta(1-z)\int_{\frac{Q^2}{\mu_R^2}}^1 \frac{d\lambda^2}{\lambda^2}A^I\left(a_s(\lambda^2\mu_R^2)\right)\end{aligned}$$

Now it is now straight forward to determine all $\overline{G}^{\,I}(a_s(Q^2), 1, z, \epsilon)$ from the available informations. The functions $\overline{G}^{\,I}(a_s(Q^2), 1, z, \epsilon)$ can be expanding in powers of $a_s(Q^2)$ as

$$\overline{G}^{\,I}(a_s(Q^2), 1, z, \epsilon) = \sum_{k=1}^{\infty} a_s^k(Q^2)\, \overline{G}_k^{\,I}(z, \epsilon) \tag{2.66}$$

The solution of the soft function to the Eq. (2.61) can be obtained as for $\ln \hat{\mathcal{F}}^I(Q^2)$ in Eq. (2.52). Expanding the soft distribution functions in powers of bare coupling $\hat{a}_s$ as

$$\Phi^I\left(\hat{a}_s, Q^2, \mu_0^2, z, \epsilon\right) = \sum_{k=1}^{\infty} \hat{a}_s^k \left(\frac{Q^2}{\mu_0^2}\right)^{k\frac{\epsilon}{2}} S_\epsilon^k\, \hat{\Phi}^{I,(k)}(z, \epsilon) \tag{2.67}$$

The solution should be:

$$\hat{\Phi}^{I,(k)}(z, \epsilon) = \hat{\mathcal{L}}_{\mathcal{F}}^{I,(k)}(\epsilon)\left(A_k^I \to -\delta(1-z)\; A_k^I,\;\; \mathcal{G}_k^I(\epsilon) \to \overline{G}_k^{\,I}(z, \epsilon)\right) \tag{2.68}$$

The finite functions $\overline{G}_k^{\,I}(z, \epsilon)$ can be determined by applying the mass factorisation formalism, ensuring that the corresponding coefficient functions $\Delta_{sv}^{I,(k)}$ remain finite. Due to the renormalisation group (RG) invariance of the soft functions and the straightforward rescaling of the momentum, $Q \to (1-z)Q$, it follows that the expansion below also satisfies the associated integro-differential equation:

$$\begin{aligned}
\Phi_{sv}^I(\hat{a}_s, Q^2, \mu_0^2, z, \epsilon) &= \Phi_{sv}^I(\hat{a}_s, Q^2(1-z)^2, \mu_0^2, \epsilon) \\
&= \sum_{k=1}^{\infty} \hat{a}_s^k \left(\frac{Q^2(1-z)^2}{\mu_0^2}\right)^{k\frac{\epsilon}{2}} S_\epsilon^k \left(\frac{k\,\epsilon}{1-z}\right) \hat{\phi}^{\,I,(k)}(\epsilon)
\end{aligned} \tag{2.69}$$

For convenience, we redefine the functions by using $\overline{\mathcal{G}}_k^I(\epsilon)$ in place of $\overline{G}_k^I(\epsilon)$, where both are connected through the relation:

$$\sum_{k=1}^{\infty} a_s^k \left(\frac{Q^2(1-z)^2}{\mu_0^2}\right)^{k\epsilon} \overline{\mathcal{G}}_k^I(\epsilon) = \sum_{k=1}^{\infty} \hat{a}_s^k \left(\frac{Q^2(1-z)^2}{\mu_0^2}\right)^{k\epsilon} S_\epsilon^k \overline{G}_k^I(\epsilon), \tag{2.70}$$

then

$$\hat{\phi}^{I,(k)}(\epsilon) = \hat{\mathcal{L}}_F^{I,(k)}(\epsilon)\left(A_k^I \to -A_k^I, \mathcal{G}_k^I(\epsilon) \to \overline{\mathcal{G}}_k^I(\epsilon)\right) \tag{2.71}$$

The explicit expression of the soft functions $\hat{\phi}^{I,(k)}$ is given in Apppendix A.2 in Eq. (A.14). The z-independent constants $\overline{\mathcal{G}}^I(\epsilon)$ appearing in $\hat{\phi}^{\,I,(k)}(\epsilon)$ can be determined by utilizing the form factors, mass factorization kernels, and coefficient functions $\Delta_{sv}^{I,(k-1)}$, each expanded in powers of ϵ to the required precision. This determination is done by matching both the pole and finite parts in ϵ of $\hat{\phi}^{\,I,(k)}(\epsilon)$ with those arising from the form factors, the overall renormalization constants, the splitting functions, and the lower-order contributions from $\Delta_{sv}^{I,(k-1)}$. As a result, we obtain

$$\begin{aligned}
\overline{\mathcal{G}}_1^{\,I}(\epsilon) &= -f_1^I + \sum_{j=1}^{\infty} \epsilon^j \overline{\mathcal{G}}_1^{\,I,(j)} \\
\overline{\mathcal{G}}_2^{\,I}(\epsilon) &= -f_2^I - 2\beta_0 \overline{\mathcal{G}}_1^{\,I,(1)} + \sum_{j=1}^{\infty} \epsilon^j \overline{\mathcal{G}}_2^{\,I,(j)} \\
\overline{\mathcal{G}}_3^{\,I}(\epsilon) &= -f_3^I - 2\beta_1 \overline{\mathcal{G}}_1^{\,I,(1)} - 2\beta_0 \left(\overline{\mathcal{G}}_2^{\,I,(1)} + 2\beta_0 \overline{\mathcal{G}}_1^{\,I,(2)}\right) + \sum_{j=1}^{\infty} \epsilon^j \overline{\mathcal{G}}_3^{\,I,(j)}
\end{aligned} \tag{2.72}$$

The explicit expression of the coefficients $\overline{\mathcal{G}}_k^{I,(j)}$ in Eq. (2.72) are given in Appendix A.2 in Eq. (A.15).

Using such compensating $\hat{\phi}^{I,(i)}(\epsilon)$ and the following expansion,

$$\frac{1}{1-z}\left[(1-z)^2\right]^{i\frac{\epsilon}{2}} = \frac{1}{i\epsilon}\delta(1-z) + \sum_{j=0}^{\infty} \frac{(i\epsilon)^j}{j!}\mathcal{D}_j \tag{2.73}$$

we obtain $\overline{G}_i^{\,I}(z,\epsilon)$ upto three loop level. We find that the finite functions $\overline{G}_i^{\,I}(z,\epsilon)$ have the following decomposition in terms of cusp anomalous dimension A_i^I and f_i^I that appear in the form factors :

$$\begin{aligned}
\overline{G}_1^{\,I} &= -f_1^I\ \delta(1-z) + 2A_1^I\ \mathcal{D}_0 + \sum_{k=1}^{\infty} \epsilon^k \overline{g}_1^{\,I,k}(z) \\
\overline{G}_2^{\,I} &= -f_2^I\ \delta(1-z) + 2A_2^I\ \mathcal{D}_0 - 2\beta_0\ \overline{g}_1^{\,I,1}(z) + \sum_{k=1}^{\infty} \epsilon^k\ \overline{g}_2^{\,I,k}(z) \\
\overline{G}_3^{\,I} &= -f_3^I\ \delta(1-z) + 2A_3^I\ \mathcal{D}_0 - 2\beta_1\ \overline{g}_1^{\,I,1}(z) - 2\beta_0\Big(\overline{g}_2^{\,I,1}(z) + 2\beta_0\ \overline{g}_1^{\,I,2}(z)\Big) \\
&\quad + \sum_{k=1}^{\infty} \epsilon^k\ \overline{g}_3^{\,I,k}(z)
\end{aligned} \tag{2.74}$$

The explicit expression of anomalous given in Appendix B.2 and the coefficients $\overline{g}_k^{\,I,j}$ in Eq. (2.74) are given in Appendix A.2 in Eq. (A.16).

We observe that the soft distribution functions corresponding to DY and Higgs production processes exhibit maximal non-Abelian characteristics, specifically:

$$\Phi^q(\hat{a}_s, Q^2, \mu_0^2, z, \epsilon) = \frac{C_F}{C_A}\,\Phi^g(\hat{a}_s, Q^2, \mu_0^2, z, \epsilon) \tag{2.75}$$

up to three-loop order. However, this feature does not persist at the level of the cross section corrections ($\Delta^I_{\rm sv}$), which do not share this non-Abelian proportionality due to the form factors,. The universal nature of the soft distribution function becomes evident when we observe that, after factoring out the Born-level contribution, the soft part of the cross section remains unaffected by the spin, color, flavor, or any other quantum numbers. Its dependence lies solely on the gauge group underlying the interaction, such as SU(N). Consequently, once the soft distribution function is determined for a particular process, for example, Higgs boson production via gluon fusion, this universality allows us to infer the soft distribution functions for other related processes as well.

2.4.2 Next-to-soft distribution function

The expression presented in Eq. (2.76) serves as a foundational formula for systematically deriving soft-virtual (SV) and next-to-soft virtual (NSV) corrections to Δ^I at successive orders in perturbation theory, whereas in Eq. (2.40) presents only SV terms. Its utility lies in the fact that, once the relevant components in Eq. (2.42) are determined with sufficient precision, this formulation enables one to extract specific SV and NSV terms to all orders in the strong coupling constant a_s using results computed at lower orders.

$$\Delta^I(z, Q^2, \mu_F^2, \mu_R^2, \epsilon) = C \exp\left(\Psi^I(z, Q^2, \mu_F^2, \mu_R^2, \epsilon)\right)\Big|_{\epsilon=0}, \quad I = q, g \tag{2.76}$$

With the complete set of information on the SV coefficients at hand, we now proceed to analyze the structure of $\Phi^I_{\rm nsv}$ in detail using Eq. (2.61).

By subtracting the K+G equation corresponding to the SV part, $\Phi^I_{\rm sv}$, from Eq. (2.61), we find that $\Phi^I_{\rm nsv}$ satisfies the differential equation

$$Q^2 \frac{d}{dQ^2}\Phi^I_{\rm nsv}(\hat{a}_s, Q^2, \mu_R^2, \mu_0^2, z, \epsilon) = \frac{1}{2}\overline{G}^I_L\left(\hat{a}_s, \frac{Q^2}{\mu_R^2}, \frac{\mu_R^2}{\mu_0^2}, z, \epsilon\right), \tag{2.77}$$

where $\overline{G}^I_L$ is defined as the difference

$$\overline{G}^I_L = \overline{G}^I - \overline{G}^I_{\rm sv}, \tag{2.78}$$

and admits the perturbative expansion

$$\overline{G}_L^I\left(\hat{a}_s, \frac{Q^2}{\mu_R^2}, \frac{\mu_R^2}{\mu_0^2}, z, \epsilon\right) = \sum_{k=1}^{\infty} \hat{a}_s^k \left(\frac{Q^2(1-z)^2}{\mu_R^2}\right)^k S_\epsilon^k \overline{G}_L^{I,(k)}(z,\epsilon). \tag{2.79}$$

Integrating Eq. (2.77), we obtain the structure of Φ^I_{nsv}:

$$\Phi^I_{\text{nsv}}(\hat{a}_s, \mu_0^2, Q^2, z, \epsilon) = \sum_{k=1}^{\infty} \hat{a}_s^k \left(\frac{Q^2(1-z)^2}{\mu_0^2}\right)^{k\epsilon} S_\epsilon^k \, \phi_k^I(z,\epsilon). \tag{2.80}$$

The coefficients $\phi_k^I(z,\epsilon)$ in Eq. (2.80) can be decomposed into singular and finite parts in ϵ:

$$\phi_k^I(z,\epsilon) = \phi_{s,k}^I(z,\epsilon) + \phi_{f,k}^I(z,\epsilon), \tag{2.81}$$

where the singular part, $\phi_{s,k}^I$, follows a structure analogous to Eq. (2.48) with the replacement

$$\phi_{s,k}^I(z,\epsilon) = \mathcal{K}^{I,(k)}(\epsilon)\Big|_{A^I \to -L^I(z)}, \tag{2.82}$$

where $L^I(a_s(\mu_R^2), z)$ can be expanded in powers of $a_s(\mu_R^2)$ as

$$L^I(a_s(\mu_R^2), z) = \sum_{k=1}^{\infty} a_s^k(\mu_R^2) L_k^I(z). \tag{2.83}$$

The finite part $\phi_{f,k}^I(z,\epsilon)$ remains regular in the limit $\epsilon \to 0$, and it can be expressed in terms of the finite coefficients $G_{L,k}^I(z,\epsilon)$ as well. The finite contributions $\phi_{f,k}^I(z,\epsilon)$ to the non-soft-virtual (NSV) part are given order-by-order by

$$\begin{aligned}
\phi_{f,1}^I(z,\epsilon) &= \frac{1}{\epsilon}\overline{G}_L^{I,(1)}(z,\epsilon),\\
\phi_{f,2}^I(z,\epsilon) &= \frac{1}{\epsilon^2}\left(-\beta_0\overline{G}_L^{I,(1)}(z,\epsilon)\right) + \frac{1}{2\epsilon}\left(\overline{G}_L^{I,(2)}(z,\epsilon)\right),\\
\phi_{f,3}^I(z,\epsilon) &= \frac{1}{\epsilon^3}\left(\frac{4}{3}\beta_0^2\overline{G}_L^{I,(1)}(z,\epsilon)\right) - \frac{1}{\epsilon}\left(\frac{1}{3}\beta_1\overline{G}_L^{I,(1)}(z,\epsilon) + \frac{4}{3}\beta_0\overline{G}_L^{I,(2)}(z,\epsilon)\right) + \frac{1}{3\epsilon}\overline{G}_L^{I,(3)}(z,\epsilon),\\
\phi_{f,4}^I(z,\epsilon) &= \frac{1}{\epsilon^4}\left(-2\beta_0^3\overline{G}_L^{I,(1)}(z,\epsilon)\right) + \frac{1}{\epsilon^3}\left(\frac{4}{3}\beta_0\beta_1\overline{G}_L^{I,(1)}(z,\epsilon) + 3\beta_0^2\overline{G}_L^{I,(2)}(z,\epsilon)\right)\\
&\quad \frac{1}{\epsilon^2}\left(-\frac{1}{6}\beta_2\overline{G}_L^{I,(1)}(z,\epsilon) - \frac{1}{2}\beta_1\overline{G}_L^{I,(2)}(z,\epsilon) - \frac{3}{2}\beta_0\overline{G}_L^{I,(3)}(z,\epsilon)\right) + \frac{1}{4\epsilon}\overline{G}_L^{I,(4)}(z,\epsilon).
\end{aligned} \tag{2.84}$$

The $\overline{G}^{I,(k)}_{L}(z,\epsilon)$ are expressed as

$$\overline{G}^{I,(k)}_{L}(z,\epsilon) = \chi^{I,(k)}_{L}(z) + \sum_{i=1}^{\infty} \epsilon^{i} \overline{G}^{I,(k)}_{L,i}(z), \tag{2.85}$$

where the $\chi^{I,(k)}_{L}(z)$ coefficients are given in terms of coefficients $\overline{G}^{I,(k)}_{L,i}(z)$ in Appendix A.3 in Eq. (A.17).

Here, the terms $\overline{G}^{I,(k)}_{L,i}(z)$ are expanded in powers of $\ln(1-z)$:

$$\overline{G}^{I,(k)}_{L,i}(z) = \sum_{j=0}^{k+i-1} \overline{G}^{I,(k,j)}_{L,i} \ln^{j}(1-z), \tag{2.86}$$

where the upper limit $k+i-1$ reflects the perturbative order and ϵ dependence.

The NSV part $\Phi^{I}_{\rm nsv}$ can thus be reorganized as

$$\Phi^{I}_{\rm nsv}(\hat{a}_s, \mu_0^2, q^2, z, \epsilon) = \int_{\mu_F^2}^{Q^2(1-z)^2} \frac{d\lambda^2}{\lambda^2} \Big(L^{I}(a_s(\lambda^2), z) + \phi^{I,f}(a_s(Q^2(1-z)^2), z, \epsilon) \Big) \\ + \phi^{I,s}(a_s(\mu_F^2), z, \epsilon), \tag{2.87}$$

where L^I is finite as $\epsilon \to 0$ and $\phi^{I,s}$ contains the $1/\epsilon$ divergences. For $c = f, s$, the function $\phi^{I}_{c}(a_s(\lambda^2), z)$ is given by:

$$\phi^{I}_{c}(a_s(\lambda^2), z, \epsilon) = \sum_{k=1}^{\infty} \hat{a}_s^{k} \left(\frac{\lambda^2}{\mu_0^2}\right)^{k\frac{\epsilon}{2}} \phi^{I}_{c,k}(z,\epsilon), \tag{2.88}$$

Renormalization group invariance of $\Phi^{I}_{\rm nsv}$ leads to

$$\mu_F^2 \frac{d}{d\mu_F^2} \phi^{I,s}(a_s(\mu_F^2), z) = L^{I}(a_s(\mu_F^2), z). \tag{2.89}$$

Since Ψ^I (defined earlier) must be finite order-by-order in a_s as $\epsilon \to 0$, we find the structure of L^I to be

$$L^{I}(a_s, z) = \sum_{k=1}^{\infty} a_s^{k} \left(C^{I}_{k} \ln(1-z) + D^{I}_{k} \right), \tag{2.90}$$

identifying C^I_k and D^I_k with the NSV components of the Altarelli-Parisi splitting functions.

Their relation with cusp (A_k^I) and collinear (B_k^I) anomalous dimensions reads:

$$\begin{aligned}
&C_1^I = 0, && D_1^I = -A_1^I, \\
&C_2^I = (A_1^I)^2, && D_2^I = -A_2^I + A_1^I\left(B_1^I - \beta_0\right), \\
&C_3^I = 2A_1^I A_2^I, && D_3^I = -A_3^I + A_1^I\left(B_2^I - \beta_1\right) + A_2^I\left(B_1^I - \beta_0\right).
\end{aligned} \tag{2.91}$$

Expanding the finite contribution $\phi^{I,f}$ in a_s, we have

$$\begin{aligned}
\phi^{I,f}(a_s(Q^2(1-z)^2), z) &= \sum_{k=1}^{\infty} a_s^k(Q^2(1-z)^2)\bar{\phi}_k^I(z), \\
\bar{\phi}_k^I(z) &= \sum_{j=0}^{k} \bar{\phi}_k^{I,(j)} \ln^j(1-z),
\end{aligned} \tag{2.92}$$

where coefficients $\bar{\phi}_k^{I,(j)}$ are determined in terms of the unrenormalized $\overline{G}_{L,i}^{I,(k,j)}$.

Explicitly,

$$\begin{aligned}
\bar{\phi}_1^{I,(j)} &= \overline{G}_{L,1}^{I,(1,j)}, \quad (j = 0, 1), \\
\bar{\phi}_2^{I,(j)} &= \frac{1}{2}\overline{G}_{L,1}^{I,(2,j)} + \beta_0 \overline{G}_{L,2}^{I,(1,j)}, \quad (j = 0, 1, 2), \\
\bar{\phi}_3^{I,(j)} &= \frac{1}{3}\overline{G}_{L,1}^{I,(3,j)} + \frac{2}{3}\beta_1 \overline{G}_{L,2}^{I,(1,j)} + \frac{2}{3}\beta_0 \overline{G}_{L,2}^{I,(2,j)} + \frac{4}{3}\beta_0^2 \overline{G}_{L,3}^{I,(1,j)}, \quad (j = 0, 1, 2, 3), \\
\bar{\phi}_4^{I,(j)} &= \frac{1}{4}\overline{G}_{L,1}^{I,(4,j)} + \frac{1}{2}\beta_2 \overline{G}_{L,2}^{I,(1,j)} + \frac{1}{2}\beta_1 \overline{G}_{L,2}^{I,(2,j)} + \frac{1}{2}\beta_0 \overline{G}_{L,2}^{I,(3,j)} + 2\beta_0\beta_1 \overline{G}_{L,3}^{I,(1,j)} \\
&\quad + \beta_0^2 \overline{G}_{L,3}^{I,(2,j)} + 2\beta_0^3 \overline{G}_{L,4}^{I,(1,j)}, \quad (j = 0, 1, 2, 3, 4).
\end{aligned} \tag{2.93}$$

Additionally, coefficients like $\overline{G}_{L,2}^{I,(1,3)}$, $\overline{G}_{L,2}^{I,(1,4)}$, $\overline{G}_{L,2}^{I,(2,4)}$, and $\overline{G}_{L,3}^{I,(1,4)}$ are vanish.

The coefficients $\overline{G}^{I,(k,j)}L, i$ can be determined by comparing the known perturbative expansions of Δ^I, $\hat{\mathcal{F}}^I$, Z^I, Φsv^I, and Γ^I in powers of α_s^k, using the double expansion in ϵ^k and $\ln^j(1-z)$.

Specifically, for Drell-Yan and bottom quark annihilation up to $\mathcal{O}(a_s^2)$, the relevant coefficients $\overline{G}_{L,i}^{I,(k,j)}$ in Eq. (2.93) are given in Appendix A.3 in Eq. (A.18). Similarly, for Higgs and ZH production through gluon fusion are given in Eq. (A.19).

It is important to note that, unlike the soft-virtual finite coefficients, the $\overline{G}_{L,i}^{I,(k,j)}$ do not satisfy maximal non-abelian relations beyond one loop.

Recent advancements have yielded third-order contributions to the soft-virtual function Δ^I in the Drell-Yan (DY) process, as reported in [213]. Corresponding results for

Higgs boson production via gluon fusion and bottom quark annihilation were presented in [69, 70, 91]. At this order, the complete expressions for form factors (FFs), anomalous dimensions Γ_I, and soft-virtual terms $\Phi^I_{\rm sv}$ are now available, including the necessary renormalization constants.

These developments allow us, in principle, to extract the relevant soft-virtual coefficients $G^{(L,i)}_{j,k}$ up to three loops. However, due to the absence of full analytic results for the second-order corrections to Δ^q in powers of ϵ, it remains challenging to fully determine the $G^{(L,i)}_{j,k}$ coefficients. Nevertheless, specific linear combinations of these, denoted by $\bar{\phi}^{I,(j)}_k$, can still be obtained for processes with initial states $I = q$ (DY), $I = b$ (bottom fusion), and $I = g$ (gluon fusion), up to the third order.

For example, in the Drell-Yan quark annihilation and in gluon fusion Higgs production process, the extracted coefficients $\bar{\phi}^{I,(j)}_k$ in Eq. (2.93) are given in Appendix A.3 in Eq. (A.20) and Eq. (A.22) respectiely.

Interestingly, although the soft-virtual (SV) functions $\Phi^{\rm nsv}_I$ for quarks and gluons are structurally distinct, they display universality up to second order, i.e., they are independent of the underlying hard scattering process. For instance, $\Phi^{\rm nsv}_q$ for DY matches with that of Higgs production via $b\bar{b}$ annihilation [91]. Similar agreement is found with VH production via quark annihilation:

$$\bar{\phi}^{q,(j)}_k|_{q\bar{q}\to\ell^+\ell^-+X} = \bar{\phi}^{q,(j)}_k|_{q\bar{q}\to VH+X} = \bar{\phi}^{q,(j)}_k|_{b\bar{b}\to H+X}, \quad k = 0, 1, 2.$$

A similar universality is observed for gluon-initiated processes:

$$\bar{\phi}^{g,(j)}_k|_{gg\to H+X} = \bar{\phi}^{g,(j)}_k|_{gg\to ZH+X}, \quad k = 0, 1, 2.$$

However, at the third order, this universality breaks. For example, the coefficient $\bar{\phi}^{(3)}_b$ for $b\bar{b} \to H$ deviates from its DY counterpart for $k = 0, 1$ reported in the thesis [214]:

$$\begin{aligned}
\bar{\phi}^{b,(0)}_3 &= \bar{\phi}^{q,(0)}_3 - 16 C_A C_F \left(C_A - 2C_F\right), \\
\bar{\phi}^{b,(1)}_3 &= \bar{\phi}^{q,(1)}_3 + 8 C_A C_F \left(C_A - 2C_F\right), \\
\bar{\phi}^{b,(k)}_3 &= \bar{\phi}^{q,(k)}_3, \quad \text{for } k = 2, 3.
\end{aligned}$$

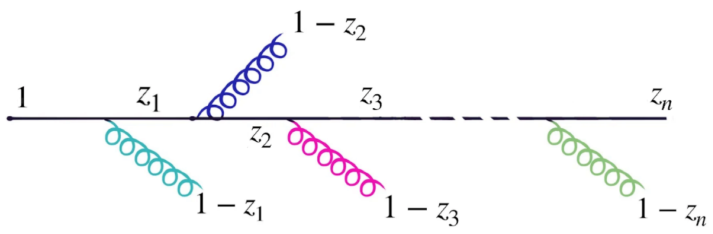

FIGURE 2.2: Emission of n gluons from a quark line, with gluon energy fractions relative to the emitting quark and quark energy fractions measured from the initial quark energy.

The origin of this breaking at third order, especially for $k = 0, 1$, as computed using state-of-the-art higher-order results [69, 70, 91, 213], requires further investigation, potentially within a more refined factorisation framework.

2.4.3 Threshold Resummation

The generic partonic coefficient function Δ^I_{ab} in Eq. (2.37) receives significant contributions in the kinematic region where $z \to 1$, which typically arises due to soft gluon emissions. To illustrate this, let us consider a simplified scenario involving a quark that sequentially emits n gluons, as shown in Fig. 2.2. Each emitted gluon carries away a small fraction of the quark's energy, denoted as $1 - z_i$, where z_i is close to unity. Consequently, after n emissions, the quark retains only a fraction $z = z_1 z_2 \cdots z_n$ of its original energy. This final value of z appears as the argument in the coefficient function. For every gluon emitted, the coefficient function develops terms that become large in the limit $z_i \to 1$, corresponding to soft emissions. When integrating over the phase space of the emitted gluons, these soft enhancements result in singular structures, typically represented by distributions such as $\mathcal{D}$-functions. At the partonic threshold, where the threshold variable z approaches its kinematic limit ($z \to 1$), the threshold corrections become dominant. These corrections appear through distributions such as $\delta(1-z)$ and $\mathcal{D}_i(z)$ as introduced in Eq. (2.37), along with powers of $\ln(1-z)$. As z approaches unity, the logarithmic terms $\ln(1-z)$ grow significantly, whereas the strong coupling constant a_s remains small, making the product $a_s \ln(1-z)$ approximately of order one. Under such circumstances, a fixed-order perturbative expansion is no longer reliable. Therefore, it becomes essential to resum these large logarithmic contributions to all orders. Resummation provides a reorganized perturbative expansion that systematically includes the dominant logarithms at each order, thereby leading to stable and trustworthy predictions even after truncation. It is important to note that the emergence of large logarithms is a consequence of truncating the perturbative series, and a complete all-order summation would yield physically meaningful results.

To develop the resummation formalism, we utilize the structure of the soft-collinear distribution derived in the previous section. By employing the relation in Eq. (2.73) and appropriately factoring out the soft divergences from Eq. (2.69), we arrive at an integral representation for the soft-collinear distribution.

$$
\begin{aligned}
\Phi^I_{\rm sv}(\hat{a}_s, Q^2, \mu_0^2, z, \epsilon) \quad = \quad & \left(\frac{1}{1-z} \left\{ \int_{\mu_R^2}^{Q^2(1-z)^2} \frac{d\lambda^2}{\lambda^2} A^I \left(a_s(\lambda^2)\right) + \overline{G}^I_{\rm sv} \left(a_s \left(Q^2(1-z)^2\right), \epsilon\right) \right\} \right)_+ \\
& + \delta(1-z) \quad \sum_{k=1}^{\infty} \hat{a}_s^k \left(\frac{Q^2}{\mu_0^2}\right)^{k\frac{\epsilon}{2}} S_\epsilon^k \, \hat{\phi}^{I,(k)}(\epsilon) \\
& + \left(\frac{1}{1-z}\right)_+ \quad \sum_{k=1}^{\infty} \hat{a}_s^k \left(\frac{\mu_R^2}{\mu_0^2}\right)^{k\frac{\epsilon}{2}} S_\epsilon^k \, \overline{K}^{I,(k)}(\epsilon)
\end{aligned}
\tag{2.94}
$$

The third line of the above equation precisely cancels the $\mathcal{D}_0$ term arising from the mass factorization kernel. The term $\phi^{I,(k)}$ appearing in the second line contains both divergent (pole) and finite contributions. The pole terms specifically cancel against those from the form factor and the $\delta(1-z)$ component of the mass factorization kernel.

An alternative approach for resumming these large logarithms involves the use of Soft-Collinear Effective Theory (SCET), which has been extensively explored in the literature [215–217]. In this thesis, however, we focus on the traditional resummation method. Direct resummation in z-space poses significant technical difficulties due to the complexity of the convolution integrals involved. In contrast, working in Mellin-N space greatly simplifies the analysis, as the convolutions transform into ordinary products. This simplification enables a systematic resummation of the dominant logarithmic contributions to all orders. In the subsequent discussion, we outline the procedure for implementing the resummation in Mellin-N space.

Mellin Transformation

Given that the integrand consists of multiple convolutions, it is advantageous to perform the analysis in Mellin-N space, where convolutions simplify into ordinary products. The

Mellin transform of a function $f(z)$ is defined as

$$\mathcal{I}[f](N) = \int_0^1 dz\, z^{N-1} f(z), \tag{2.95}$$

Furthermore, the Mellin transform of a convolution, as introduced in Eq. (2.41), satisfies the relation

$$\mathcal{I}[A \otimes B](N) = \mathcal{I}[A](N)\,\mathcal{I}[B](N), \tag{2.96}$$

where $\otimes$ denotes the convolution operation. The threshold limit in Mellin-N space is characterized by the transformation:

$$z \to 1 \quad \Longrightarrow \quad N \to \infty \tag{2.97}$$

In this limit, the Dirac delta function $\delta(1-z)$ maps to a constant, while the plus-distributions $\mathcal{D}_k(z)$ and $\ln^k(1-z)(\mathcal{J}_k)$ correspond to powers of logarithms in terms of $\ln N$.

$$\begin{aligned}
\mathcal{I}[\mathcal{D}_0] &= \frac{1}{2N} - \ln \overline{N}, \\
\mathcal{I}[\mathcal{D}_1] &= -\frac{1}{2N} + \frac{\zeta_2}{2} - \frac{\ln \overline{N}}{2N} + \frac{1}{2}\ln^2 \overline{N}, \\
\mathcal{I}[\mathcal{D}_2] &= \frac{\zeta_2}{2N} + \frac{\ln \overline{N}}{N} - \zeta_2 \ln \overline{N} + \frac{\ln^2 \overline{N}}{2N} - \frac{1}{3}\ln^3 \overline{N} - \frac{2\zeta_3}{3}, \\
\mathcal{I}[\mathcal{D}_3] &= -\frac{3\zeta_2}{2N} + \frac{3\zeta_2^2}{4} + \frac{3\zeta_4}{2} - \frac{3\zeta_2 \ln \overline{N}}{2N} - \frac{3\ln^2 \overline{N}}{2N} + \frac{3}{2}\zeta_2 \ln^2 \overline{N} \\
&\quad - \frac{\ln^3 \overline{N}}{2N} + \frac{1}{4}\ln^4 \overline{N} - \frac{\zeta_3}{N} + 2\ln \overline{N}\zeta_3, \\
\mathcal{I}[\mathcal{D}_4] &= \frac{3\zeta_2^2}{2N} + \frac{3\zeta_4}{N} + \frac{6\zeta_2 \ln \overline{N}}{N} - 3\zeta_2^2 \ln \overline{N} - 6\zeta_4 \ln \overline{N} \\
&\quad + \frac{3\zeta_2 \ln^2 \overline{N}}{N} + \frac{2\ln^3 \overline{N}}{N} - 2\zeta_2 \ln^3 \overline{N} + \frac{\ln^4 \overline{N}}{2N} - \frac{1}{5}\ln^5 \overline{N} \\
&\quad + \frac{4\zeta_3}{N} - 4\zeta_2\zeta_3 + \frac{4\ln \overline{N}\zeta_3}{N} - 4\ln^2 \overline{N}\zeta_3 - \frac{24\zeta_5}{5},
\end{aligned} \tag{2.98}$$

$$\begin{aligned}
\mathcal{I}[\mathcal{D}_5] &= -\frac{15\zeta_2^2}{2N} - \frac{15\zeta_4}{N} + \frac{915\zeta_6}{16} - \frac{15\zeta_2^2 \ln \overline{N}}{2N} - \frac{15\zeta_4 \ln \overline{N}}{N} - \frac{15\zeta_2 \ln^2 \overline{N}}{N} \\
&\quad + \frac{15}{2}\zeta_2^2 \ln^2 \overline{N} + 15\zeta_4 \ln^2 \overline{N} - \frac{5\zeta_2 \ln^3 \overline{N}}{N} - \frac{5\ln^4 \overline{N}}{2N} + \frac{5}{2}\zeta_2 \ln^4 \overline{N} \\
&\quad - \frac{\ln^5 \overline{N}}{2N} + \frac{1}{6}\ln^6 \overline{N} - \frac{10\zeta_2\zeta_3}{N} - \frac{20\ln \overline{N}\zeta_3}{N} + 20\zeta_2 \ln \overline{N}\zeta_3 \\
&\quad - \frac{10\ln^2 \overline{N}\zeta_3}{N} + \frac{20}{3}\ln^3 \overline{N}\zeta_3 + \frac{20\zeta_3^2}{3} - \frac{12\zeta_5}{N} + 24\ln \overline{N}\zeta_5;
\end{aligned} \tag{2.99}$$

The Mellin transforms of $\ln^k(1-z)$ functions are given below

$$
\begin{aligned}
\mathcal{I}[\mathcal{J}_0] &= \frac{1}{N},\\
\mathcal{I}[\mathcal{J}_1] &= -\frac{\ln \overline{N}}{N},\\
\mathcal{I}[\mathcal{J}_2] &= \frac{\zeta_2}{N} + \frac{\ln^2 \overline{N}}{N},\\
\mathcal{I}[\mathcal{J}_3] &= -\frac{3\zeta_2 \ln \overline{N}}{N} - \frac{\ln^3 \overline{N}}{N} - \frac{2\zeta_3}{N},\\
\mathcal{I}[\mathcal{J}_4] &= \frac{3\zeta_2^2}{N} + \frac{6\zeta_4}{N} + \frac{6\zeta_2 \ln^2 \overline{N}}{N} + \frac{\ln^4 \overline{N}}{N} + \frac{8\ln \overline{N}\zeta_3}{N},\\
\mathcal{I}[\mathcal{J}_5] &= -\frac{15\zeta_2^2 \ln \overline{N}}{N} - \frac{30\zeta_4 \ln \overline{N}}{N} - \frac{10\zeta_2 \ln^3 \overline{N}}{N} - \frac{\ln^5 \overline{N}}{N}\\
&\quad - \frac{20\zeta_2\zeta_3}{N} - \frac{20\ln^2 \overline{N}\zeta_3}{N} - \frac{24\zeta_5}{N}.
\end{aligned} \tag{2.100}
$$

Where $\overline{N} = N\exp(\gamma_E)$. The Mellin transforms of other functions are given below [218]:

$$
\begin{aligned}
\mathcal{I}\left[\delta(1-z)\right] &= 1,\\
\mathcal{I}\left[\left((1-z)^{n-1}\right)_+\right] &= \Gamma(n)\left(\frac{\Gamma(N)}{\Gamma(N+n)} - \frac{1}{\Gamma(1+n)}\right),\\
\mathcal{I}\left[z^{-n/2}\left((1-z)^{n-1}\right)_+\right] &= \Gamma(n)\left(\frac{\Gamma(N-\frac{n}{2})}{\Gamma(N+\frac{n}{2})} - \frac{1}{\Gamma(1+n)}\right),\\
\mathcal{I}\left[\left(z^{-n/2}(1-z)^{n-1}\right)_+\right] &= \Gamma(n)\left(\frac{\Gamma(N-\frac{n}{2})}{\Gamma(N+\frac{n}{2})} - \frac{\Gamma(1-\frac{n}{2})}{\Gamma(1+\frac{n}{2})}\right),\\
\mathcal{I}\left[\left(\log^{n-1}\frac{1}{z}\right)_+\right] &= \Gamma(n)\left(N^{-n}-1\right).
\end{aligned} \tag{2.101}
$$

Soft-virtual (SV) resummation

By combining the form factor and the mass factorization kernel with the soft function presented in Eq. (2.94), performing the renormalization of the coupling constant, and subsequently solving the resulting expressions in Mellin space, we arrive at the resummed formulation. In Mellin space, the finite soft-virtual (SV) cross section is given by:

$$
\begin{aligned}
\Delta_N^I &= C_0^I(Q^2,\mu_R^2,\mu_F^2)\exp\left(\int_0^1 dz \frac{z^{N-1}-1}{1-z}\left\{\int_{\mu_R^2}^{Q^2(1-z)^2}\frac{d\lambda^2}{\lambda^2}A^I\left(a_s(\lambda^2)\right) + D^I\left(a_s\left(Q^2(1-z)^2\right)\right)\right)\right\}\\
&= C_0(Q^2,\mu_R^2,\mu_F^2)\exp\left\{\ln g_0^I(a_s(\mu_R^2)) + G_N^I(\omega)\right\}\\
&= \overline{g}_0^I(Q^2,\mu_R^2,\mu_F^2)\exp\left\{G_N^I(\omega)\right\}
\end{aligned} \tag{2.102}
$$

Here, $\omega = 2\beta_0 a_s \ln N$, and $D^I\left(a_s\left(Q^2(1-z)^2\right)\right)$ represents the well-known threshold exponent as discussed in [219, 220], which is connected to the soft-virtual (SV) coefficients through the following relation:

$$\begin{aligned} D^I\left(a_s\left(Q^2(1-z)^2\right)\right) &= \sum_{k=1}^{\infty} a_s^k\left(Q^2(1-z)^2\right) D_k^I \\ &= 2\,\overline{G}_{\rm sv}^I\left(a_s\left(Q^2(1-z)^2\right),\epsilon\right)\Big|_{\epsilon=0} \end{aligned} \tag{2.103}$$

Comparing the results in Eq. (2.103) with the Eq. (2.70), we find

$$D_k^I = 2\,\overline{\mathcal{G}}_k^{\,I}\Big|_{\epsilon=0} \tag{2.104}$$

The quantity C_0^I is specific to the underlying hard scattering process and corresponds to the $\delta(1-z)$ contributions originating from the form factor and the soft function; notably, it is independent of N. The remaining terms in the integral are universal.

The Mellin transformation in Eq. (2.102) separates the expression into an N-dependent part, denoted by $G_N^I(\omega)$, and an N-independent part, represented by $\ln g_0^I$. Combining the N-independent part with C_0^I defines $\overline{g}_0^I$ through

$$\overline{g}_0^I(Q^2,\mu_R^2,\mu_F^2) = C_0^I(Q^2,\mu_R^2,\mu_F^2)\,g_0^I(a_s(\mu_R^2)), \tag{2.105}$$

where $\overline{g}_0^I(a_s(\mu_R^2))$ can be expanded perturbatively as

$$\overline{g}_0^I(a_s(\mu_R^2)) = \sum_{k=0}^{\infty} a_s^k(\mu_R^2)\,\overline{g}_0^{I,(k)}. \tag{2.106}$$

The integral structure of Eq. (2.102) was first introduced in seminal works by Sterman [219] and by Catani and Trentadue [220]. The function G_N^I systematically captures and resums all the large-N logarithms to all orders, and admits the perturbative expansion:

$$G_N^I(Q^2,\omega) = \ln N\,g_1^I(Q^2,\omega) + g_2^I(Q^2,\omega) + a_s\,g_3^I(Q^2,\omega) + a_s^2\,g_4^I(Q^2,\omega) + \cdots. \tag{2.107}$$

The explicit forms of the universal coefficients g_k^I for DY-type processes are provided in Appendix B.1. The explicit forms of the process dependent coefficients $g_0^{I,(k)}$ for DY-type and ZZ production processes are provided in Appendix B.1 and Appendix C.1 respectively. Each term in this expansion captures contributions to all orders: the first term resums the leading logarithms (LL), the second resums the next-to-leading logarithms (NLL), and so forth. Including higher-order terms systematically enhances the logarithmic accuracy of the resummed predictions. A detailed discussion of the resummation framework will be presented in the following chapters. Moreover, in the next section, we extend the formalism to also resum next-to-threshold logarithmic contributions.

Next-to-Soft-virtual (NSV) resummation

A recent body of work [178, 221–224] has introduced a new approach for systematically resumming the next-to-soft virtual (NSV) logarithms that emerge in the diagonal partonic channels. Within this framework, the soft-virtual (SV) and NSV contributions to the partonic cross section are reorganized in Mellin space, enabling a more refined resummation structure beyond the conventional leading threshold terms. In Eq. (2.102) the Mellin moment of the exponent takes the following form,

$$G_N^I(\omega) = G_N^{I,\rm sv}(\omega) + G_N^{I,\rm nsv}(\omega). \tag{2.108}$$

The Mellin moments $G_N^{I,\rm sv}$ and $G_N^{I,\rm nsv}$ are have the following form,

$$\begin{aligned} G_N^{I,\rm sv} &= \ln(\overline{N})\ g_1^I(\omega) + \sum_{n=1}^{\infty} a_s^{n-1}(\mu_R^2)\ g_{n+1}^I(\omega)\,, \\ G_N^{I,\rm nsv} &= \frac{1}{N}\sum_{n=0}^{\infty} a_s^n(\mu_R^2)\ \left(\overline{g}_{n+1}^I(\omega) + \sum_{k=0}^{n} h_{nk}^I(\omega)\ln^k \overline{N}\right)\,, \end{aligned} \tag{2.109}$$

Here, $\overline{N} = N\exp(\gamma_E)$, where γ_E represents the Euler–Mascheroni constant, and $\omega = 2\beta_0\alpha_s(\mu_R^2)\ln\overline{N}$. The leading term in the exponent $G_N^{I,\rm sv}$ determines the logarithmic accuracy at the leading logarithmic (LL) level, with each subsequent term contributing to higher logarithmic precisions. The coefficients g_n^I are process-independent and rely solely on the type of initial partons—quarks or gluons. To achieve $\overline{\rm LL}$ accuracy in the resummation of next-to-soft virtual (NSV) logarithms, one needs to include the corresponding NSV exponents $\overline{g}_1^I$ and h_{00}^I, in addition to the standard LL contributions. These NSV resume coefficients are given in chapter 4 for the incoming gluon channel. Attaining higher logarithmic accuracies requires incorporating further terms in the expansion of G_N^I. Starting at the next-to-leading logarithmic (NLL) or $\overline{\rm NLL}$ level, one must also account for the N-independent constant term $\overline{g}_0^I$ same as given in Eq. (2.106), which admits a perturbative series expansion.

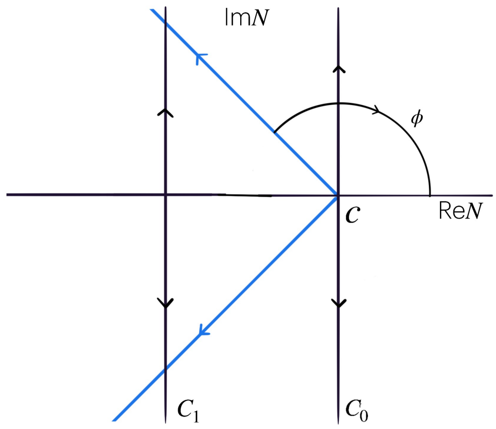

FIGURE 2.3: Integration contour of Mellin inversion as given in Eq. (2.110).

Inverse Mellin Transformation and Matching

After obtaining the all-order resummed partonic cross-section in Mellin (N) space, it is essential to perform a Mellin inverse transformation to retrieve the results in the physical z-space. This section addresses the technical aspects of performing the Mellin inversion. The resummed cross-section in the hadronic variable τ is given by the inverse Mellin integral

$$\sigma(\tau) = \frac{1}{2\pi i}\sum_{k=0}^{\infty} a_s^k \int_{c-i\infty}^{c+i\infty} dN\, \tau^{-N} \Delta_N^{(k)}, \tag{2.110}$$

where c is a real constant chosen such that the integral converges, and the integration contour lies to the right of all singularities of the integrand. The contour of integration in Eq. (2.110) is shown in Fig. 2.3. The contour denoted as C_0, can be deformed to an equivalent path C_1 that will give the same result, provided no poles lie between them.

To facilitate numerical evaluation, the above expression can be recast in terms of real variables using the parametrization $N = c + ze^{i\phi}$ with $z \in [0, \infty)$:

$$\sigma(\tau) = \frac{1}{\pi}\sum_{n=0}^{\infty} a_s^n \int_0^{\infty} dz\, \mathrm{Im}\left[e^{i\phi}\tau^{-c-ze^{i\phi}} \Delta^{(n)}_{N=c+ze^{i\phi}}\right], \tag{2.111}$$

where the angle ϕ must be chosen greater than $\pi/2$ to ensure numerical stability. To carry out the Mellin inversion, we adopt the approach known as the *minimal prescription* [225], wherein the integration contour is selected such that the Landau pole lies to the right, and all other singularities are positioned to the left of the contour. Following the methodology in [226] and we use the values $c = 1.9$ and $\phi = 3\pi/4$ for numerical stability in our analysis.

However, the integrand can develop singularities at specific values of N, notably at the so-called Landau pole $N = N_L$, defined by the condition $\omega = 2\beta_0 a_s \ln N = 1$. To avoid such unphysical singularities, several regularization schemes have been proposed in the literature, including the Minimal Prescription (MP) and Borel-based approaches. The constant c in the Mellin inversion must be selected such that all singularities are located to the left of the contour, while the Landau pole and its higher-order analogs lie well to the right, ensuring a reliable and stable numerical evaluation.

To consistently combine resummed and fixed-order results, care must be taken to avoid double-counting contributions that appear in both. A naive sum of the two would result in the soft-virtual (SV) terms being counted twice. This can be understood by examining the structure of the resummed series in Eq. (2.102). For instance, retaining the exponent and the prefactor $\overline{g}_0^I$ up to first order and truncating the expansion at $\mathcal{O}(a_s)$ reproduces the NLO soft-virtual terms along with next-to-leading logarithmic (NLL) contributions to all higher orders. Similarly, extending both the exponent and $\overline{g}_0^I$ to second order yields NNLO soft-virtual terms and next-to-next-to-leading logarithmic (NNLL) accuracy for higher-order corrections. Therefore, a direct addition of the resummed result to the fixed-order one leads to duplication of the SV terms.

To remedy this, one subtracts the overlapping SV and NSV terms present in both the fixed-order and resummed results—a procedure known as *matching*. The matched cross-section is given by

$$
\begin{aligned}
Q^2 \frac{\mathrm{d}\sigma_{ab}^{\mathrm{N}^n\mathrm{LO}+\overline{\mathrm{N}^n\mathrm{LL}}}}{\mathrm{d}Q^2} =& Q^2 \frac{\mathrm{d}\sigma_{ab}^{\mathrm{N}^n\mathrm{LO}}}{\mathrm{d}Q^2} + \sum_{ab\in\{gg,q\bar{q}\}} \widehat{\sigma}_{ab}^{(0)}(Q^2) \int_{c-i\infty}^{c+i\infty} \frac{\mathrm{d}N}{2\pi i} \tau^{-N} f_{a,N}(\mu_F) f_{b,N}(\mu_F) \\
& \times \left(Q^2 \frac{\mathrm{d}\widehat{\sigma}_{N,ab}^{\overline{\mathrm{N}^n\mathrm{LL}}}}{\mathrm{d}Q^2} - Q^2 \frac{\mathrm{d}\widehat{\sigma}_{N,ab}^{\overline{\mathrm{N}^n\mathrm{LL}}}}{\mathrm{d}Q^2}\bigg|_{\mathrm{tr}} \right) . \qquad (2.112)
\end{aligned}
$$

where $f_{a,N}$ and $f_{b,N}$ are the Mellin moments of the parton distribution functions, and the contour C is chosen as described in the Mellin inversion procedure.

The inclusion of the second term within the brackets ensures the removal of duplicated singular contributions that are already accounted for in the fixed-order (FO) computation, represented by the final term in the above expression in Eq. (2.112). For example, achieving N^{3}LL accuracy matched to N^{3}LO requires retaining $\mathcal{O}(a_s^2)$ terms in the exponent of the resummed expression and subtracting all logarithmically enhanced terms up to N^{3}LO from the resummed part.

This matching framework provides a consistent way to combine the resummed and fixed-order results and is adaptable to various levels of accuracy. In this thesis, we perform precision studies for the charged and neutral Drell-Yan production, VH production, bottom quark annihilation to Higgs production, gluon fusion ZH production and ZZ production processes within the Standard Model, focusing on threshold resummation in QCD. Further details and results will be discussed in the subsequent chapters.

Chapter 3

Resummation of color singlet processes in Standard Model

Inclusive production of colorless final states at hadron colliders occupies a central role in precision tests of the Standard Model (SM) and searches for new physics. Among these, Drell–Yan (DY) production, associated Higgs production with a vector boson (VH), and Higgs production via bottom quark annihilation ($b\bar{b} \to H$) represent a class of processes often referred to as DY-type. These processes are characterized by their color-singlet final states and share a common QCD structure that makes them particularly amenable to resummation of soft-gluon contributions. Due to their clean experimental signatures and the theoretical control offered by perturbative QCD (pQCD), they have served as important probes for both SM parameters and possible deviations indicative of beyond the Standard Model physics.

In Chapter 2, we introduced the theoretical framework of threshold resummation within perturbative QCD. There, we outlined how radiative corrections near the partonic threshold lead to large logarithmic contributions that jeopardize the convergence of fixed-order perturbation theory. In such kinematic configurations—where the invariant mass of the colorless final state nearly equals the partonic center-of-mass energy—the suppression of real gluon emission enhances the sensitivity to soft-gluon effects. These logarithms can be systematically organized and resummed to all orders using established techniques in

Mellin space, providing improved predictions that are both more accurate and less sensitive to scale variations. In this chapter, we apply that formalism to compute threshold-enhanced contributions for several important color-singlet production processes at hadron colliders.

3.1 Introduction

Color singlet production processes are important to understand properties of elementary particles, the proton structure as well as to extract fundamental quantities like coupling and masses at the colliders [227] like the Large Hadron Collider (LHC). From a theoretical point of view, they are relatively easier to understand, and experimentally, they often provide clear signatures. Processes like the Drell-Yan (DY) productions [228] are standard candles at the hadron colliders and are important for luminosity monitoring. On the other hand processes like Higgs-strahlung where a Higgs boson (H) is produced in association with a massive vector boson $(V = Z, W)$ are important to understand Higgs boson properties and also to search new physics beyond the Standard Model (SM). In this chapter, we focus our study on a few such processes. In particular, we studied the neutral Drell-Yan (nDY) production where a Z boson or virtual γ decays to a lepton-antilepton pair, charged DY (cDY) where a W boson decays to a lepton and a neutrino, associated production of Higgs boson with a vector boson like Z or W, and Higgs boson production through bottom quark annihilation. All these processes are produced through quark annihilation at the born level. The next-to-leading order (NLO) QCD corrections to the DY production process were computed about 40 years ago [32, 33, 229–232], and the next-to-next-to-leading order (NNLO) QCD results are now known [43] for quite some time. The higher order QCD corrections have also been studied in the BSM context [233–235].

Recently the fixed order (FO) predictions have been improved to next-to-next-to-next-to leading order (N^{3}LO) [69, 71, 72, 91, 213, 236–238] and public codes are available [73, 236, 239–241] which provide the flexibility of studying N^{3}LO cross section with different parameters, parton distribution functions (PDFs) and scales. There is also recent progress on the EW corrections which could be competitive as the QCD correction in the higher orders. At NLO, the EW corrections for massive gauge bosons have been performed in [242–250], whereas mixed EW-QCD corrections are also studied recently at NNLO [251–254] and are known to give contributions as large as -1.5% of NLO QCD corrections in the high invariant mass region. The mixed QCD-QED corrections for $b\bar{b}H$ can be found in [255]

Color-singlet processes such as Drell-Yan (DY) lepton pair production, Higgs production in association with a vector boson (VH), and Higgs production via bottom quark annihilation ($b\bar{b} \to H$) have been extensively studied at the LHC by both ATLAS and CMS collaborations. These processes serve as clean probes of the Standard Model (SM) due to their relatively low background and well-understood theoretical frameworks. The DY process provides stringent tests of electroweak couplings and parton distribution functions, while VH production channels contribute significantly to precision measurements of Higgs boson properties. In recent years, the evidence for bottom quark-induced Higgs production has also gained attention, particularly in boosted or high-mass regimes where sensitivity improves.

Fig. 3.1 shows representative invariant mass distributions for the DY process, comparing the measured CMS [1] data with SM predictions. The agreement is generally good, but certain kinematic regions, especially near threshold or in the high-invariant-mass tail, exhibit larger uncertainties. These regions are sensitive to higher-order QCD effects, motivating improved theoretical calculations including soft-gluon resummation. In Fig. 3.2, experimental data are compared with SM theoretical predictions from CMS [2] and ATLAS [3] for VH production with Higgs decay to $b\bar{b}$ and experimental data show good agreement with SM predicted results. Where the μ parameter is defined as the ratio of experimental observation over SM prediction.

While improving the FO calculations, it is essential to push precision frontiers, for often they are not sufficient to correctly describe the data. In particular, FO predictions are plagued by the large logarithmic contributions which appear at each order of perturbation theory. A particular class of these enhanced logarithms appear in the threshold region when partonic threshold variable $z \to 1$. Truncated FO predictions at a relatively lower order are insufficient to capture the dominant contributions from the large threshold logarithms. On the other hand, the universality of these logarithms allows us to resum them to all orders and capture significant contribution which is essential to compare to the experimental predictions.

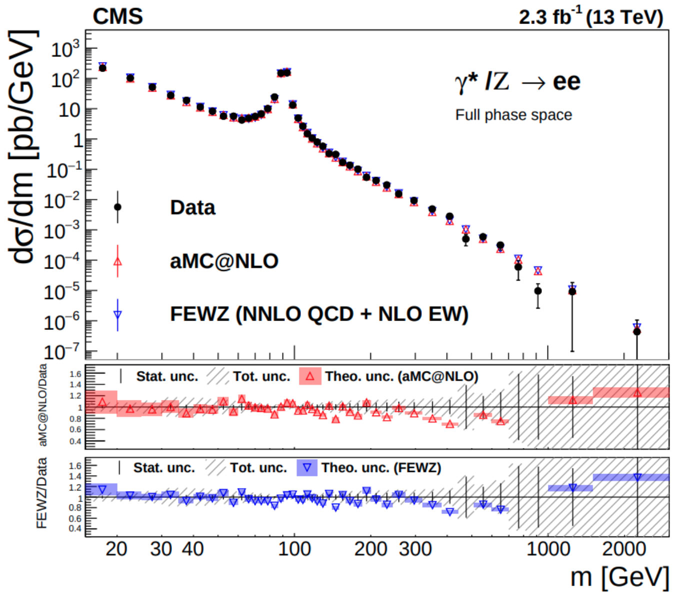

FIGURE 3.1: The invariant mass distributions for DY production channels experimental data compared with SM theoretical predictions from CMS [1].

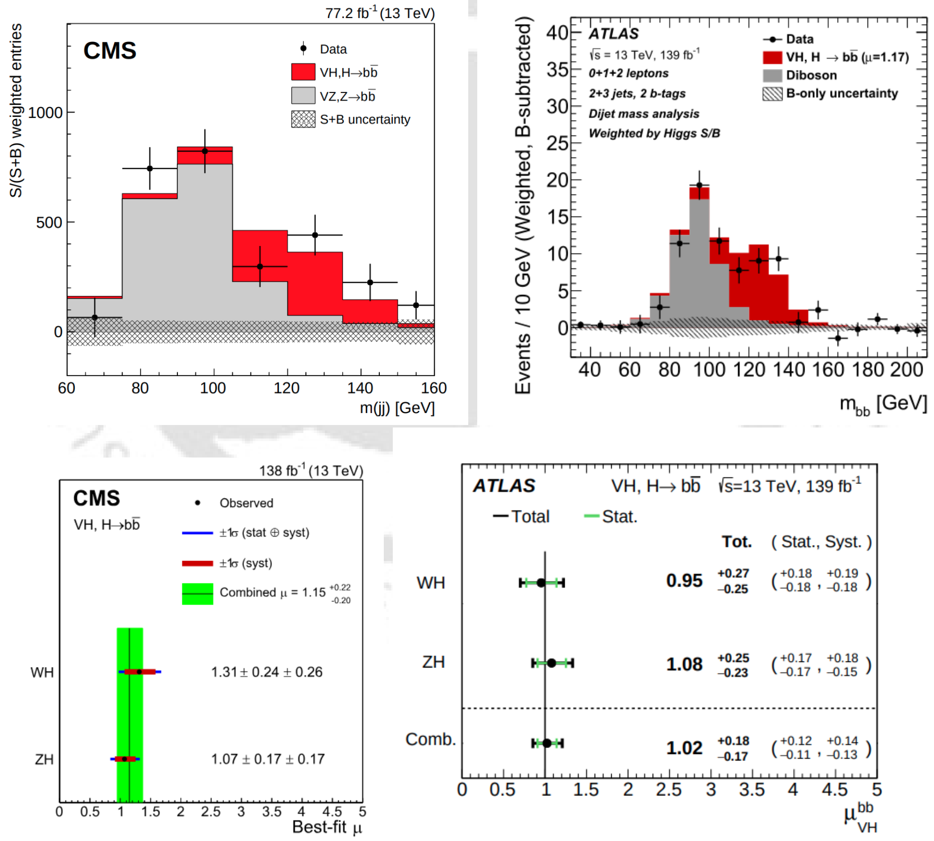

FIGURE 3.2: The experimental data are compared with SM theoretical predictions from CMS [2] and ATLAS [3] for VH production with Higgs decay to $b\bar{b}$.

The singular part of the fixed order contribution *viz.* the soft-virtual (SV) corrections to these processes are known for a long time through N^{3}LO and beyond [85–87, 114, 256–263]. Some of these results have been used to perform threshold resummation up to N^{3}LL. Threshold resummation has been well studied from the early days of QCD for a wide range of processes [219, 220]. This is possible due to refactorization [77–79, 81, 82, 180, 225, 264–269] of partonic cross sections in terms of soft and hard functions in the threshold region. For color-singlet productions, they are extensively studied to N^{3}LL accuracies [127, 239, 257, 260, 270–275] and even to N^{4}LL [261–263] for some processes in the SM. In general the inclusion of threshold resummation results into better perturbative convergence with an improved scale uncertainty. In [272], it was pointed out that the threshold resummation is important in the DY invariant mass distribution in the moderate and high invariant regions and results 2% correction to the fixed order. The scale uncertainty reduces to below 1% in the high invariant mass region $Q > 1500$ GeV where a matching at third order was limited only to the SV part. A general framework has been provided for arbitrary color singlet production in [276, 277]. Beyond the SM (BSM), these are also studied for a wide range of models and stringent bounds have been obtained with models parameters with precise N^{3}LL results [89, 278–287]. However, one also needs to match the threshold logarithmic contributions with the FO results to capture the subleading terms which become important at higher orders as well. The recent results on the FO frontiers allow us to study this with the availability of a fixed order code `n3loxs` [73] shipped with a range of color-singlet processes at N^{3}LO.

The purpose of the present chapter is thus to perform a complete study with properly matching N^{3}LL resummed results with the newly available N^{3}LO results. We extract all the process-dependent and universal coefficients needed for N^{3}LL resummation following the formalism developed in [78, 79, 81, 82, 180]. It is worth mentioning that the Higgs boson production in gluon fusion at the LHC has been studied extensively in the literature. The mass of the Higgs boson being around 125 GeV, the underlying parton fluxes at high energy hadron colliders are large. In addition to the fact that the lowest order dominant contribution comes from the gluon fusion channel, the QCD corrections cannot be neglected even beyond NNLO in QCD. This led to the computation of higher order QCD corrections to N^{3}LO QCD in the fixed order and to N^{3}LL accuracy in the context of resummation, in order to achieve the robust precision studies for this process. The

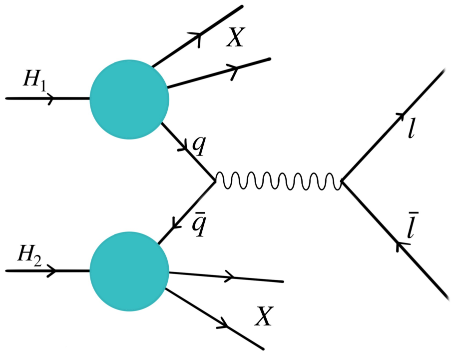

FIGURE 3.3: A schematic representation of Drell-Yan production at a hadron collider.

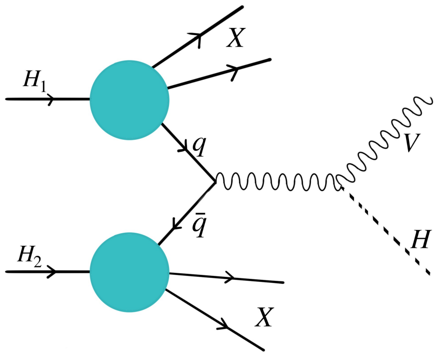

FIGURE 3.4: A schematic representation of VH production at a hadron collider.

details of these precision studies can be found in [51, 53, 70, 85, 87, 239, 271, 278, 288–290]. Hence, we will not repeat them here but rather focus on the other color-singlet production processes at hadron colliders. The chapter is organized as follows: in Sec. 3.2, we briefly lay out the theoretical framework providing the essential formulas to perform threshold resummation and the matching. In Sec. 3.3 we present the phenomenological results for different color-singlet processes in the context of LHC, and finally we conclude in Sec. 3.4.

3.2 Theoretical Framework

The hadronic cross section for colorless production at the hadron collider is given by,

$$\sigma(Q^2) = \sum_{a,b=q,\bar{q},g} \int_0^1 \mathrm{d}x_1 \int_0^1 \mathrm{d}x_2 \; f_a(x_1,\mu_F^2) \; f_b(x_2,\mu_F^2) \int_0^1 \mathrm{d}z \; \hat{\sigma}^{(0)} \Delta^q_{ab}(z,Q^2,\mu_F^2) \delta(\tau - z x_1 x_2)\,, \tag{3.1}$$

where $\sigma(Q^2) \equiv Q^2 \mathrm{d}\sigma/\mathrm{d}Q^2$ for the DY-type processes, a schematic representation of Drell-Yan production at the LHC is shown in Fig. 3.3 and $\sigma(Q^2) \equiv \sigma(M_H^2)$ for $b\bar{b}H$ process. Note that for the total production cross section for VH, we integrate this over the invariant mass Q of the final state VH. A schematic representation of VH production at the LHC is shown in Fig. 3.4. The hadronic and partonic threshold variables τ and z are defined as

$$\tau = \frac{Q^2}{S}, \qquad z = \frac{Q^2}{\hat{s}}\,, \tag{3.2}$$

where S and $\hat{s}$ are the hadronic and partonic center of mass energies respectively. τ and z are thus related by $\tau = x_1 x_2 z$. The partonic coefficient Δ^q_{ab} can be further decomposed as follows given in Eq. (2.39). The overall normalization factor $\hat{\sigma}^{(0)}$ depends on the process under study. In particular, the processes under consideration take the following forms,

$$\begin{aligned} \hat{\sigma}^{(0)}_{DY}(Q^2) &= \frac{\pi}{n_c}\left[\mathcal{F}^{(0)}_{DY}(Q^2)\right], \qquad \text{with } DY \in \{nDY, cDY, ZH, WH\}\,, \\ \hat{\sigma}^{(0)}_{b\bar{b}H} &= \frac{\pi m_b^2(\mu_R^2)\tau}{6 M_H^2 v^2}\,, \end{aligned} \tag{3.3}$$

where,

$$
\begin{aligned}
\mathcal{F}^{(0)}_{nDY}(Q^2) =& \frac{4\alpha^2}{3S}\Bigg[Q_q^2 - \frac{2Q^2(Q^2-M_Z^2)}{\left((Q^2-M_Z^2)^2+M_Z^2\Gamma_Z^2\right)c_w^2 s_w^2} Q_q g_e^V g_q^V \\
&+ \frac{Q^4}{\left((Q^2-M_Z^2)^2+M_Z^2\Gamma_Z^2\right)c_w^4 s_w^4}\Big((g_e^V)^2+(g_e^A)^2\Big)\Big((g_q^V)^2+(g_q^A)^2\Big)\Bigg], \\
\mathcal{F}^{(0)}_{cDY}(Q^2) =& \frac{4\alpha^2}{3S}\left[\frac{Q^4|V_{qq'}|^2}{\left((Q^2-M_W^2)^2+M_W^2\Gamma_W^2\right)s_w^4}\Big((g_e^{'V})^2+(g_e^{'A})^2\Big)\Big((g_q^{'V})^2+(g_q^{'A})^2\Big)\right], \\
\mathcal{F}^{(0)}_{ZH}(Q^2) =& \frac{\alpha^2}{S}\left[\frac{M_Z^2Q^2\lambda^{1/2}(Q^2,M_H^2,M_Z^2)\left(1+\frac{\lambda(Q^2,M_H^2,M_Z^2)}{12M_Z^2/Q^2}\right)}{((Q^2-M_Z^2)^2+M_Z^2\Gamma_Z^2)c_w^4 s_w^4}\Big((g_q^V)^2+(g_q^A)^2\Big)\right], \\
\mathcal{F}^{(0)}_{WH}(Q^2) =& \frac{\alpha^2}{S}\left[\frac{M_W^2Q^2|V_{qq'}|^2\lambda^{1/2}(Q^2,M_H^2,M_W^2)\left(1+\frac{\lambda(Q^2,M_H^2,M_W^2)}{12M_W^2/Q^2}\right)}{((Q^2-M_W^2)^2+M_W^2\Gamma_W^2)s_w^4}\Big((g_q^{'V})^2+(g_q^{'A})^2\Big)\right].
\end{aligned}
\tag{3.4}
$$

Here, $V_{qq'}$ are the CKM matrix coefficients with $Q_q + Q_{q'} = \pm 1$ and

$$
\begin{aligned}
g_a^A &= -\frac{1}{2}T_a^3\,, \qquad & g_a^V &= \frac{1}{2}T_a^3 - s_w^2 Q_a\,, \\
g_a^{'A} &= -\frac{1}{2\sqrt{2}}\,, \qquad & g_a^{'V} &= \frac{1}{2\sqrt{2}}\,,
\end{aligned}
\tag{3.5}
$$

where Q_a is the electric charge and T_a^3 is the weak isospin of the fermions. Here, M_V and M_H are the masses of the weak gauge boson and Higgs boson respectively, m_b is the mass of the bottom quark and v being the vacuum expectation value. The function λ which appears in the VH case is defined as

$$
\lambda(z,y,x) = \left(1-\frac{x}{z}-\frac{y}{z}\right)^2 - 4\frac{xy}{z^2}\,. \tag{3.6}
$$

The Fig. 3.5 schematically illustrates the different contributions to the Drell–Yan process

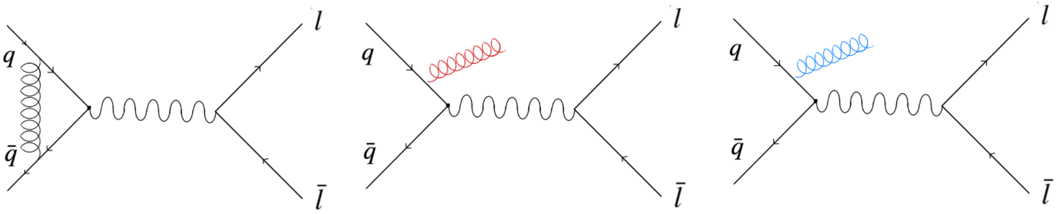

FIGURE 3.5: The next-to-leading order feynman diagrams for Drell–Yan production at LHC.

at higher orders in QCD. On the left, the one-loop virtual diagram represents purely virtual corrections, where no real gluon is emitted. These corrections are encoded in the *soft-virtual* terms of the cross-section and are characterized by distributions such as $\delta(1-z)$. In the central diagram, a soft gluon, shown in red, is emitted in addition to the virtual corrections. This emission remains unresolved in the detector and also contributes to the soft-virtual part of the cross-section due to its infrared nature and characterized in terms of plus-distributions ($\mathcal{D}$) and $\delta(1-z)$. Finally, the rightmost diagram shows the emission of a hard gluon, depicted in blue, which is distinguishable and contributes to the *regular* terms in the cross-section that are finite as $z \to 1$. These regular contributions represent hard real radiation and are not captured by the threshold-resummed soft-virtual approximation. The equation provided earlier reflects this decomposition, where the soft-virtual contributions dominate in the threshold limit, while the regular terms become relevant away from this limit.

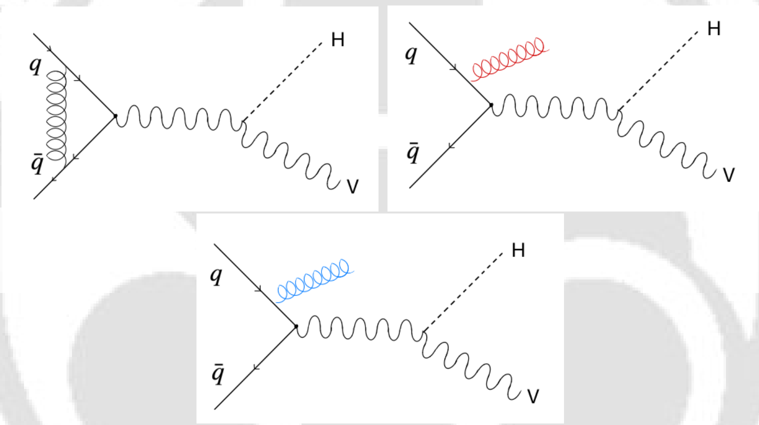

FIGURE 3.6: The next-to-leading order feynman diagrams for VH production at LHC.

The Fig. 3.6 schematically represents the different kinematic regions contributing to the NLO QCD corrections in the associated production of a Higgs boson with a vector boson (VH). The top left diagram illustrates the one-loop virtual correction, where no real radiation is present; this contribution is purely virtual and yields infrared divergences that are captured by the soft-virtual terms in Eq. (2.39). The top right diagram depicts the emission of a soft gluon, shown in red, which leads to soft singularities that also contribute to the soft-virtual component. Together, these two configurations form the soft-virtual (SV) structure, dominant near threshold. The bottom diagram shows a hard, non-collinear gluon emission (blue), which contributes to the regular, non-singular part of the cross-section away from threshold. This decomposition into SV and regular parts allows for an efficient organization of perturbative corrections, particularly relevant for resummation near the partonic threshold.

The singular part of the partonic coefficient has a universal structure which gets contributions from the underlying hard form factor [208, 209, 291–293], mass factorization kernels [210, 211], and soft radiations [81, 82, 204–207]. All of these are infrared divergent which, when regularized and combined give finite contributions. The finite singular part of these has the universal structure in terms of $\delta(1-z)$ and plus-distributions $\mathcal{D}_i = [\ln(1-z)^i/(1-z)]_+$ as mention in the previous cahapter in Eq. (2.37). These large distributions can be resummed to all orders in the threshold limit ($z \to 1$). Threshold resummation is conveniently performed in the Mellin (N) space where the convolution structures become a simple product.

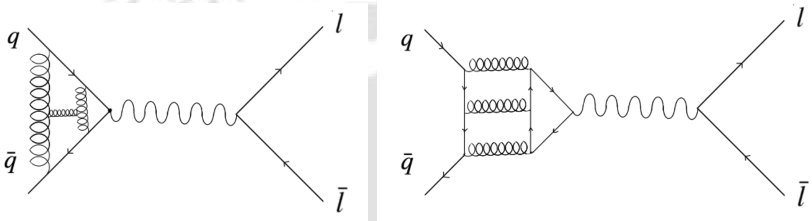

FIGURE 3.7: The N^{3}LO order few feynman diagrams for DY production at LHC.

The partonic coefficient for the DY-type processes ($I = q$) in the Mellin space is organized and given in Eq. (2.102).

$$\hat{\sigma}_N^{\mathrm{N^nLL}} = \int_0^1 \mathrm{d}z\ z^{N-1} \Delta^{\mathrm{sv}}(z) \equiv \overline{g}_0^q \exp\left(G_N^q\right) \tag{3.7}$$

The factor $\overline{g}_0^q$ is independent of the Mellin variable, whereas the threshold enhanced large logarithms are resummed through the exponent G_N^q. The resummed accuracy is determined through the successive terms from the exponent G_N^q, which up to N^{3}LL takes the form as given in Eq. (2.107). The coefficients required to do resummation at this order are $g_1^q(\overline{N})$, $g_2^q(\overline{N})$, $g_3^q(\overline{N})$ and $g_4^q(\overline{N})$. These coefficients are universal and only depend on the partonic flavors being either quark or gluon. Their explicit form can be found in e.g. [77, 180] and are also given for qurak in the Appendix B.

In order to achieve complete resummed accuracy one also needs to know the N–independent coefficient $\overline{g}_0^q$ in Eq. (2.106) up to sufficient accuracies. In particular, up to N^{3}LL, required process dependent coefficients are $\overline{g}_0^{q,(1)}$,$\overline{g}_0^{q,(2)}$ and $\overline{g}_0^{q,(3)}$. All these coefficients $\overline{g}_0^{q,(k)}$ are given in Appendix B.1 up to three-loop level. The three-loop level few virtual diagrams are shown in Fig. 3.7 which will contribution in the process-dependent coefficient $\overline{g}_0^{q,(3)}$. It is also possible to resum part (or all) of the $\overline{g}_0^q$ by including them in the exponent [239, 262, 267, 271, 272], which however have subleading effect as these contributions are not dominated in the threshold region.

To obtain the results in z space, one needs to do the Mellin inversion as in Eq. (2.110) and we follow the procedure mention in section 2.4.3 to get the final matched results. The $f_{a,N}$ are the Mellin transformed PDF similar to the partonic coefficient in Eq. (2.112) and can be evolved e.g. using the publicly available code QCD-PEGASUS [226]. However, for practical purposes, it can be also approximated by directly using z–space PDF following [77, 220, 294].

3.3 Numerical Results

In this section, we present numerical results for various color singlet production processes discussed in the previous section in the context of the LHC. Unless specified otherwise, in our numerical analysis we use MMHT2014 [295] parton distribution functions (PDFs) throughout taken from the `LHAPDF` [296]. The LO and NLO cross sections are obtained by convolving the respective coefficient functions with MMHT2014lo68cl and MMHT2014nlo68cl PDFs, while the NNLO and N^{3}LO cross sections are obtained with MMHT2014nnlo68cl PDF sets. In all these cases, the central set (iset=0) is the standard choice. Our default choice of the a_s is the same as the one used in the `n3loxs` code, and it varies order by order in the perturbation theory. The fine structure constant is $\alpha \simeq 1/132.184142$. The masses of the weak gauge bosons being $m_Z = 91.1876$ GeV and $m_W = 80.379$ GeV with the corresponding total decay widths of $\Gamma_Z = 2.4952$ GeV and $\Gamma_W = 2.085$ GeV. The Weinberg angle is $\sin^2\theta_{\rm w} = (1 - m_W^2/m_Z^2)$ and is calculated internally. This corresponds to the weak coupling $G_F \simeq 1.166379 \times 10^{-5}$ GeV^{-2}. The mass of the Higgs boson is taken to be $m_H = 125.1$ GeV and the vacuum expectation value is $v = 246.221$ GeV. Finally, the pole masses of the bottom and top quarks are taken to be $m_b = 4.78$ GeV and $m_t = 172.76$ GeV, while their running masses are $m_b(m_b) = 4.18$ GeV and $m_t(m_t) = 162.7$ GeV. In our calculation, the CKM matrix elements are $V_{ud} = 0.97446$, $V_{us} = 0.22452$, $V_{ub} = 0.00365$, $V_{cd} = 0.22438$, $V_{cs} = 0.97359$ and $V_{cb} = 0.04214$. The default choice of center mass energy of the incoming protons is 13 TeV, unless it is mentioned otherwise.

The unphysical renormalization and factorization scales are chosen to be $\mu_R = \mu_F = Q$, where Q is the invariant mass of the dilepton or the invariant mass of the vector and Higgs bosons in the final state. For the case of Higgs production in bottom annihilation, however, the default scale choice is $\mu_R = m_H$ and $\mu_F = m_H/4$ following the suggestion from Ref.[91]. For all the processes we have considered here, the scale uncertainties are estimated by varying the unphysical scales as mention in section 2.3.1, in the range so that $|\ln(\mu_R/\mu_F)| < \ln 4$. The symmetric scale uncertainty is calculated from the maximum absolute deviation of the cross section from that obtained with the central/default scale choice. To estimate the impact of the higher order corrections from FO and resummation, we define the following ratios of the cross sections which are useful in the experimental analysis:

$$\mathrm{K}_{\mathrm{N}^i\mathrm{LO}} = \frac{\sigma_{\mathrm{N}^i\mathrm{LO}}}{\sigma_{\mathrm{LO}}} \quad \text{and} \quad \mathrm{R_{ij}} = \frac{\sigma_{\mathrm{N}^i\mathrm{LO+N}^i\mathrm{LL}}}{\sigma_{\mathrm{N}^j\mathrm{LO}}} \quad \text{with} \quad i,\, j = 0, 1, 2 \text{ and } 3\,\cdot \tag{3.8}$$

The parameters $\mathrm{K}_{\mathrm{N}^i\mathrm{LO}}$ and $\mathrm{R_{ij}}$, serve as useful indicators for understanding the convergence behavior of perturbative expansions. The ratio $\mathrm{K}_{\mathrm{N}^i\mathrm{LO}}$ measures the relative size of higher-order corrections compared to the leading order. If $\mathrm{K}_{\mathrm{N}^i\mathrm{LO}}$ approaches unity as i increases, it suggests that successive corrections become smaller, indicating good convergence of the perturbative series. Similarly, the ratios $\mathrm{R_{ij}}$ compare predictions at closely related perturbative orders including logarithmic resummations. Stability of $\mathrm{R_{ij}}$ values near one implies the resummation results are consistent and corrections are small, providing further evidence of convergence. Overall, monitoring the behavior of $\mathrm{K}_{\mathrm{N}^i\mathrm{LO}}$ and $\mathrm{R_{ij}}$ across different orders allows one to quantify the reliability and convergence properties of the perturbation series in a given process.

3.3.1 Neutral DY production

For the neutral DY case, the fixed order results and the associated uncertainties have been discussed in Ref.[73] in greater detail. Hence, we will not repeat them here, instead we focus on the resummed results. In the left panel of Fig. 3.8, we present the invariant mass distribution $Q^2 d\sigma/dQ^2$ up to N^{3}LO+N^{3}LL by varying Q from 250 GeV to 3000 GeV. The corresponding R_{i0}-factors defined above are given in the right panel. It can be seen that R_{20} is larger than R_{30} here up to about $Q = 2000$ GeV, and then they slowly converge to each other, while R_{10} being smaller than these two for the entire Q

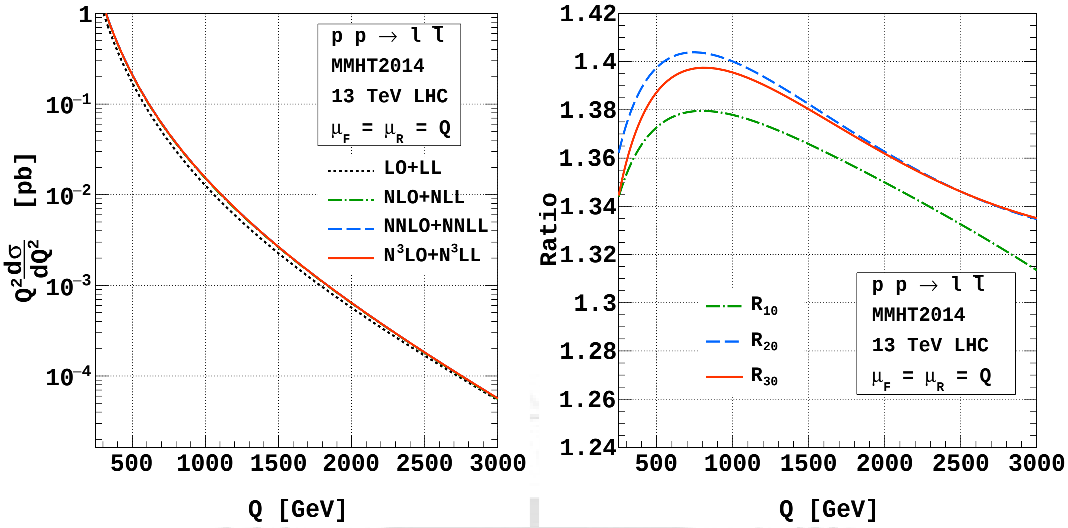

FIGURE 3.8: Invariant mass distribution for the enhancement in the resummed cross section of DY for 13 TeV LHC (left panel) and the resummed cross section over fixed order LO are shown here (right panel) through R_{ij} is defined in Eq. (5.9).

region considered. We also present the R_{ii}-factors which estimate the contribution of higher order threshold logarithms over the respective FO results. The effect of threshold resummation is prominent at NLO. However, its contribution at N^{3}LO level is very small. This is expected as the FO results for DY case are converging already at NNLO level onwards, unlike the case of Higgs production in gluon fusion channel [51, 53, 69, 70]. Here, the resummed results at N^{3}LO+N^{3}LL demonstrate excellent convergence of the perturbation theory.

At this level of precision, it is also important to consider effects from power corrections. As a first step, one can consider the next-to-soft-virtual (NSV) corrections by taking into account the logarithms of the kind $\ln^i(1-z)$. In the context of the nDY process, a detailed phenomenology at LHC has been studied in Refs. [223, 274]. In Ref. [274], these NSV logarithms have been resummed to next-to-next-to-leading logarithmic accuracy and a comparison of the same has been carried out with the SV resummed result. It is found that the differences between the SV and NSV resummations are about 4% at LL, 2.84% at NLL and 0.85% at NNLL accuracy for $Q = 1000$ GeV. At higher invariant mass, the differences do not change much, *e.g.* at $Q = 2000$ GeV, the differences are about 4%, 2.8% and 0.89% respectively. A general observation is that the difference between SV and NSV resummations is less sensitive to the value of Q and that this difference decreases with higher logarithmic accuracy. If this trend were to continue, at N^{3}LL the difference between SV and NSV resummed results could be about 0.1%. This translates to a rough estimate of the order of 0.1% theory uncertainty due to the missing power corrections. It is also worth noting that the NSV logarithms from other partonic channels will also contribute to the cross section. However, a detailed study of such power corrections is beyond the scope of the present work.

3.3.2 Charged DY production

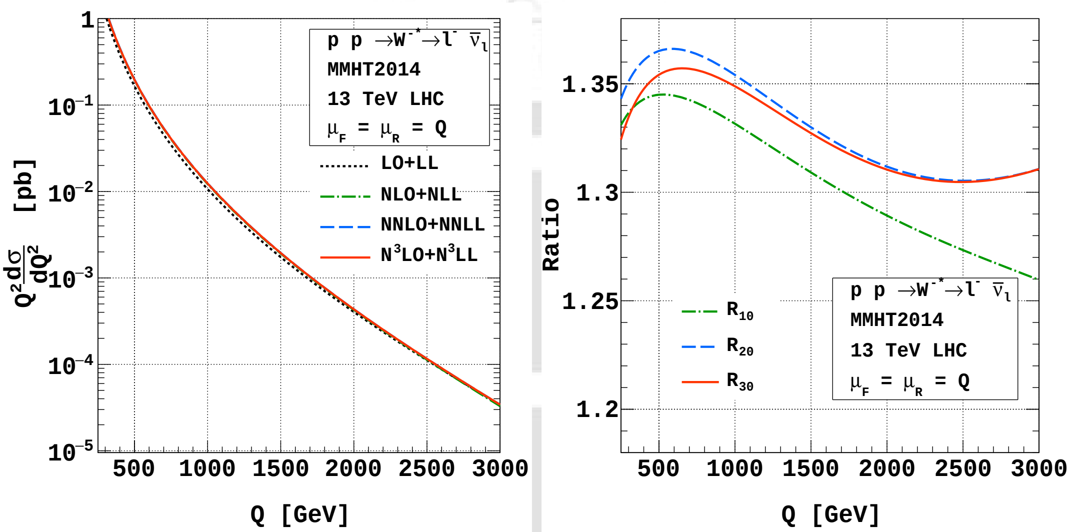

FIGURE 3.9: Invariant mass distribution for the enhancement in the resummed cross section of charge current DY (W^{-*}) for 13 TeV LHC (left panel) and the resummed cross section over fixed order LO are shown here (right panel) through R_{ij} is defined in Eq. (3.8).

Similar to the neutral DY case, we present in Fig. 3.9, the invariant mass distribution (left panel) for charge DY(W^{-*}) case up to N^{3}LO+N^{3}LL accuracy and the corresponding R_{i0} factors (right panel). For the case of charged DY, the corresponding parton fluxes are different from those of neutral DY case. This will clearly result in a slightly different behavior of the higher order corrections. This together with the NLL enhancement of the cross sections can explain the behavior of the R-factors noticed. Quantitatively, the impact of QCD corrections in the high invariant mass region ($Q \geq 2500$ GeV) are smaller than the corresponding ones for neutral DY case.

Similar results have been obtained for W^{+*} and the corresponding R_{i0} factors are shown in Fig. 3.10. Again, owing to the different underlying parton fluxes that are different starting from the Born level, the behavior of these R_{i0}-factors is expected to be different from those of both neutral DY and W^{-*}.

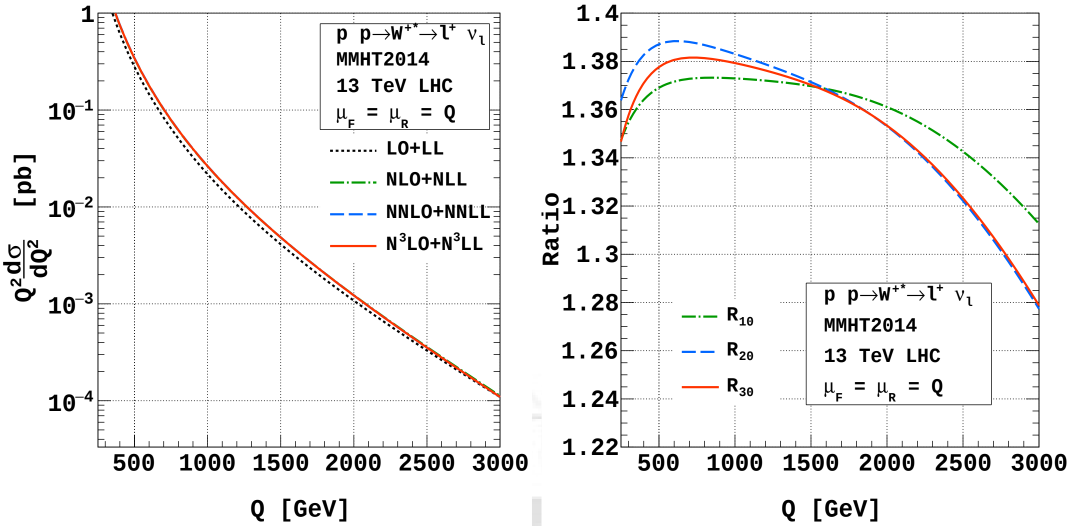

FIGURE 3.10: Invariant mass distribution for the enhancement in the resummed cross section of charge current DY (W^{+*}) for 13 TeV LHC (left panel) and the resummed cross section over fixed order LO are shown here (right panel) through R_{ij} is defined in Eq. (3.8).

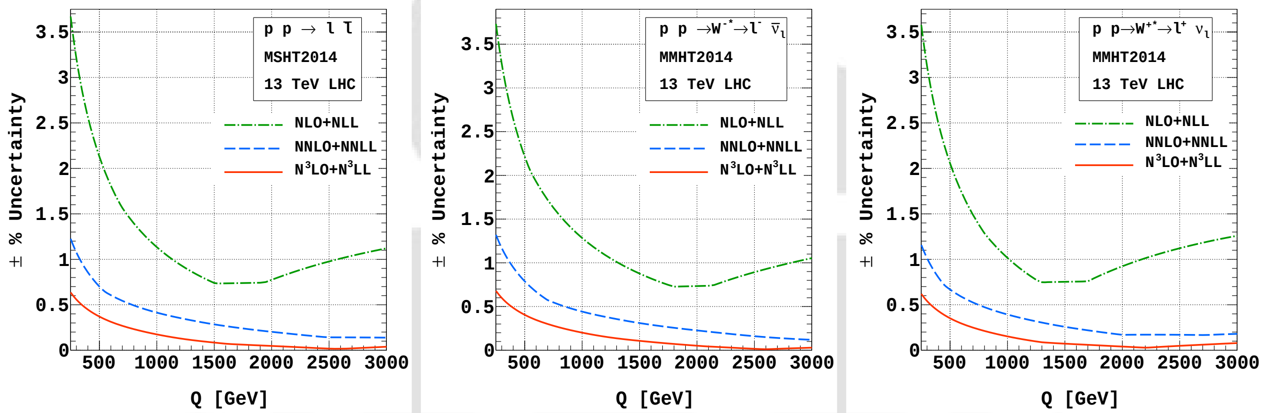

FIGURE 3.11: The 7-point scale uncertainty for neutral DY [nDY] (left panel), charged DY [cDY] W^{-*} (middle panel) and W^{+*}(right panel)

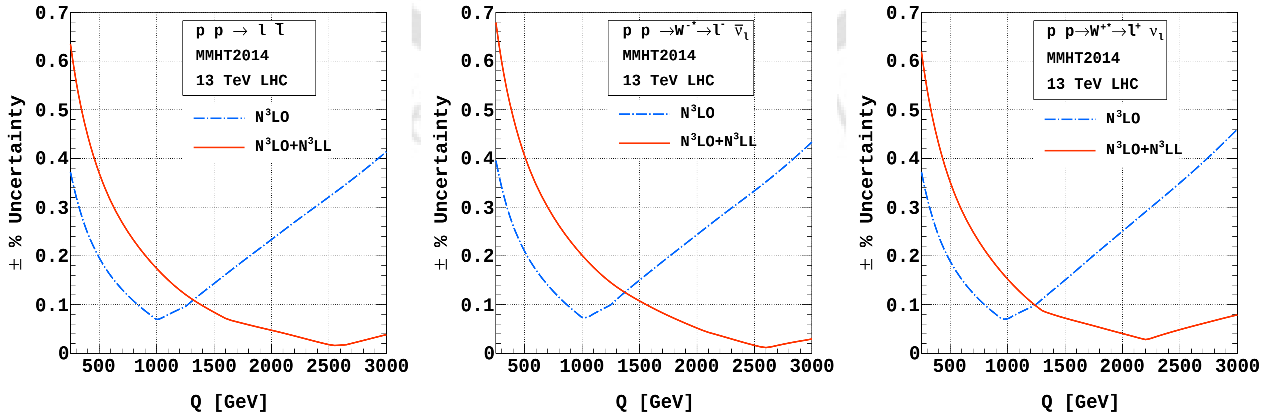

FIGURE 3.12: Comparison of 7-point scale uncertainty between resum and fixed order results for neutral DY [nDY] (left panel), charged DY [cDY] W^{-*} (middle panel) and W^{+*}(right panel).

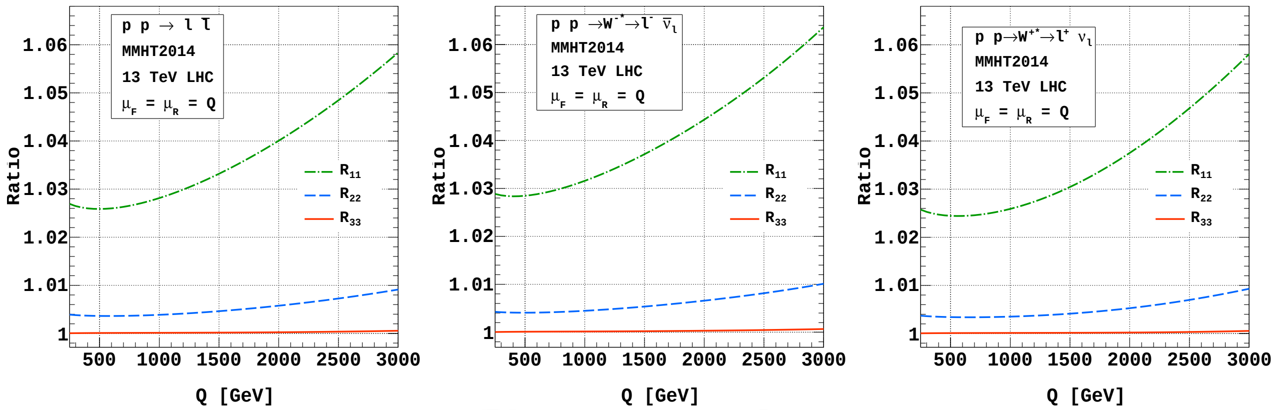

FIGURE 3.13: Resummed enhancement over respective fixed order are shown here for neutral DY (left panel), charged DY W^{-*} (middle panel) and W^{+*} (right panel) through R_{ij} defined in Eq. (3.8).

Besides, the resummed results at N^{3}LO+N^{3}LL play a significant role in reducing the conventional 7-point scale uncertainties. The scale uncertainties in the resummed predictions up to N^{3}LO+N^{3}LL accuracy are given in Fig. 3.11 for neutral DY (left panel), for W^{-*} (middle panel) and for W^{+*} (right panel). While the FO scale uncertainties for neutral DY case at $Q = 3000$ GeV are found to get reduced from about 1.5% at NNLO level to about 0.4% at N^{3}LO level, the same in the resummed results are found to get significantly reduced from about 0.2% at NNLO+NNLL level to almost about 0.1% at N^{3}LO+N^{3}LL level. Thus, DY process is one of the processes for which the theoretical predictions available to-date are the most precise, any uncertainties that can still be present in these cross sections are only due to the PDFs. We will discuss the uncertainty due to PDFs later. It should be noted here that the scale uncertainties in the resummation context will not show improvement over the FO results in the low Q-region, say below 1000 GeV, where the threshold logarithms are not the sole dominant contributions to the cross sections. However, the scale uncertainties in the resummed results will get reduced in the high Q region. To elaborate on this, we compare and contrast the 7-point scale uncertainties in FO and resummed results at third order in QCD (see Fig. 3.12). The scale uncertainties in the low Q region (where regular terms and other parton channel contributions are non-negligible) are smaller for FO case, while they are smaller for resummed case in the high Q region (where the threshold logarithms are important).

To see the effects of resummation over FO results at a given order, it is quite useful to use the factors R_{ii} defined in Eq. (3.8). We plot in Fig. 3.13 these factors R_{11}, R_{22} and R_{33} for all three different DY processes as a function of the invariant mass of the dileptons. In all these plots, we can see the R_{11} contribution is dominant particularly in the high Q region, while the R_{33} is almost unity except for a small contribution in the high invariant mass distribution.

3.3.3 VH production

In this section, we present the numerical results for the Higgs production in association with a massive vector boson $V = Z, W^-, W^+$. We present results for both the invariant mass distribution and the total production cross sections at hadron colliders for different center of mass energies. However, for invariant mass distribution our results are confined to only DY process i.e. the production of an off-shell gauge boson followed by its decay to on-shell V and H.

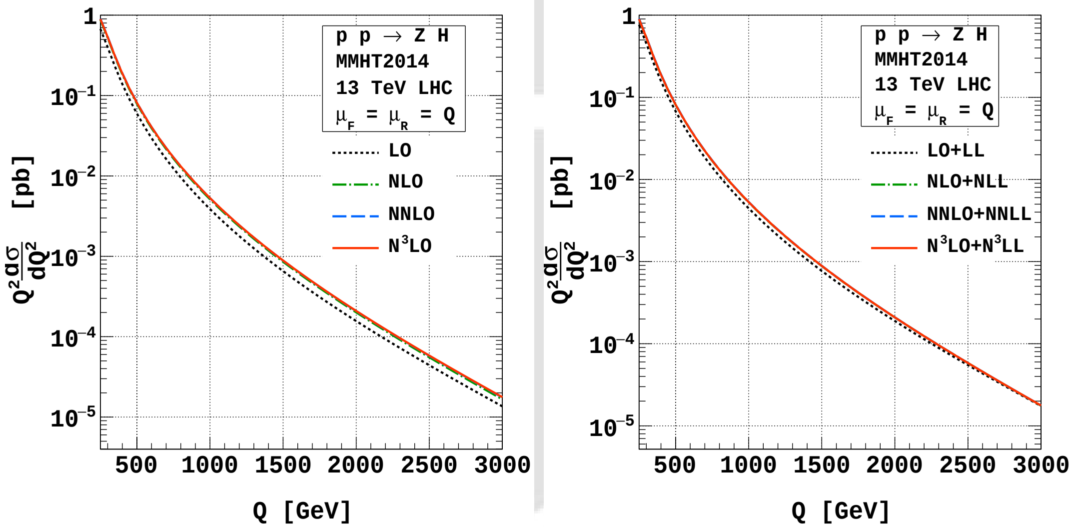

FIGURE 3.14: Invariant mass distribution of ZH for 13 TeV LHC fixed order (left panel) and the resummed (right panel).

It is worth noting that the total production cross sections for these processes up to NNLO are available through the public code `vh@nnlo` [108]. The updated version `vh@nnlo 2.1` [110] of the code can handle both the SM Higgs and other BSM scenarios where Higgs can be produced in association with a gauge boson. In this version, the code is also interfaced with `MCFM` [297] to produce invariant mass distributions up to NNLO level.

In the present context, we provide the invariant mass distribution up to third order ($\mathrm{N^3LO+N^3LL}$). To achieve this we use the invariant mass distributions of DY processes available at $\mathrm{N^3LO}$ level through `n3loxs` [73] code, and we numerically incorporate the

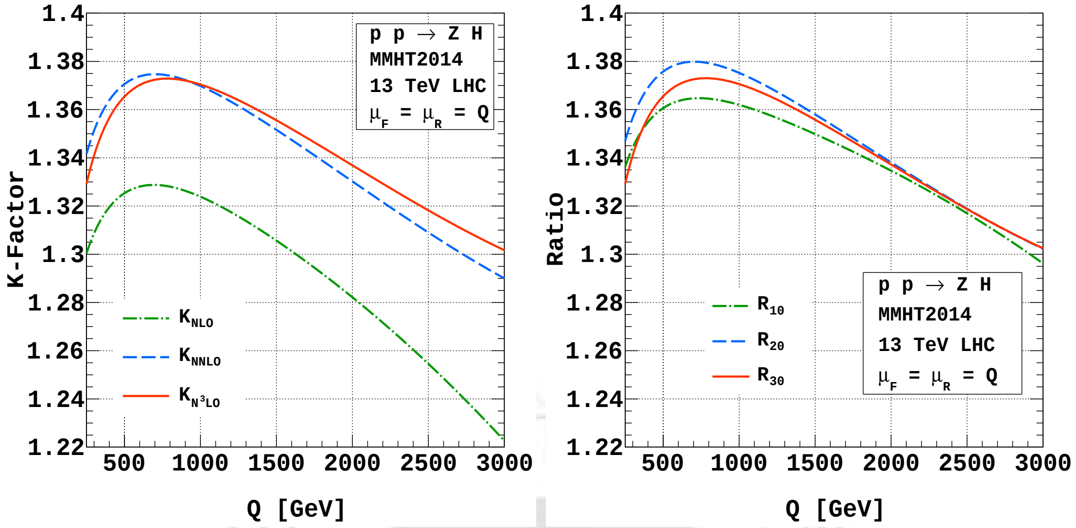

FIGURE 3.15: K-factor for fixed order of ZH for 13 TeV LHC (left panel) and the enhancement in the resummed cross section over fixed order LO are shown here (right panel) through R_{ij} is defined in Eq. (3.8).

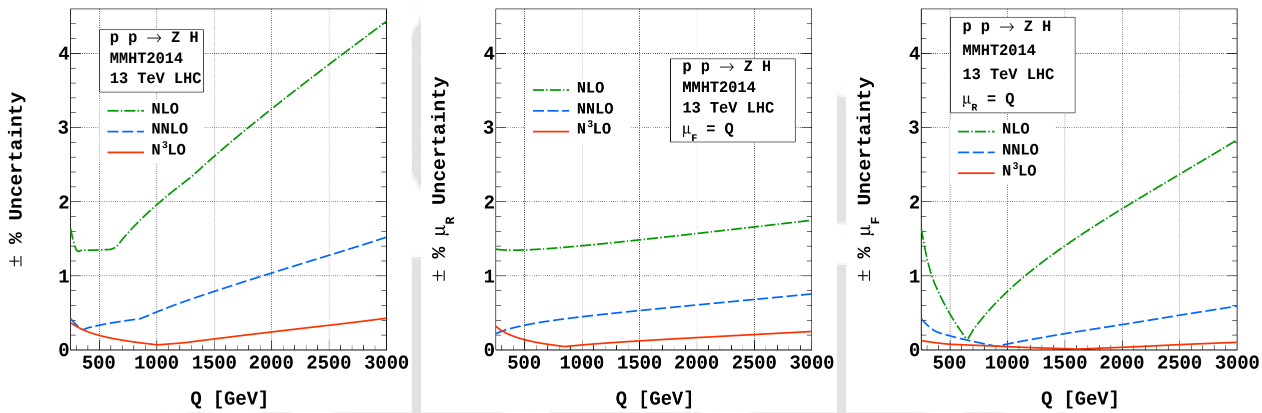

FIGURE 3.16: The 7-point scale uncertainty (left panel), μ_R scale uncertainty (middle panel) and μ_F scale uncertainty (right panel) up to N^{3}LO for ZH production.

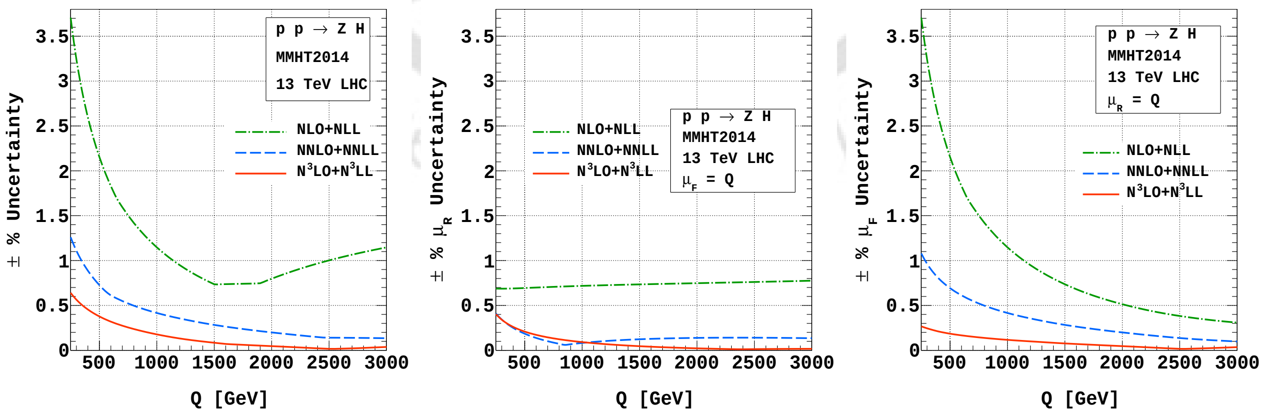

FIGURE 3.17: The 7-point scale uncertainty (left panel), μ_R scale uncertainty (middle panel) μ_F scale uncertainty (right panel) up to N^{3}LO+N^{3}LL for ZH production.

decay of the off-shell vector boson to V and H instead of to leptons, using the Eq.(2) and Eq.(3) of Ref.[110]. For consistency, we reproduce the results obtained from `vh@nnlo`

2.1 up to NNLO for VH invariant mass distribution. We then extend our analysis to the fixed order N^{3}LO level. For the resummation case, we use our in-house numerical code, similar to the one used for dilepton production case discussed in previous sections.

In Fig. 3.14, we plot the invariant mass distribution of VH at FO (left panel) and at resum level (right panel) up to third order (N^{3}LO+N^{3}LL) for ZH production process by varying Q from 250 GeV to 3000 GeV. Because the branching of off-shell V^* to VH is different from that to dileptons, the production cross sections will certainly be different from that of the neutral DY production of dileptons. However, the corresponding K-factors and R-factors are defined in Eq. (3.8), expected to be almost same as those of neutral DY case due to the cancellation of the branching part in these ratios.

$\sqrt{S}$ (TeV)	7.0	8.0	13.0	13.6	100.0
LO	$0.2363 \pm 0.36\%$	$0.2908 \pm 1.00\%$	$0.5934 \pm 3.81\%$	$0.6324 \pm 4.06\%$	$8.1105 \pm 13.57\%$
NLO	$0.3164 \pm 1.55\%$	$0.3878 \pm 1.50\%$	$0.7754 \pm 1.36\%$	$0.8245 \pm 1.36\%$	$9.1445 \pm 4.40\%$
NNLO	$0.3280 \pm 0.41\%$	$0.4017 \pm 0.37\%$	$0.8005 \pm 0.35\%$	$0.8508 \pm 0.36\%$	$9.1215 \pm 0.94\%$
N^{3}LO	$0.3266 \pm 0.25\%$	$0.3996 \pm 0.27\%$	$0.7943 \pm 0.32\%$	$0.8441 \pm 0.33\%$	$8.9790 \pm 0.49\%$
LO+LL	$0.2706 \pm 1.48\%$	$0.3319 \pm 1.45\%$	$0.6721 \pm 4.20\%$	$0.7158 \pm 4.44\%$	$9.0406 \pm 13.86\%$
NLO+NLL	$0.3260 \pm 4.34\%$	$0.3992 \pm 4.33\%$	$0.7966 \pm 4.31\%$	$0.8469 \pm 4.31\%$	$9.3550 \pm 5.39\%$
NNLO+NNLL	$0.3295 \pm 1.40\%$	$0.4034 \pm 1.43\%$	$0.8036 \pm 1.53\%$	$0.8542 \pm 1.53\%$	$9.1500 \pm 1.77\%$
N^{3}LO+N^{3}LL	$0.3266 \pm 0.46\%$	$0.3996 \pm 0.49\%$	$0.7943 \pm 0.57\%$	$0.8441 \pm 0.58\%$	$8.9795 \pm 0.75\%$

TABLE 3.1: ZH production cross section (in pb) for different $\sqrt{S}$ with 7-point scale uncertainty.

$\sqrt{S}$ (TeV)	$\sigma^{DY,ZH}_{\text{N}^3\text{LO}}$	$\sigma^{DY,ZH}_{\text{N}^3\text{LO+N}^3\text{LL}}$	$\sigma^{tot,ZH}_{\text{N}^3\text{LO}}$	$\sigma^{tot,ZH}_{\text{N}^3\text{LO+N}^3\text{LL}}$
7.0	$0.3266 \pm 0.25\%$	$0.3266 \pm 0.46\%$	$0.3534 \pm 1.25\%$	$0.3534 \pm 1.17\%$
8.0	$0.3996 \pm 0.27\%$	$0.3996 \pm 0.49\%$	$0.4373 \pm 1.36\%$	$0.4373 \pm 1.28\%$
13.0	$0.7943 \pm 0.32\%$	$0.7943 \pm 0.57\%$	$0.9112 \pm 1.79\%$	$0.9112 \pm 1.67\%$
13.6	$0.8441 \pm 0.33\%$	$0.8441 \pm 0.58\%$	$0.9728 \pm 1.86\%$	$0.9728 \pm 1.75\%$
100.0	$8.9790 \pm 0.49\%$	$8.9795 \pm 0.75\%$	$13.2674 \pm 4.57\%$	$13.2678 \pm 4.39\%$

TABLE 3.2: ZH production cross section (in pb) of DY-type N^{3}LO, DY-type N^{3}LO+N^{3}LL, total N^{3}LO and total resummed N^{3}LO+N^{3}LL which are defined in Eq. (3.9) and Eq. (3.10) for different $\sqrt{S}$ with 7-point scale uncertainty.

In Fig. 3.15, we present these K-factors (left panel) and R-factors (right panel) up to third order (N^{3}LO+N^{3}LL). The corresponding scale uncertainties for the ZH production case are shown for FO in Fig. 3.16 and for the resum case in Fig. 3.17. We notice that

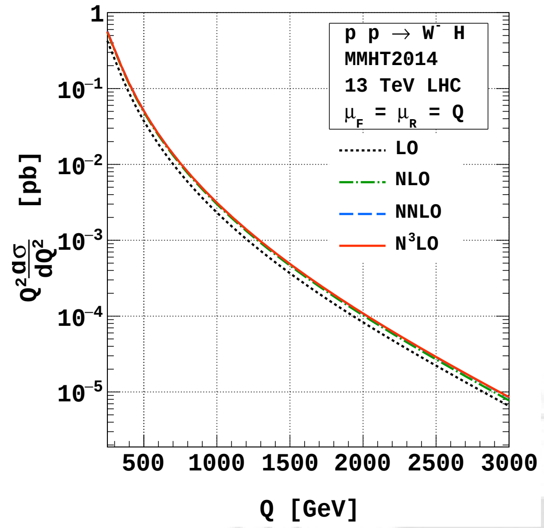

FIGURE 3.18: Invariant mass distribution of W^-H for 13 TeV LHC fixed order (left) and the resummed (right).

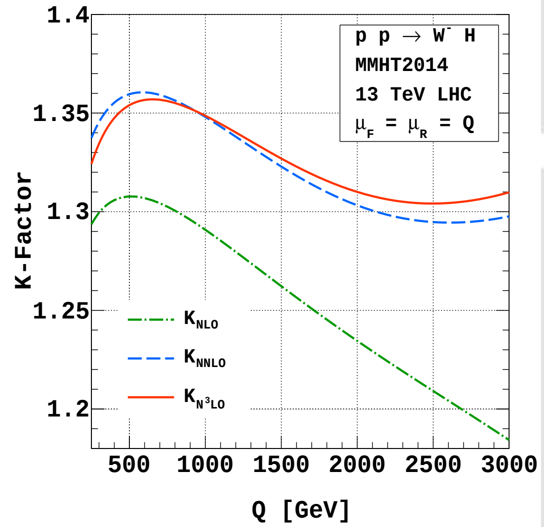

FIGURE 3.19: K-factor for fixed order of W^-H for 13 TeV LHC (left) and the enhancement in the resummed cross section over fixed order LO are shown here (right) through R_{ij} is defined in Eq. (3.8).

the behavior of the scale uncertainties for FO is the same as that for the neutral DY case. For completeness, in Fig. 3.16, we show separately the uncertainties due to the 7-point scale variations (left panel), those due to only μ_R for fixed $\mu_F = Q$ (middle panel) and those due to only μ_F for fixed $\mu_R = Q$ (right panel) for FO results. We find that the factorization scale uncertainties at higher orders, namely, at NNLO and N^{3}LO level are smaller than those due to the renormalization scale. In Fig. 3.17, we show similar plots as those in Fig. 3.16 but for resummed results. However, here we find that the factorization scale uncertainties are larger than the uncertainties due to the renormalization scale variations. This is expected because in the resummation case, the factorization scale dependence is included only from the threshold regions and that too in the $q\bar{q}$ channel. However, at the fixed order at N^{3}LO level, this is not the case as the full μ_F scale dependence is included in the coefficient functions at this order. We also notice that in general the scale uncertainties in FO results in the high Q region increase but very slowly. On the contrary, the scale uncertainties in the resummed predictions decrease with increasing Q. This is because in the high Q region the bulk of the cross sections are dominated by threshold logarithms and are resummed to all orders in the perturbation theory.

In Fig. 3.18 and Fig. 3.20, we show the results for invariant mass distribution of W^-H and W^+H production processes respectively. The corresponding K-factors and R_{i0}-factors are shown in Fig. 3.19 and Fig. 3.21. The results for the invariant mass distribution differ from those of the respective dilepton production processes through off-shell W^- and W^+ gauge bosons. However, the ratios K and R-factors are almost the same. Due to the underlying parton fluxes, these K-factors and R-factors for WH production case, on the other hand, will certainly be different from those of ZH case. In Fig. 3.22, we show the 7-point scale uncertainties in the invariant mass distribution of W^-H and W^+H processes.

For these new results i.e. the invariant mass distribution for VH process at N^{3}LO and N^{3}LO+N^{3}LL, we compare the 7-point scale uncertainties in FO and in resum results Fig. 3.23. The behavior of the scale uncertainties is almost identical to that of the neutral DY case (see Fig. 3.12), namely, the scale uncertainties are smaller in the low Q region for FO case, while the same is true for resum case in the high Q region. There is a very small and negligible difference between ZH case and neutral DY case, which is mostly due to the presence of photon contribution in the latter case.

We also present in Fig. 3.24, the ratios R_{ii} for $i = 1, 2, 3$ for ZH, W^-H and W^+H cases. It is also worth noting that with the automation of most of the NLO calculations [298, 299], the NLO results are readily available for these processes and hence it will be particularly useful to estimate the R_{i1} for $i = 1, 2, 3$. We plot these R_{i1} factors for all these VH processes in Fig. 3.25 as a function of Q. We notice that in general approximately for $Q > 2000$ GeV, both R_{21} and R_{31} merge with each other. However, their values are different for different processes. In the high Q region around 3000 GeV,

R_{31} being the largest for W^-H case and is about 1.105 while it is the smallest and is about 1.03 for W^+H case, whereas the corresponding one for ZH case is about 1.065.

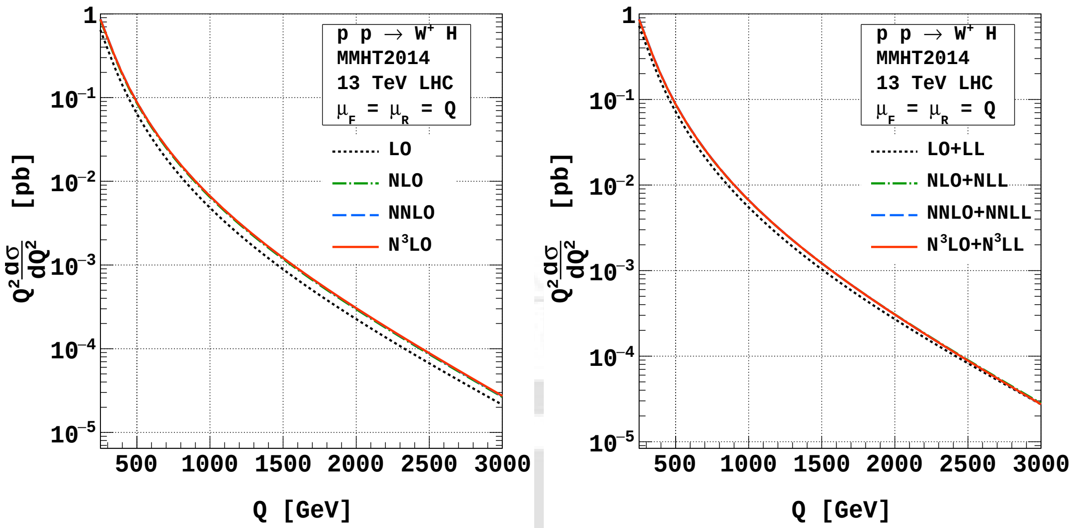

FIGURE 3.20: Invariant mass distribution of W$^+$H for 13 TeV LHC fixed order (left panel) and the resummed (right panel).

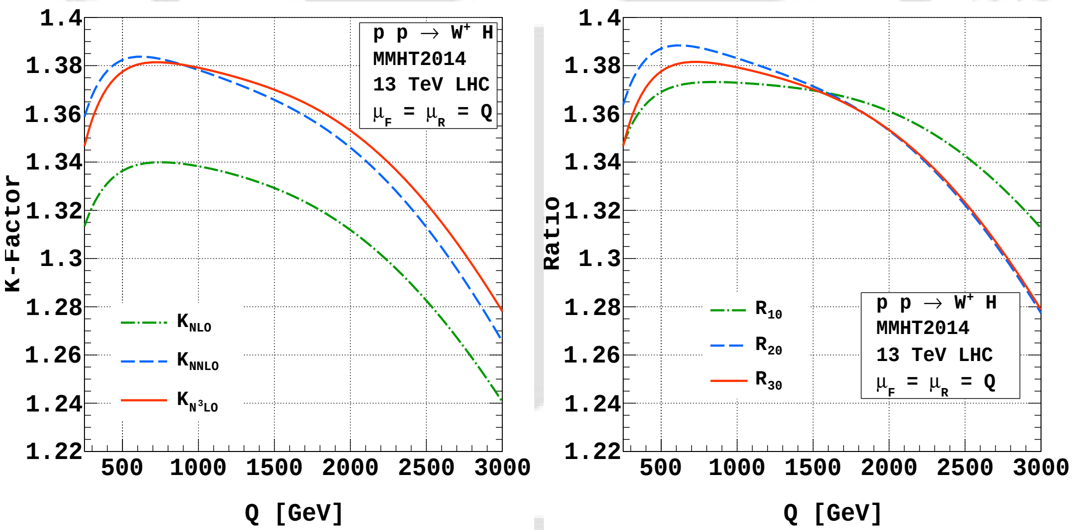

FIGURE 3.21: K-factor for fixed order of W$^+$H for 13 TeV LHC (left panel) and the enhancement in the resummed cross section over fixed order LO are shown here (right panel) through R_{ij} is defined in Eq. (3.8).

For the VH production process, we also give the total production cross sections obtained by integrating the invariant mass distributions over the entire Q region that is kinematically accessible. First, we give these total cross sections for DY type ZH production processes from LO to N^{3}LO+N^{3}LL for different center of mass energies $\sqrt{S} = 7, 8, 13, 13.6$ and 100 TeV in Table 3.1. The corresponding 7-point scale uncertainties are also provided for each case. For the total production cross sections, the bulk of the contribution comes essentially from the low Q region and hence the corresponding

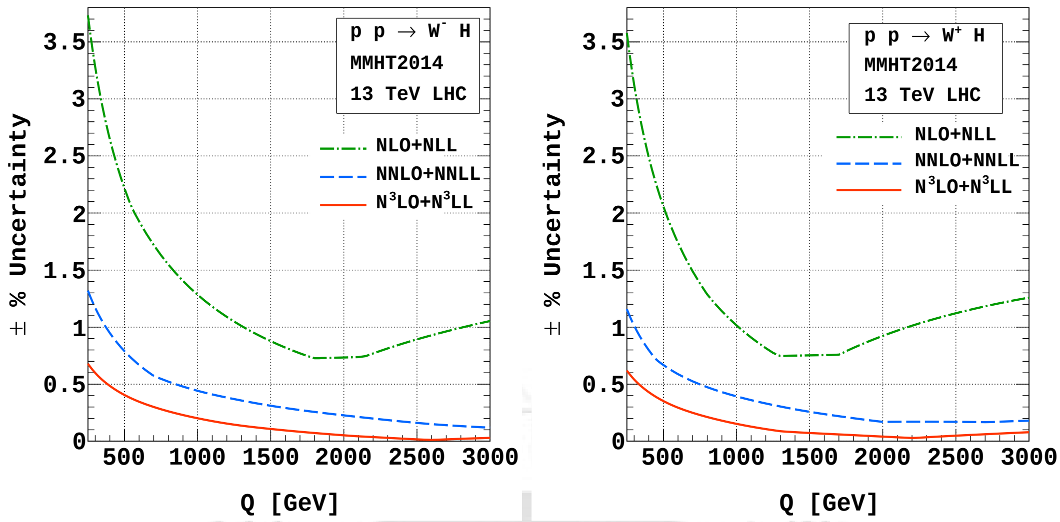

FIGURE 3.22: The resummed 7-point scale uncertainties for W^-H (left panel) and W^+H (right panel) up to N^3LO+N^3LL.

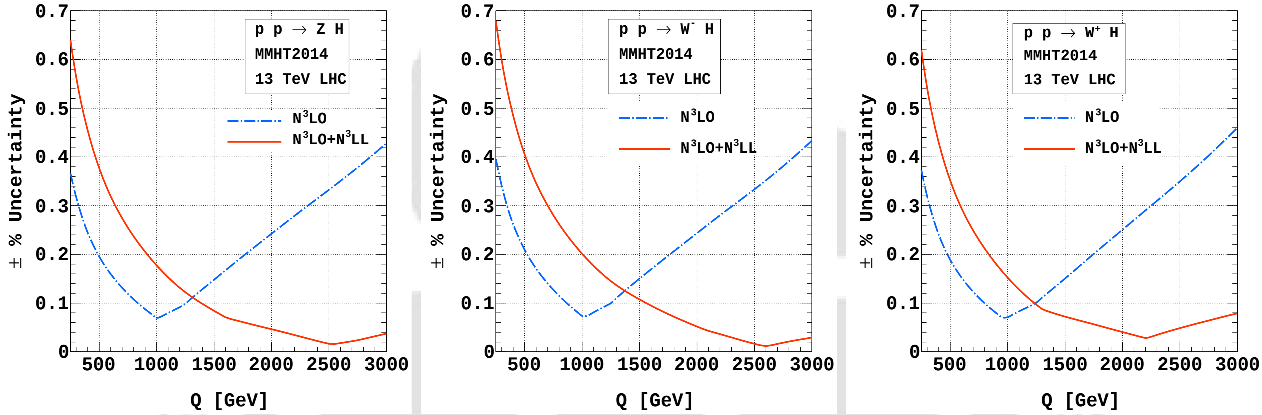

FIGURE 3.23: The 7-point scale uncertainty comparison for different Higgs associated production ZH (left panel), W^-H (middle panel) and W^+H (right panel) between resum and fixed order results.

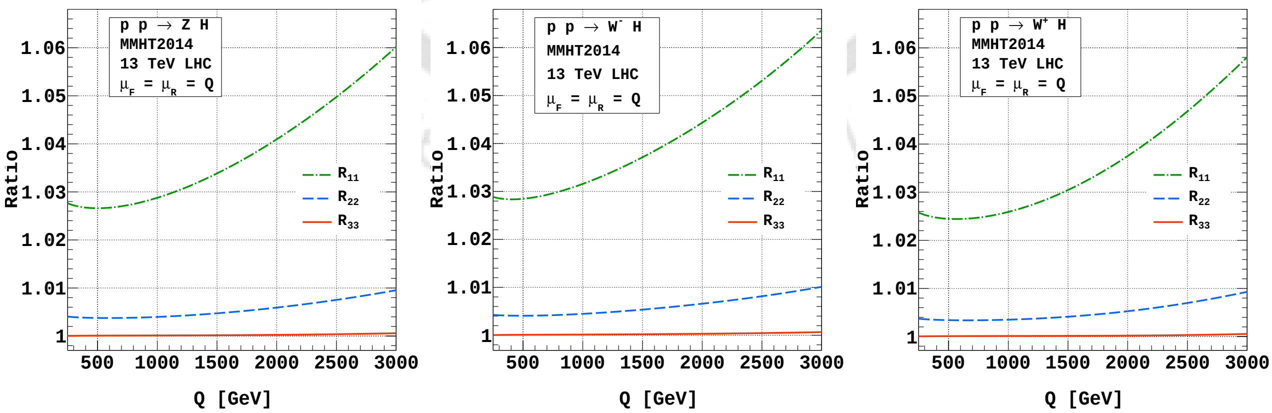

FIGURE 3.24: The enhancement in the resummed cross section over fixed order are shown here for different Higgs associated production ZH (left panel), W^-H (middle panel) and W^+H (right panel) through R_{ij} is defined in Eq. (3.8).

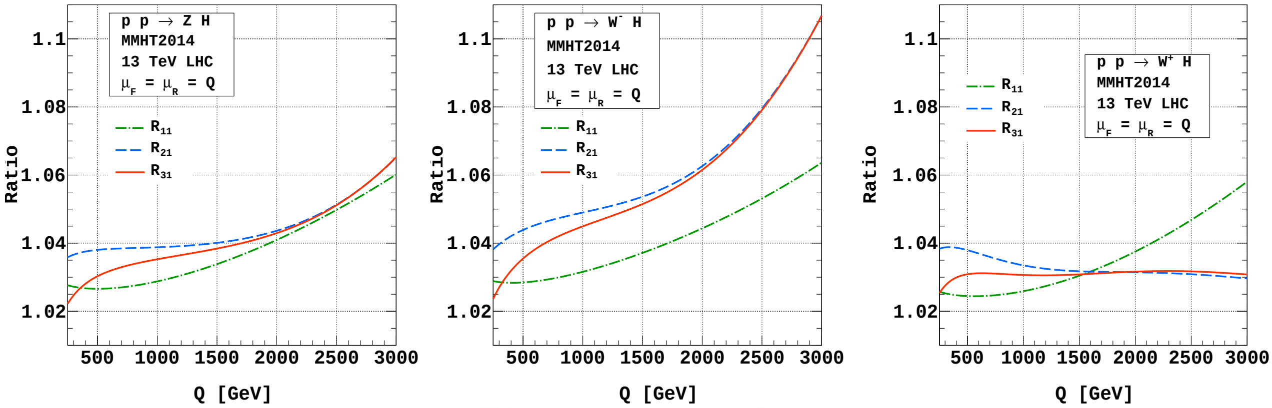

FIGURE 3.25: Enhancement resummed cross section over NLO are shown here for different Higgs associated production ZH (left panel), W^-H (middle panel) and W^+H (right panel). The factor R_{ij} is defined in Eq. (3.8).

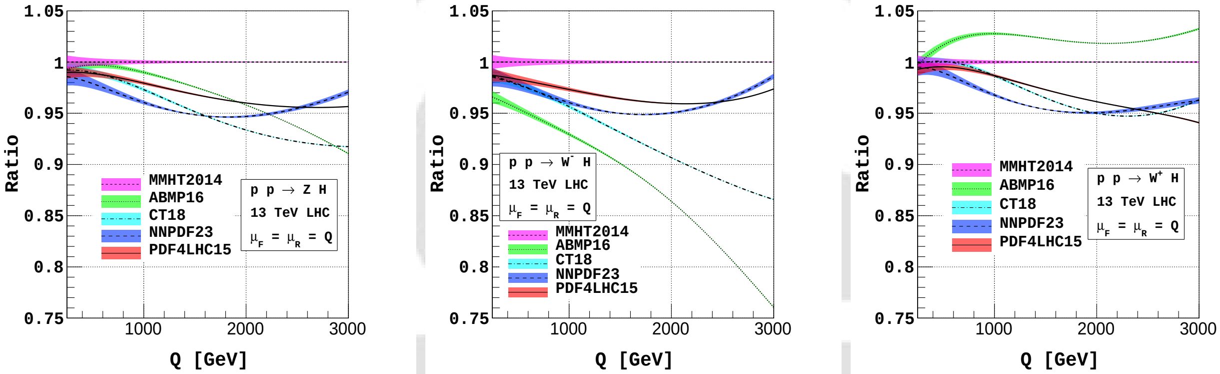

FIGURE 3.26: Behavior of invariant mass distributions at N^{3}LO+N^{3}LL for ZH (left panel), W^-H (middle panel) and W^+H (right panel) with 7-point scale variation in band for different PDF groups (central value) normalized to the default choice of MMHT2014.

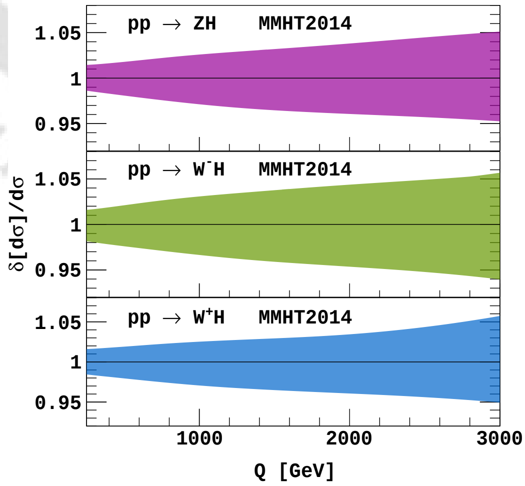

FIGURE 3.27: The intrinsic PDF uncertainties in the resummed predictions for VH production processes at N^{3}LO+N^{3}LL, obtained from MMHT2014nnlo68cl PDF sets.

scale uncertainties in the resummed results are predominantly due to those coming from the FO results that enter through matching procedure. Hence, the scale uncertainties are smaller for FO case than those for the resum case. However, one can clearly see these scale uncertainties decrease for any center of mass energy as we go from LO to $\mathrm{N^3LO}$ in FO, or as we go from LO+LL to $\mathrm{N^3LO{+}N^3LL}$ in the resummation series. For example, for the 13.6 TeV case, the scale uncertainties at LO are 4.06% and get reduced to about 0.33%, while those at LO+LL are 4.44%, and they get reduced to about 0.58% at $\mathrm{N^3LO{+}N^3LL}$. In Table 3.3, we present similar results for W^-H case and in Table 3.5 for W^+H case. In all these results, the general observation is that the scale uncertainties do increase with the center of mass energy $\sqrt{S}$ of the incoming hadrons.

Finally, in the context of VH production, we note that the DY type contributions do not fully give the complete FO predictions for VH case. Starting from $\mathcal{O}(a_s^2)$, particularly the ZH process receives contributions from the gluon fusion channel [116], bottom annihilation channel as well as the heavy top-loop contributions [300]. For the gluon fusion channel, the LO order contribution formally comes at the same order as NNLO of DY type ZH production process and the results for this channel are available already. The higher order NLO corrections to this gluon fusion channel which contribute at $\mathcal{O}(a_s^3)$ level appear at the same order as the $\mathrm{N^3LO}$ of DY type corrections, and these NLO corrections to the gluon fusion channel in the effective theory [119] have been computed already. It is worth noting that in the recent past, there has been a significant amount of progress toward the computation of the NLO corrections to this gluon fusion process considering the finite top quark mass effects [121–126, 301]. The top-loop contributions are available at the a_s^2 level [300] and are implemented in the `vh@nnlo 2.1` code. In the present context, we consider all these three contributions to the ZH production process and define the total production cross section defined as

$$\sigma^{tot,ZH}_{\mathrm{N^3LO}} = \sigma^{\mathrm{DY,ZH}}_{\mathrm{N^3LO}} + \sigma^{gg}(a_s^3) + \sigma^{\mathrm{top}}(a_s^2) + \sigma^{b\bar{b}} \tag{3.9}$$

$$\sigma^{tot,ZH}_{\mathrm{N^3LO+N^3LL}} = \sigma^{\mathrm{DY,ZH}}_{\mathrm{N^3LO+N^3LL}} + \sigma^{gg}(a_s^3) + \sigma^{\mathrm{top}}(a_s^2) + \sigma^{b\bar{b}} \tag{3.10}$$

where the power of a_s in the parenthesis denotes the highest order up to which the respective contribution has been taken into account. These additional contributing Feynman diagrams are shown in Fig. 3.28. We present these results for the ZH case in Table 3.2.

For the case WH production, there will be no contribution from gluon fusion as well as bottom annihilation processes, however, there will be contribution from top-loops from NNLO onwards. Hence, we define the total production cross sections for WH case as

$$\sigma^{tot,WH}_{\mathrm{N^3LO}} = \sigma^{\mathrm{DY,WH}}_{\mathrm{N^3LO}} + \sigma^{\mathrm{top}}(a_s^2) \tag{3.11}$$

$$\sigma^{tot,WH}_{\mathrm{N^3LO+N^3LL}} = \sigma^{\mathrm{DY,WH}}_{\mathrm{N^3LO+N^3LL}} + \sigma^{\mathrm{top}}(a_s^2). \tag{3.12}$$

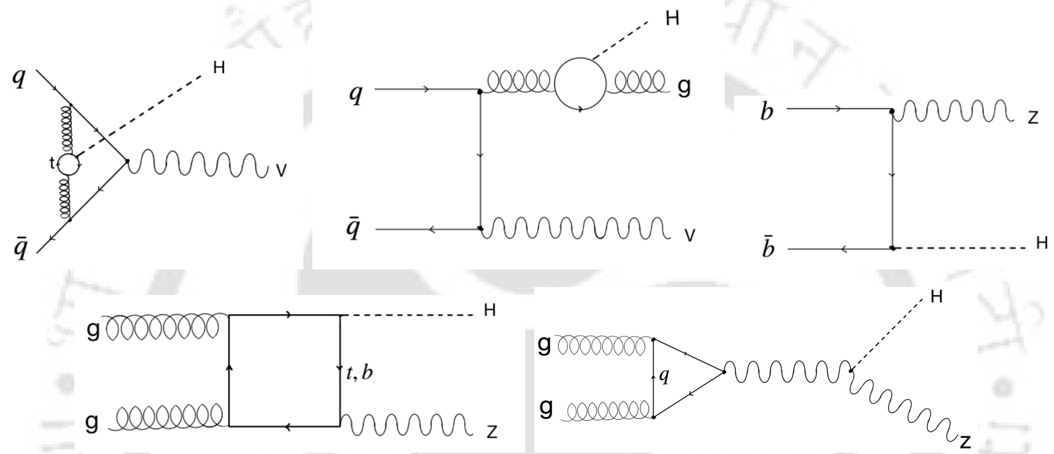

FIGURE 3.28: The feynman diagrams for VH production additional contributing channels at LHC.

These production cross sections up to N^{3}LO+N^{3}LL are given in Table 3.4 for W^-H and in Table 3.6 for W^+H cases. We also note that at this level, the electroweak corrections [111, 112] are also competitive. For the current LHC energies, they are about -5.28% for ZH and -6.88% for WH total production cross sections. This can easily be implemented in the analysis, however, we did not consider them for simplicity and focus only on the QCD corrections.

Finally, we estimate the uncertainties in our predictions for VH invariant mass distributions due to the choice of the PDFs used in our analysis. For this, we compute the invariant mass distributions at N^{3}LO+N^{3}LL using different choice of PDFs : ABMP16 [302], CT18 [303], NNPDF23 [304] and PDF4LHC15 [305]. All these sets are considered at NNLO level and the invariant mass distributions are obtained for central set (iset=0). We obtain these results normalized with respect to those obtained from our default choice of MMHT2014nnlo PDFs (iset=0) and for the central scale choice and

$\sqrt{S}$ (TeV)	7.0	8.0	13.0	13.6	100.0
LO	$0.1625 \pm 0.46\%$	$0.2021 \pm 1.27\%$	$0.4262 \pm 4.04\%$	$0.4553 \pm 4.28\%$	$6.1486 \pm 13.49\%$
NLO	$0.2144 \pm 1.55\%$	$0.2660 \pm 1.50\%$	$0.5524 \pm 1.37\%$	$0.5891 \pm 1.44\%$	$6.9628 \pm 4.39\%$
NNLO	$0.2234 \pm 0.39\%$	$0.2769 \pm 0.35\%$	$0.5716 \pm 0.38\%$	$0.6093 \pm 0.39\%$	$6.9645 \pm 0.97\%$
N^{3}LO	$0.2223 \pm 0.28\%$	$0.2752 \pm 0.30\%$	$0.5667 \pm 0.36\%$	$0.6039 \pm 0.36\%$	$6.8460 \pm 0.54\%$
LO+LL	$0.1872 \pm 1.56\%$	$0.2320 \pm 1.68\%$	$0.4847 \pm 4.42\%$	$0.5175 \pm 4.65\%$	$6.8494 \pm 13.71\%$
NLO+NLL	$0.2214 \pm 4.55\%$	$0.2744 \pm 4.53\%$	$0.5683 \pm 4.46\%$	$0.6059 \pm 4.46\%$	$7.1248 \pm 5.39\%$
NNLO+NNLL	$0.2245 \pm 1.49\%$	$0.2782 \pm 1.52\%$	$0.5741 \pm 1.60\%$	$0.6118 \pm 1.61\%$	$6.9867 \pm 1.79\%$
N^{3}LO+N^{3}LL	$0.2223 \pm 0.53\%$	$0.2752 \pm 0.55\%$	$0.5667 \pm 0.63\%$	$0.6039 \pm 0.63\%$	$6.8464 \pm 0.81\%$

TABLE 3.3: W^-H production cross section (in pb) for different $\sqrt{S}$ with 7-point scale uncertainty.

$\sqrt{S}$ (TeV)	$\sigma^{DY,W^-H}_{\text{N}^3\text{LO}}$	$\sigma^{DY,W^-H}_{\text{N}^3\text{LO+N}^3\text{LL}}$	$\sigma^{tot,W^-H}_{\text{N}^3\text{LO}}$	$\sigma^{tot,W^-H}_{\text{N}^3\text{LO+N}^3\text{LL}}$
7.0	$0.2223 \pm 0.28\%$	$0.2223 \pm 0.53\%$	$0.2245 \pm 0.09\%$	$0.2245 \pm 0.34\%$
8.0	$0.2752 \pm 0.30\%$	$0.2752 \pm 0.55\%$	$0.2781 \pm 0.08\%$	$0.2781 \pm 0.36\%$
13.0	$0.5667 \pm 0.36\%$	$0.5667 \pm 0.63\%$	$0.5739 \pm 0.13\%$	$0.5739 \pm 0.42\%$
13.6	$0.6039 \pm 0.36\%$	$0.6039 \pm 0.63\%$	$0.6117 \pm 0.13\%$	$0.6117 \pm 0.42\%$
100.0	$6.8460 \pm 0.54\%$	$6.8464 \pm 0.81\%$	$6.9963 \pm 0.35\%$	$6.9967 \pm 0.61\%$

TABLE 3.4: W^-H production cross section (in pb) of DY-type N^{3}LO, DY-type N^{3}LO+N^{3}LL, total N^{3}LO and total resummed N^{3}LO+N^{3}LL which are defined in Eq. (3.11) and Eq. (3.12) for different $\sqrt{S}$ with 7-point scale uncertainty.

$\sqrt{S}$ (TeV)	7.0	8.0	13.0	13.6	100.0
LO	$0.2820 \pm 0.30\%$	$0.3409 \pm 1.08\%$	$0.6583 \pm 3.77\%$	$0.6983 \pm 4.00\%$	$7.7331 \pm 13.06\%$
NLO	$0.3805 \pm 1.57\%$	$0.4582 \pm 1.53\%$	$0.8676 \pm 1.40\%$	$0.9183 \pm 1.40\%$	$8.7881 \pm 4.38\%$
NNLO	$0.3944 \pm 0.42\%$	$0.4750 \pm 0.39\%$	$0.8975 \pm 0.37\%$	$0.9497 \pm 0.38\%$	$8.7460 \pm 1.01\%$
N^{3}LO	$0.3927 \pm 0.25\%$	$0.4725 \pm 0.27\%$	$0.8906 \pm 0.33\%$	$0.9422 \pm 0.34\%$	$8.6026 \pm 0.54\%$
LO+LL	$0.3201 \pm 1.39\%$	$0.3861 \pm 1.49\%$	$0.7409 \pm 4.14\%$	$0.7856 \pm 4.37\%$	$8.5904 \pm 13.33\%$
NLO+NLL	$0.3911 \pm 4.13\%$	$0.4707 \pm 4.12\%$	$0.8897 \pm 4.12\%$	$0.9416 \pm 4.12\%$	$8.9811 \pm 5.26\%$
NNLO+NNLL	$0.3960 \pm 1.34\%$	$0.4768 \pm 1.37\%$	$0.9008 \pm 1.46\%$	$0.9532 \pm 1.47\%$	$8.7719 \pm 1.68\%$
N^{3}LO+N^{3}LL	$0.3927 \pm 0.45\%$	$0.4725 \pm 0.48\%$	$0.8907 \pm 0.56\%$	$0.9423 \pm 0.57\%$	$8.6032 \pm 0.79\%$

TABLE 3.5: W^+H production cross section (in pb) for different $\sqrt{S}$ with 7-point scale uncertainty.

present them in Fig. 3.26 for ZH (left panel), W^-H (middle panel) and for W^+H (right panel). The bands for each of the PDF sets in these figures represent the corresponding 7-point scale uncertainties, which are found to get reduced with Q for all the PDF sets considered here except those for NNPDF23 sets. For the latter choice of PDF sets, the scale uncertainties are found to decrease first with Q up to about 1500 GeV, and then

$\sqrt{S}$ (TeV)	$\sigma^{DY,W^+H}_{\text{N}^3\text{LO}}$	$\sigma^{DY,W^+H}_{\text{N}^3\text{LO+N}^3\text{LL}}$	$\sigma^{tot,W^+H}_{\text{N}^3\text{LO}}$	$\sigma^{tot,W^+H}_{\text{N}^3\text{LO+N}^3\text{LL}}$
7.0	$0.3927 \pm 0.25\%$	$0.3927 \pm 0.45\%$	$0.3965 \pm 0.11\%$	$0.3965 \pm 0.27\%$
8.0	$0.4725 \pm 0.27\%$	$0.4725 \pm 0.48\%$	$0.4774 \pm 0.09\%$	$0.4774 \pm 0.29\%$
13.0	$0.8906 \pm 0.33\%$	$0.8907 \pm 0.56\%$	$0.9017 \pm 0.13\%$	$0.9017 \pm 0.36\%$
13.6	$0.9422 \pm 0.34\%$	$0.9423 \pm 0.57\%$	$0.9541 \pm 0.13\%$	$0.9542 \pm 0.36\%$
100.0	$8.6026 \pm 0.54\%$	$8.6032 \pm 0.79\%$	$8.7865 \pm 0.37\%$	$8.7871 \pm 0.60\%$

TABLE 3.6: W^+H production cross section (in pb) of DY-type N^{3}LO, DY-type N^{3}LO+N^{3}LL, total N^{3}LO and total resummed N^{3}LO+N^{3}LL which are defined in Eq. (3.11) and Eq. (3.12) for different $\sqrt{S}$ with 7-point scale uncertainty.

they slowly increase with Q. The uncertainty in these predictions due to the choice of different PDF sets is smaller in the low Q-region and is at the most 4%, but these uncertainties tend to increase with Q. In the high Q region $Q > 2000$ GeV, the deviations from MMHT2014 results are in general larger for ABMP16 and CT18 PDF sets for ZH and W^-H processes. The deviations at $Q = 2000$ GeV for ZH case are about 4.2%, 6.6%, 5.3% and 4.0% for ABMP16, CT18, NNPDF23 and PDF4LHC15 PDF sets respectively. The similar numbers for $Q = 3000$ GeV are about 9.0%, 8.3%, 2.9% and 4.3% respectively. The deviations are largest for the case W^-H in the high Q region and are about 20% for ABMP16 sets.

It is worth studying the intrinsic PDF uncertainties in our resummed predictions due to the parametrization of the PDFs themselves. For this, we use the MMHT2014nnlo68cl PDF sets and compute the cross sections due to all the 51 different sets and estimate the asymmetric uncertainties as provided by the `LHAPDF` routines. We present these uncertainties in our resummed results for VH productin cross sections at N^{3}LO+N^{3}LL accuracy normalized with respect to those obtained with the central set. These results are shown in Fig. 3.27 for the ZH, W^-H and W^+H processes, with uncertainties reaching about 5% in the high invariant mass region.

3.3.4 $b\bar{b}H$ production

As a final process, we consider the Higgs boson production in bottom quark annihilation process at the LHC. A schematic representation of H production through bottom quark annihilation at the LHC is shown in Fig. 3.29. This process has already been studied up to NNLO+NNLL by some of the authors in [257] including a detailed uncertainty analysis.

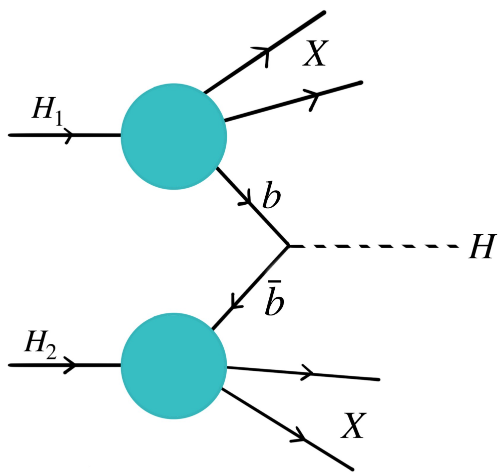

FIGURE 3.29: A schematic representation of H production through bottom quark annihilation at a hadron collider.

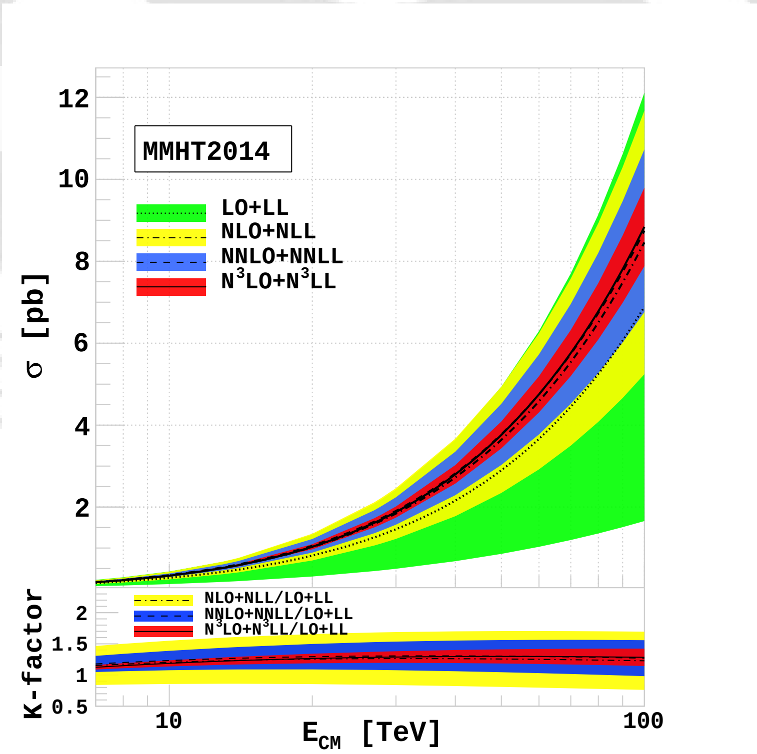

FIGURE 3.30: The $b\bar{b}H$ cross section for different center of mass energy at different order and the corresponding K-factor with respect to LO+LL.

In [257], the work also has been extended to N^{3}LO+N^{3}LL including the estimation of uncertainties only due to unphysical renormalization scale. However, in this work, we complement these studies by considering the $b\bar{b} \to H$ production cross sections along with a detailed 7-point scale uncertainties for the choice of parameters given before. We present in Fig. 3.30 these production cross sections from LO+LL to N^{3}LO+N^{3}LL along with the respective scale uncertainties at hadron colliders for different center of mass energy $\sqrt{S}$ values from 7 TeV to 100 TeV. For $\sqrt{S} = 13.6$ TeV, we find that these 7-point scale uncertainties is 5.26% at N^{3}LO and is 4.98% at N^{3}LO+N^{3}LL. The scale uncertainties are found to get reduced with higher logarithmic accuracy in resummation while at any given order in perturbation theory they are in general found to increase with $\sqrt{S}$.

3.4 Conclusions

We have studied the threshold effect on the color singlet processes DY, associated VH productions and Higgs production through bottom quark annihilation. To achieve this, we have used the universal and process dependent resum coefficients that are known by some of us up to N^{3}LL. Thanks to the recent publicly available `n3loxs` code that we are able to perform the complete matching at the third order in QCD thus incorporating missing regular contributions at this order. We performed a detailed phenomenology for neutral DY, charged DY production of dileptons, Higgs production in association with massive vector boson ($V = Z/W$) in the DY-type process as well as for the Higgs production in bottom quark annihilation process. We presented our results for the dilepton and VH invariant mass distributions as well as the total production cross sections for VH and $b\bar{b}H$ processes. For the case of VH production process, the resummed corrections over the fixed order N^{3}LO results are found to be very small, thus demonstrating a very good convergence of the perturbation series. We observe that the FO results have smaller scale uncertainties in the low Q region. However, the resummation gives significant reduction of the conventional 7-point scale uncertainties to as small as 0.1% in the high invariant mass region $Q \geq 1500$ GeV of VH production processes. For the associated Higgs production with a Z boson, the gluon fusion channel and top-loop contributions from NNLO onward are also important [121–126, 301] at the accuracy that we considered here. We have included these contributions in our inclusive total production cross sections for VH processes. To tame down the uncertainties further, we note that the resummation in gluon fusion channel is equally important. For the DY and DY-type

VH production processes we have considered here, the theory uncertainties after the resummation to N^{3}LL accuracy has been achieved are very much under control. However, the PDF uncertainties are still large which can be reduced with the availability of N^{3}LO level PDFs and more experimental data. Further, at this precision level the electroweak corrections are also important to bring the total theory uncertainties under control.

Chapter 4

Soft gluon resummation for gluon fusion ZH production in QCD

The associated production of the Higgs boson with a massive vector boson, such as the Z boson, plays a vital role in precision Higgs studies at hadron colliders. While the dominant contribution to ZH production arises from the Drell–Yan (DY) type quark-antiquark annihilation process, there exists an important subleading contribution via the loop-induced gluon fusion channel, $gg \to ZH$. Although formally suppressed by the strong coupling constant α_s, the gluon-initiated process is numerically significant at the Large Hadron Collider (LHC), particularly in kinematic regions with high partonic center-of-mass energies. Its importance is further amplified by the increasing gluon luminosity at higher collision energies, and thus demands a dedicated theoretical treatment.

In the chapter 3, we focused on the threshold resummation for DY-type color-singlet processes, including Drell–Yan, associated VH production, and Higgs production via bottom quark annihilation. Those processes share a common QCD structure where the colorless final state is initiated by quark-antiquark pairs, and the soft gluon resummation are governed by universal factorization properties. Here, we have studied soft gluon resummation for the gluon pair case by using the universal factorization properties. We employed a unified framework using soft-virtual (SV) resummation techniques in Mellin space, matched to fixed-order results, and demonstrated how these corrections improve theoretical predictions by stabilizing the perturbative expansions, then extended to next-to-soft-virtual corrections to reduce the scale dependence.

4.1 Introduction

The discovery of the Higgs boson [8, 10, 11] at the Large Hadron Collider (LHC) [27, 28] marks a significant milestone in particle physics. Following this breakthrough, the primary focus of the LHC has been the precise measurement of the Higgs boson's properties and couplings. Such efforts not only deepen our understanding of the Higgs boson itself but also open new avenues for exploring physics beyond the Standard Model (BSM). Many BSM scenarios predict weak couplings to the Higgs boson at collider energies in the TeV range. Evidence of such interactions may manifest as deviations in total cross-sections or distributions for Higgs boson processes. Therefore, precise experimental measurements, combined with accurate theoretical predictions, are critical for identifying potential BSM signatures. The associated Higgs production with a vector boson at the LHC is of particular importance in probing Higgs coupling to the weak gauge bosons. Furthermore, it is crucial to constrain the sign of the top quark Yukawa coupling and examine its CP structure [306–308]. Keeping in mind the importance of this process, the ATLAS and CMS experiments are actively conducting precise measurements for this process [2, 3, 309–317]. Precise theoretical predictions are thus essential to complement the improved experimental results for this channel.

At the LHC, the Higgs boson is produced in association with Z boson primarily through the Drell-Yan (DY) type subprocess ($q\bar{q} \to Z^* \to ZH$) at the leading order (LO) in the strong coupling (α_s) expansion. The higher order Quantum Chromodynamics (QCD) correction for this channel thus closely follow the DY process and has been computed up to next-to-next-to leading order (N2LO) [104, 106, 108–110, 297, 318, 319] and recently to next-to-next-to-next-to leading order (N3LO) [73] accuracy. The perturbative series for the DY-type contribution converges very quickly with next-to-leading order (NLO) amounting to around 30% correction to LO, whereas N2LO, N3LO receive around 3%, -0.8% corrections respectively relative to preceding orders. Additionally, the conventional theoretical scale uncertainty reduces to sub-percent level. The ZH process also gets a contribution from the bottom quark annihilation through the t-channel diagrams at the LHC. This involves a bottom Yukawa coupling (y_b) and its contribution is found

[259] to be at the sub-percent level. Furthermore, the Electro-Weak (EW) effects for this DY-type process have been computed to NLO [111] and a correction of around -5% was observed compared to the NLO QCD result. When fiducial cuts are applied, these corrections can grow significantly, reaching -10% to -20% of the NLO QCD distributions [112].

Compared to the DY process, the ZH process receives additional QCD contributions starting from N2LO. One such contribution involves Feynman diagrams where the Higgs boson is radiated from the massive top quark loop in the quark annihilation subprocess. Their contribution has been estimated [300] to be below 3%. Another type of subprocess which appear for the first time at N2LO i.e. at $\mathcal{O}(\alpha_s^2)$) is the ZH production through gluon fusion. Although the gluon fusion subprocess for ZH production is suppressed by two orders of strong couplings compared to the quark-antiquark annihilation subprocess, the suppression, however, is compensated considerably by the large gluon flux at the LHC. Therefore, starting from N2LO, this subprocess contributes dominantly. Due to its importance, the gluon fusion subprocess is being studied in great detail in the literature. The leading order of this subprocess (which contributes to $\mathcal{O}(\alpha_s^2)$) is a loop-induced process where ZH is produced through massive quark loop with top quark giving the dominant contributions. The LO of this subprocess has been computed with exact top quark mass in [115, 118] and is shown to provide correction of around 7% compared to the NLO QCD DY-type contribution (in contrast, the N2LO QCD DY-type contributes only around 3% compared to NLO DY) with a scale uncertainty of around 25%.

At the leading order and using the covariant R_ξ gauge, the process in which two gluons produce a Higgs boson along with a Z boson ($gg \to HZ$) is mediated by different types of loop diagrams involving heavy quarks. These loops can be broadly classified into box and triangle types. The box diagrams include heavy quarks like the top and bottom quarks, which interact more strongly with the Higgs boson. However, it is important to note that these contributions vanish in the limit of very large quark masses. The triangle diagrams can proceed through a virtual Z boson, where only the axial (chiral) part of the Z boson coupling contributes due to a symmetry rule known as Furry's theorem. In this case, only heavy quarks from the third generation make a non-zero contribution, since the lighter quarks effectively cancel out. Interestingly, only the longitudinal polarization state of the Z boson plays a role here, which simplifies the theoretical calculation by removing complications related to transverse polarization states, as guaranteed by the

Landau-Yang theorem [320, 321]. Another set of triangle diagrams involves the would-be Goldstone boson that couple to the massive quark loops in the traigular graph, followed by the decay of Goldstone boson to Z boson and Higgs boson. These contributions come exclusively from loops involving massive quarks. These diagrams are proportional to both the corresponding Yukawa couplings and the quark's third component of weak isospin. In the limit of heavy quark masses, their contribution approaches a constant value. While the box diagrams do not depend on the choice of gauge, the triangle contributions individually do. Nonetheless, when the two types of triangle diagrams are combined for a given quark generation, their total effect becomes independent of the gauge, which is necessary for any physically meaningful prediction.

Several efforts were made to further improve the accuracy for gluon subprocess by calculating its NLO ($\mathcal{O}(\alpha_s^3)$) contribution. This requires computation of two-loop amplitudes involving multiple scales, including three masses: the Higgs boson mass (M_H), the Z boson mass (M_Z), and the top quark mass (m_t) as well as two Mandelstam variables. The presence of these large number of scales significantly increases the computational complexity. However, the calculation becomes significantly simpler in the infinite top-mass limit (EFT), where the NLO correction has been computed [119] within the framework of this EFT approximation for this subprocess. Nevertheless, there are continuous efforts to take into consideration of full mass dependence. The NLO real and virtual contributions have been computed using an asymptotic expansion of the top-quark mass [120]. Additionally, two-loop amplitudes have been evaluated through a high-energy and large-m_t expansion, utilizing the Padé approximation [301], as well as through a transverse momentum expansion [122]. The combined effects of the high-energy expansion and transverse momentum expansion were further explored in [124, 126]. The NLO cross-section and invariant mass distribution have also been obtained by incorporating the full top-mass dependence, alongside a small-mass expansion for M_H and M_Z [123]. More recently, two-loop virtual corrections have been computed with full top-mass effects [121], followed by a determination of the cross-section with full top-mass dependence at NLO in [125]. The total cross-section at NLO shows an approximately 100% increase compared to the LO result, with the scale uncertainty reduced to around 15%. In contrast, the distributions like transverse momentum of the Higgs boson, within the fiducial volume can exhibit corrections as large as a factor of 10.

In the previous chapter in Fig. 3.2, the experimental data are compared with SM theoretical predictions from CMS [2] and ATLAS [3] for VH production with Higgs decay to $b\bar{b}$ and experimental data show good agreement with SM predicted results. But certain kinematic regions, especially near threshold or in the high-invariant-mass tail, exhibit larger uncertainties. These regions are sensitive to higher-order QCD effects, motivating improved theoretical calculations including soft-gluon resummation.

The fixed order results for this subprocess still suffer from the large threshold logarithms arising from soft gluons emission. These large logarithms need to be resummed to have reliable predictions. The size of the NLO corrections indicates that this subprocess will receive significant contributions from the threshold logarithms similar to the Higgs case. Resummation of these large soft (SV) logarithms is well-established in the literature [79, 81, 82, 180, 219, 220, 268, 269, 277, 322] and have been applied to many colorless processes [77, 78, 89, 183, 239, 260, 260, 262, 271, 278–282, 323–325] leading to improved predictions for inclusive cross-sections and invariant mass distributions. Recently, efforts were made to incorporate the next-to-soft (NSV) threshold effects for colorless productions [178, 222, 223, 263, 326–333]. For the ZH production in the DY-type channel, the effects of soft gluons have been estimated in [181] to next-to-next-to-next-to-leading logarithmic (N3LL) accuracy matched to N3LO fixed order in QCD. A better perturbative convergence has been observed for threshold resummation for invariant mass distribution of ZH pair. For the gluon fusion ZH process, the effects of soft gluons have been studied [127] for the total cross-section to next-to-leading logarithmic (NLL) accuracy matched to NLO in QCD in the EFT approximation where a correction about 15% of NLO was obtained. Similar accuracy for the invariant mass distribution is still missing.

The goal of this chapter is to improve the gluon fusion ZH process by incorporating soft and next-to-soft gluon resummation for both the total cross-section and the invariant mass distribution of the ZH pair. We work in the exact Born-improved gluon fusion channel, which has been shown to work effectively for the Higgs case, and we expect similar behavior for the ZH process. For NSV resummation, we closely follow the approach outlined in [178, 222]. Additionally, we present the complete result at $\mathcal{O}(\alpha_s^3)$, improved with SV threshold resummation from both quark and gluon channels for ZH production.

The chapter is organized as follows: In Sec. 4.2, we introduce the key theoretical formulas and present the coefficients required for performing SV and NSV resummation up to the necessary order. In Sec. 4.3, we provide a phenomenological study for the gluon fusion subprocess, combining it with the DY-type contributions to present complete results for pp collisions at $\mathcal{O}(\alpha_s^3)$ accuracy. Finally, we conclude in Sec. 4.4.

4.2 Theoretical Framework

The hadronic cross-section for ZH production in proton collision is provided in QCD factorization as,

$$Q^2\frac{\mathrm{d}\sigma}{\mathrm{d}Q^2} = \sum_{a,b}\int_0^1 \mathrm{d}x_1 \int_0^1 \mathrm{d}x_2\; f_a(x_1,\mu_F^2)\, f_b(x_2,\mu_F^2) \int_0^1 \mathrm{d}z\; \delta\left(\tau - z x_1 x_2\right) Q^2 \frac{\mathrm{d}\widehat{\sigma}_{ab}(z,\mu_F^2)}{\mathrm{d}Q^2}\,, \tag{4.1}$$

where $f_{a,b}$ are the parton distribution functions (PDFs) for parton a,b in the incoming hadrons and $\widehat{\sigma}_{ab}$ is the partonic coefficient function. The hadronic and partonic threshold variables $\tau = Q^2/S$ and $z = Q^2/\widehat{s}$ are defined in terms of respective center-of-mass energies S and $\widehat{s}$. Here Q is the invariant mass of the ZH system and μ_F is the factorisation scale. The partonic coefficient function can be decomposed (suppressing all scale dependencies) as,

$$Q^2\frac{\mathrm{d}\widehat{\sigma}_{ab}(z)}{\mathrm{d}Q^2} = \widehat{\sigma}^{(0)}_{ab}(Q^2)\Big(\delta_{ba}\Delta^{\mathrm{sv}}_{ab}\,(z) + \Delta^{\mathrm{reg}}_{ab}\,(z)\Big)\,. \tag{4.2}$$

The term $\Delta^{\mathrm{sv}}_{ab}$ appears only for the diagonal subprocesses $(gg, q\bar{q})$ and is known as the soft-virtual (SV) partonic coefficient and it captures the leading singular terms in the $z \equiv 1-\bar{z} \to 1$ limit. The $\Delta^{\mathrm{reg}}_{ab}$ term, on the other hand, contains subleading or regular contributions in the variable z. In general, they follow the expansion in the strong coupling at the renormalisation scale $\alpha_s(\mu_R^2) \equiv 4\pi a_s(\mu_R^2)$ as,

$$\Delta^{\mathrm{sv}}_{ab}(z) = \sum_{n=0}^{\infty} a_s^n(\mu_R^2)\;\delta_{ab}\left(\Delta^{(n)}_{\delta}\;\delta(\bar{z}) + \sum_{k=0}^{2n-1}\Delta^{(n)}_{\mathcal{D}_k}\;\mathcal{D}_k(\bar{z})\right)\,,\ \text{with } ab \in \{gg, q\bar{q}\}\,, \tag{4.3}$$

$$\Delta^{\mathrm{reg}}_{ab}(z) = \Delta^{\mathrm{nsv}}_{ab}(z) + \sum_{n=0}^{\infty} a_s^n(\mu_R^2)\Delta^{(n)}_{ab}(z) = \sum_{n=0}^{\infty} a_s^n(\mu_R^2)\left(\sum_{k=0}^{2n-1}\Delta^{(n)}_{ab,\ln_k}\;\ln^k(\bar{z}) + \Delta^{(n)}_{ab}(z)\right)\,,$$

where $\delta(\bar{z})$ is the Dirac delta distribution and $\mathcal{D}_k(\bar{z}) \equiv \left[\ln^k(\bar{z})/\bar{z}\right]_+$ are the plus-distributions. At the leading order, all the coefficients vanish except $\Delta^{(0)}_{\delta} = 1$. Here $\Delta^{(n)}_{ab,\ln_k}$ are the next-to-soft (NSV) coefficients which get contributions from both diagonal as well as off-diagonal channels. The last term in the above expression $\Delta_{ab}^{(n)}(z)$ vanishes in the soft limit $\bar{z} \equiv 1 - z \to 0$. Note that the singular SV part of the partonic coefficient has a universal structure which gets contributions from the underlying hard form factor, mass factorization kernels [210, 211] and soft radiations [81, 82, 204–207]. All of these are infrared divergent which however when regularized and combined give finite contributions.

The Born normalization factor $\widehat{\sigma}_{ab}^{(0)}$ in Eq. (4.2) takes the following form for $q\bar{q}$ subprocess,

$$\widehat{\sigma}_{q\bar{q}}^{(0)}(Q^2) = \left(\frac{\pi\alpha^2}{n_c S}\right)\left[\frac{M_Z^2 \lambda^{1/2}(Q^2, M_H^2, M_Z^2)\left(1 + \frac{\lambda(Q^2, M_H^2, M_Z^2)}{12 M_Z^2/Q^2}\right)}{(Q^2 - M_Z^2)^2 c_w^4 s_w^4}\left((g_q^V)^2 + (g_q^A)^2\right)\right], \tag{4.4}$$

with $g_a^A = -\frac{1}{2}T_a^3$, $g_a^V = \frac{1}{2}T_a^3 - s_w^2 Q_a$, Q_a being the electric charge and T_a^3 being the weak isospin of the fermions. Here, α is the fine structure constant, s_w, c_w are the sine and cosine of the Weinberg angle respectively, and $n_c = 3$ in QCD. M_Z and M_H are the masses of the Z boson and Higgs boson respectively and the function λ is defined as $\lambda(z, y, x) = (1 - x/z - y/z)^2 - 4xy/z^2$.

For the gluon fusion subprocess, in the infinite top mass limit, the Born factor takes the form [119],

$$\widehat{\sigma}_{gg}^{(0),\mathrm{EFT}}(Q^2) = \left(\frac{\sqrt{\pi}\; a_s(\mu_R^2)\alpha}{16 s_w^2 c_w^2}\right)^2 \left(\frac{Q^2}{M_Z^4}\right)\lambda^{\frac{3}{2}}(Q^2, M_H^2, M_Z^2)\,. \tag{4.5}$$

In the infinite top mass approximation, the full NLO correction to the gluon fusion subprocess is known [119]. In particular, the SV and NSV coefficients up to NLO are given as,

$$\begin{aligned}
\Delta_\delta^{(1)} =& \left(\frac{56}{27} + 8\zeta_2\right)C_A + \frac{64}{9}T_F n_f + \left(\frac{46}{9}C_A - 2\beta_0\right)\ln\left(\frac{\mu_F^2}{Q^2}\right) - 2\beta_0 \ln\left(\frac{\mu_F^2}{\mu_R^2}\right) \\
&+ \frac{\widehat{\sigma}_{(\mathrm{virt,red})}}{a_s(\mu_R^2)\widehat{\sigma}_{gg}^{(0),\mathrm{EFT}}(Q^2)}\,, \\
\Delta_{\mathcal{D}_0}^{(1)} =& -\Delta_{gg,\ln_0}^{(1)} + 8C_A = -8C_A \ln\left(\frac{\mu_F^2}{Q^2}\right)\,, \\
\Delta_{\mathcal{D}_1}^{(1)} =& -\Delta_{gg,\ln_1}^{(1)} = 16 C_A\,.
\end{aligned} \tag{4.6}$$

Here $\widehat{\sigma}_{(\text{virt,red})}$ is the "virtual reducible" contribution arising from Feynman diagrams involving two quark triangles which in the infinite top mass limit takes the form [119],

$$
\begin{aligned}
\widehat{\sigma}_{(\text{virt,red})} = & \int d\widehat{t}\, a_s(\mu_R^2)\frac{4}{3}\left(\frac{\sqrt{\pi}a_s(\mu_R^2)\alpha}{16 s_w^2 c_w^2}\right)^2 \frac{1}{\widehat{s}M_Z^4} \\
& \times\Bigg\{ M_H^2 \left(-1+\frac{M_Z^2}{\widehat{t}-M_Z^2}+\ln\left(\frac{-\widehat{t}}{M_Z^2}\right)\frac{M_Z^2}{\widehat{t}-M_Z^2}-\ln\left(\frac{-\widehat{t}}{M_Z^2}\right)\frac{M_Z^4}{\left(\widehat{t}-M_Z^2\right)^2}\right) \\
& +(\widehat{s}-M_Z^2)\left(-1-\frac{M_Z^2}{\widehat{t}-M_Z^2}+\ln\left(\frac{-\widehat{t}}{M_Z^2}\right)\frac{\widehat{t}M_Z^2}{\left(\widehat{t}-M_Z^2\right)^2}\right)+(\widehat{t}\leftrightarrow\widehat{u})\Bigg\},
\end{aligned}
\tag{4.7}
$$

where $\widehat{u}, \widehat{t}$ are the partonic Mandelstam variables.

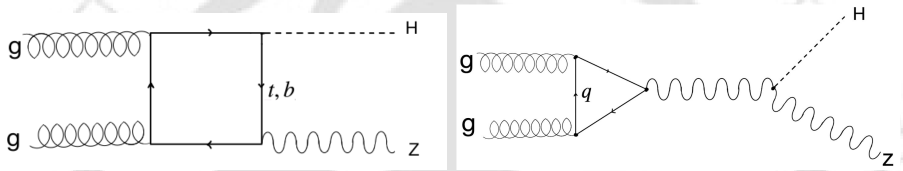

FIGURE 4.1: The leading order feynman diagram for gluon fusion ZH production.

The born coefficient in the exact theory, on the other hand, contains Feynman diagrams involving triangle and box diagrams as shown in Fig. 4.1 with heavy top quark dependence. It can be expressed in terms of helicity amplitudes for triangle and box diagrams as,

$$
\widehat{\sigma}_{gg}^{(0)}(Q^2) = \left(\frac{\sqrt{\pi}a_s(\mu_R^2)\alpha}{16 s_w^2}\right)^2 \frac{1}{8\widehat{s}^2}\int \mathrm{d}\widehat{t} \sum_{\lambda_g,\lambda_g',\lambda_Z}\left|\mathcal{M}^{\triangle}_{\lambda_g\lambda_g'\lambda_Z}+\mathcal{M}^{\square}_{\lambda_g\lambda_g'\lambda_Z}\right|^2 . \tag{4.8}
$$

The exact expression for these helicity amplitudes for two gluons and a Z boson can be found in [118].

In figure Fig. 4.2 illustrates the different contributions to the gluon-gluon initiated associated production of a Higgs boson with a Z boson. On the top left, the one-loop virtual diagram captures the purely virtual corrections, where no real radiation is emitted. The top right diagram shows the emission of a soft gluon, represented in red, from the virtual configuration. This soft radiation, though real, does not significantly alter the kinematics and is treated in conjunction with the virtual terms, forming the so-called soft-virtual (SV) contributions. These dominate near the production threshold, where the final state carries most of the partonic energy. In contrast, the bottom diagram

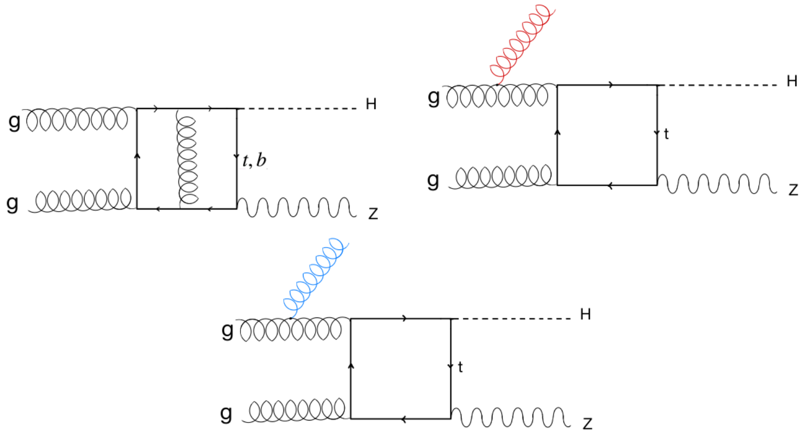

FIGURE 4.2: The next-to-leading order few feynman diagrams for gluon fusion ZH production at LHC.

features the emission of a hard gluon, shown in blue, which leads to real radiation with substantial momentum. Such configurations are classified under regular contributions, as they do not exhibit the same threshold enhancements. The distinction between SV and regular terms is reflected in the analytic structure of the cross-section, with SV terms captured by plus distributions and delta functions in the partonic variable z, while regular terms are finite in the limit $z \to 1$. The decomposition of the higher-order QCD corrections into these two components is essential for understanding the behavior of the perturbative series and for improving resummation predictions in the $gg \to ZH$ channel.

These large distributions appearing in the Δ^{SV} can be resummed to all orders in the threshold limit $z \to 1$. Typically, resummation is performed in the Mellin N-space where plus-distributions become simple logarithm in Mellin variable (N). The threshold limit $z \to 1$ translates into $N \to \infty$ limit. Recently a formalism has been proposed [178, 221–224] to also resum the NSV logarithms arising out of the diagonal channel. Essentially the partonic SV and NSV coefficients in the Mellin space can be organized as in Eq. (2.102) and G_N^g ($I = g$ for gluon fusion case) can be written as in Eq. (2.108) for SV and NSV exponent.

$$\frac{1}{\widehat{\sigma}^{(0)}_{ab}(Q^2)} Q^2 \frac{\mathrm{d}\widehat{\sigma}^{\overline{\mathrm{N}n\mathrm{LL}}}_{N,ab}}{\mathrm{d}Q^2} = \int_0^1 \mathrm{d}z \; z^{N-1} \left(\Delta^{\mathrm{sv}}_{ab}(z) + \Delta^{\mathrm{nsv}}_{ab}(z)\right) \equiv \overline{g}^g_0(Q^2) \exp\left(G^{g,\mathrm{sv}}_N + G^{g,\mathrm{nsv}}_N\right) . \tag{4.9}$$

The factor $\overline{g}_0^g$ is independent of the Mellin variable and contains process-dependent information. The leading threshold enhanced large logarithms and the next-to soft logarithms in Mellin space are resummed through the exponent $G_N^{g,\text{sv}}$ and $G_N^{g,\text{nsv}}$ respectively. The resummed accuracy is determined through the successive terms from both the exponent G_N^g which takes the form as in Eq. (2.109). The first term in the Eq. (2.109) is the expansion of G_N^{sv} corresponds to the leading logarithmic (LL) accuracy, whereas the inclusion of successive terms defines higher accuracies. These coefficients (g_n^g) are universal and only depend on the partonic flavours being either quark or gluon. In order to obtain $\overline{\text{LL}}$ accuracy in NSV resummation, one has to consider NSV exponents $\overline{g}_1^g$ and h_{00}^g in addition to the LL terms. Similarly, for higher accuracies, one has to consider the next terms in the expansion of G_N^g. Note that starting from NLL ($\overline{\text{NLL}}$), one has to also consider the N-independent $\overline{g}_0^g$ coefficients whose perturbative expansion takes the form as in Eq. (2.106). The explicit form of the resum exponent for SV and NSV resummation can be found *e.g.* in [77, 180]. Up to NLL($\overline{\text{NLL}}$) one requires the following coefficients for gluon fusion channel,

$$
\begin{aligned}
g_1^g(\omega) &= \frac{1}{\beta_0}\Bigg\{C_A\left(8\left(1+\frac{\overline{\omega}}{\omega}L_\omega\right)\right)\Bigg\},\\
g_2^g(\omega) &= \frac{1}{\beta_0^3}\Bigg\{C_A\beta_1\left(4\omega+4L_\omega+2L_\omega^2\right)+C_An_f\beta_0\left(\frac{40}{9}\left(\omega+L_\omega\right)\right)\\
&\quad+C_A^2\beta_0\left(\left(-\frac{268}{9}+8\zeta_2\right)\left(\omega+L_\omega\right)\right)+C_A\beta_0^2\left(4L_\omega\ln\left(\frac{Q^2}{\mu_R^2}\right)+4\omega\ln\left(\frac{\mu_F^2}{\mu_R^2}\right)\right)\Bigg\},\\
\overline{g}_1^g(\omega) &= \frac{1}{\beta_0}\Bigg\{C_A\left(4L_\omega\right)\Bigg\},\\
\overline{g}_2^g(\omega) &= \frac{1}{\overline{\omega}\beta_0^2}\Bigg\{C_AC_Fn_f\left(-8(\omega+L_\omega)\right)+C_A^2n_f\left(-\frac{40}{3}(\omega+L_\omega)\right)+C_A^3\left(\frac{136}{3}(\omega+L_\omega)\right)\\
&\quad+C_An_f\beta_0\left(\frac{40}{9}\omega\right)+C_A^2\beta_0\left(-\frac{268}{9}+8\zeta_2\right)\omega+C_A\beta_0^2\left(-8+4\ln\left(\frac{Q^2}{\mu_R^2}\right)-4\overline{\omega}\ln\left(\frac{\mu_F^2}{\mu_R^2}\right)\right)\Bigg\},\\
h_{00}^g(\omega) &= \frac{1}{\beta_0}\Bigg\{C_A\left(-8L_\omega\right)\Bigg\},\\
h_{10}^g(\omega) &= \frac{1}{\overline{\omega}\beta_0^2}\Bigg\{C_A\beta_1\left(-8(\omega+L_\omega)\right)+C_An_f\beta_0\left(-\frac{80}{9}\omega\right)+C_A^2\beta_0\left(\frac{536}{9}-16\zeta_2\right)\omega\\
&\quad+C_A\beta_0^2\left(8-8\ln\left(\frac{Q^2}{\mu_R^2}\right)+8\overline{\omega}\ln\left(\frac{\mu_F^2}{\mu_R^2}\right)\right)\Bigg\},\\
h_{11}^g(\omega) &= \frac{1}{\overline{\omega}^2\beta_0}\Bigg\{C_A^2\left(32\omega\overline{\omega}^2-4\omega\right)\Bigg\},
\end{aligned}
\tag{4.10}
$$

where $\overline{\omega}=1-\omega$ and $L_\omega=\ln(\overline{\omega})$. Note that up to the required order $\overline{\text{NLL}}$, the SV and NSV exponents are the same as the ggH case. Up to NLL($\overline{\text{NLL}}$) accuracy, one also needs the process dependent coefficient $\overline{g}_0^{g,(1)}$ and the gluon fusion ZH process the coefficient we found it to be,

$$\overline{g}_0^{g,(1)}(Q^2) = \left(\frac{56}{27} + 16\zeta_2\right) C_A + \frac{64}{9} T_F\, n_f - 2\beta_0 \ln\left(\frac{\mu_F^2}{\mu_R^2}\right) + \left(\frac{46}{9} C_A - 2\beta_0\right) \ln\left(\frac{\mu_F^2}{Q^2}\right) + \frac{\widehat{\sigma}_{(\mathrm{virt,red})}}{a_s(\mu_R^2)\widehat{\sigma}_{gg}^{(0)}(Q^2)} \,. \tag{4.11}$$

Note that both $\overline{g}_0^g$ and G_N^g are scheme-dependent which is related to the ambiguity in exponentiation of certain constant terms (e.g. γ_E) coming from Mellin transformation along with the large-N terms (see e.g. [325] for a detailed discussion). In the context of LHC, it has been observed that the so-called $\overline{N}$-scheme provides a faster perturbative convergence for the resummed series. In this scheme, the constant $\overline{g}_0^g$ is independent of γ_E.

The resummed result in Eq. (4.9) has to be finally matched with the available fixed order results to incorporate the hard regular contribution and, at the same time, avoid double counting of SV(NSV) logarithms. The matching with the fixed order is usually performed using the *minimal prescription* [225] and we follow the procedure mention in section 2.4.3 to get the final matched results at $\overline{\mathrm{N}n\mathrm{LL}}$ resummation. Note that similar matching procedure is done for the SV resummation. The $f_{a,N}$ are the Mellin transformed PDF similar to the partonic coefficient in Eq. (2.112) and can be evolved e.g. using publicly available code QCD-PEGASUS [226]. However, for practical purposes, it can be also approximated by directly using z–space PDF following [77, 220]. Essentially, for SV resummation, this will contain all the fixed order singular logarithms and for NSV resummation, it will contain additional NSV terms from the diagonal channel. In the next section, we study the impact of SV and NSV resummation on the gluon subprocess at LHC.

4.3 Numerical Results

In this section, we present numerical results for ZH associated production at the LHC. The default center-of-mass energy of the incoming protons is set to 13.6 TeV. Unless specified otherwise, our numerical analysis employs the `PDF4LHC21_40` [334] parton distribution functions (PDFs) throughout, as provided by `LHAPDF` [296]. In all these cases, the central set is the standard choice. The strong coupling is provided through the `LHAPDF` routine. The fine structure constant is taken as $\alpha \simeq 1/127.93$. The masses of the weak gauge bosons are set to be $M_Z = 91.1880$ GeV and $M_W = 80.3692$ GeV [335] with the corresponding total decay widths of $\Gamma_Z = 2.4955$ GeV. The Weinberg angle is then given by $\sin^2\theta_{\rm w} = (1 - m_W^2/m_Z^2)$. This corresponds to the weak coupling $G_F \simeq 1.2043993808 \times 10^{-5}\ \text{GeV}^{-2}$. The mass of the Higgs boson is set to $M_H = 125.2$ GeV.

In the gluon fusion channel, only the top quark contribution is considered at the lowest order, with the top quark pole mass set to $m_t = 172.57$ GeV. For this case, we chose the pole mass of the bottom quark to be $m_b = 4.78$ GeV. The unphysical renormalization (μ_R) and factorization scales (μ_F) are set to the invariant mass (Q) of the ZH pair. The scale uncertainties are estimated by simultaneously varying these unphysical scales as mention in section 2.3.1, in the range $[Q/2, 2Q]$ keeping the constraint $|\ln(\mu_R/\mu_F)| < \ln 4$ (known as the 7-point scale uncertainty) and taking the maximum absolute deviation of the cross-section from that obtained with the central scale choice. To estimate the impact of the higher order corrections from FO and resummation, we define the following ratios of the cross-sections,

$$K_{nm} = \frac{\sigma^{\text{N}n\text{LO}}}{\sigma_c^{\text{N}m\text{LO}}}, R_{nm} = \frac{\sigma^{\text{N}n\text{LO+N}n\text{LL}}}{\sigma_c^{\text{N}m\text{LO}}} \text{ and } \overline{R}_{nm} = \frac{\sigma^{\text{N}n\text{LO+}\overline{\text{N}n\text{LL}}}}{\sigma_c^{\text{N}m\text{LO}}}. \tag{4.12}$$

The subscript 'c' in the above expressions indicates that the corresponding quantity is evaluated at the central scale choice. As stated earlier, the lowest order process for ZH production through the gluon fusion channel contributes at $\mathcal{O}(\alpha_s^2)$ level, which formally should be considered at N2LO in the perturbation theory. Consequently, we have used the N2LO PDF for the computation of LO and higher order corrections to the gluon fusion process.

4.3.1 Invariant mass distribution

We first look into the invariant mass distribution of ZH pair. As mentioned in Sec. 4.1, the computation of higher-order corrections is non-trivial due to the involvement of multiple scales and one can work with EFT to reduce this complexity. For inclusive production of ZH pair, the total cross-section differs between these two approaches by

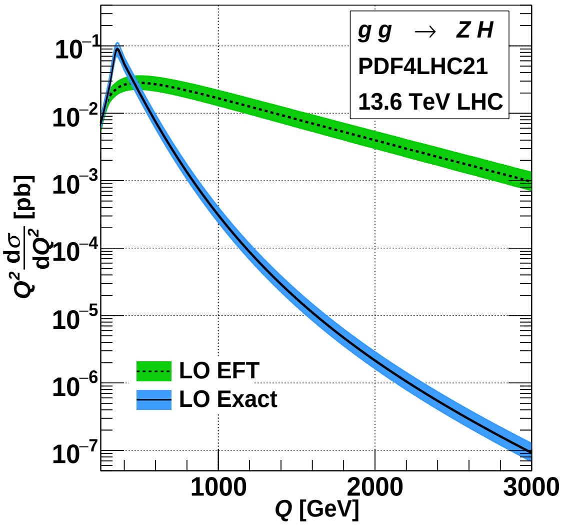

FIGURE 4.3: Invariant mass distribution of ZH for the gluon fusion channel at LO for EFT and Exact theories at 13.6 TeV LHC are presented. The bands correspond to the theoretical uncertainty using 7-point scale variation.

around 31% at LO. However, the difference is more pronounced in the invariant mass distribution as can be seen from Fig. 4.3. The band in this plot corresponds to the 7-point scale uncertainty as described above. Although the differential cross-section is comparable in the low invariant mass region, the shape differs significantly in the higher invariant mass region. Therefore, it is essential to include the finite top quark mass effect to produce the correct behavior for the invariant mass distribution. On the other hand, the total cross-section with finite top quark mass effect at NLO differs only by 5% [125] from the same in EFT. In fact, the exact LO captures the shape of the distribution in bulk and the effect of top mass on the NLO correction will have less impact on the shape of the distribution. Therefore, working with a Born-improved theory where the LO is rescaled by the exact top quark effect and NLO corrections in the EFT, will reduce the complexity while retaining essential features of QCD corrections, in particular the effects of soft radiation where we are interested in. In the rest of the chapter, we use this exact Born-improved EFT NLO cross-section for all purposes.

The fixed order results[1] have been computed with the publicly available code `vh@nnlo` [108, 110, 119] and for resummation, we have developed an in-house code to handle the Mellin inversion described in the end of Sec. 4.2. We first verified our code by

[1] At NLO with exact top quark dependence, there are also Z radiated diagrams where a Z boson is emitted from the external light quark line. These kind of diagrams will contribute to $\mathcal{O}(\alpha_s^3 y_t^2)$ (y_t being the top quark Yukawa coupling) i.e. the same order as the gluon fusion subprocess at exact NLO. Their effects could be as large as 10 times [126] the LO results.

reproducing the known result for the total resummed cross-section for ZH production up to NLO+NLL [127] in the N-scheme. We further reproduced the known result for inclusive resummed Higgs cross-section up to NLO+NLL both in N- and $\overline{N}$-schemes. As discussed in Sec. 4.2, the $\overline{N}$-scheme offers a faster perturbative convergence with a better control on the scale uncertainty and we chose to use this scheme for all of our studies in this chapter.

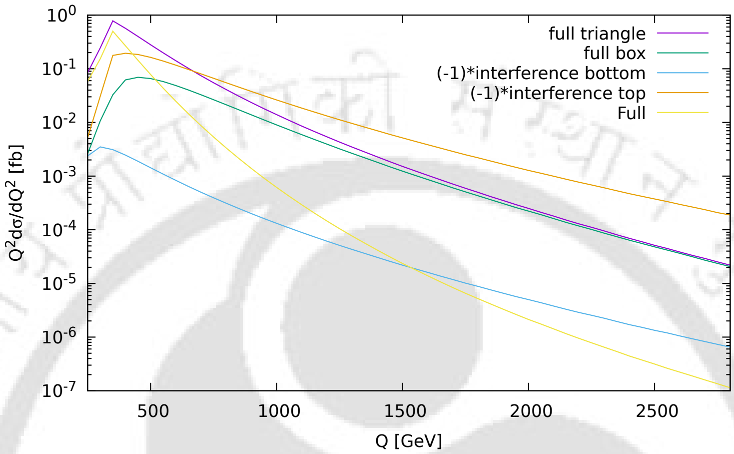

FIGURE 4.4: Different contributions of $gg \to ZH$ at LO in exact theory.

In the gluon fusion induced ZH production process at leading order (LO) in the Standard Model, the computation incorporates quark-loop contributions with full dependence on the top and bottom quark masses. The LO contribution arises from two types of diagrams: triangle and box diagrams. The triangle diagram involves quark loops that couple the gluons to the Z and Higgs bosons, while the box diagram represents a four-point interaction connecting the initial gluons to the ZH final state through a closed quark loop.

Different contributions of $gg \to ZH$ at LO in exact theory is presented in Fig. 4.4. In this analysis, we retain the exact quark mass dependence and examine the individual contributions. The curve labeled as `full triangle` includes both top and bottom quark effects within the triangle diagrams. Similarly, the `full box` line represents the contribution from the box diagrams including both quark flavors. Interference effects between the triangle and box topologies are also significant. These are displayed separately as negative contributions: `(-1)*interference bottom` and `(-1)*interference top`, indicating the destructive interference between the triangle and box diagrams, decomposed according to the respective quark flavor in the loops. The complete LO contribution, labeled as `Full`, combines all the aforementioned effects, providing a comprehensive description of the leading-order cross section as a function of the invariant mass Q of the ZH system.

The resulting plot illustrates the behavior of $Q^2 d\sigma/dQ^2$ over a wide kinematic range in Q, capturing the dominance of top quark contributions in the high-energy regime and highlighting the non-trivial interference structure among loop diagrams.

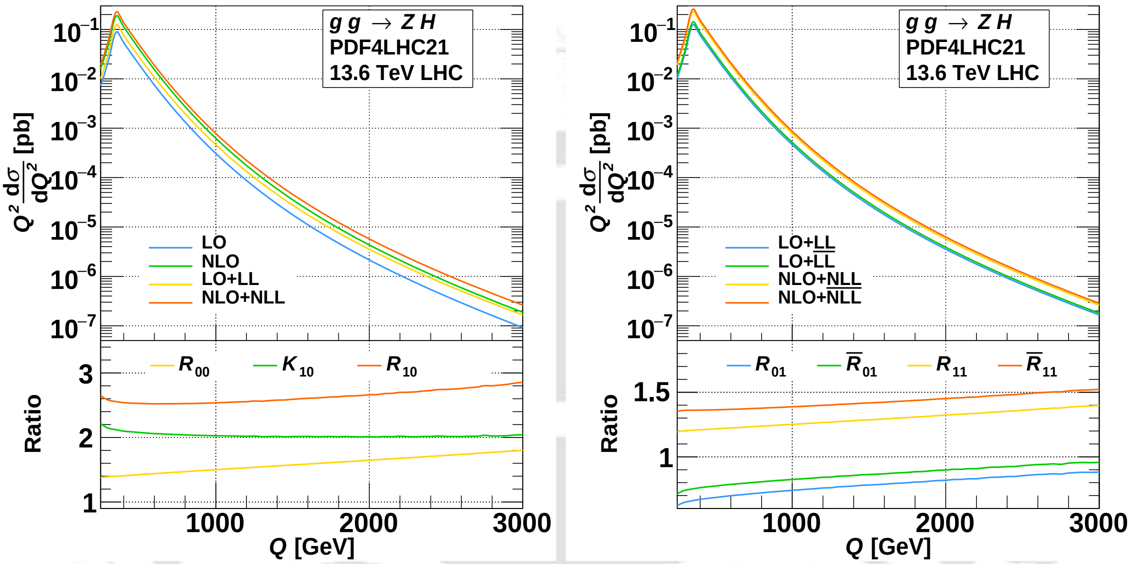

FIGURE 4.5: Comparison between the Born-improved fixed order and resummed results with corresponding ratios as defined in Eq. (5.9) are shown here. In the left panel; a comparison between fixed order and SV resummation are shown, and in the right panel; a comparison among fixed order, SV resummation and NSV resummation are presented.

On the left panel of Fig. 4.5, we compare the SV resummation with the fixed order result up to NLO(NLL) level, and we observe the expected behavior of better perturbative convergence for the SV resummed series. This is further evidenced from the lower inset where the ratios are displayed. From the ratio K_{10}, it is evident that the NLO correction can reach to around 100% compared to LO across most of the kinematic region considered. The LO+LL correction captures a significant portion of the higher order effects and provides an additional contribution of 80% of the LO, particularly in the high invariant mass region (Q = 3000 GeV). This clearly demonstrates that the soft gluon effect is dominant for this process. The NLO+NLL correction also shows a significant enhancement (through the R_{10} factor), reaching around 2.8 times the LO, particularly in the high invariant mass region. On the right panel of Fig. 4.5, we further compare the LO with LO+$\overline{\text{LL}}$ results and NLO+NLL with the new NLO+$\overline{\text{NLL}}$ results. Through the ratios R_{11} and $\overline{R}_{11}$ on the bottom panel there, we observe that NLO+NLL corrections account for about 20% of NLO in the low invariant mass region and rise to approximately 40% in the high invariant mass region. The NSV resummation at NLO+$\overline{\text{NLL}}$, on the other hand, contributes an additional 12% − 15% correction over NLO+NLL across most of the invariant mass region.

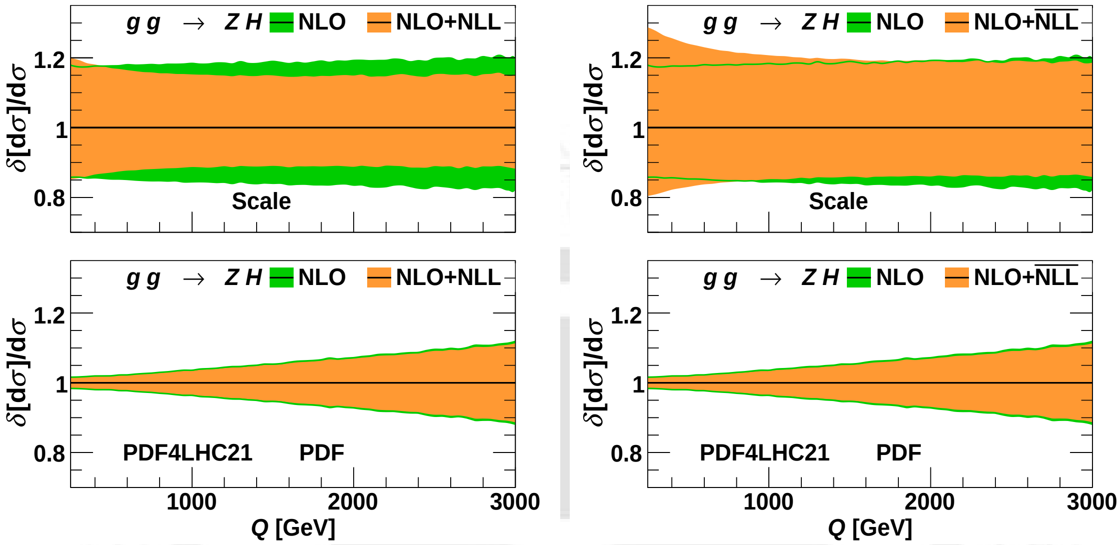

FIGURE 4.6: The 7-point scale uncertainty (upper panel) and the PDF uncertainty (lower panel) of gluon fusion ZH production are compared for Born-improved SV (left) and NSV resummation (right) against their corresponding fixed order results at 13.6 TeV LHC.

In Fig. 4.6, we have also analyzed different sources of uncertainties in these predictions. In general, the scale uncertainties at NLO are around 20% which gets reduced to around 15% in NLO+NLL distribution, particularly in the high invariant mass region as shown in the left panel of Fig. 4.6. In contrast, the NSV resummation at NLO+$\overline{\text{NLL}}$ does not show similar scale reduction over NLO, particularly in the low invariant mass region. In the high invariant mass region, it marginally improves the scale uncertainty over the NLO results. In the bottom panels of Fig. 4.6, we compare the PDF uncertainties for both SV and NSV resummed cases against the fixed order. These uncertainties generally increase with Q as PDFs are well-constrained in the small-x region relevant to the ZH threshold production, whereas at large-x, these are poorly constrained resulting in significant uncertainties of around 10% at NLO in the high-Q region. The SV and NSV resummed results show marginal improvements in PDF uncertainties by around 0.8% over the NLO.

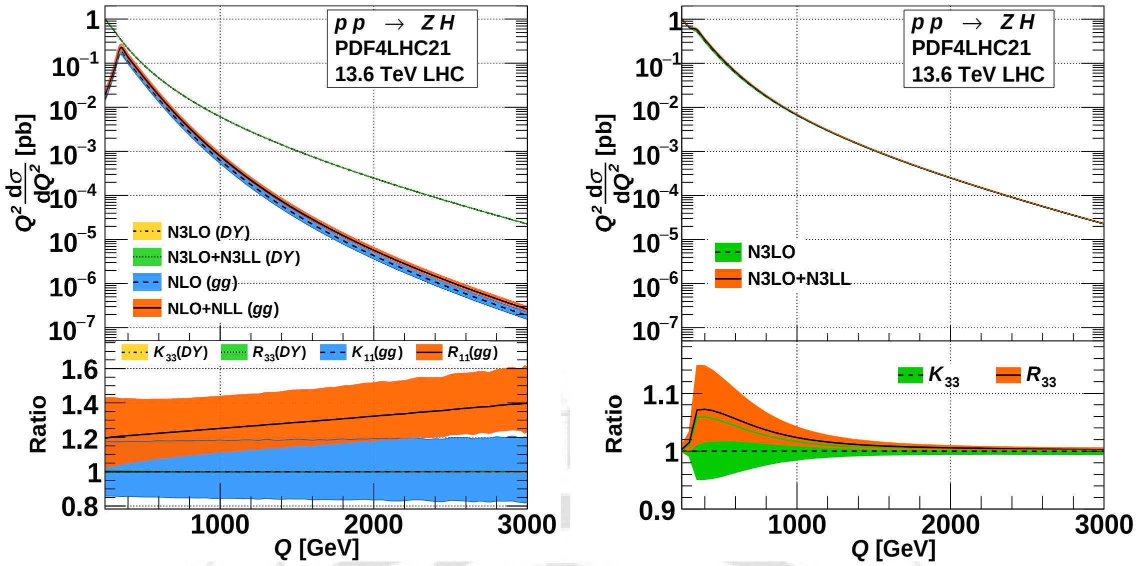

FIGURE 4.7: Left: The DY and gluon subprocesses contributions are shown for fixed order and SV resummed cases with the corresponding ratios at the bottom and its uncertainty from the scale variation. Right: The combined contribution at the highest accuracy for the fixed order and the SV resummed order are shown along with the scale uncertainties.

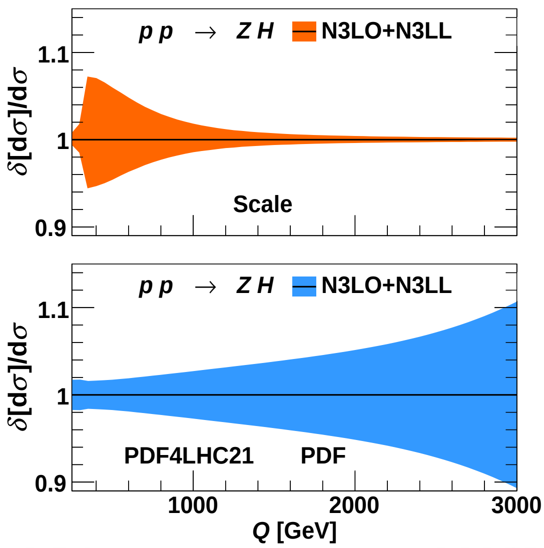

FIGURE 4.8: The 7-point scale uncertainty (upper panel) and the PDF uncertainty (lower panel) are shown for the $pp \to ZH$ process at 13.6 TeV LHC.

$$
\begin{aligned}
Q^2 \frac{d\sigma_{pp}^{\rm N3LO}}{dQ^2} &= Q^2 \frac{d\sigma_{\rm DY}^{\rm N3LO}}{dQ^2} + Q^2 \frac{d\sigma_{gg}^{\rm NLO}}{dQ^2}\,, \\
Q^2 \frac{d\sigma_{pp}^{\rm N3LO+N3LL}}{dQ^2} &= Q^2 \frac{d\sigma_{\rm DY}^{\rm N3LO+N3LL}}{dQ^2} + Q^2 \frac{d\sigma_{gg}^{\rm NLO+NLL}}{dQ^2}\,. \qquad (4.13)
\end{aligned}
$$

For completeness, we combine the gluon fusion results with other subprocesses for ZH

contribution to obtain full $pp \to ZH$ results at $\mathcal{O}(\alpha_s^3)$ level. Particularly, in the fixed order case, we combine the contributions arising from the DY-type channel with that from the gluon fusion channel at $\mathcal{O}(\alpha_s^3)$ as given in Eq. (4.13). For resummation case, we chose to use the SV resummed results. While NSV resummation shows some enhancement over the SV resummed results (as seen from Fig. 4.5), it still lacks contributions from off-diagonal channels. Moreover, one would also require the NSV accuracy for the DY-type subprocess for which the relevant ingredients are still missing. Hence we combine the fixed order results with SV resummed results for both DY-type and gluon fusion channels. The required N3LO+N3LL SV resummed results for the DY-type channel given in the chapter 3. In the left panel of Fig. 4.7, we show these results separately for both DY-type and gluon fusion channels along with the scale uncertainties. Note that the relative scale uncertainty for the DY-type is not visible on the scale of this plot. The right panel of Fig. 4.7 shows the combined results for invariant mass distribution at N3LO and N3LO+N3LL. The bottom panel highlights the enhancement from N3LO through the K_{33} and R_{33} factors. In Fig. 4.8, we show the scale and PDF uncertainties for the combined results at N3LO+N3LL. The PDF uncertainty increases with Q, reaching around 10.6% in the high invariant mass region. On the other hand, the scale uncertainty is largest at the top threshold ($Q \sim 2m_t$), reaching up to 6% and decreasing significantly in the high-Q region, reducing to as low as 0.1%.

4.3.2 Total cross-section

Finally, we also present the total cross-section for the resummed results by integrating the invariant mass distributions up to $\sqrt{S}$. The Table 4.1 provides the total cross-sections for the gluon fusion channel at fixed order and at SV and NSV resummation. Alongside, we also provide various uncertainties arising from 7-point scale variation, non-perturbative PDF set, and the variation of the strong coupling constant $\alpha_s(M_Z)$. For the later we consider a variation in the 1σ range leading to a variation in the range $\alpha_s^-(M_Z) = 0.1165$ and $\alpha_s^+(M_Z) = 0.1195$. With the central choice for $\alpha_s^c(M_Z) = 0.118$ same as the PDF, we obtain the final uncertainty through $\delta(\alpha_s) = \pm \max \left|\sigma(\alpha_s^\pm(M_Z)) - \sigma(\alpha_s^c(M_Z))\right| / \sigma(\alpha_s^c(M_Z))$. Additionally, we also present the combined uncertainties from PDF and α_s by adding the respective errors in quadrature. The largest source of uncertainty arises from the scale

Order	cross-section (fb)	Scale	δ(PDF)	$\delta(\alpha_s)$	$\delta(\text{PDF} + \alpha_s)$
σ_{gg}^{LO}	60.25	±24.6%	±0.68%	±2.07%	±2.18%
σ_{gg}^{NLO}	124.74	±15.3%	±0.71%	±2.60%	±2.70%
$\sigma_{gg}^{\text{LO+LL}}$	84.74	±27.5%	±0.69%	±2.45%	±2.55%
$\sigma_{gg}^{\text{NLO+NLL}}$	151.30	±19.4%	±0.71%	±2.93%	±3.01%
$\sigma_{gg}^{\text{LO+}\overline{\text{LL}}}$	96.27	±29.3%	±0.69%	±2.60%	±2.69%
$\sigma_{gg}^{\text{NLO+}\overline{\text{NLL}}}$	170.73	±27.0%	±0.71%	±3.16%	±3.24%

TABLE 4.1: The ZH production cross-sections (in fb) are presented at exact LO, and Born-improved NLO, along with corresponding SV and NSV resummed results at 13.6 TeV LHC with 7-point scale, PDF and α_s uncertainties.

variation which at NLO+NLL level are around 19.4%, indicating the need for further improvements through higher-order computation.

Order	cross-section (pb)	Scale	δ(PDF)	$\delta(\alpha_s)$	$\delta(\text{PDF} + \alpha_s)$
$\sigma_{\text{DY}}^{\text{N3LO}}$	0.8416	±0.28%	±0.77%	±0.14%	±0.78%
$\sigma_{\text{DY}}^{\text{N3LO+N3LL}}$	0.8416	±0.55%	±0.77%	±0.14%	±0.78%
$\sigma_{tot}^{\text{N3LO}}$	0.9776	±1.94%	±0.65%	±0.47%	±0.80%
$\sigma_{tot}^{\text{N3LO+N3LL}}$	1.0042	±2.98%	±0.63%	±0.58%	±0.86%

TABLE 4.2: ZH production cross-section (in pb) of DY-type N3LO, DY-type N3LO+N3LL, total N3LO and total resummed N3LO+N3LL which are defined in Eq. (4.14) for different 13.6 TeV LHC with 7-point scale, PDF and α_s uncertainties.

In Table 4.2, we present the total production cross-section of ZH at the LHC by combining contributions from different channels. Particularly, in the fixed order case, we combine the contributions arising from the DY-type channel ($\sigma_{\text{DY}}^{\text{N3LO}}$), the bottom-quark initiated t-channel ($\sigma_{b\bar{b}}$), the gluon fusion channel (σ_{gg}^{NLO}), and contribution coming from Higgs radiation from top quark loop in the quark annihilation channel ($\sigma_{\text{top}}(a_s^2)$) as described in Sec. 4.1, corresponding feynman diagram are given in Fig. 4.9 and defined in

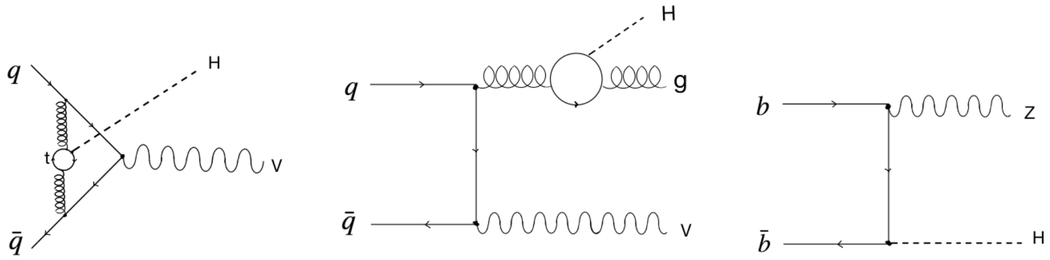

FIGURE 4.9: The feynman diagrams for ZH production additional contributing channels at LHC.

Eq. (4.14),

$$
\begin{aligned}
\sigma_{tot}^{\text{N3LO}} &= \sigma_{\text{DY}}^{\text{N3LO}} + \sigma_{gg}^{\text{NLO}} + \sigma_{\text{top}}(a_s^2) + \sigma_{b\bar{b}}\,, \\
\sigma_{tot}^{\text{N3LO+N3LL}} &= \sigma_{\text{DY}}^{\text{N3LO+N3LL}} + \sigma_{gg}^{\text{NLO+NLL}} + \sigma_{\text{top}}(a_s^2) + \sigma_{b\bar{b}}\,.
\end{aligned} \tag{4.14}
$$

For the resummation case, we improve the fixed order for the DY-type channel by SV resummation at N3LO+N3LL and for the gluon channel by resummation at NLO+NLL. For the DY-type channel, resummation has very little effect in this order and the major improvement is obtained through the gluon fusion channel. For the total cross-section, the resummation improves the cross-section by around 2.7% compared to the fixed order, whereas the scale uncertainty increases by 1%. This can be traced to the fact that, total cross-section receives significant contributions from the low invariant mass region, where the factorisation scale uncertainty remains significant. However, all other sources of uncertainties remain small, contributing less than 1%.

4.4 Conclusion

To summarize, we have investigated the impact of soft gluon resummation on the ZH production process in the gluon fusion channel at the LHC. In the low invariant mass region, near the top-pair threshold ($Q \sim 2m_t$), the gluon fusion channel at $\mathcal{O}(\alpha_s^2)$ level contributes around 20% of the dominant DY-type channel, highlighting its significance and the necessity of including its contribution.

We first obtained the Born improved NLO corrections by rescaling the exact LO results with the mass dependent NLO K-factor obtained from the Effective theory. Using the universal cusp anomalous dimensions, splitting kernels, we have performed the SV and the NSV resummation and presented numerical results for the invariant mass distribution as well as the production cross sections to NLO+NLL($\overline{\text{NLL}}$) accuracy for the current LHC energies. The NLO corrections contribute as large as 100% of LO for the total ZH production cross-section in the gluon fusion channel. We observed that the SV (NSV) resummation contributes an additional 19.4% (35.3%) at NLL ($\overline{\text{NLL}}$) level over NLO in the low Q-region. In the high invariant mass regions (around $Q = 3000$ GeV), this SV(NSV) resummation reduces the 7-point scale uncertainties at NLO level by a few percent 5.0%(1.4%). Besides the scale uncertainties, we have also quantified the uncertainties due to the PDFs on resummed results and these are found to be around 1.6% in the low invariant mass region.

Finally, for experimental analysis, we combine the contributions from different subprocesses, including the soft gluon resummation effects, and present comprehensive results for the invariant mass distribution as well as the total production cross sections at the LHC. We note that except for the uncertainties due to the non-perturbative inputs from PDFs, the theoretical uncertainties in the high invariant mass region are well under control. However, to advance the precision for this process further, the higher order corrections beyond NLO for the gluon fusion channel will be essential.

Chapter 5

Threshold resummation for Z-boson pair production at NNLO+NNLL

The production of vector boson pairs, such as ZZ, at hadron colliders plays a crucial role in testing the Standard Model (SM) and probing possible deviations arising from new physics. As a purely electroweak process at leading order, ZZ production provides a clean environment for precision measurements, including the study of triple gauge couplings and background estimation for Higgs boson measurements and searches for heavy resonances. Among the diboson processes, ZZ production is especially significant due to its fully leptonic final state, which offers excellent experimental resolution. The high precision expected in such measurements necessitates a corresponding accuracy in theoretical predictions.

In the context of Quantum Chromodynamics (QCD), the dominant contribution to ZZ production at the LHC arises from the annihilation of a quark and antiquark ($q\bar{q}$), similar to Drell–Yan (DY)-type color-singlet processes. This resemblance allows us to adopt the resummation techniques previously developed for DY, associated VH production, and Higgs production via bottom quark annihilation. These processes all involve initial-state radiation from color-charged partons and result in a color-neutral final state. As a result, their soft-gluon dynamics exhibit universal factorization properties near threshold, which we exploit in our resummation framework.

In this chapter, we focus on the threshold resummation for the process $q\bar{q} \to ZZ$ at the LHC, performed up to next-to-next-to-leading order plus next-to-next-to-leading logarithmic (NNLO+NNLL) accuracy. To address this, we implement an all-orders resummation of soft-gluon contributions using the formalism introduced in earlier chapters. The universal behavior of QCD radiation near threshold is again exploited to factorize and resum the dominant logarithmic contributions. The resummation is carried out in Mellin-N space, where the convolution structure simplifies and logarithmic terms exponentiate naturally. This approach allows us to capture both the leading and next-to-leading logarithms systematically, thereby extending the predictive power of our framework to the ZZ final state.

5.1 Introduction

The production of a pair of massive gauge bosons (Z) at the Large Hadron Collider (LHC) is an important process which has been studied very well, both theoretically and experimentally. This process offers very clean signals that can be used to test the prediction of the Standard Model (SM) precisely, thanks to their moderately large production cross sections at the current LHC energies. The process can also be used for testing the SM electroweak symmetry breaking mechanism as well as in the study of fundamental weak interactions among elementary particles. Owing to the large coupling between the Higgs and massive gauge bosons, the process plays an important role in the Higgs sector. One of the important decay modes of Higgs being to a pair of massive gauge bosons, either ZZ or WW.

The experimental signature of this process typically involves either four charged leptons, two leptons plus missing energy or two leptons plus two jets or four jet events. Out of these, the decay to four charged leptons provides a very clean signal in the collider experiments, that led to the measurement of these final states both at the ATLAS and CMS experiments for different centre of mass energies e.g. 5.02 TeV [336], 7 TeV [130, 131, 337, 338], 8 TeV [338–343], 13 TeV [343–348] and 13.6 TeV [349]. Such measurements can be used to probe the trilinear gauge couplings as well as to probe the possible hidden new physics . From the theoretical point of view, a similar study can easily be extended to the production of a pair of new massive gauge bosons.

Owing to the importance of this process, a precise knowledge of this process, specifically their production cross sections as well as various kinematic distributions at the current LHC and future high energetic hadron colliders, is very important. In the perturbative Quantum Chromodynamics (pQCD), the leading order (LO) predictions for this process have been available for a long time [350–353]. It is well known that the LO predictions are unreliable and are contaminated with large theoretical uncertainties. The next-to-leading order (NLO) calculations in pQCD were obtained for both on-shell as well as off-shell Z-bosons decaying to a pair of leptons. The NLO QCD corrections for this process can be found in Ref. [354–356]. The NLO QCD results, matched with Parton Shower (NLO+PS) has been studied in Monte Carlo programmes like POWHEG [357, 358] and aMC@NLO [359]. The ZZ production at the LHC has been analyzed in the context of Beyond Standard Model (BSM) scenarios as well [360]. It is to be noted that at the lowest order in the perturbation theory, this is a quark anti-quark initiated process similar to the Drell-Yan (DY) production of dileptons. However, the Z-boson pair production process has more similarities to the diphoton production process, as both them involve identical particles in the final state, and both are t and u channel processes, whereas DY is a s-channel process (s,t and u being the Mandelstam variables). For the diphoton production process even at LO, simple kinematic cuts are required to avoid divergences in the forward region, whereas for the case of ZZ production the mass of the Z-boson avoids such divergences, and hence the total production cross section is finite even in absence of any kinematic cuts. However, in the high invariant mass region, or in the region where Z-boson carries much larger kinetic energy compared to the rest mass energy, both the processes can have similar behaviour in the cross sections, the special difference being the isolation algorithm to be used in the case of di-photon production process.

Precision studies entail going beyond NLO. However, for the Z boson pair production process, even the NNLO results are challenging for both analytical as well numerical calculations. The full NNLO calculations have been carried out in [361–363] in QCD for the quark annihilation process. It is also worth noting that the NNLO corrections are computed for both on-shell Z-boson [132, 364] case as well as for off-shell Z-bosons [67, 133] followed by their decay to lepton final states. With the availability of two loop helicity amplitudes [363], the differential distributions for the latter case also became possible. Fiducial cross sections and distributions are also available for the vector boson pair production processes [133, 365]. Additionally, the leading-order process in the gluon fusion channel, $gg \to ZZ$, also contributes at $\mathcal{O}(\alpha_s^2)$. In the low invariant mass region, the gluon fluxes for LHC energies are very large and hence the contribution from this channel near the hadronic threshold region is very crucial and can not be neglected. Going beyond NNLO for Z-boson pair production processes is a challenging task. On the other hand, for DY and Higgs production this has been achieved. Recently the full $\mathrm{N^3LO}$ results for DY have become available and can be found in Ref. [71–73, 213] and soft-virtual (SV) [181, 325, 366] and next-to-soft-virtual (NSV) [178, 221, 333] threshold resummation of DY-type processes are available. The Higgs production through gluon fusion channel $\mathrm{N^3LO}$ results are available in [69, 367] and SV [239, 271, 278, 368] and NSV [178, 222, 287] threshold resummation results are also available. For Higgs production via bottom quark annihilation, SV [324] and NSV [369] resummation results are also available. Rapidity resummation for DY processes are available for SV [370, 371] and NSV [179, 372–374]. Rapidity distribution for the Higgs production at the threshold to third order in the gluon fusion channel can be found in [375]. For the DY type processes, the threshold results at third order can be found in [114, 258]. Rapidity resummation for gluon fusion channel Higgs production is available for SV [376] and NSV [179, 377] cases. Rapidity resummation for Higgs production via bottom quark annihilation is also available at NNLO+NNLL in Ref. [378]. Nevertheless, for the Z-boson pair in the final state, there has been a tremendous effort to go beyond NNLO. Transverse momentum resummation for vector boson pair production is available up to NNLO+$\mathrm{N^3LL}$ [379, 380]. The parton shower matched with NNLO (NNLO+PS) are recently studied using $\mathrm{MINNLO_{PS}}$ [381] method for the ZZ production. The LO matching with parton shower results are available for the gluon fusion channel as well in Ref. [382]. The NLO corrections to this channel have also become available [383–386]. However, their contribution in the high invariant mass region ($\geq$ 2000 GeV) becomes much smaller than those in the quark annihilation channel. The NLO results matching with parton shower (NLO+PS) results for gluon fusion channel with massless quarks are also available [387]. Finally, at this precision level, the electroweak corrections can not be ignored for precision studies and the NLO EW corrections to this process have been computed in [388–390]. Using SCET formalism, threshold resummation for vector boson pair production is available up to NLO+NNLL [134].

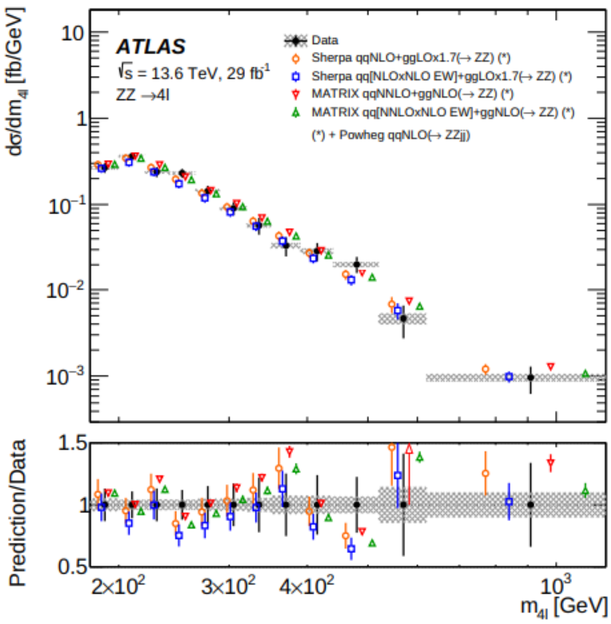

FIGURE 5.1: The experimental data are compared with SM theoretical predictions from ATLAS [4] for ZZ production with Z-boson decay to four leptons.

The ATLAS collaborations [4] have reported high-precision measurements of the invariant mass and transverse momentum distributions of the ZZ system at various center-of-mass energies, such as 13.6 TeV. The Fig. 5.1 illustrates the measured invariant mass distribution of the ZZ system compared to the theoretical predictions. These measurements show excellent agreement with SM predictions at next-to-next-to-leading order (NNLO) in QCD. While the threshold resummation for the final state on-shell Z-bosons has been achieved to NLO+NNLL level, it is necessary to go beyond this accuracy. The Z-boson pair production cross section has been measured at the LHC experiments using 13 TeV data obtained from the 137 fb^{-1} luminosity. The measured total production cross-section is 17.4 pb with an error of about 0.8 pb [348]. The invariant mass distribution also has been measured up to 1 TeV region. With the upcoming HL-LHC, the integrated luminosity is expected to reach $3000-4000$ fb^{-1}, which allows the measurement of ZZ events in this TeV region with more statistical data. For the planned FCC-hh [391], the increase in parton fluxes along with the integrated luminosity of $20-30$ ab^{-1} can enhance the invariant mass distributions by a few orders of magnitude, thus allowing the measurement of the ZZ events beyond 1 TeV region even more precisely. At this level of experimental precision, adequate theoretical predictions are necessary. In this work, we attempt to increase the theoretical precision by performing the resummation at NNLL accuracy and give the results after matching them to the available fixed order results at the NNLO level.

This chapter is organized as follows: We present the theoretical framework in section 5.2. Details of the phenomenological analysis and the numerical results are presented in section 5.3. Finally, in section 5.4, we summarize our observations.

5.2 Theoretical Framework

The hadronic cross-section for Z-boson pair production can be written in terms of its partonic counterpart as following:

$$\frac{d\,\sigma}{d\,Q} = \sum_{a,b=\{q,\bar{q},g\}} \int_0^1 dx_1 \int_0^1 dx_2 \; f_a(x_1, \mu_F^2)\, f_b(x_2, \mu_F^2) \int_0^1 dz \;\delta\,(\tau - z x_1 x_2)\, \frac{d\,\hat{\sigma}_{ab}}{d\,Q}\,. \quad (5.1)$$

Here Q is the invariant mass of the final states. The hadronic and partonic threshold variables τ and z are defined as

$$\tau = \frac{Q^2}{S}, \qquad z = \frac{Q^2}{s}\,, \quad (5.2)$$

where S and s are the hadronic and partonic center of mass energies, respectively. τ and z are thus related by $\tau = x_1 x_2 z$.

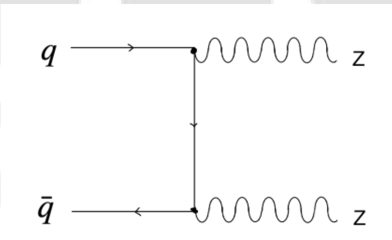

FIGURE 5.2: The leading order feynman diagram for ZZ production at LHC

The leading order Drell-Yan (DY) type parton level process as in Fig. 5.2 has the generic form

$$q(p_1) + \bar{q}(p_2) \to Z(p_3) + Z(p_4). \quad (5.3)$$

The leading-order (LO) cross-section $\hat{\sigma}^{(0)}_{q\bar{q}}$ for Z-boson pair production can be written as,

$$\frac{d\hat{\sigma}^{(0)}_{q\bar{q}}}{dQ} = \frac{1}{2s}\int dPS_2 \, \mathcal{M}_{(0,0)}, \tag{5.4}$$

where dPS_2 is the 2-body phase space integration and $\mathcal{M}_{(0,0)}$ is the born amplitude, which in $d = 4-2\epsilon$ dimensions is given below,

$$\begin{aligned}\mathcal{M}_{(0,0)} =& B_f \, \mathrm{N}(c_a^4 + 6c_a^2\, c_v^2 + c_v^4)\frac{4}{t^2\, u^2}\Big\{ -m_z^4 t^2 + 8m_z^4 tu + t^3 u - m_z^4 u^2 + tu^3 - 4m_z^2 tu(t+u) \\ & + \epsilon\left(-2m_z^4 t^2 - 6m_z^4 tu - 2t^3 u + 2m_z^4 u^2 + 2t^2 u^2 - 2tu^3 + 4m_z^2 tu(t+u)\right) \\ & + \epsilon^2\left(-m_z^4 t^2 - 2m_z^4 tu + t^3 u - m_z^4 u^2 + 2t^2 u^2 + tu^3\right)\Big\}. \end{aligned} \tag{5.5}$$

In Eq. (5.5) the kinematical variables s, t and u are defined as,

$$(p_1+p_2)^2 = s\,, \quad (p_1-p_3)^2 = t\,, \quad (p_2-p_3)^2 = u \quad \text{and} \quad s+t+u = 2m_z^2, \tag{5.6}$$

$$B_f = \frac{(4\pi\alpha)^2}{4\mathrm{N}^2}\,, \qquad c_v = \frac{\left(T_3^f - 2\,\sin^2\theta_{\mathrm{w}} Q_f\right)}{2\,\sin\theta_{\mathrm{w}}\cos\theta_{\mathrm{w}}}\,, \qquad c_a = \frac{1}{4\,\sin\theta_{\mathrm{w}}\cos\theta_{\mathrm{w}}}\,,$$

where the Q_f and T_3^f are the electric charge and third component of weak isospin of the fermion f and θ_{w} is the weak mixing angle. Here m_z is the mass of Z-boson, N is the SU(N) color, and α is the fine structure constant. Here, we have dealt with γ_5 in d-dimension using Larin's prescription [392].

Beyond LO, the partonic cross section receives corrections originating from virtual and real contributions. It is interesting to study the cross-section in the soft limit, which is defined by, $z \to 1$. This means that the initial partonic center of mass energy is almost used to produce the final state pair of Z-bosons, and small energy is left to produce soft partons. In this limit, the partonic cross section can be organized as follows:

$$\frac{d\,\hat{\sigma}_{ab}}{d\,Q} = \frac{d\,\hat{\sigma}^{(0)}_{ab}}{d\,Q}\left(\Delta^{\mathrm{sv}}_{ab}\left(z,\mu_F^2\right) + \Delta^{\mathrm{reg}}_{ab}\left(z,\mu_F^2\right)\right)\,. \tag{5.7}$$

The term $\Delta^{\rm sv}_{ab}$ is known as the soft-virtual (SV) partonic coefficient and captures all the singular terms in the $z \to 1$ limit. Only quark-antiquark or gluon-gluon sub-processes contribute to this SV cross-section. The $\Delta^{\rm reg}_{ab}$ term contains regular (hard) contributions in the variable z. Both these contributions are expanded in a perturbative series of the strong coupling constant. In our work, we consider such an expansion up to NNLO in QCD. It is to be noted that the overall normalization factor $d\hat{\sigma}^{(0)}_{ab}/dQ$ depends on the process under study.

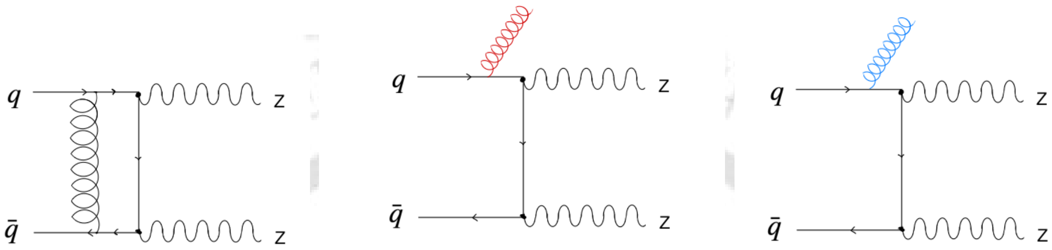

FIGURE 5.3: The next-to-leading order feynman diagram for ZZ production at LHC

In Fig. 5.3 schematically illustrates the different components contributing to the NLO corrections for the $q\bar{q} \to ZZ$ process. The leftmost diagram represents the one-loop virtual correction, involving internal gluon exchange without any additional radiation. This contribution is captured by the purely virtual part of the amplitude and becomes relevant in the threshold region, where the available energy is just sufficient to produce the ZZ pair. The central diagram shows the emission of a soft gluon, depicted in red, from the initial-state quark or antiquark. Such soft emissions, though real, do not significantly change the kinematics of the final-state bosons and are included in the soft-virtual (SV) terms of the cross section. Together, the virtual and soft gluon contributions form the SV approximation, which dominates near partonic threshold. On the other hand, the rightmost diagram depicts the emission of a hard gluon, shown in blue, which carries substantial energy and alters the final-state kinematics. This contribution belongs to the regular (hard real) part of the cross section and becomes important away from threshold. These components are systematically organized in Eq. (5.7), where the SV terms account for the singular behavior near threshold, while the regular terms describe hard radiation and are free of threshold enhancements.

The singular part of the partonic coefficient has a universal structure which gets contributions from the underlying hard form factor [208, 209, 291–293], mass factorization kernels [210, 211, 393] and soft radiations [81, 82, 204–207]. According to the KLN theorem, these infrared divergences, when regularized and combined, yield finite contributions. After the infrared cancellation, the finite part of these has the universal structure in terms of $\delta(1-z)$ and plus-distributions $\mathcal{D}_i = [\ln(1-z)^i/(1-z)]_+$. In the threshold limit, $z \to 1$, the plus distributions contribute dominantly to the SV cross section. These large distributions can be resummed to all orders in the threshold limit. Threshold resummation is conveniently performed in the Mellin (N) space where the convolution structures become simple product.

The partonic coefficient in the Mellin space is organized as follows in Eq. (2.102).

$$\hat{\sigma}_N^{\mathrm{N^nLL}} = \int_0^1 \mathrm{d}z \; z^{N-1} \Delta_{ab}^{\mathrm{sv}}(z) \equiv \overline{g}_0^q \exp\left(G_N^q\right) . \tag{5.8}$$

The factor $\overline{g}_0^q$ is independent of the Mellin variable and process dependent, whereas the threshold enhanced large logarithms ($\ln^i N$ in Mellin space) are resummed through the exponent G_N^q. The resummed accuracy is determined through the successive terms from the exponent G_N^q which up to NNLL and required coefficients are $g_1^q(\overline{N})$, $g_2^q(\overline{N})$ and $g_3^q(\overline{N})$ as given in Eq. (2.107). These coefficients are universal and only depend on the partonic flavors being either quark or gluon. Their explicit form can be found for DY-type processes taken from *e.g.* [77, 180] and given in Appendix B.1. In order to achieve complete resummed accuracy one also needs to know the N–independent coefficient $\overline{g}_0^q$ as mention in Eq. (2.106) up to sufficient accuracies. In particular, up to NNLL, required process dependent coefficients are $\overline{g}_0^{q,(1)}$ and $\overline{g}_0^{q,(2)}$ as given in Eq. (2.106). Using the universal G_N^q and the process dependent $\overline{g}_0^q$, resummation for two Higgs boson production in the gluon fusion channel at $\mathrm{N^3LO}$ + $\mathrm{N^3LL}$ has been achieved in [394].

It is also possible to resum part (or full) of the $\overline{g}_0^q$ by including them in the exponent [239, 262, 267, 271, 272], which however have sub-leading effect as these contributions are not dominated in the threshold region.

The N-independent coefficient $\overline{g}_0^q$ is computed based on the formalism given in Ref. [277], the expression for $\overline{g}_0^{q,(1)}$ and $\overline{g}_0^{q,(2)}$ are given in Appendix C.1. The $\overline{g}_0^{q,(1)}$ requires one loop virtual computations ($\mathcal{M}_{(0,1)}$), we have computed the amplitude $\mathcal{M}_{(0,1)}$ using our in-house FORM [187] code and the expression is given in Appendix C.1. To obtain the results in z space, one needs to do the Mellin inversion as in Eq. (2.110) and description is given in section 2.4.3.

Finally, we get the final matched results as given in Eq. (2.112). In Eq. (2.110), $f_{a,N}$ are the Mellin transformed PDF, which one can obtain using publicly available code like QCD-PEGASUS [226]. However, for numerical applications, it can also be approximated by employing the z-space PDF following [77, 220].

Before we proceed to the numerical results, we add a few comments on the extraction of the resummation coefficient, $\bar{g}_0^{q,(2)}$, which is a process-dependent quantity. To obtain the full $\bar{g}_0^{q,(2)}$, we follow the procedure given in [277] and make use of the two-loop $(\mathcal{M}_{(0,2)})$ amplitudes as well as the one-loop squared amplitudes, $(\mathcal{M}_{(1,1)})$. The two-loop virtual amplitudes $\mathcal{M}_{(0,2)}$ are reconstructed using `VVamp` package [363], while the $\mathcal{M}_{(1,1)}$ is obtained by squaring $\mathcal{M}_{(0,1)}$. After performing the UV renormalization, the IR pole structure of these amplitudes is then verified using Catani's I-operator formalism [395]. The finite parts of the two-loop amplitudes are quite large in size. These amplitudes are then simplified and optimized using our in-house developed FORM routines. We have used `handyG` [396] for numerical evaluations of the generalized polylogarithms in these one-loop and two-loop amplitudes. Finally, these two-loop amplitudes have been cross checked numerically for different phase space points with those implemented in the MATRIX [363, 397–401]. The resummation formalism used here is developed in [220, 370, 376] and has been successfully used in the past in calculating NNLO+NNLL and N^{3}LO+N^{3}LL for Drell Yan processes [181, 282, 325, 368]. All the anomalous dimensions required for computing the resummed results are given in the Appendix B.

5.3 Numerical Results

In this section, we present the numerical results for the Z-boson pair production process at the LHC. For the numerical computation, we take the fine structure constant to be $\alpha = 1/132.233193$. The mass of the weak gauge bosons $m_z = 91.1876$ GeV, $m_w = 80.385$ GeV. The Weinberg angle is $\sin^2\theta_{\rm w} = (1 - m_w^2/m_z^2) = 0.222897223$. This corresponds to the weak coupling $G_F = 1.166379 \times 10^{-5}$ GeV^{-2}. The default choice of centre mass energy of the incoming protons is 13.6 TeV. Unless specified otherwise, in our numerical analysis, we use MSHT20 [402] parton distribution functions (PDFs) throughout taken from the `LHAPDF` [296]. The LO, NLO and NNLO cross-sections are obtained by convoluting the respective coefficient functions with MSHT20lo_as130, MSHT20nlo_as120 and MSHT20nnlo_as118 PDF sets, using the central set (iset=0) as the default choice.

The strong coupling constant a_s is taken from `LHAPDF` [296], and it varies order by order in the perturbation theory. For our analysis, we consider the number of light quark flavours as $n_f = 5$. For the fixed order calculations, we have used the package `MATRIX` [397]. The fixed order results from MATRIX are checked against those obtained from the MadGraph package [403] up to NLO and are found to be in good agreement. The fixed order NNLO results have been checked with the numbers quoted in the literature [132, 133]. The resummation results are obtained using the in-house developed numerical code.

The unphysical renormalization and factorization scales are set to $\mu_R = \mu_F = Q$, where Q is the invariant mass of the Z-boson pair production in the final state. The scale uncertainties are estimated by varying the unphysical as mention in section 2.3.1, in the range so that $|\ln(\mu_R/\mu_F)| \leq \ln 2$. The symmetric scale uncertainty is calculated from the maximum of the absolute deviation of the cross-section from that obtained with the central/default scale choice. To estimate the impact of the higher-order corrections from FO and resummation, we define the following ratios of the cross-sections which are useful in the experimental analysis:

$$K_{\rm ij} = \frac{\sigma_{\rm N^iLO}}{\sigma_{\rm N^jLO}}\,,\ R_{\rm ij} = \frac{\sigma_{\rm N^iLO+N^iLL}}{\sigma_{\rm N^jLO}} \quad \text{and} \quad L_{\rm ij} = \frac{\sigma_{\rm N^iLO+N^iLL}}{\sigma_{\rm N^jLO+N^jLL}} \quad \text{with } i,\, j = 0, 1 \text{ and } 2\,\cdot \tag{5.9}$$

In Fig. 5.4 , we present the fixed order results for the invariant mass distribution of the Z-boson pair production from $2m_z$ to 1300 GeV up to NNLO+NNLL in QCD. For the range of Q-variation considered here, the distribution varies over three orders of magnitude. In the lower panel, the corresponding fixed order as well as the resummed K-factors, as defined in Eq. (5.9) are given. The NLO K-factor K_{10} here varies from about 1.22 at Q = 200 GeV to about 1.58 at Q = 1300 GeV. As can be seen from Fig. 5.4, the variation of K_{10} above Q = 500 GeV is mild. However, the NNLO K-factor K_{20} slowly but continuously increases from about 1.29 to about 1.94 for the Q range considered here. This clearly shows additional contributions coming from second order corrections in the higher Q-region, which are due to the real correction sub-processes like $qq' \to ZZqq'$. A more detailed discussion of this kind of contributions can be found in the Ref. [389]. The resummation has been achieved in the Mellin space where large logarithms of kind

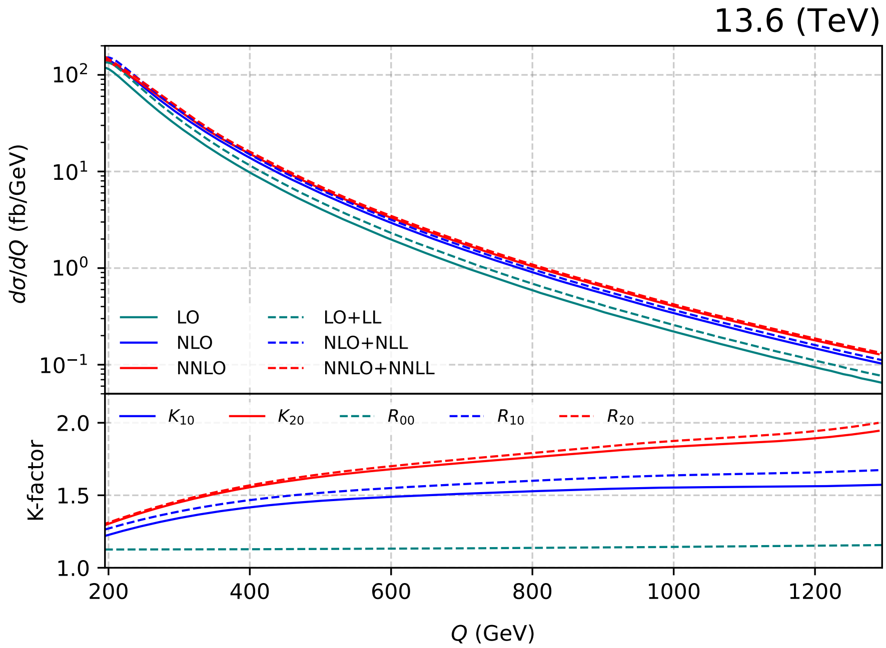

FIGURE 5.4: Resummed predictions for the Z-boson pair invariant mass distribution (upper panel) and the corresponding K-factors(lower panel) up to NNLO+NNLL.

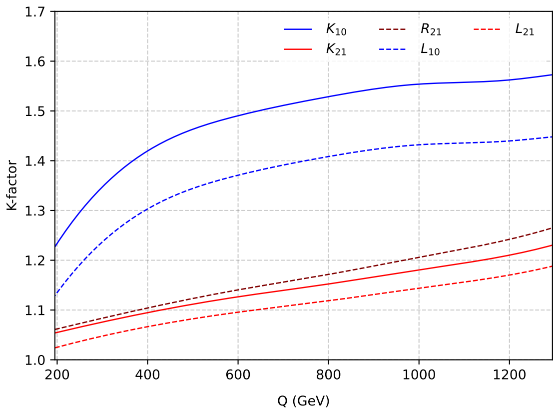

FIGURE 5.5: K-factors for the fixed order and resummed results for Z-boson pair production(see Eq. (5.9) for details).

$\ln(\bar{N})$ have been resummed to NNLL accuracy as outlined in the text. From R_{00}, we see that the LL resummation enhances the LO results by about 15% for $Q = 1300$ GeV. While the NLO corrections are as big as 58%, the corresponding NLO+NLL results are about 68% of LO for the same Q region. The corresponding contribution from NNLO is about 94% where the NNLL resummation adds an additional few percent, making the NNLO+NNLL contributions sizable, about 99% of LO.

To better estimate the size of higher order corrections beyond a certain fixed order as well as that of resummed contributions at different logarithmic accuracy, we present various

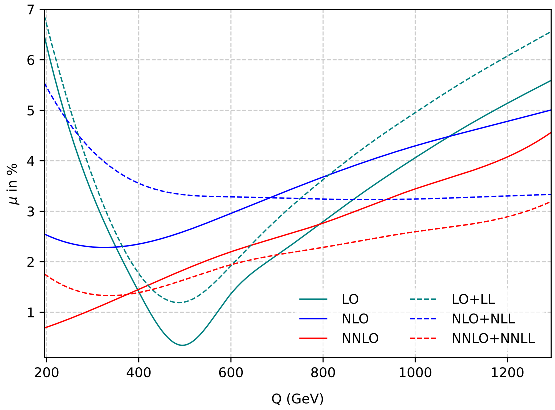

FIGURE 5.6: Seven point scale uncertainties for Z-boson pair production up to NNLO+NNLL.

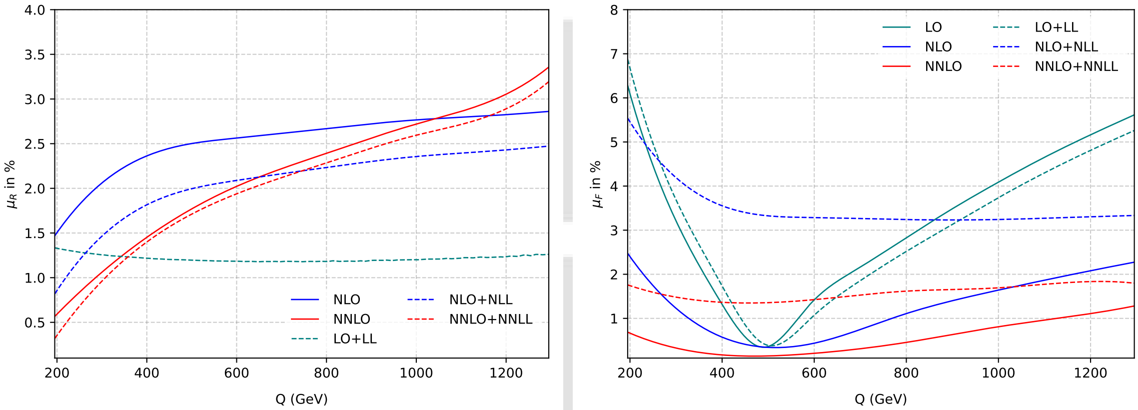

FIGURE 5.7: Renormalization(left) and factorization(right) scale uncertainties for Z-boson pair production up to NNLO+NNLL.

K-factors of the kind $K_{i,i-1}$, $R_{i,i-1}$ and $L_{i,i-1}$, in Fig. 5.5. We notice that, in general, L_{ij} are smaller compared to the respective K_{ij}, indicating that the threshold logarithms of a given accuracy (LL, NLL, ...) capture a substantial contribution of the higher order corrections. Moreover, we notice that the gap between K_{21} and L_{21} is smaller than that between K_{10} and L_{10}, demonstrating a nice convergence of the higher order QCD corrections. Further, it is evident that the former gap is almost independent of Q while the latter gap increases with Q. We also notice that while the L_{10} is about as large as 1.45, the L_{21} is smaller and is about 1.18. This indicates that the contribution of the second order terms and the tower of further sub-leading logarithms (NNLL) that are not included in NLO+NLL are about 18% of NLO+NLL, and are still non-negligible for precision studies.

The underlying theory uncertainties in these distributions up to NNLO+NNLL due to the variation of arbitrary factorization and renormalization scales are presented in Fig. 5.6.

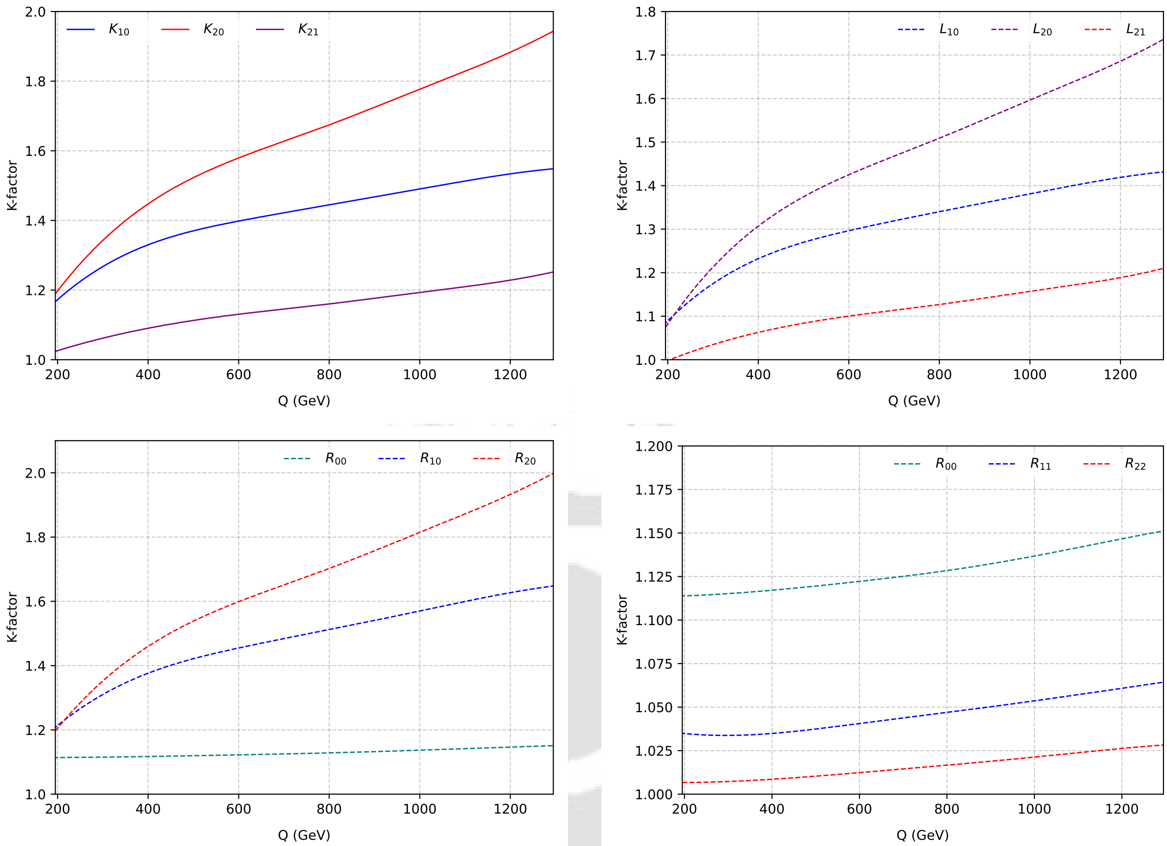

FIGURE 5.8: K-factors as defined in Eq. (5.9) but using same NNLO PDFs at various orders in the perturbation theory.

Here, the complete 7-point scale variations, as discussed in the text, have been presented where the maximum uncertainty in the low Q-region at LO is about 6.5%. However, the inclusion of higher order NLO and NNLO corrections reduce this uncertainty to as low as 2.6% and to less than 1.0% respectively, for $Q = 200$ GeV. The general observation is that these scale uncertainties are found to increase with Q, which for the NNLO case are found to change from about 0.7% to about 4.5%.

For higher Q values, the threshold logarithms are dominant and as a result of resummation, the corresponding scale uncertainties are expected to be smaller than those in the fixed order ones. We see that the scale uncertainties increase from LO to LO+LL, this is because for the process under study there is no μ_R scale dependence at LO. On the other hand, the 7-point scale uncertainties at NLO+NLL (NNLO+NNLL) become smaller than those at NLO(NNLO) beyond $Q = 700(400)$ GeV. While for NNLO, the scale uncertainties reach up to 4.5% in high Q regions, the corresponding ones at NNLO+NNLL level reach up to 3.2%.

In the low Q region, the resummation is found to enhance the scale uncertainties compared to the corresponding fixed order results. This is due to the fact that in the low Q region, the regular terms coming from the hard non-collinear gluons as well as those from the other parton channels are also important. However being non-universal, they can not be resummed to all orders in the perturbation theory. As a result, the resummation cannot improve the scale uncertainties in the fixed order results in the low Q region.

In the left panel of Fig. 5.7, we present the uncertainties due to only the renormalization scale by keeping the $\mu_F = Q$ fixed. Similarly, in the right panel, the uncertainties due to only factorization scale variations for fixed $\mu_R = Q$ are given. It is also worth noting that while performing the resummation, the large partonic threshold logarithms are resummed to all orders in the perturbation series that is expanded in a_s, and hence the uncertainties due to μ_R are expected to be smaller for a given μ_F as shown in the left panel of Fig. 5.7. However, the scale μ_F enters both the PDFs as well as the parton coefficient functions. The uncertainty due to μ_F need not decrease as a result of resummation where the PDFs used are extracted at a particular fixed order. Such a behaviour of μ_F scale uncertainty can be seen in the right panel of Fig. 5.7 and has already been reported in the literature [178, 181, 221, 222, 280, 281, 287, 324, 325, 366, 370, 376, 377].

To study the convergence of the perturbation series, it is useful to keep the PDFs fixed and study how the cross sections vary at different orders. For this, we present the K-factors obtained from the invariant mass distribution computed with NNLO PDFs, to NNLO+NNLL accuracy. Thus, the same a_s is used both at NLO and NNLO. In the top left panel of Fig. 5.8, we present the fixed order K-factors, K_{10}, K_{20} and K_{21}. For a faster converging perturbation series, the factor $K_{i,i-1}$ is supposed to be as close to unity as possible. While the K_{10} has the usual NLO K-factor information and is as large as 55%, from the K_{21} we see that the NNLO corrections could contribute an additional 25% of NLO results. From the behaviour of K_{21}, we see that the second-order corrections are small, but they increase with Q. Similar results are presented but for L_{ij} in the top right panel of Fig. 5.8. By definition, these ratios will estimate the contribution of higher order corrections over and above at least LO+LL level. Hence, these are smaller than the corresponding fixed order K-factors K_{ij}. In the bottom left panel of Fig. 5.8, we present the resummed K-factors R_{i0} to estimate the size of the resummed results above the LO predictions. We notice that the difference $(R_{20} - R_{10})$ is less than $(R_{10} - R_{00})$ for the whole invariant mass region considered here. In the bottom right panel of Fig.

5.8, we plot R_{ii} that gives the information about the resummed contributions over and above the corresponding fixed order corrections. We notice that the contribution from the resummed corrections for any given i is smooth but slowly increasing as Q increases. From R_{22}, we can estimate the size of higher logarithmic terms beyond NNLO to be around 2.8% of NNLO for $Q = 1300$ GeV.

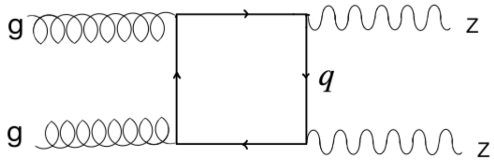

FIGURE 5.9: The feynman diagram for gluon fusion ZZ production at LHC.

The total production cross sections, after integrating over the invariant mass region over the full kinematic region, for LHC energies are substantially large for the Z-boson pair production process. These production cross sections have been given in the Table 5.1 up to NNLO+NNLL accuracy, along with the theory uncertainties due to the seven-point scale variations for different centre of mass energies of the incoming protons. We notice that for any given centre of mass energy, the cross sections increase while the uncertainties decrease as we go from LO to NLO, in the fixed order case. However, the uncertainties will increase from NLO to NNLO due to the gluon fusion channel opening up from the second order in perturbation theory corresponding feynman diagram shown in Fig. 5.9, and hence new contributions will add up to the renormalization scale uncertainties. The gluon fluxes for the LHC energies near the $2m_z$ region is quite large, and this gluon fusion channel contributes about 9.3% of LO Z-boson pair production at 13.6 TeV LHC energy. To systematically quantify the uncertainties in the perturbation theory, we define the second-order cross section without this gluon fusion channel and call it NNLO$_{q\bar{q}}$. The scale uncertainties in this total production cross sections, LO, NLO and NNLO$_{q\bar{q}}$ are found to systematically decrease from 4.24% to 1.07% for 13.6 TeV LHC energy. This behaviour remains similar for other centre of mass energies. We notice a similar behaviour in the total production cross sections after the resummation has been performed, i.e. the scale uncertainties decrease from 4.62% to 1.42%, as we go from LO+LL to NNLO+NNLL. However, the NNLO+NNLL has a somewhat larger scale uncertainty compared to the one in NNLO. This is simply because of the definition of total production cross section where the invariant mass has been integrated out from

$Q_{\rm min} = 2m_z$ to $\sqrt{S}$. In the lower Q-region the contribution from other channels like qg-sub-process can not be ignored. However, with increasing $Q_{\rm min}$ in the total production cross-section, the scale uncertainties in NNLO+NNLL are expected to be smaller than those in NNLO, as evident from Fig. 5.6. The NLO corrections for the gluon fusion channel, in the massless quark limit, are about 68% of its LO for the current LHC energies [383]. The inclusion of massive top quark loops is found to increase this correction to about 73% [386]. Finally, at this NNLO+NNLL accuracy in the perturbation theory, the NLO EW correction for Z-boson pair production also becomes important. The EW corrections are negative, and for total production, they are found to be around -6.2%, while the mixed NNLO QCD×EW corrections are about -5.7% for 13 TeV LHC. For the invariant mass distribution, the EW corrections amount to -15% at 1 TeV [389]. Finally, we note that the uncertainties due to the non-perturbative PDFs are also important. These PDF uncertainties for the $q\bar{q}$ initiated DY processes are found to be about 3% around the 1 TeV region [181]. The ZZ production process also takes place via $q\bar{q}$ initial states, and hence a similar PDF uncertainty is expected around $Q = 1$ TeV.

$\sqrt{S}$	13.0 TeV	13.6 TeV	100.0 TeV
LO	$10.958 \pm 4.00\%$ pb	$11.664 \pm 4.24\%$ pb	$138.617 \pm 13.84\%$ pb
NLO	$14.380 \pm 1.92\%$ pb	$15.284 \pm 1.91\%$ pb	$169.090 \pm 5.13\%$ pb
NNLO$_{q\bar{q}}$	$15.427 \pm 1.01\%$ pb	$16.437 \pm 1.07\%$ pb	$184.438 \pm 1.69\%$ pb
NNLO	$16.418 \pm 2.22\%$ pb	$17.521 \pm 2.30\%$ pb	$212.344 \pm 3.81\%$ pb
LO+LL	$12.353 \pm 4.37\%$ pb	$13.143 \pm 4.62\%$ pb	$153.653 \pm 14.10\%$ pb
NLO+NLL	$14.890 \pm 4.49\%$ pb	$15.824 \pm 4.56\%$ pb	$174.162 \pm 7.76\%$ pb
NNLO$_{q\bar{q}}$+NNLL	$15.527 \pm 1.39\%$ pb	$16.543 \pm 1.42\%$ pb	$185.348 \pm 2.53\%$ pb
NNLO+NNLL	$16.518 \pm 1.84\%$ pb	$17.627 \pm 1.93\%$ pb	$213.254 \pm 3.64\%$ pb

TABLE 5.1: Inclusive cross section for Z-boson pair production for different center of mass energies of the incoming protons, along with the corresponding 7-point scale uncertainties.

5.4 Summary

To summarize, we have performed the threshold resummation for the production of a pair of Z-bosons at the energies of LHC, by resumming the threshold logarithms to NNLL accuracy in QCD. The final state having two massive particles makes the process dependent one-loop and two-loop virtual corrections more difficult compared to the massless final state like di-lepton or di-photon, or one-massive final state like Higgs boson. The presence of such virtual amplitudes makes not only the fixed order computation but also the resummation a challenging task to achieve numerically. In this work, we have performed this resummation by systematically matching to the known fixed order NNLO results (from the package `MATRIX`) and present our phenomenological results to NNLO+NNLL accuracy for both the total production cross sections as well as for the invariant mass distribution of the Z-boson pair, for the current LHC energies, 13.0 and 13.6 TeV, as well as for the upcoming future 100 TeV collider. We notice that the NNLL resummed results in general enhance the cross sections and contribute an additional few percent to the known NNLO results. We have also presented the theory uncertainties by varying the unphysical renormalization and factorization scales from $Q/2$ to $2Q$. We find that, after performing the resummation, the scale uncertainties of about 4.5% in NNLO cross sections get reduced to about 3.2% at NNLO+NNLL level for the invariant mass region $Q = 1.3$ TeV. The availability of these resummed results are expected to augment the current physics programme of the precision studies in the context of LHC and future hadron colliders.

Chapter 6

Pseudo-scalar decay to three parton at NNLO to higher orders in ϵ

THE computation of higher-order quantum corrections plays a pivotal role in achieving precise theoretical predictions for Higgs-related observables at the LHC. While scalar Higgs production via gluon fusion has been explored to remarkable accuracy, its pseudo-scalar counterpart also attracts significant attention in various extensions of the Standard Model (SM), such as the two-Higgs-doublet models (2HDM) and the minimal supersymmetric standard model (MSSM). These models predict the existence of additional CP-odd scalar bosons whose discovery would be a clear signal of new physics.

In the chapter 2, we have employed the formalism for fixed-order computations in perturbative QCD, including ultraviolet (UV) renormalization and the treatment of infrared (IR) divergences using dimensional regularization in $d = 4 + \epsilon$ space-time dimensions. These tools are essential for organizing the divergences that arise in multi-loop computations and for isolating the finite parts that contribute to observable quantities. Furthermore, we have discussed the application of resummation techniques to key processes such as Drell–Yan, associated Higgs production with a vector boson (VH), ZZ production, and Higgs production via bottom quark annihilation. These studies provide a strong theoretical framework for handling soft and collinear radiation in high-energy collisions.

Building upon this foundation, we now turn our attention to multi-loop computations relevant for the decay of a pseudo-scalar Higgs boson into three partons.

In this chapter, we extend the results to compute the two-loop amplitudes relevant for the decay of a pseudo-scalar Higgs boson A into three partons (gluons and quark-antiquark pairs) in higher powers of ϵ. Such amplitudes are crucial ingredients for the NNLO and beyond calculations of pseudo-scalar production in association with jets at hadron colliders. Importantly, to perform a complete and consistent calculation at next-to-next-to-next-to-leading order (N^{3}LO), it is necessary to retain terms beyond the finite part in the dimensional regulator ϵ. The interference between the higher-order loop amplitudes and the ϵ-expanded lower-order ones introduces contributions that survive in the physical limit $\epsilon \to 0$, hence their inclusion is essential.

6.1 Introduction

The Higgs boson was discovered in 2012 at the Large Hadron Collider (LHC) at CERN, using the data collected during the Run-I phase of LHC [27, 28]. Ever since its discovery, establishing its CP properties [135, 136] as well as the measurement of its couplings to the Standard Model (SM) particles has gained significant importance at the collider experiments [404–406]. A study of these properties is vital in confirming that the observed scalar is the SM Higgs boson and in understanding the electroweak symmetry-breaking mechanism [8, 9, 11, 12, 407] responsible for the generation of masses of fermions and gauge bosons.

In the SM, the dominant mode of the Higgs production channel is via gluon fusion channel, where the Higgs boson couples to massive top loops. The other important production channels include the Higgs-strahlung process [108], Vector Boson Fusion process [408, 409], Higgs associated production processes [410, 411]. In the gluon fusion channel (via triangular quark loop), in the exact theory, one needs to consider all the heavy quark flavours whose coupling with the Higgs boson can not be neglected. However, the Leading Order (LO) predictions in the perturbative Quantum Chromodynamics (QCD) for the Higgs production in the gluon fusion channel suffer from large theory uncertainties necessitating the higher order QCD corrections to this process. The lowest order being already a loop-induced process, the computation of higher order corrections quickly become non-trivial. However, in the limit where the top mass is heavier than the Higgs boson mass ($m_t \to \infty$), one can use the effective theory (EFT) where the heavy quark degrees of freedom can be integrated out and the lowest order process in the gluon fusion process can be described in terms of an effective vertex coupling the Higgs boson to gluons. The higher order corrections thus in the EFT become an easier realization. The Next-to-Leading-Order (NLO) [412, 413] corrections in the EFT in this gluon fusion channel are found to contribute by more than 100% [47, 48] of the LO and the corresponding theory uncertainties due to the unphysical renormalization and factorization scales were found to get reduced.These large QCD corrections indicate the necessity to go beyond NLO towards the computation of Next-to-Next-to-Leading Order (NNLO) predictions. These were computed in [53, 152, 153] and are found to enhance the cross sections by an additional 60% and also found to stabilize the cross sections against the variation of unphysical scales in the calculation.

The error introduced in these EFT results because of neglecting the finite quark mass effects were estimated to be around 5% at NLO [48, 149, 171, 414] and those at NNLO are about 0.62% [415]. Owing to the importance of the SM Higgs boson, and with improved statistics in the experimental data, it has become essential to go beyond NNLO towards the computation of Next-to-Next-to-Next-to-Leading Order (N^{3}LO) computation. Such a computation was possible in the context of EFT [69, 70, 416, 417], which gives additional 10% correction, thanks to the available gluon Form Factors (FFs), universal soft-collinear distribution [258], and the mass factorization kernels [210, 211].

The Higgs boson is the most sought-after particle in the SM. However, in spite of its discovery, the SM has many shortfalls, like the origin of neutrino mass, unification of the gauge couplings, and the observed relic abundance. Many New Physics (NP) scenarios were proposed in this direction to address these issues and are studied in the context of physics Beyond the SM (BSM). Such BSM scenarios like Supersymmetry[146], technicolor [418], and extra-dimensions [419, 420] typically have further symmetries or new particle content, inevitably including the scalar sector as well. As a result, an experimental search for various BSM scenarios is going on both at the ATLAS and CMS detectors at the LHC. In the context of scalar sector, one such particle studied well is the pseudo-scalar particle in the Minimal Supersymmetric Standard Model (MSSM) [421]. In the MSSM, after the electroweak symmetry breaking, there are three neutral (h, H, A) and two charged Higgs ($H^{\pm}$) particles [139–145, 422]. Out of these three neutral particles, h, H are CP even scalars while A is CP odd pseudo-scalar particle.

There have been long attempts to establish the CP properties of the discovered Higgs boson at the LHC, and all such efforts have clearly indicated that the observed Higgs boson is CP even [404–406]. However, the search for CP-odd scalar particles in the collider experiments is very crucial. One open and interesting possibility is that the observed Higgs boson could have a small mixture of this pseudo-scalar component. From the theory side, the production of the pseudo-scalar at the collider experiments takes place in gluon fusion channel, very much similar to the case of SM Higgs boson. The main difference being that the pseudo-scalar in the EFT has two different operators O_G and O_J. Being gluon-fusion induced process, the higher order corrections (NLO, NNLO etc.) as well as the theory uncertainties due to μ_R and μ_F in the production of pseudo-scalar boson at the LHC are very much similar to those for the SM Higgs boson.

The NLO inclusive production of a pseudo-scalar Higgs boson has been computed in [148], while the NNLO corrections can be found in [152, 153]. Efforts to include N^{3}LO corrections for pseudo-scalar have been made in [278, 368]. The amplitudes for di-Higgs and di-pseudo-Higgs at NNLO also can be found in [423, 424]. To probe further the properties of the (pseudo-)scalar boson and its couplings to the SM particles, it is necessary to study various differential distributions like transverse momentum [425, 426] and rapidity distributions [374, 376], along the lines of the CP even Higgs. For the Higgs transverse momentum distribution, the Higgs boson gets recoiled against the jets at the lowest order itself. The higher order corrections to such observable is non-trivial. The higher order corrections to process of Higgs + 1 jet have been computed up to NNLO in [156–161, 427]. The NLO corrections for pseudo-scalar Higgs in association with a jet can be found in [172, 173, 412, 413], while the NNLO corrections for the same process has been recently presented in [175]. These NLO cross sections are found to increase the LO result by 80%, while the NNLO QCD corrections enhance the cross sections by an additional 36%. The scale uncertainties at NLO and NNLO are about 38% and 22% respectively [175]. This large scale uncertainties indicate missing higher orders, making a full N^{3}LO computation important for this process.

In perturbative Quantum Chromodynamics (QCD), virtual corrections to scattering amplitudes exhibit infrared (IR) singularities due to soft and collinear gluon emissions.

These divergences manifest as poles in the dimensional regulator ϵ, introduced via dimensional regularization with $d = 4 + \epsilon$. The structure of these poles is universal and can be systematically predicted using factorization theorems and infrared evolution equations. At the one-loop level, the amplitude exhibits simple poles up to $\mathcal{O}(1/\epsilon^2)$, while at two loops, the pole structure extends to $\mathcal{O}(1/\epsilon^4)$. In general, for an L-loop amplitude, the IR divergence behaves as

$$\mathcal{M}^{(L)} \sim \sum_{k=0}^{2L} \frac{1}{\epsilon^k} \mathcal{C}_k^{(L)}, \tag{6.1}$$

where $\mathcal{C}_k^{(L)}$ are coefficients depending on the kinematic variables and color structure of the process. Importantly, in order to construct finite cross sections at the next order, one must account not only for the singular terms but also for the *higher-order* terms in ϵ from lower-loop amplitudes. For example, in the computation of finite parts at the three-loop level, the $\mathcal{O}(\epsilon^n)$ terms (with $n > 0$) from the two-loop amplitudes contribute through the interference with the singular structure of the one-loop or tree-level amplitude. These contributions arise in the squared matrix elements and are crucial for obtaining consistent and accurate predictions. Therefore, for precision QCD predictions at three loops, it is essential to compute the two-loop amplitudes beyond the finite part, retaining terms up to positive powers of ϵ. These higher-order ϵ-terms serve as vital ingredients in canceling divergences and assembling finite, physical observables.

Going beyond NNLO to these differential distributions, both for Higgs as well as pseudo-scalar Higgs boson cases, is highly non-trivial. However, attempts are ongoing to go beyond NNLO. One such important ingredient required at N^{3}LO level is the underlying lower order virtual corrections expanded to higher powers in dimensional regulator ϵ. For N^{3}LO level computation, one needs the one loop results expanded to ϵ^4, the two loop results expanded to ϵ^2, and three loop level results expanded to ϵ^0 level. In the context of Higgs + 1 jet, the two loop results expanded to ϵ^2 have been recently computed in [428]. It is essential to study the corresponding contributions for the production of pseudo-scalar Higgs boson + 1 jet at hadron colliders. In this chapter, we perform the two-loop computation for the pseudo-scalar decay to three partons and present the results expanded to ϵ^2. In brief, our chapter contains the following: (i) $\mathcal{O}(\epsilon^1)$ and $\mathcal{O}(\epsilon^2)$ of the matrix elements at NNLO, (ii) $\mathcal{O}(\epsilon^3)$ and $\mathcal{O}(\epsilon^4)$ of the matrix elements at NLO, (iii) Implementation of the optimised matrix elements and making it publicly available. This computation with appropriate crossing symmetry relations will give the required result for the pseudo-scalar + 1 jet. After checking the IR poles as predicted in [429], we further make a numerical study of the finite pieces by computing the coefficients of ϵ^i ($i \geq 0$) for both $A \to ggg$ and $A \to q\bar{q}g$ cases at one-loop as well as two-loop level in QCD. We implement the above mentioned finite pieces in FORTRAN-95 routines and discuss the subtleties associated with such numerical implementations.

This chapter is organized as follows: We present the theoretical framework and kinematics in section 6.2, and 6.3 respectively. Calculation details are presented in section 6.4. We also present the IR and UV renormalization of the amplitudes in sections 6.5 and 6.6 respectively. Then we present some numerical results of the amplitudes in section 6.7. Finally, we summarize our observations in section 6.8.

6.2 Theoretical details

A pseudo-scalar Higgs boson couples to heavy quarks through the Yukawa interaction. In the limit of infinite quark mass limit the resulting effective Lagrangian can be written as follows [177]:

$$\mathcal{L}^A_{\text{eff}} = \Phi^A(x)\Big[-\frac{1}{8}C_G O_G(x) - \frac{1}{2}C_J O_J(x)\Big] \tag{6.2}$$

where Φ^A being the the pseudo-scalar Higgs boson. C_G and C_J are Wilson coefficients that results after integrating the heavy top quark loop. In other words, they carry the heavy quark mass dependencies. The Wilson coefficients are computed [177] by considering the vertex diagrams where the pseudo-scalar Higgs couples to the gluons or light quarks via top quark loops. While C_G does not receive any QCD corrections beyond one loop, owing to Adler-Bardeen theorem [430], C_J starts at second order in QCD perturbation theory. The Feynman diagrams for A decay to 3 partons at leading order (LO) are given in Fig. 6.1.

Denoting the strong coupling constant by $a_s = \frac{g_s^2}{16\pi^2}$, the expression for C_G and C_J are as follows [177]:

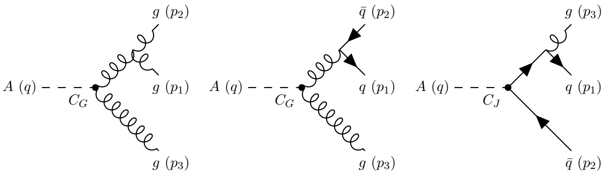

FIGURE 6.1: Feynman diagram for A decay to 3 partons at LO.

$$\begin{aligned} C_G &= a_s C_G^{(1)} \\ C_J &= \left(a_s C_J^{(1)} + a_s^2 C_J^{(2)} + ...\right) C_G \\ \text{with } C_G^{(1)} &= -2^{\frac{5}{4}} G_F^{\frac{1}{2}} \cot\beta,\ C_J^{(1)} = -C_F(\frac{3}{2} - 3\ln\frac{\mu_R^2}{m_t^2}). \end{aligned} \tag{6.3}$$

In the above equation, β is the ratio of the vacuum expectation values of the two Higgs fields in the MSSM, m_t is the top quark mass, C_F is the SU(N) color and G_F is the Fermi constant.

The operators, $O_G(x)$ and $O_J(x)$ in Eq. 6.2 are defined in terms of the Standard Model fermionic and gluonic fields as follows:

$$O_G(x) = G_a^{\mu\nu} \tilde{G}_{a,\mu\nu} \equiv \epsilon_{\mu\nu\rho\sigma} G_a^{\mu\nu} G_a^{\rho\sigma}\,, \tag{6.4}$$

$$O_J(x) = \partial_\mu \left(\bar{\psi}\gamma^\mu\gamma_5\psi\right)\,. \tag{6.5}$$

In above $G^{\mu\nu}$ is the gluonic field strength tensor and ψ represents the light fermionic fields. The operator $O_J(x)$ being a chiral quantity, contains γ_5 and the Levi-Civita tensor $\varepsilon^{\mu\nu\rho\sigma}$, which are both four dimensional objects. These quantities are not well defined for $d \neq 4$ dimensions; thus it is essential to choose a proper definition of them. We shall follow the definition introduced by 't Hooft and Veltman in the article [190]:

$$\gamma_5 = i\frac{1}{4!}\varepsilon_{\nu_1\nu_2\nu_3\nu_4}\gamma^{\nu_1}\gamma^{\nu_2}\gamma^{\nu_3}\gamma^{\nu_4}\,. \tag{6.6}$$

The contraction of $\varepsilon_{\nu_1\nu_2\nu_3\nu_4}$ is as follows:

$$\varepsilon_{\mu_1\nu_1\rho_1\sigma_1}\,\varepsilon^{\mu_2\nu_2\rho_2\sigma_2} = \begin{vmatrix} \delta^{\mu_2}_{\mu_1} & \delta^{\nu_2}_{\mu_1} & \delta^{\rho_2}_{\mu_1} & \delta^{\sigma_2}_{\mu_1} \\ \delta^{\mu_2}_{\nu_1} & \delta^{\nu_2}_{\nu_1} & \delta^{\rho_2}_{\nu_1} & \delta^{\sigma_2}_{\nu_1} \\ \delta^{\mu_2}_{\rho_1} & \delta^{\nu_2}_{\rho_1} & \delta^{\rho_2}_{\rho_1} & \delta^{\sigma_2}_{\rho_1} \\ \delta^{\mu_2}_{\sigma_1} & \delta^{\nu_2}_{\sigma_1} & \delta^{\rho_2}_{\sigma_1} & \delta^{\sigma_2}_{\sigma_1} \end{vmatrix} \tag{6.7}$$

We shall elaborate on γ_5 in the section 6.5.

6.3 Kinematics

We shall use the same notation as used in the article [174]. Considering the process:

$$A(q) \to B(p_1) + C(p_2) + D(p_3) \tag{6.8}$$

for $\{B, C, D\} = \{g, g, g\}$ or $\{B, C, D\} = \{q, \bar{q}, g\}$. The Mandelstam invariants are defined as:

$$s = (p_1 + p_2)^2, t = (p_1 + p_3)^2, u = (p_2 + p_3)^2, q^2 = Q^2. \tag{6.9}$$

Where Q is the mass of pseudo-scalar Higgs boson and they satisfy the conservation relation:

$$s + t + u = Q^2 \tag{6.10}$$

In this work, we will work with the dimensionless variables:

$$x = \frac{s}{Q^2},\ y = \frac{u}{Q^2},\ z = \frac{t}{Q^2}. \tag{6.11}$$

Our amplitudes are valid in the following kinematical regions of the decay phase space:

$$x = 1 - y - z,\ 0 \leq y \leq 1 - z,\ 0 \leq z. \tag{6.12}$$

6.4 Calculational details

We closely follow the calculational procedure as outlined in [174]. We first generate the diagrams with QGRAF [185]. Our next step is to construct the amplitudes from these diagrams. In order to facilitate the discussions let us introduce some notations for the amplitudes:

$$|\mathcal{A}_f\rangle = \sum_{\Lambda=G,J} C_\Lambda(a_s)|\mathcal{M}_f^\Lambda\rangle \tag{6.13}$$

There are total four sub-amplitudes $|\mathcal{M}_f^\Lambda\rangle$. When $f = ggg$ we can have the sub-amplitude $|\mathcal{M}_{ggg}^{OG}\rangle$ and the corresponding Wilson coefficients is C_G. For the same final state, we can have the sub-amplitude $|\mathcal{M}_{ggg}^{OJ}\rangle$ and the corresponding Wilson coefficients is C_J. When $f = q\bar{q}g$, similarly we can construct two more sub-amplitudes. While for $f = ggg$, $|\mathcal{M}_{ggg}^{G}\rangle$ starts at $\mathcal{O}(g_s)$, it is not true for $\Lambda = J$. However for $f = q\bar{q}g$ we have amplitides at $\mathcal{O}(g_s)$ for $\Lambda = \{G, J\}$. As a next step we construct the quantity $\mathcal{S}_f = \langle\mathcal{A}_f|\mathcal{A}_f\rangle$, which we can use to express the results at the cross section level. In order to do so, we process the QGRAF output, perform the Dirac and SU(N) color manipulations with our in-house codes in FORM [187]. The result of these algebraic manipulations can be expressed in terms of thousands scalar Feynman integrals and some coefficients which depend on the Mandelstam invariants. With suitable momentum transformations, these huge number of Feynman integrals can be grouped under a minimal set of topologies. We perform these momentum shifts using the public package REDUZE2 [189, 431]. For our current work, we have considered these minimal topologies to be the one presented in [428]. It is to be noted that the topologies considered in [428](henceforth we call them new) can be related to the ones in [432, 433] (henceforth we call them old)via the transformations:

$$\text{Planar}_{\text{old}} \xrightarrow{s\to u, u\to t, t\to s} \text{Planar}_{\text{new}} \tag{6.14}$$

$$\text{Non planar1}_{\text{old}} \xrightarrow{s\to t, u\to u, t\to s} \text{Non planar}_{\text{new}} \tag{6.15}$$

$$\text{Non planar2}_{\text{old}} \xrightarrow{s\to u, u\to t, t\to s} \text{Non planar}_{\text{new}} \tag{6.16}$$

However, within each topology, we still have many Feynman integrals. Exploiting the linear relations that these Feynman integrals share among themselves, we can find a minimum number of integrals, which are called Master integrals(MIs), for each of the topologies considered above. We have generated these identities using the public package KIRA [434], which implements Laporta algorithm [435], and uses integration by parts (IBP) [436, 437] and Lorentz invariance identities [438]. The number of MI at one loop is 7 while the same at two loop is 89. These integrals have been analytically computed in the recent work [428], where the authors have expressed the results, up to $\mathcal{O}(\epsilon^2)$, in terms of Generalised Polylogarithms (GPLs). Here ϵ is the dimensional regularization parameter, which is used to regulate the ultraviolet (UV) and infrared (IR) divergences. We have used these MIs and obtained the unrenormalised amplitudes $\mathcal{S}_{ggg}$ and $\mathcal{S}_{q\bar{q}g}$. It is to be noted that in the work [432, 433] the results of the MIs, for the same topologies as in our current work, were presented up to $\mathcal{O}(\epsilon^0)$, in terms of Harmonic Polylogarithms. While it is not entirely possible to relate the special functions appearing in [432, 433] to that of [428], some of them can be shown to be related. In the section 6.6 we shall present some of these identities.

It is to be noted that during the intermediate stages of the calculations, the size of the polynomials becomes enormous, which results in final file sizes of $\sim$ a few GB. We have simplified the IBP rules, using MultivariateApart [439] which helps to partial fraction the polynomials appearing in our computations. As a result, we could reduce the relevant file sizes to less than 100 MB. This would later on help to efficiently implement the amplitudes numerically.

For completion we present the relevant formulas for $\mathcal{S}_{ggg}$ and $\mathcal{S}_{q\bar{q}g}$ below:

$$\mathcal{S}_{ggg} = a_s^3 \left(C_G^{(1)}\right)^2 \Bigg[S_g^{G,(0)} + a_s S_g^{G,(1)} \tag{6.17}$$

$$+ a_s^2 \Big(S_g^{G,(2)} + 2 C_J^{(1)} S_g^{GJ,(1)} \Big) \Bigg] \tag{6.18}$$

where

$$\begin{aligned} S_g^{G,(0)} &= \langle \mathcal{M}_{ggg}^{G,(0)} | \mathcal{M}_{ggg}^{G,(0)} \rangle \,, \\ S_g^{G,(1)} &= 2 \langle \mathcal{M}_{ggg}^{G,(0)} | \mathcal{M}_{ggg}^{G,(1)} \rangle \,, \\ S_g^{GJ,(1)} &= \langle \mathcal{M}_{ggg}^{G,(0)} | \mathcal{M}_{ggg}^{J,(1)} \rangle \,, \\ S_g^{G,(2)} &= \langle \mathcal{M}_{ggg}^{G,(1)} | \mathcal{M}_{ggg}^{G,(1)} \rangle + 2 \langle \mathcal{M}_{ggg}^{G,(0)} | \mathcal{M}_{ggg}^{G,(2)} \rangle \end{aligned} \tag{6.19}$$

where $\mathcal{M}_{ggg}^{G,(n)}$ is the matrix element at $\mathcal{O}(\alpha_s^n)$. Similarly for $A \to q\bar{q}g$, we find

$$\mathcal{S}_{q\bar{q}g} = a_s^3 \left(C_G^{(1)}\right)^2 \Bigg[S_q^{G,(0)} + a_s\Big(2S_q^{G,(1)} \tag{6.20}$$

$$+2C_J^{(1)} S_q^{JG,(0)}\Big) + a_s^2\Big(S_q^{G,(2)} + C_J^{(1)} S_q^{JG,(1)}$$

$$+ \left(C_J^{(1)}\right)^2 S_q^{J,(0)} + 2C_J^{(2)} S_q^{JG,(0)}\Big)\Bigg] \tag{6.21}$$

where

$$\begin{aligned}
S_q^{G,(0)} &= \langle \mathcal{M}_{q\bar{q}g}^{G,(0)} | \mathcal{M}_{q\bar{q}g}^{G,(0)} \rangle \,, \\
S_q^{J,(0)} &= \langle \mathcal{M}_{q\bar{q}g}^{J,(0)} | \mathcal{M}_{q\bar{q}g}^{J,(0)} \rangle \,, \\
S_q^{G,(1)} &= \langle \mathcal{M}_{q\bar{q}g}^{G,(0)} | \mathcal{M}_{q\bar{q}g}^{G,(1)} \rangle \,, \\
S_q^{JG,(0)} &= \langle \mathcal{M}_{q\bar{q}g}^{J,(0)} | \mathcal{M}_{q\bar{q}g}^{G,(0)} \rangle \,, \\
S_q^{G,(2)} &= \langle \mathcal{M}_{q\bar{q}g}^{G,(1)} | \mathcal{M}_{q\bar{q}g}^{G,(1)} \rangle + 2\langle \mathcal{M}_{q\bar{q}g}^{G,(0)} | \mathcal{M}_{q\bar{q}g}^{G,(2)} \rangle \,, \\
S_q^{JG,(1)} &= 2\langle \mathcal{M}_{q\bar{q}g}^{J,(1)} | \mathcal{M}_{q\bar{q}g}^{G,(0)} \rangle + 2\langle \mathcal{M}_{q\bar{q}g}^{J,(0)} | \mathcal{M}_{q\bar{q}g}^{G,(1)} \rangle \,.
\end{aligned} \tag{6.22}$$

In the next section we shall discuss their UV and IR renormalizations.

6.5 UV renormalization

The unrenormalised matrix elements that we obtained in the last section have singularities which can be regulated by going to $d = 4 + \epsilon$ dimensions, where the singularities manifest themselves in inverse powers of ϵ. These singularities are of UV and IR origin. This section is devoted to discussing the UV singularities, which are first regulated in dimensional regularization. Next we renormalise the coupling constant as well as that of the composite operators. As we shall see, the latter is a non-trivial task.

The bare coupling constant is renormalized by renormalization constant (Z) and spherical factor S_ϵ as given in Eq. (2.7). where $S_\epsilon = \exp\left[(\gamma_E - \ln 4\pi)\epsilon/2\right]$ and the explicit expression of renormalization constant as given in Eq. (2.12) up to second order in a_s is

$$Z = 1 + a_s \left[\frac{2}{\epsilon}\beta_0\right] + a_s^2 \left[\frac{4}{\epsilon^2}\beta_0^2 + \frac{1}{\epsilon}\beta_1\right] \tag{6.23}$$

β_i are the coefficients of the QCD β-functions [197], given in Eq. (2.13). Next, we turn to renormalization of the composite operators, $O_G(x)$ and $O_J(x)$. Their renormalization is closely connected to the definition of γ_5 that we used earlier. The prescription of γ_5 used in Eq. 6.6 fails to satisfy Ward identities. In addition $\{\gamma_\mu, \gamma_5\} \neq 0$ in d dimensions. As a first step to overcome the problem, we need to define the axial singlet current correctly, which is as follows [392]:

$$J^5_\mu = \bar{\psi}\gamma_\mu\gamma_5\psi \tag{6.24}$$

To get back the renormalization invariance of the singlet axial current, a finite renormalization should be performed [392, 440], which we refer to as Z^s_5. Thus the renormalized axial singlet current reads as:

$$J^5_{\mu,R} = Z^s_5 Z^s_{\overline{MS}} i\frac{1}{3!}\varepsilon^{\mu\nu_1\nu_2\nu_3}\bar{\psi}\gamma_{\nu_1}\gamma_{\nu_2}\gamma_{\nu_3}\psi \tag{6.25}$$

where $Z^s_{\overline{MS}}$ is the overall operator renormalization constant. The corresponding expression, computed using operator product expansion, till third order in the strong coupling constant can be found in [392, 441]. One of us in [442] has calculated $Z^s_{\overline{MS}}$ by demanding the universality of the IR poles in form factor for decay of a pseudo-scalar Higgs to a quark-antiquark pair, or to two gluons. By demanding the operator relation of the axial anomaly, Z^s_5 was first determined upto $\mathcal{O}(\alpha_s^2)$ in [392] which was verified later in [442].

As a result the bare operator $[O_J]_B$ gets renormalised by

$$[O_J]_R = Z^s_5 Z^s_{\overline{MS}} [O_J]_B \equiv Z_{JJ} [O_J]_B \ , \tag{6.26}$$

The bare operator $[O_J]_B$ mixes under renormalisation, and the formula to get the renormalised counterpart is as follows:

$$[O_G]_R = Z_{GG} [O_G]_B + Z_{GJ} [O_J]_B \tag{6.27}$$

The expressions for Z_{JJ}, Z_{GG} and Z_{GJ} were computed in [392, 441], and was later found out by an independent calculation in the work [442]. Their expressions can be found in the Appendix D.2.

6.6 IR regularisation

The UV renormalised amplitudes contain divergences coming from the IR sector, due to the presence of massless particles. For a n-loop amplitude, these singularities factorize in the color space in terms of the lower $n-1$ loop amplitudes. This factorization was first shown by Catani, in his work [429], where the IR singularities for a n-point 2 loop amplitude were predicted, and then encoded in terms of universal subtraction operators. However, the $1/\epsilon$ pole was not fully predicted in [429]. The predictions of Catani were later shown in [443] to be related to factorization and resummation properties of QCD amplitudes. Using soft-collinear effective theory, Becher and Neubert [444] generalised Catani's predictions to arbitrary number of loops and legs, for SU(N) gauge theory. The authors in [444] conjectured that for any n-jet operator in soft-collinear effective theory the IR singularities can be factorized in a multiplicative renormalization factor, which is constructed out of cusp anomalous dimensions of Wilson loops with light like segments [445, 446].

We have checked that the IR poles that appear in our computation, at one and two loop level, are the same as the ones predicted in [429]. For completion, we present the universal subtraction operators below:

$$
\begin{aligned}
|\mathcal{M}_f^{\Sigma,(1)}\rangle =& 2\mathbf{I}_f^{(1)}(\epsilon)|\mathcal{M}_f^{\Sigma,(0)}\rangle + |\mathcal{M}_f^{\Sigma,(1)fin}\rangle \\
|\mathcal{M}_f^{\Sigma,(2)}\rangle =& 4\mathbf{I}_f^{(2)}(\epsilon)|\mathcal{M}_f^{\Sigma,(0)}\rangle + 2\mathbf{I}_f^{(1)}(\epsilon)|\mathcal{M}_f^{\Sigma,(1)}\rangle + \\
& |\mathcal{M}_f^{\Sigma,(2)fin}\rangle\,,
\end{aligned}
\tag{6.28}
$$

where UV renormalised amplitudes are denoted by $|\mathcal{M}_f^{\Sigma,(n)}\rangle$ and

$$\begin{aligned}\mathbf{I}^{(1)}_{ggg}(\epsilon) = F_p\left(C_A\frac{4}{\epsilon^2}-\frac{\beta_0}{\epsilon}\right)\Bigg[\Big(-\frac{s}{\mu_R^2}\Big)^{\frac{\epsilon}{2}}+\\ \Big(-\frac{t}{\mu_R^2}\Big)^{\frac{\epsilon}{2}}+\Big(-\frac{u}{\mu_R^2}\Big)^{\frac{\epsilon}{2}}\Bigg],\end{aligned} \tag{6.29}$$

$$\begin{aligned}\mathbf{I}^{(1)}_{q\bar{q}g}(\epsilon) = F_p\Bigg\{\left(\frac{4}{\epsilon^2}-\frac{3}{\epsilon}\right)(C_A-2C_F)\left[\left(-\frac{s}{\mu_R^2}\right)^{\frac{\epsilon}{2}}\right]\\ +\left(-\frac{4C_A}{\epsilon^2}+\frac{3C_A}{2\epsilon}+\frac{\beta_0}{2\epsilon}\right)\left[\left(-\frac{t}{\mu_R^2}\right)^{\frac{\epsilon}{2}}+\left(-\frac{u}{\mu_R^2}\right)^{\frac{\epsilon}{2}}\right]\Bigg\},\end{aligned}$$

$$\begin{aligned}\mathbf{I}^{(2)}_f(\epsilon) = -\frac{1}{2}\mathbf{I}^{(1)}_f(\epsilon)\left[\mathbf{I}^{(1)}_f(\epsilon)-\frac{2\beta_0}{\epsilon}\right]+\\ \frac{e^{\frac{\epsilon}{2}\gamma_E}\Gamma(1+\epsilon)}{\Gamma(1+\frac{\epsilon}{2})}\left[-\frac{\beta_0}{\epsilon}+K\right]\mathbf{I}^{(1)}_f(2\epsilon)+\mathbf{H}^{(2)}_f(\epsilon)\end{aligned} \tag{6.30}$$

with

$$K=\left(\frac{67}{18}-\zeta_2\right)C_A-\frac{10}{9}T_Fn_f,\ F_p=-\frac{1}{2}\frac{e^{-\frac{\epsilon}{2}\gamma_E}}{\Gamma(1+\frac{\epsilon}{2})}$$

$$\begin{aligned}\mathbf{H}^{(2)}_{ggg}(\epsilon) =\frac{3}{\epsilon}\Bigg\{C_A^2\left(-\frac{5}{24}-\frac{11}{48}\zeta_2-\frac{1}{4}\zeta_3\right)+\\ C_An_f\left(\frac{29}{54}+\frac{1}{24}\zeta_2\right)-\frac{1}{4}C_Fn_f-\frac{5}{54}n_f^2\Bigg\},\end{aligned} \tag{6.31}$$

$$\begin{aligned}\mathbf{H}^{(2)}_{q\bar{q}g}(\epsilon) =\frac{1}{\epsilon}\Bigg\{C_A^2\left(-\frac{5}{24}-\frac{11}{48}\zeta_2-\frac{1}{4}\zeta_3\right) \qquad (6.32)\\ +C_An_f\left(\frac{29}{54}+\frac{1}{24}\zeta_2\right)+C_Fn_f\left(-\frac{1}{54}-\frac{1}{4}\zeta_2\right)\\ +C_AC_F\left(-\frac{245}{216}+\frac{23}{8}\zeta_2-\frac{13}{2}\zeta_3\right)+ \qquad (6.33)\\ C_F^2\left(\frac{3}{8}-3\zeta_2+6\zeta_3\right)-\frac{5}{54}n_f^2\Bigg\}.\end{aligned}$$

We have checked the IR singular parts of $\mathcal{S}_{ggg}$ and $\mathcal{S}_{q\bar{q}g}$ to Catani's prediction and have found perfect agreement. In addition, we also checked the IR poles and finite part of our result to our earlier computation [174], where the latter result was expressed in terms of Harmonic Polylogarithms. We have analytically checked the IR poles to the ones appearing in [174] and the corresponding transformations that were needed are:

$$
\begin{aligned}
&H(0;y) \to G(0;y), H(0;z) \to G(0;z), \qquad (6.34)\\
&H(1;z) \to -G(1;z), H(1-z;y) \to -G(1-z;y),\\
&H(z;y) \to G(-z;y), H(0,0;y) \to G(0,0;y),\\
&H(0,0;z) \to G(0,0;z), H(0,1;z) \to -G(0,1;z),\\
&H(0,1-z;y) \to -G(0,1-z;y),\\
&H(1,0;y) \to -G(0;y)G(1;y) + G(0,1;y),\\
&H(1,0;z) \to -G(0;z)G(1;z) + G(0,1;z),\\
&H(0,0,1-z;y) \to -G(0,0,1-z;y),\\
&H(1-z,0;y) \to -G(0;y)G(1-z;y) + G(0,1-z;y),\\
&H(1-z,1-z;y) \to \frac{1}{2}G(1-z;y)^2,\\
&H(z,1-z;y) \to -G(-z,1-z;y),\\
&H(1-z,z;y) \to G(1;z)G(-z;y) - (G(1;z)+\\
&G(1-z;y))G(-z;y) + G(-z,1-z;y),\\
&H(0,0,0;y) \to \frac{1}{6}G(0;y)^3, H(0,0,0;z) \to \frac{1}{6}G(0;z)^3,\\
&H(0,0,1;y) \to -G(0,0,1;y),\\
&H(0,0,1;z) \to -G(0,0,1;z), H(1,1;z) \to G(1,1;z),\\
&H(0,1,0;y) \to -G(0;y)G(0,1;y) + 2G(0,0;1,y),\\
&H(0,1,0;z) \to -G(0;z)G(0,1;z) + 2G(0,0,1;z),\\
&H(0,1,1;z) \to -\zeta_2 G(1;z) + \frac{1}{2}G(0;z)G(1;z)^2 -\\
&G(1;z)(-\zeta_2 + G(1,0;z)) + G(1,1,0;z),\\
&H(0,1,1;y) \to -\zeta_2 G(1;y) + \frac{1}{2}G(0;y)G(1;y)^2 -\\
&G(1;y)(-\zeta_2 + G(1,0;y)) + G(1,1,0;y),\\
&H(0,1-z,0;y) \to -G(0,1-z,0;y),\\
&H(1,0,0;y) \to -G(1,0,0;y),\\
&H(1,0,0;z) \to -G(1,0,0;z),\\
&H(1,0,1;z) \to G(1,0,1;z), H(1,1,0;z) \to G(1,1,0;z),\\
&H(1,1,1;z) \to -G(1,1,1;z),
\end{aligned}
$$

$$
\begin{aligned}
&H(1-z,0,0;y) \to -G(1-z,0,0;y),\\
&H(1-z,0,1-z;y) \to G(1-z,0,1-z;y),\\
&H(1-z,1-z,0;y) \to G(1-z,1-z,0;y),\\
&H(1-z,1-z,1-z;y) \to -G(1-z,1-z,1-z;y),\\
&H(1-z,z,1-z;y) \to G(1-z;y)G(-z,1-z;y)-\\
&2(\zeta_2 G(1;z) - \zeta_2(G(1;z)+G(1-z;y))+\\
&\frac{1}{2}G(1-z;y)^2(G(0;z)+G(-z;y))+G(1-z;y)\\
&G(1,0;z)+G(0;z)G(1-z,1-z;y)-G(1-z;y)\\
&(-\zeta_2+G(0;z)G(1-z;y)+G(1,0;z)+\\
&G(1-z,-z;y))+G(1-z,1-z,-z;y)),\\
&H(z,1-z,1-z;y) \to \zeta_2 G(1;z) - \zeta_2(G(1;z)\\
&+G(1-z;y))+\frac{1}{2}G(1-z;y)^2(G(0;z)+G(-z;y))\\
&+G(1-z;y)G(1,0;z)+G(0;z)G(1-z,1-z;y)-\\
&G(1-z;y)(-\zeta_2+G(0;z)G(1-z;y)+G(1,0;z)+\\
&G(1-z,-z;y))+G(1-z,1-z,-z;y),\\
&H(0,1-z,1-z;y) \to G(0,1-z,1-z;y).
\end{aligned}
$$

We have used PolyLogTools [447] and various relations among HPL's to generate these identities. The definitions of GPLs and HPLs are given in Appendix D.1. The finite part of our new result matches numerically to our earlier computation [174] for several phase space points. It is also to be noted that the finite part in [174] was recently confirmed in the article [175]. This validates our computational framework. In the next section, we discuss the numerical implementation of our results at $\mathcal{O}(\epsilon)$ and $\mathcal{O}(\epsilon^2)$.

6.7 Numerical implementation

In this section, we discuss about the numerical implementation of our matrix elements. In order to achieve a fast numerical grid, we have simplified the two-loop analytical results, at each order in ϵ, with our in-house routines in Mathematica. Thus we were able to get files containing analytical results of sizes $\sim$ 600 KB, 2.5 MB and 11 MB for $\mathcal{O}(\epsilon^0)$, $\mathcal{O}(\epsilon)$ and $\mathcal{O}(\epsilon^2)$ respectively. These analytical results will contribute to a full three-loop computation for the type of process under study. This means that our results need to be integrated over the allowed phase space regions, as desired by experimental searches, using the Monte Carlo technique. The allowed phase space region can be seen in Eq. 6.12. We have implemented the analytical results in a FORTRAN-95 code, which can be easily used with any phase space generator. As we shall see the implementation part is a non-trivial task.

In any Monte Carlo program, the matrix elements are numerically evaluated over the phase space regions until the desired accuracy is achieved. Of course, the number of phase space points needed depends on the accuracy demanded for phenomenological studies. It is thus essential to efficiently implement the huge analytical results, such that the time spent during the numerical runs in the computer algebra part is minimal. This means that the analytical results need to be simplified and then optimized in a way that helps to achieve the desired ease during numerical evaluations. It is known that compiler level optimizations can help to minimize program execution time. We have used the optimization routines implemented in FORM [448] to proceed with our numerical implementations of the analytical results. It uses Horner schemes along with Monte-Carlo tree search [449] to optimize the analytical results. It has multiple optimization settings from which a user can choose. At NLO we have optimized the results using the highest setting (O4) and present our results, in electronic form, up to $\mathcal{O}(\epsilon^4)$. At NNLO, for S_{ggg}, at $\mathcal{O}(\epsilon^0)$, the O4 optimization in FORM takes $\sim$ 20 min, O3 takes $\sim$ 1.5 hours and O2 takes $\sim$ 10 min. For $S_{q\bar{q}g}$ the $\mathcal{O}(\epsilon^0)$ result takes $\sim$ 35 min to optimize, at O4 setting. At $\mathcal{O}(\epsilon)$ along with O4 optimization , S_{ggg} takes $\sim$ 5 hours while $S_{q\bar{q}g}$ takes $\sim$ 4 hours to produce an optimized result. For $\mathcal{O}(\epsilon^2)$ the analytical expression grows more in size. Also, the number of GPLs that arise in this order increases almost 4 times that of the previous order. In addition we get GPLs of higher weights, as compared to the previous orders. These factors complicate the optimization process. Finally, we got the optimized result (using O4) in $\sim$ 16 hours. After the optimizations, compiling all the two-loop Fortran files takes $\sim$ 10 min on a 3.2 GHz computer, with 32 CPUs and 64 GB RAM. All of the above optimization programs were run with the threaded version of FORM [450].

With the optimized results implemented in FORTRAN-95, we shall now discuss about our numerical implementation. To evaluate the GPLs we have used handyG [396]. To see the behaviour of our matrix elements in different phase space regions, we consider the following cases:

$$\begin{aligned}&\mathrm{I}: 0.1 < y < 1 - z \;\&\&\; 0.1 < z < 1\\&\mathrm{II}: y \leq 10^{-4} \;\&\&\; z \leq 10^{-3}\end{aligned} \tag{6.35}$$

At NLO, for S_{ggg}, the $\mathcal{O}(\epsilon^0)$ and $\mathcal{O}(\epsilon^1)$, matrix element takes ~ 100 μs to run, per phase point. At $\mathcal{O}(\epsilon^2)$, $\mathcal{O}(\epsilon^3)$ and $\mathcal{O}(\epsilon^4)$, the time this matrix element takes to run per phase space point are 1 ms, 100 ms and 1 s respectively. At NNLO, we present our findings in Table 6.1.

Order \ Matrix elements	S_{ggg}	$S_{q\bar{q}g}$
$\mathcal{O}(\epsilon^0)_{\mathrm{I}}$	5 ms	5 ms
$\mathcal{O}(\epsilon^1)_{\mathrm{I}}$	150 ms	170 ms
$\mathcal{O}(\epsilon^2)_{\mathrm{I}}$	22.0 s	25.3 s
$\mathcal{O}(\epsilon^0)_{\mathrm{II}}$	6 ms	6 ms
$\mathcal{O}(\epsilon^1)_{\mathrm{II}}$	180 ms	200 ms
$\mathcal{O}(\epsilon^2)_{\mathrm{II}}$	18.2 s	20.2 s

TABLE 6.1: Approximate CPU user-time needed to run the optimized matrix elements at two loop-level for one phase space point.

We observe that at NNLO, the time $S_{q\bar{q}g}/S_{ggg}$ takes to run per phase space point is the same for cases I and II. Also, the time of running, per phase space point, for $S_{q\bar{q}g}$ is almost the same as S_{ggg}. In addition, we notice that the time of execution of the matrix elements for $\mathcal{O}(\epsilon^3)$, at NLO is almost the same as $\mathcal{O}(\epsilon^1)$ at NNLO. However, the $\mathcal{O}(\epsilon^2)$ result at NNLO takes ~ 20 times more time to run per phase space point, compared to the $\mathcal{O}(\epsilon^4)$ matrix elements at NLO. Finally, we provide all the numerical routines in the form of ancillary files [451].

In Fig. 6.2 - 6.7, we present the variation of the real part for the two-loop amplitudes at different orders in ϵ. We also observe that the $\mathcal{O}(\epsilon^2)$ contribution for S_{ggg} is about 100 times large compared to $S_{q\bar{q}g}$.

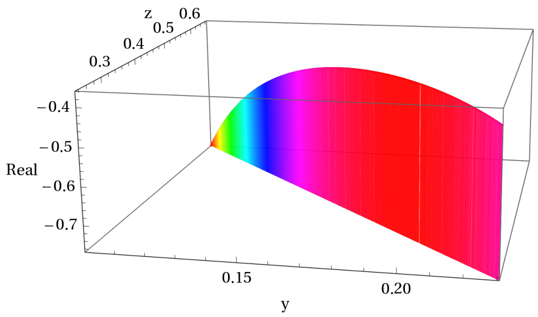

FIGURE 6.2: Real part of $\mathcal{O}(\epsilon^0)_{\rm I}$ for the process S_{ggg}

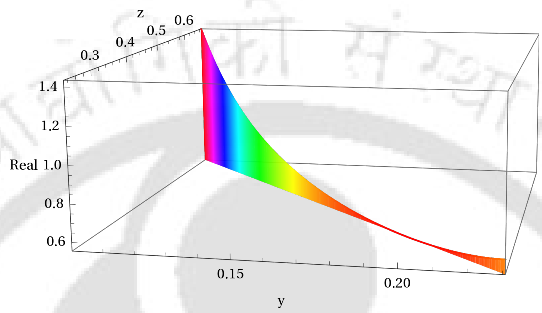

FIGURE 6.3: Real part of $\mathcal{O}(\epsilon^1)_{\rm I}$ for the process S_{ggg}

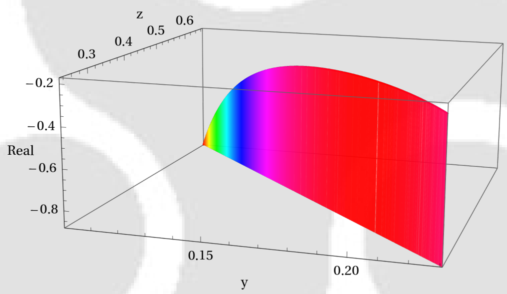

FIGURE 6.4: Real part of $\mathcal{O}(\epsilon^2)_{\rm I}$ for the process S_{ggg}

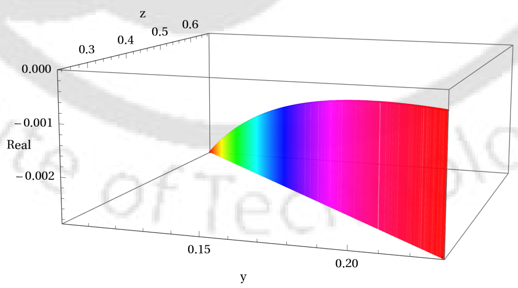

FIGURE 6.5: Real part of $\mathcal{O}(\epsilon^0)_{\rm I}$ for the process $S_{q\bar{q}g}$

6.8 Summary

In this chapter, we have analytically computed for the first time the matrix elements for the decay of a pseudo-scalar Higgs boson to ggg and $q\bar{q}g$, which contribute beyond

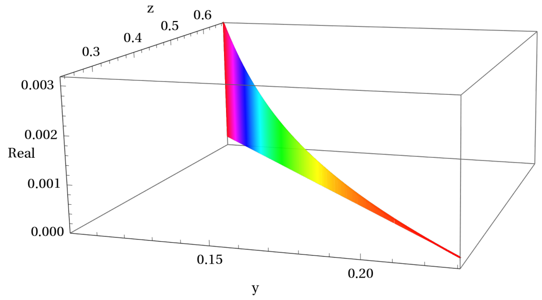

FIGURE 6.6: Real part of $\mathcal{O}(\epsilon^1)_{\rm I}$ for the process $S_{q\bar{q}g}$

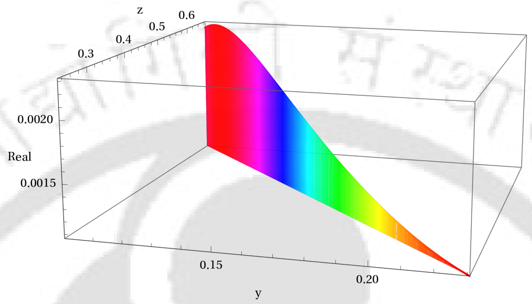

FIGURE 6.7: Real part of $\mathcal{O}(\epsilon^2)_{\rm I}$ for the process $S_{q\bar{q}g}$

NNLO in QCD. Precisely we computed $\mathcal{O}(\epsilon^3)$ and $\mathcal{O}(\epsilon^4)$ at NLO and $\mathcal{O}(\epsilon^1)$ and $\mathcal{O}(\epsilon^2)$ amplitudes at NNLO, which contributes to a full three loop cross section for the processes under consideration. We have obtained these amplitudes by working in an effective theory with the heavy quark integrated out. The proper definition of γ_5 is essential in $d > 4$ dimensions, and this fails to satisfy the Ward identity. In order to get back the renormalization invariance of the singlet axial current, a finite renormalization is needed. Using the renormalization constants Z_{GG}, Z_{GJ}, Z_{JJ}, we have obtained the $\mathcal{O}(\epsilon^1)$ and $\mathcal{O}(\epsilon^2)$ contributions at NNLO. We have checked our computation with the IR predictions from Catani [429], and found perfect agreement. In order to check our IR poles to the one from [174], we have analytically mapped the HPLs to GPLs, the resulting identities we have presented in this chapter. We have hugely simplified the analytical results with our in-house codes, which later helped for our numerical implementation. We have also checked our results at $\mathcal{O}(\epsilon^0)$ with NNLO results calculated in [174] and found perfect agreement. Keeping in mind that these amplitudes can form a part of some Monte Carlo codes, we have presented the numerical implementation of them, in FORTRAN-95 routines. In order to reduce the compilation time as well as to evaluate the amplitudes faster, we have optimised the results with FORM. The optimization of the matrix elements at different loops as well as different orders in ϵ presents different challenges, which we have discussed in detail in this chapter. We have discussed about our numerical implementation of the matrix elements, by evaluating them in different phase space regions. Our findings about the speed of evaluation per phase space points, beyond NNLO, are reported in Table 6.1. Finally, we provide the numerical implementations in FORTRAN-95 routines, which can be used with any Monte Carlo phase space generator. Our results will be important for the precise predictions of pseudo-scalar Higgs in association with a jet, beyond NNLO.

Chapter 7
Summary

The Large Hadron Collider (LHC) is the most advanced and powerful particle accelerator built to date, and offers an unique opportunity to explore the fundamental building blocks of nature. With its unprecedented centre-of-mass energy and high luminosity, the LHC enables detailed investigations of particle interactions across a broad range of kinematic regimes. As the energy frontier continues to be pushed forward, the demand for precise theoretical predictions becomes increasingly vital. Accurate theoretical calculations are essential not only to confirm the Standard Model (SM) with high confidence but also to identify any potential deviations that may signal the existence of new physics beyond the SM (BSM).

The discovery potential of the LHC relies on a synergistic relationship between high-precision measurements and equally precise theoretical predictions. Theoretical uncertainties must be reduced to match or surpass the experimental ones to enable unambiguous interpretations. This necessitates the inclusion of higher-order quantum corrections, particularly from Quantum Chromodynamics (QCD) and the electroweak sector. Among these, perturbative QCD corrections play a dominant role in most LHC processes due to the strong interaction nature of proton-proton collisions.

In this thesis, we have focused on systematically improving the precision of QCD predictions for key processes at the LHC by computing higher-order corrections and resumming dominant contributions in specific kinematic regions. These computations are not only crucial for validating the SM but also for setting stringent constraints on various BSM scenarios by comparing theory with data.

Our work covers precision studies of several processes that are phenomenologically important and theoretically rich. These include Drell-Yan production, Higgs boson production via bottom quark annihilation, VH production, ZZ production and pseudo-scalar boson decay to three partons. Here, we have gone beyond fixed-order calculations by incorporating threshold resummation techniques, which are essential when partonic processes approach their kinematic thresholds. In such regions, large logarithmic corrections can spoil the convergence of the perturbative series unless resummed to all orders.

The Drell-Yan process, in particular, has served as a cornerstone for testing QCD dynamics and searching for BSM effects due to its clean leptonic final state. We have performed precision computations up to N^{3}LO + N^{3}LL in QCD for such processes using threshold resummation techniques and exploiting the universal structure of QCD amplitudes at higher loops. Our studies extend to other processes such as VH production, ZH production in gluon fusion and ZZ production, as well as to pseudo-scalar decays to three partons, for the latter case multi-loop amplitude computations are carried out.

Overall, the results presented in this thesis contribute significantly to the ongoing effort of refining theoretical predictions at the LHC. They provide essential ingredients for experimental analyses and enhance our ability to probe the Standard Model and search for physics beyond it with greater accuracy.

In chapter 3, we have investigated the Drell-Yan (DY) process and the associated production of a Higgs boson with a vector boson (VH production) and present the invariant mass distributions for all such processes. While next-to-next-to-next-to-leading order (N^{3}LO) QCD corrections for these processes are known and demonstrate good convergence, we observed that in the region of large invariant masses—where the phase space is squeezed—threshold logarithms become prominent and can compromise the reliability of the perturbative expansion. To address this, we employed Mellin-space threshold resummation to capture and systematically resum the dominant logarithmic terms up to next-to-next-to-next-to-leading logarithmic (N^{3}LL) accuracy.

Our resummed results, when matched to fixed-order calculations, showed excellent perturbative stability. In particular, the N^{3}LL contributions to both DY and VH processes were found to be numerically small, indicating that the perturbative series is well-behaved even in the threshold region. One of the key benefits of resummation is the reduction of theoretical uncertainties, especially those associated with the arbitrary choices of renormalization and factorization scales. These unphysical scales, although necessary in intermediate steps of perturbative computations, introduce a residual ambiguity in final predictions. As expected, the magnitude of this uncertainty diminishes with increasing perturbative order.

For the Drell-Yan process at high invariant mass, the fixed-order N^{3}LO prediction exhibited a scale uncertainty of approximately 0.4%. After incorporating threshold resummation, this was further reduced to around 0.1%, highlighting the effectiveness of our resummation approach. A similar trend was observed for the VH production process, where both the invariant mass distribution and total cross-section benefited from improved precision due to resummation effects.

In addition to these processes, we extended our analysis to the Higgs boson production via bottom quark annihilation. This mode, although subdominant compared to gluon fusion, plays an important role in scenarios with enhanced bottom Yukawa couplings, such as in certain extensions of the Standard Model. For this process, we performed a full N^{3}LL threshold resummation and matched it with the available N^{3}LO fixed-order results. The inclusion of threshold-enhanced contributions led to a modest reduction in scale uncertainties—from 5.26% at N^{3}LO to 4.98% after resummation—once again underscoring the importance of all-order resummation in improving theoretical control.

Overall, the methods and results presented in this thesis provide high-precision QCD predictions that are essential for interpreting data from current and future LHC runs. They also serve as benchmarks for ongoing efforts in precision phenomenology, especially in testing the Standard Model, and search for subtle signs of new physics through deviations in high-precision observables.

The associated production of a Higgs boson with a Z boson plays a significant role in precision studies of the SM at the LHC. While the dominant mechanism for this process is the DY-like quark-antiquark annihilation channel, an additional contribution arises from the gluon-gluon fusion process via a heavy-quark loop. Although this loop-induced gluon fusion contribution formally enters at $\mathcal{O}(a_s^2)$, it is non-negligible even at leading order (LO), contributing approximately 9% to the total cross section in comparison to the DY-type channel. Its relevance becomes even more pronounced in the high invariant mass region of the ZH system, making it an essential component in precision phenomenology.

In chapter 4, we have extended the theoretical understanding of the gluon fusion channel for ZH production by performing threshold resummation of soft-gluon effects at next-to-leading logarithmic (NLL) accuracy, matched with next-to-leading order (NLO) fixed-order QCD corrections. Our analysis employs the Born-improved approach to reliably model the invariant mass distribution of the ZH system in this channel.

The fixed-order NLO corrections to the gluon fusion contribution are very large as observed for Higgs production in the gluon fusion channel. This is particularly evident in the invariant mass distribution, where corrections can reach up to 100% relative to the LO prediction. The resummation of soft-gluon logarithms further modifies this behavior, especially in the high invariant mass region. Specifically, we find that NLL resummation contributes an additional $\sim 40\%$ enhancement over the NLO result in the tail region of the distribution, indicating the growing importance of logarithmic effects at large scales.

A critical aspect of high-precision predictions is the control over theoretical uncertainties. We observe that the scale uncertainty at NLO in the high invariant mass regime, around 3000 GeV, is approximately 20%. After including the resummed soft-virtual (SV) corrections, this uncertainty is reduced to roughly 15%, demonstrating the stabilizing effect of threshold resummation and the improvement in the reliability of theoretical predictions. We further estimate the next-to-soft-virtual resummation for this subprocess at the same accuracy ($\overline{\text{NLL}}$) in the Born improved theory and present our predictions for the invariant mass distribution.

In addition to differential results, we also compute the total cross section for ZH production in the gluon fusion channel. The resummation-enhanced prediction increases the total cross-section by approximately 21% compared to the fixed-order NLO result. This sizable increase underlines the importance of including resummation effects when aiming for precision predictions at the LHC.

For completeness, we incorporate the contributions from all relevant subprocesses to the total ZH production cross section. This includes not only the DY-like quark-antiquark initiated channel but also the loop-induced gluon fusion channel with top and bottom quark loops. Our final result for the inclusive production cross section at the LHC thus reflects a comprehensive treatment of all significant QCD effects up to NLO+NLL accuracy in the gluon fusion channel, supplemented by fixed-order calculations for the DY-like and heavy-quark contributions.

In conclusion, our study highlights the phenomenological importance of the gluon fusion contribution to ZH production, particularly in the high invariant mass region where it becomes dominant. The inclusion of threshold resummation significantly improves the theoretical precision and reduces scale uncertainties. These refined predictions are essential for precision studies of the Higgs sector at the LHC and for probing possible deviations from the Standard Model.

As a final component of our investigation into threshold resummation techniques, we have analyzed the production of Z-boson pairs at the LHC. This process is an important benchmark in the electroweak sector and serves both as a signal channel and a background in many searches for new physics and Higgs boson studies. Achieving high theoretical precision for this process is thus of both practical and theoretical significance.

In chapter 5, we performed soft-gluon threshold resummation at next-to-next-to-leading logarithmic (NNLL) accuracy, matched consistently with the fixed-order QCD predictions up to next-to-next-to-leading order (NNLO) for ZZ production at LHC. The analysis focused on improving predictions for the invariant mass distribution of the ZZ production and the total production cross-section at the LHC energies.

The impact of NNLL threshold resummation becomes especially relevant in the high invariant mass regime, where logarithmically enhanced contributions from soft gluon emissions can significantly influence the perturbative series. For instance, at $Q = 1300$ GeV, the resummed prediction exhibits a 2.8% enhancement over the NNLO result for the differential cross-section. More crucially, this improvement is accompanied by a notable reduction in theoretical uncertainty. The 7-point scale variation at this value of Q reduces from 4.56% at NNLO to 3.19% at NNLO+NNLL. This highlights the improved stability of the prediction upon including higher-order logarithmic terms.

In addition to the differential distribution, we examined the total inclusive cross-section. The effect of resummation here is subtler but still relevant in the context of precision phenomenology. The NNLL corrections lead to an enhancement of approximately 0.6% compared to the NNLO value. Furthermore, the residual scale uncertainty is reduced from 2.30% at NNLO to 1.93% after incorporating NNLL resummation. These results reaffirm the utility of threshold resummation in improving both the central value and the theoretical precision of predictions, especially when small discrepancies can have a significant impact on the interpretation of experimental data.

Overall, the study of ZZ production under threshold resummation strengthens our ability to provide precision theoretical inputs for the LHC program. It complements similar investigations performed for other color-singlet final states such as Drell-Yan and Higgs production, and demonstrates the broad applicability and robustness of soft-gluon resummation in the QCD framework. The reduction in theoretical uncertainties and the consistent enhancement in cross-sections further underscore the importance of including resummation effects in precision collider phenomenology.

In addition to the resummation studies covered throughout this thesis, a significant portion of the work has been devoted to multi-loop amplitude calculations, which play a critical role in improving the precision of theoretical predictions in QCD. A particularly relevant process in this context is the decay of a pseudo-scalar Higgs boson to three partons in chapter 6. This decay channel, considered within an effective theory framework, has been studied at the two-loop level in higher power of the dimensional regulator, marking an essential step toward achieving next-to-next-to-next-leading order ($\mathrm{N^3LO}$) accuracy and laying the foundation for future three-loop computations.

The calculation of two-loop amplitudes inherently involves handling divergences that appear as poles in the dimensional regularization parameter ϵ. These singularities arise due to infrared (IR) and ultraviolet (UV) divergences typical of multi-loop integrals in gauge theories. As part of this study, we have performed the complete loop integration and provided the resulting expressions, explicitly separating the divergent terms from the finite parts. Moreover, the results include contributions beyond the finite order, namely the terms proportional to positive powers of ϵ. Such terms, though not required for NNLO cross sections directly, are indispensable for constructing finite remainders and for matching to three-loop matrix elements, which are necessary for next-to-next-to-next-to-leading order ($\mathrm{N^3LO}$) accuracy.

To facilitate the practical use of these amplitudes, we have developed a numerical implementation of our results. The scalar functions involved are computed using the `handyG` package, which allows efficient evaluation of the Goncharov polylogarithms and harmonic polylogarithms that appear in the analytic expressions. Despite the complexity and size of the two-loop amplitudes, we find that the numerical evaluation at a given phase space point is highly efficient, typically requiring only a few seconds for the coefficient of ϵ amplitudes —and at most around 20 seconds—for the coefficient of ϵ^2 amplitudes.

An additional noteworthy feature of this work is the consideration of analytic continuation and crossing symmetry. By appropriately crossing external legs in the computed amplitudes, one can obtain the corresponding results for pseudo-scalar Higgs production in association with a jet, a process of direct phenomenological relevance at the LHC. Since the three-loop virtual corrections for such processes are currently under active development, our two-loop decay amplitudes—including the positive ϵ-power terms—serve as crucial ingredients for assembling consistent and renormalized higher-order results.

Altogether, this component of the thesis makes a substantial contribution toward advancing our understanding of pseudo-scalar Higgs bosons at hadron colliders. The analytic structure of the amplitudes, along with their efficient numerical implementation, provides a valuable tool for future phenomenological studies, especially in exploring possible signals of beyond the Standard Model physics through pseudo-scalar interactions at high energies. Furthermore, the methods and computational techniques employed here can be generalized to other multi-loop processes, reinforcing the broader applicability of the framework developed in this work.

In this thesis, we have carried out a comprehensive investigation into the precision computation of observables relevant to hadron collider phenomenology within the framework of perturbative QCD. Our focus has been directed toward processes that play a central role in testing the SM and probing scenarios beyond it, using both fixed-order calculations and resummation techniques.

One of the key achievements of this work is the advancement of theoretical predictions to a level of precision that supports high-accuracy studies at the LHC and complements ongoing experimental efforts. For the processes studied, including Drell-Yan production, Higgs boson production in association with a vector boson, Z-boson pair and pseudo-scalar decays, we have obtained results with theoretical uncertainties reduced to the sub-percent level, reaching accuracies up to 0.1%. These predictions represent the most precise QCD results currently available for these channels and are expected to significantly contribute to ongoing and future analyses of LHC data.

We have also computed the uncertainties arising from the parton distribution functions (PDFs), which encode non-perturbative aspects of proton structure. By exploring the interplay between different sources of theoretical uncertainty, we have provided a reliable estimate of our predictions. In this thesis, we have also discussed the impact of parton distribution function (PDF) uncertainties on precision predictions. While the theoretical uncertainties arising from factorization and renormalization scale variations are well under control—typically at the level of 0.1% for Drell-Yan-type processes—the uncertainties associated with PDFs remain significantly larger, particularly in the high invariant mass region where they can reach up to 10%. To reduce these PDF-induced uncertainties, it is essential to incorporate more data with higher statistics in the high invariant mass region, which will help constrain the PDFs more precisely and improve the reliability of theoretical predictions in this kinematic domain.

The computed pseudo-scalar decay amplitude presented in this work provides a valuable ingredient for phenomenological studies. It can be used to investigate pseudo-scalar Higgs boson production in association with jets at hadron colliders, enabling more precise predictions and a deeper understanding of beyond the Standard Model scenarios. In this context, we performed precise multi-loop computations relevant for decay and production processes. The amplitudes obtained include terms beyond the finite part in dimensional regularization, which are essential for matching to three-loop results. These high-precision results can be used to place stringent bounds on model parameters in various BSM scenarios, especially those involving extended Higgs sectors such as the Two-Higgs-Doublet Model (2HDM) or supersymmetric frameworks.

To conclude, the results and methods developed in this thesis represent a meaningful contribution to precision collider phenomenology. They enhance our ability to perform rigorous tests of the Standard Model and to search for new physics through high-precision observables. As both theoretical and experimental tools evolve, the approaches undertaken here will remain essential in interpreting data from current and next-generation particle colliders.

Appendix A

Phase space and Distribution Coefficients

A.1 Phase Space for Invariant mass Observable

In high-energy particle collisions, computing the total or differential cross-section for final-state particles requires integrating over the available phase space. The phase space element encodes the kinematically allowed configurations of final-state momenta, subject to energy-momentum conservation. For processes involving two or three particles in the final state, the phase space can be expressed in a Lorentz-invariant form and systematically reduced by suitable variable transformations.

Two body kinematics to invariant mass distribution

For a two-body final state, the phase space is relatively simple and is completely determined by the masses of the initial and final particles. The total cross section for two-body final states can be written as,

$$\begin{aligned}\sigma_{total} &= \frac{1}{64\pi^2 \hat{s}^2} \int dx_2 \int dx_1 \int d(cos\theta) \int d\phi \;\; |\mathcal{M}|^2 \;\; \delta(x_1 x_2 - \tau) \\ &= \frac{1}{32\pi \hat{s}^2} \int dx_2 \;\; \frac{d\sigma}{dx_2}\end{aligned} \tag{A.1}$$

Two body kinematics cases partonic ($\hat{s}$) and hadronic center of mass energy (S) can be written as,

$$\begin{aligned}\hat{s} &= x_1 x_2 S = Q^2 \\ dx_2 &= \frac{2Q}{x_1 S} dQ\end{aligned} \tag{A.2}$$

Now, the invariant mass (Q) differential distribution can be written differential expression of x_2,

$$\frac{d\sigma}{dQ} = \frac{2Q}{x_1 S} \frac{d\sigma}{dx_2} \tag{A.3}$$

Now total cross section can be written as,

$$\begin{aligned}\sigma_{total} &= \frac{1}{32\pi\hat{s}^2}\int dQ\frac{d\sigma}{dQ} \\ &= \frac{1}{32\pi\hat{s}^2}\int dQ\frac{d\sigma}{dx_2}\frac{2Q}{x_1 S}\end{aligned} \tag{A.4}$$

Now the invariant mass distribution can be written as,

$$\begin{aligned}\frac{d\sigma_{total}}{dQ} &= \frac{1}{32\pi\hat{s}^2}\frac{d\sigma}{dx_2}\frac{2Q}{x_1 S} \\ &= \frac{1}{32\pi\hat{s}^2}\int dx_1\frac{2Q}{x_1 S}\int d(cos\theta)\ \ |\mathcal{M}|^2\ \ \delta(x_1x_2-\tau)\end{aligned} \tag{A.5}$$

Three body kinematics to invariant mass distribution

In contrast, for three-body final states, the phase space becomes richer and more complex, typically involving five independent kinematic variables. The 3-body phase space production cross section can be written as,

$$\begin{aligned}\sigma_{total} &= \int dE_5\int ds_{34}\int ds_{45}\int d\theta\int d\phi\ \ |\mathcal{M}|^2 \\ &= \int dE_5\ \ \frac{d\sigma}{dE_5}\end{aligned} \tag{A.6}$$

Here, we consider two particles colide with momentum p_1 and p_2 and three-body particles produces with momentum p_3, p_4 and p_5. The invariant quantities are $s_{34} = (p_3+p_4)^2$ and $s_{45} = (p_4+p_5)^2$. From the three-body final state kinematics, if the mass of the third particle has mass m_5 then we can write from the four-momentum conservation,

$$\begin{aligned}E_5 &= \frac{\hat{s}-Q^2+m_5^2}{2\sqrt{\hat{s}}} \\ |dE_5| &= \frac{Q}{\sqrt{\hat{s}}}dQ\end{aligned} \tag{A.7}$$

Here E_5 energy of the third particle in the centre of mass frame. For specific x_1 and x_2, $\hat{s}$ is fixed only Q and E_5 will change. Then we can write,

$$\begin{aligned}\frac{d\sigma}{dE_5} &= \frac{d\sigma}{dQ}\frac{dQ}{dE_5} \\ &= \frac{\sqrt{\hat{s}}}{Q}\frac{d\sigma}{dQ}\end{aligned} \tag{A.8}$$

Instead of integrating over the entire phase space, we can make this invariant mass distribution by removing one integration of E_5 and converting it to an invariant mass distribution. We have to multiply the corresponding conversion factor. It will give better results and Monte-Carlo error with fewer Vegas points.

$$
\begin{aligned}
\sigma_{total} &= \int dQ \ \frac{d\sigma}{dQ} \\
&= \int dQ \ \frac{Q}{\sqrt{\hat{s}}} \frac{d\sigma}{dE_5}
\end{aligned}
\tag{A.9}
$$

Now the invariant mass distribution for three-body case can be written as,

$$
\begin{aligned}
\frac{d\sigma_{total}}{dQ} &= \frac{Q}{\sqrt{\hat{s}}} \frac{d\sigma}{dE_5} \\
&= \frac{Q}{\sqrt{\hat{s}}} \int ds_{34} \int ds_{45} \int d\theta \int d\phi \ \ |\mathcal{M}|^2
\end{aligned}
\tag{A.10}
$$

A.2 Soft distribution Coefficient

The coefficients $\mathcal{K}^{I,(k)}$ in Eq. (2.48) are given below,

$$
\begin{aligned}
\mathcal{K}^{I,1}(\epsilon) &= \frac{1}{\epsilon}\Bigg(- 2A_1^I\Bigg) \\
\mathcal{K}^{I,2}(\epsilon) &= \frac{1}{\epsilon^2}\Bigg(2\beta_0 A_1^I\Bigg) + \frac{1}{\epsilon}\Bigg(- A_2^I\Bigg) \\
\mathcal{K}^{I,3}(\epsilon) &= \frac{1}{\epsilon^3}\Bigg(- \frac{8}{3}\beta_0^2 A_1^I\Bigg) + \frac{1}{\epsilon^2}\Bigg(\frac{2}{3}\beta_1 A_1^I + \frac{8}{3}\beta_0 A_2^I\Bigg) + \frac{1}{\epsilon}\Bigg(- \frac{2}{3}A_3^I\Bigg) \\
\mathcal{K}^{I,4}(\epsilon) &= \frac{1}{\epsilon^4}\Bigg(4\beta_0^3 A_1^I\Bigg) + \frac{1}{\epsilon^3}\Bigg(- \frac{8}{3}\beta_0\beta_1 A_1^I - 6\beta_0^2 A_2^I\Bigg) \\
&\quad + \frac{1}{\epsilon^2}\Bigg(\frac{1}{3}\beta_2 A_1^I + \beta_1 A_2^I + 3\beta_0 A_3^I\Bigg) + \frac{1}{\epsilon}\Bigg(- \frac{1}{2}A_4^I\Bigg)
\end{aligned}
\tag{A.11}
$$

The bare form factor coefficients $\hat{\mathcal{L}}_{\mathcal{F}}^{I,(k)}$ in Eq. (2.52) are given below

$$
\begin{aligned}
\hat{\mathcal{L}}_{\mathcal{F}}^{I,(1)} &= \frac{1}{\epsilon^2}\Bigg(- 2A_1^I\Bigg) + \frac{1}{\epsilon}\Bigg(\mathcal{G}_1^I(\epsilon)\Bigg) \\
\hat{\mathcal{L}}_{\mathcal{F}}^{I,(2)} &= \frac{1}{\epsilon^3}\Bigg(\beta_0 A_1^I\Bigg) + \frac{1}{\epsilon^2}\Bigg(- \frac{1}{2}A_2^I - \beta_0\mathcal{G}_1^I(\epsilon)\Bigg) + \frac{1}{2\epsilon}\mathcal{G}_2^I(\epsilon) \\
\hat{\mathcal{L}}_{\mathcal{F}}^{I,(3)} &= \frac{1}{\epsilon^4}\Bigg(- \frac{8}{9}\beta_0^2 A_1^I\Bigg) + \frac{1}{\epsilon^3}\Bigg(\frac{2}{9}\beta_1 A_1^I + \frac{8}{9}\beta_0 A_2^I + \frac{4}{3}\beta_0^2\mathcal{G}_1^I(\epsilon)\Bigg)
\end{aligned}
$$

$$+\frac{1}{\epsilon^2}\Bigg(-\frac{2}{9}A_3^I-\frac{1}{3}\beta_1\mathcal{G}_1^I(\epsilon)-\frac{4}{3}\beta_0\mathcal{G}_2^I(\epsilon)\Bigg)+\frac{1}{\epsilon}\Bigg(\frac{1}{3}\mathcal{G}_3^I(\epsilon)\Bigg)$$

$$\hat{\mathcal{L}}_{\mathcal{F}}^{I,(4)}=\frac{1}{\epsilon^5}\Bigg(\beta_0^3A_1^I\Bigg)+\frac{1}{\epsilon^4}\Bigg(-\frac{2}{3}\beta_0\beta_1A_1^I-\frac{3}{2}\beta_0^2A_2^I-2\beta_0^3\mathcal{G}_1^I(\epsilon)\Bigg)$$

$$+\frac{1}{\epsilon^3}\Bigg(\frac{1}{12}\beta_2A_1^I+\frac{1}{4}\beta_1A_2^I+\frac{3}{4}\beta_0A_3^I+\frac{4}{3}\beta_0\beta_1\mathcal{G}_1^I(\epsilon)+3\beta_0^2\mathcal{G}_2^I(\epsilon)\Bigg)$$

$$+\frac{1}{\epsilon^2}\Bigg(-\frac{1}{8}A_4^I-\frac{1}{6}\beta_2\mathcal{G}_1^I(\epsilon)-\frac{1}{2}\beta_1\mathcal{G}_2^I(\epsilon)-\frac{3}{2}\beta_0\mathcal{G}_3^I(\epsilon)\Bigg)+\frac{1}{\epsilon}\Bigg(\frac{1}{4}\mathcal{G}_4^I(\epsilon)\Bigg) \tag{A.12}$$

The explicit expression of the universal kernels in Eq. (2.59) are given below

$$\Gamma_I^{(1)}(z,\epsilon)=\frac{1}{\epsilon}P_I^{(0)}(z)$$

$$\Gamma_I^{(2)}(z,\epsilon)=\frac{1}{\epsilon^2}\Bigg(\frac{1}{2}P_I^{(0)}(z)\otimes P_I^{(0)}(z)-\beta_0P_I^{(0)}(z)\Bigg)+\frac{1}{\epsilon}\Bigg(\frac{1}{2}P_I^{(1)}(z)\Bigg)$$

$$\Gamma_I^{(3)}(z,\epsilon)=\frac{1}{\epsilon^3}\Bigg(\frac{4}{3}\beta_0^2P_I^{(0)}(z)-\beta_0P_I^{(0)}(z)\otimes P_I^{(0)}(z)$$

$$+\frac{1}{6}P_I^{(0)}(z)\otimes P_I^{(0)}(z)\otimes P_I^{(0)}(z)\Bigg)+\frac{1}{\epsilon^2}\Bigg(\frac{1}{2}P_I^{(0)}(z)\otimes P_I^{(1)}(z)$$

$$-\frac{1}{3}\beta_1P_I^{(0)}(z)-\frac{4}{3}\beta_0P_I^{(1)}(z)\Bigg)+\frac{1}{\epsilon}\Bigg(\frac{1}{3}P_I^{(2)}(z)\Bigg)$$

$$\Gamma_I^{(4)}(z,\epsilon)=\frac{1}{\epsilon^4}\Bigg(\frac{1}{24}P_I^{(0)}(z)\otimes P_I^{(0)}(z)\otimes P_I^{(0)}(z)\otimes P_I^{(0)}(z)$$

$$-\frac{1}{2}\beta_0P_I^{(0)}(z)\otimes P_I^{(0)}(z)\otimes P_I^{(0)}(z)+\frac{11}{6}\beta_0^2P_I^{(0)}(z)\otimes P_I^{(0)}(z)-2\beta_0^3P_I^{(0)}(z)\Bigg)$$

$$+\frac{1}{\epsilon^3}\Bigg(\frac{1}{4}P_I^{(0)}(z)\otimes P_I^{(0)}(z)\otimes P_I^{(1)}(z)-\frac{1}{3}\beta_1P_I^{(0)}(z)\otimes P_I^{(0)}(z)$$

$$-\frac{11}{6}\beta_0P_I^{(0)}(z)P_I^{(1)}(z)+\frac{4}{3}\beta_0\beta_1P_I^{(0)}(z)+3\beta_0^2P_I^{(1)}(z)\Bigg)$$

$$+\frac{1}{\epsilon^2}\Bigg(\frac{1}{3}P_I^{(0)}(z)\otimes P_I^{(2)}(z)+\frac{1}{8}P_I^{(1)}(z)\otimes P_I^{(1)}(z)-\frac{1}{6}\beta_2 P_I^{(0)}(z)$$

$$-\frac{1}{2}\beta_1 P_I^{(1)}(z)-\frac{3}{2}\beta_0 P_I^{(2)}(z)\Bigg)+\frac{1}{\epsilon}\Bigg(\frac{1}{4}P_I^{(3)}(z)\Bigg) \tag{A.13}$$

The explicit expression of the universal soft functions $\hat{\phi}^{I,(k)}$ in Eq. (2.71) are given below

$$\begin{aligned}
\hat{\phi}^{I,(1)} &= \frac{1}{\epsilon^2}\Bigg(2A_1^I\Bigg)+\frac{1}{\epsilon}\Bigg(\overline{\mathcal{G}}_1^I(\epsilon)\Bigg)\\
\hat{\phi}^{I,(2)} &= \frac{1}{\epsilon^3}\Bigg(-\beta_0 A_1^I\Bigg)+\frac{1}{\epsilon^2}\Bigg(\frac{1}{2}A_2^I-\beta_0\overline{\mathcal{G}}_1^I(\epsilon)\Bigg)+\frac{1}{2\epsilon}\overline{\mathcal{G}}_2^I(\epsilon)\\
\hat{\phi}^{I,(3)} &= \frac{1}{\epsilon^4}\Bigg(\frac{8}{9}\beta_0^2 A_1^I\Bigg)+\frac{1}{\epsilon^3}\Bigg(-\frac{2}{9}\beta_1 A_1^I-\frac{8}{9}\beta_0 A_2^I+\frac{4}{3}\beta_0^2\overline{\mathcal{G}}_1^I(\epsilon)\Bigg)\\
&\quad+\frac{1}{\epsilon^2}\Bigg(\frac{2}{9}A_3^I-\frac{1}{3}\beta_1\overline{\mathcal{G}}_1^I(\epsilon)-\frac{4}{3}\beta_0\overline{\mathcal{G}}_2^I(\epsilon)\Bigg)+\frac{1}{\epsilon}\Bigg(\frac{1}{3}\overline{\mathcal{G}}_3^I(\epsilon)\Bigg)\\
\hat{\phi}^{I,(4)} &= \frac{1}{\epsilon^5}\Bigg(-\beta_0^3 A_1^I\Bigg)+\frac{1}{\epsilon^4}\Bigg(\frac{2}{3}\beta_0\beta_1 A_1^I+\frac{3}{2}\beta_0^2 A_2^I-2\beta_0^3\overline{\mathcal{G}}_1^I(\epsilon)\Bigg)\\
&\quad+\frac{1}{\epsilon^3}\Bigg(-\frac{1}{12}\beta_2 A_1^I-\frac{1}{4}\beta_1 A_2^I-\frac{3}{4}\beta_0 A_3^I+\frac{4}{3}\beta_0\beta_1\overline{\mathcal{G}}_1^I(\epsilon)+3\beta_0^2\overline{\mathcal{G}}_2^I(\epsilon)\Bigg)\\
&\quad+\frac{1}{\epsilon^2}\Bigg(\frac{1}{8}A_4^I-\frac{1}{6}\beta_2\overline{\mathcal{G}}_1^I(\epsilon)-\frac{1}{2}\beta_1\overline{\mathcal{G}}_2^I(\epsilon)-\frac{3}{2}\beta_0\overline{\mathcal{G}}_3^I(\epsilon)\Bigg)+\frac{1}{\epsilon}\Bigg(\frac{1}{4}\overline{\mathcal{G}}_4^I(\epsilon)\Bigg)
\end{aligned} \tag{A.14}$$

The explicit expression of the coefficients $\overline{\mathcal{G}}_k^{I,(j)}$ in Eq. (2.72) are given below

$$\begin{aligned}
&\overline{\mathcal{G}}_1^{I,(1)} = C_I\left\{-3\zeta_2\right\},\\
&\overline{\mathcal{G}}_1^{I,(2)} = C_I\left\{\frac{7}{3}\zeta_3\right\},\\
&\overline{\mathcal{G}}_1^{I,(3)} = C_I\left\{-\frac{3}{16}\zeta_2^2\right\},\\
&\overline{\mathcal{G}}_2^{I,(1)} = C_I n_f\left\{-\frac{328}{81}+\frac{70}{9}\zeta_2+\frac{32}{3}\zeta_3\right\}+C_I C_A\left\{\frac{2428}{81}-\frac{469}{9}\zeta_2+4\zeta_2^2-\frac{176}{3}\zeta_3\right\},\\
&\overline{\mathcal{G}}_2^{I,(2)} = C_I C_A\left\{\frac{11}{40}\zeta_2^2-\frac{203}{3}\zeta_2\zeta_3+\frac{1414}{27}\zeta_2+\frac{2077}{27}\zeta_3+43\zeta_5-\frac{7288}{243}\right\}\\
&\qquad+C_I n_f\left\{-\frac{1}{20}\zeta_2^2-\frac{196}{27}\zeta_2-\frac{310}{27}\zeta_3+\frac{976}{243}\right\},
\end{aligned}$$

$$
\begin{aligned}
\overline{\mathcal{G}}_3^{I,(1)} = {} & C_I C_A^2 \left\{ \frac{152}{63}\zeta_3^2 + \frac{1964}{9}\zeta_2^2 + \frac{11000}{9}\zeta_2\zeta_3 - \frac{765127}{486}\zeta_2 + \frac{536}{3}\zeta_3^2 - \frac{59648}{27}\zeta_3 - \frac{1430}{3}\zeta_5 + \frac{7135981}{8748} \right\} \\
& + C_I C_A n_f \left\{ -\frac{532}{9}\zeta_2^2 - \frac{1208}{9}\zeta_2\zeta_3 + \frac{105059}{243}\zeta_2 + \frac{45956}{81}\zeta_3 + \frac{148}{3}\zeta_5 - \frac{716509}{4374} \right\} \\
& + C_I C_F n_f \left\{ \frac{152}{15}\zeta_2^2 - 88\zeta_2\zeta_3 + \frac{605}{6}\zeta_2 + \frac{2536}{27}\zeta_3 + \frac{112}{3}\zeta_5 - \frac{42727}{324} \right\} \\
& + C_I n_f^2 \left\{ \frac{32}{9}\zeta_2^2 - \frac{1996}{81}\zeta_2 - \frac{2720}{81}\zeta_3 + \frac{11584}{2187} \right\}. \qquad \text{(A.15)}
\end{aligned}
$$

where $C_I = C_F$ for $I = q(\mathrm{DY})$ and $C_I = C_A$ for $I = g(\mathrm{Higgs})$.

The explicit expression of the coefficients $\overline{g}_k^{I,(j)}$ in Eq. (2.74) are given below

$$
\begin{aligned}
\overline{g}_1^{I,1} = {} & C_I \Bigg(8\mathcal{D}_1 - 3\zeta_2\delta(1-z) \Bigg) \\
\overline{g}_1^{I,2} = {} & C_I \Bigg(-3\zeta_2\mathcal{D}_0 + 4\mathcal{D}_2 + \frac{7}{3}\zeta_3\delta(1-z) \Bigg) \\
\overline{g}_1^{I,3} = {} & C_I \Bigg(\frac{7}{3}\zeta_3\mathcal{D}_0 - 3\zeta_2\mathcal{D}_1 + \frac{4}{3}\mathcal{D}_3 - \frac{3}{16}\zeta_2^2\delta(1-z) \Bigg) \\
\overline{g}_2^{I,1} = {} & C_I C_A \Bigg(\Bigg(-\frac{1616}{27} + \frac{242}{3}\zeta_2 + 56\zeta_3 \Bigg)\mathcal{D}_0 + \Bigg(\frac{1072}{9} - 32\zeta_2 \Bigg)\mathcal{D}_1 + \Big(-88 \Big)\mathcal{D}_2 \\
& + \Bigg(\frac{2428}{81} - \frac{469}{9}\zeta_2 + 4\zeta_2^2 - \frac{176}{3}\zeta_3 \Bigg)\delta(1-z) \Bigg) + C_I n_f \Bigg(\Bigg(\frac{224}{27} - \frac{44}{3}\zeta_2 \Bigg)\mathcal{D}_0 \\
& + \Bigg(-\frac{160}{9} \Bigg)\mathcal{D}_1 + 16\mathcal{D}_2 + \Bigg(-\frac{328}{81} + \frac{70}{9}\zeta_2 + \frac{32}{3}\zeta_3 \Bigg)\delta(1-z) \Bigg) \Bigg) \\
\overline{g}_2^{I,2} = {} & C_I C_A \Bigg(\Bigg(\frac{4856}{81} - \frac{938}{9}\zeta_2 + 8\zeta_2^2 - \frac{1210}{9}\zeta_3 \Bigg)\mathcal{D}_0 + \Bigg(-\frac{3232}{27} + \frac{550}{3}\zeta_2 + 112\zeta_3 \Bigg)\mathcal{D}_1 \\
& + \Bigg(\frac{1072}{9} - 32\zeta_2 \Bigg)\mathcal{D}_2 + \Bigg(-\frac{616}{9} \Bigg)\mathcal{D}_3 \Bigg) + C_I n_f \Bigg(\Bigg(-\frac{656}{81} + \frac{140}{9}\zeta_2 + \frac{220}{9}\zeta_3 \Bigg)\mathcal{D}_0 \\
& + \Bigg(\frac{448}{27} - \frac{100}{3}\zeta_2 \Bigg)\mathcal{D}_1 + \Bigg(-\frac{160}{9} \Bigg)\mathcal{D}_2 + \Bigg(\frac{112}{9} \Bigg)\mathcal{D}_3 \Bigg) \Bigg) \\
& + \delta(1-z) \Bigg(C_I C_A \left\{ \frac{11}{40}\zeta_2^2 - \frac{203}{3}\zeta_2\zeta_3 + \frac{1414}{27}\zeta_2 + \frac{2077}{27}\zeta_3 + 43\zeta_5 - \frac{7288}{243} \right\} \\
& + C_I n_f \left\{ -\frac{1}{20}\zeta_2^2 - \frac{196}{27}\zeta_2 - \frac{310}{27}\zeta_3 + \frac{976}{243} \right\} \Bigg) \\
\overline{g}_3^{I,1} = {} & C_I C_A^2 \Bigg(\Bigg(-\frac{403861}{243} - 176\zeta_2\zeta_3 + \frac{71584}{27}\zeta_2 - \frac{5368}{15}\zeta_2^2 + \frac{9272}{3}\zeta_3 - 576\zeta_5 \Bigg)\mathcal{D}_0 \\
& + \Bigg(\frac{257140}{81} - \frac{28696}{9}\zeta_2 + \frac{1056}{5}\zeta_2^2 - \frac{5632}{3}\zeta_3 \Bigg)\mathcal{D}_1 + \Bigg(-\frac{68752}{27} + \frac{1760}{3}\zeta_2 \Bigg)\mathcal{D}_2 \\
& + \Bigg(\frac{7744}{9} \Bigg)\mathcal{D}_3 \Bigg) + C_I C_A n_f \Bigg(\Bigg(\frac{96482}{243} - \frac{2452}{3}\zeta_2 + \frac{1264}{15}\zeta_2^2 - \frac{6536}{9}\zeta_3 \Bigg)\mathcal{D}_0
\end{aligned}
$$

$$
\begin{aligned}
&+\Bigg(-\frac{72008}{81}+\frac{9056}{9}\zeta_2+\frac{448}{3}\zeta_3\Bigg)\mathcal{D}_1+\Bigg(\frac{22400}{27}-\frac{320}{3}\zeta_2\Bigg)\mathcal{D}_2+\Bigg(-\frac{2816}{9}\Bigg)\mathcal{D}_3\Bigg)\\
&+C_I n_f^2\Bigg(\Bigg(-\frac{4480}{243}+\frac{1520}{27}\zeta_2+\frac{416}{9}\zeta_3\Bigg)\mathcal{D}_0+\Bigg(\frac{4192}{81}-\frac{736}{9}\zeta_2\Bigg)\mathcal{D}_1\\
&+\Bigg(-\frac{1600}{27}\Bigg)\mathcal{D}_2+\Bigg(\frac{256}{9}\Bigg)\mathcal{D}_3\Bigg)+C_I C_F n_f\Bigg(\Bigg(\frac{1711}{9}-60\zeta_2-\frac{96}{5}\zeta_2^2-\frac{304}{3}\zeta_3\Bigg)\mathcal{D}_0\\
&+\Bigg(-220+192\zeta_3\Bigg)\mathcal{D}_1+\Bigg(64\Bigg)\mathcal{D}_2\Bigg)\\
&+\delta(1-z)\Bigg(C_I C_A^2\Bigg\{\frac{152}{63}\zeta_3^2+\frac{1964}{9}\zeta_2^2+\frac{11000}{9}\zeta_2\zeta_3-\frac{765127}{486}\zeta_2+\frac{536}{3}\zeta_3^2-\frac{59648}{27}\zeta_3\\
&\qquad-\frac{1430}{3}\zeta_5+\frac{7135981}{8748}\Bigg\}\\
&\quad+C_I C_A n_f\Bigg\{-\frac{532}{9}\zeta_2^2-\frac{1208}{9}\zeta_2\zeta_3+\frac{105059}{243}\zeta_2+\frac{45956}{81}\zeta_3+\frac{148}{3}\zeta_5-\frac{716509}{4374}\Bigg\}\\
&\quad+C_I C_F n_f\Bigg\{\frac{152}{15}\zeta_2^2-88\zeta_2\zeta_3+\frac{605}{6}\zeta_2+\frac{2536}{27}\zeta_3+\frac{112}{3}\zeta_5-\frac{42727}{324}\Bigg\}\\
&\quad+C_I n_f^2\Bigg\{\frac{32}{9}\zeta_2^2-\frac{1996}{81}\zeta_2-\frac{2720}{81}\zeta_3+\frac{11584}{2187}\Bigg\}\Bigg)
\end{aligned}
\tag{A.16}
$$

A.3 Next-to-soft distribution Coefficients

The coefficients $\chi_L^{I,(k)}(z)$ in Eq. (2.85) in terms of coefficients $\overline{G}_{L,i}^{I,(k)}(z)$ are given below

$$
\begin{aligned}
\chi_L^{I,(1)}(z) &= 0,\\
\chi_L^{I,(2)}(z) &= -2\beta_0\overline{G}_{L,1}^{I,(1)}(z),\\
\chi_L^{I,(3)}(z) &= -2\beta_1\overline{G}_{L,1}^{I,(1)}(z)-2\beta_0\left(\overline{G}_{L,1}^{I,(2)}(z)+2\beta_0\overline{G}_{L,2}^{I,(1)}(z)\right),\\
\chi_L^{I,(4)}(z) &= -2\beta_2\overline{G}_{L,1}^{I,(1)}(z)-2\beta_1\left(\overline{G}_{L,2}^{I,(1)}(z)+4\beta_0\overline{G}_{L,1}^{I,(2)}(z)\right)\\
&\quad-2\beta_0\left(\overline{G}_{L,3}^{I,(1)}(z)+2\beta_0\overline{G}_{L,2}^{I,(2)}(z)+4\beta_0^2\overline{G}_{L,1}^{I,(3)}(z)\right).
\end{aligned}
\tag{A.17}
$$

The coefficients $\overline{G}_{L,i}^{q,(k,j)}$ for Drell-Yan type in Eq. (2.93) are given below

$$
\begin{aligned}
\overline{G}_{L,1}^{q,(1,0)} &= 4C_F,\\
\overline{G}_{L,2}^{q,(1,0)} &= 3C_F\zeta_2,\\
\overline{G}_{L,3}^{q,(1,0)} &= -C_F\left(\frac{3}{2}\zeta_2+\frac{7}{3}\right),\\
\overline{G}_{L,1}^{q,(2,0)} &= C_A C_F\left(\frac{2804}{27}-\frac{290}{3}\zeta_2-56\zeta_3\right)+C_F n_f\left(-\frac{656}{27}+\frac{44}{3}\zeta_2\right)-64C_F^2\zeta_2,
\end{aligned}
$$

$$
\begin{aligned}
\overline{G}^{q,(2,1)}_{L,1} &= 20C_F(C_A - C_F),\\
\overline{G}^{q,(2,2)}_{L,1} &= -8C_F^2.
\end{aligned}
\tag{A.18}
$$

$$
\begin{aligned}
\overline{G}^{g,(1,0)}_{L,1} &= 4C_A,\\
\overline{G}^{g,(1,0)}_{L,2} &= 3C_A\zeta_2,\\
\overline{G}^{g,(1,0)}_{L,3} &= -C_A\left(\frac{3}{2}\zeta_2 + \frac{7}{3}\right),\\
\overline{G}^{g,(2,0)}_{L,1} &= C_A^2\left(\frac{2612}{27} - \frac{482}{3}\zeta_2 - 56\zeta_3\right) + C_A n_f\left(-\frac{392}{27} + \frac{44}{3}\zeta_2\right),\\
\overline{G}^{g,(2,1)}_{L,1} &= \frac{4}{3}C_A(C_A - n_f),\\
\overline{G}^{g,(2,2)}_{L,1} &= -8C_A^2.
\end{aligned}
\tag{A.19}
$$

The coefficient $\bar{\phi}^{I,(j)}_k$ in Eq. (2.93) are given below for Drell–Yan process

$$
\begin{aligned}
\bar{\phi}^{q,(0)}_1 &= 4C_F,\\
\bar{\phi}^{q,(1)}_1 &= 0,\\
\bar{\phi}^{q,(0)}_2 &= C_F C_A\left(\frac{1402}{27} - 28\zeta_3 - \frac{112}{3}\zeta_2\right) + C_F^2\left(-32\zeta_2\right) + n_f C_F\left(-\frac{328}{27} + \frac{16}{3}\zeta_2\right),\\
\bar{\phi}^{q,(1)}_2 &= 10C_F C_A - 10C_F^2,\\
\bar{\phi}^{q,(2)}_2 &= -4C_F^2,\\
\bar{\phi}^{q,(0)}_3 &= C_F C_A^2\left(\frac{727211}{729} + 192\zeta_5 - \frac{29876}{27}\zeta_3 - \frac{82868}{81}\zeta_2 + \frac{176}{3}\zeta_2\zeta_3 + 120\zeta_2^2\right)\\
&\quad + C_F^3\left(23 + 48\zeta_3 - \frac{32}{3}\zeta_2 - \frac{448}{15}\zeta_2^2\right) + C_F^2 C_A\left(-\frac{5143}{27} - \frac{2180}{9}\zeta_3 - \frac{11584}{27}\zeta_2 + \frac{2272}{15}\zeta_2^2\right)\\
&\quad + n_f C_F C_A\left(-\frac{155902}{729} + \frac{1292}{9}\zeta_3 + \frac{26312}{81}\zeta_2 - \frac{368}{15}\zeta_2^2\right)\\
&\quad + n_f C_F^2\left(-\frac{1309}{27} - \frac{496}{3}\zeta_3 + \frac{2536}{5}\zeta_2 + \frac{32}{5}\zeta_2^2\right) + n_f^2 C_F\left(\frac{12656}{729} - \frac{160}{27}\zeta_3 + \frac{704}{27}\zeta_2\right),\\
\bar{\phi}^{q,(1)}_3 &= C_A^2 C_F\left(\frac{244}{9} + 24\zeta_3 - \frac{8}{3}\zeta_2\right) + C_F C_A^2\left(-\frac{18436}{81} + \frac{544}{3}\zeta_3 + \frac{964}{9}\zeta_2\right)\\
&\quad + C_F^3\left(-\frac{64}{3} - 64\zeta_3 + \frac{80}{3}\zeta_2\right) + C_F C_A n_f\left(-\frac{256}{9} - \frac{28}{9}\zeta_2\right)\\
&\quad + n_f C_F^2\left(-\frac{3952}{81} - \frac{160}{9}\zeta_2\right),
\end{aligned}
\tag{A.20}
$$

$$
\begin{aligned}
\bar{\phi}^{q,(2)}_3 &= C_F C_A^2\left(34 - \frac{10}{3}\zeta_2\right) + C_F^2 C_A\left(-96 + \frac{52}{3}\zeta_2\right)\\
&\quad + C_F^3\left(\frac{16}{3}\right) + C_F C_A n_f\left(-\frac{10}{3}\right) + C_F^2 n_f\left(\frac{40}{3}\right)\\
\bar{\phi}^{q,(3)}_3 &= C_F^2 C_A\left(-\frac{176}{27}\right) + n_f C_F^2\left(\frac{32}{27}\right).
\end{aligned}
\tag{A.21}
$$

Analogously, for Higgs production in gluon fusion:

$$
\begin{aligned}
\bar{\phi}_1^{g,(0)} &= 4C_A, \\
\bar{\phi}_1^{g,(1)} &= 0, \\
\bar{\phi}_2^{g,(0)} &= C_A^2\left(\frac{1306}{27} - 28\zeta_3 - \frac{208}{3}\zeta_2\right) + n_f C_A\left(-\frac{196}{27} + \frac{16}{3}\zeta_2\right), \\
\bar{\phi}_2^{g,(1)} &= C_A^2\left(\frac{2}{3}\right) + n_f C_A\left(-\frac{2}{3}\right), \\
\bar{\phi}_2^{g,(2)} &= -4C_A^2, \\
\bar{\phi}_3^{g,(0)} &= C_A^3\left(\frac{563231}{729} + 192\zeta_5 - \frac{34292}{27}\zeta_3 - \frac{113600}{81}\zeta_2 + \frac{13488}{15}\zeta_2^2 + \frac{176}{3}\zeta_2\zeta_3\right), \\
&\quad + n_f C_A^2\left(-\frac{117778}{729} + \frac{1888}{9}\zeta_3 + \frac{26780}{81}\zeta_2 - \frac{232}{15}\zeta_2^2\right) \\
&\quad + n_f C_F C_A\left(-\frac{2653}{27} + \frac{616}{9}\zeta_3 + \frac{40}{3}\zeta_2 + \frac{32}{5}\zeta_2^2\right) + n_f^2 C_A\left(\frac{1568}{729} - \frac{160}{27}\zeta_3 - \frac{152}{9}\zeta_2\right), \\
\bar{\phi}_3^{g,(1)} &= C_A^3\left(-\frac{18988}{81} + \frac{448}{3}\zeta_3 + \frac{1280}{9}\zeta_2\right) \\
&\quad + n_f C_A^2\left(\frac{1568}{81} - 8\zeta_3 - \frac{248}{9}\zeta_2\right) + n_f C_F C_A\left(4 - \frac{8}{3}\zeta_2\right) + n_f^2 C_A\left(\frac{56}{27}\right), \\
\bar{\phi}_3^{g,(2)} &= C_A^3\left(-\frac{1432}{27} + \frac{40}{3}\zeta_2\right) + C_A^2 n_f\left(-\frac{164}{27} + \frac{2}{3}\zeta_2\right) + n_f C_A^2\left(\frac{8}{27}\right), \\
\bar{\phi}_3^{g,(3)} &= C_A^3\left(-\frac{176}{27}\right) + n_f C_A^2\left(\frac{32}{27}\right).
\end{aligned}
\tag{A.22}
$$

Appendix B

Resummation Coefficient for DY-type processes

B.1 RESUMMATION COEFFICIENTS

The process-dependent $\overline{g}_0^q$ coefficients for DY-type processes defined in Eq. (2.106) and are given as (defining $L_{qr} = \ln\left(Q^2/\mu_R^2\right), L_{fr} = \ln\left(\mu_F^2/\mu_R^2\right)$),

$$\overline{g}_0^{q,(1)} = C_F\Bigg\{-16 + 16\zeta_2 + \Bigg(-6\Bigg)L_{fr} + \Bigg(6\Bigg)L_{qr}\Bigg\}, \tag{B.1}$$

$$\begin{aligned}\overline{g}_0^{q,(2)} = C_F n_f &\Bigg\{\frac{127}{6} + \frac{8}{9}\zeta_3 - \frac{64}{3}\zeta_2 + \Bigg(-\frac{34}{3} + \frac{16}{3}\zeta_2\Bigg)L_{qr} + \Bigg(\frac{2}{3} + \frac{16}{3}\zeta_2\Bigg)L_{fr} \\ &+ \Bigg(-2\Bigg)L_{fr}^2 + \Bigg(2\Bigg)L_{qr}^2\Bigg\} + C_F^2\Bigg\{\frac{511}{4} - 60\zeta_3 - 198\zeta_2 + \frac{552}{5}\zeta_2^2 + \Bigg(-93 + 48\zeta_3 \\ &+ 72\zeta_2\Bigg)L_{qr} + \Bigg(93 - 48\zeta_3 - 72\zeta_2\Bigg)L_{fr} + \Bigg(-36\Bigg)L_{qr}L_{fr} + \Bigg(18\Bigg)L_{fr}^2 \\ &+ \Bigg(18\Bigg)L_{qr}^2\Bigg\} + C_A C_F\Bigg\{-\frac{1535}{12} + \frac{604}{9}\zeta_3 + \frac{376}{3}\zeta_2 - \frac{92}{5}\zeta_2^2 + \Bigg(-\frac{17}{3} + 24\zeta_3 \\ &- \frac{88}{3}\zeta_2\Bigg)L_{fr} + \Bigg(\frac{193}{3} - 24\zeta_3 - \frac{88}{3}\zeta_2\Bigg)L_{qr} + \Bigg(-11\Bigg)L_{qr}^2 + \Bigg(11\Bigg)L_{fr}^2\Bigg\},\end{aligned} \tag{B.2}$$

$$
\begin{aligned}
\overline{g}_0^{q,(3)} = {} & C_F {n_f}^2 \Big\{ -\frac{7081}{243} + \frac{16}{81}\zeta_3 + \frac{1072}{27}\zeta_2 + \frac{448}{135}\zeta_2^2 + \Big(-\frac{68}{9} + \frac{32}{9}\zeta_2 \Big) L_{qr}^2 + \Big(-\frac{8}{9} \Big) L_{fr}^3 \\
& + \Big(\frac{4}{9} + \frac{32}{9}\zeta_2 \Big) L_{fr}^2 + \Big(\frac{8}{9} \Big) L_{qr}^3 + \Big(\frac{34}{9} + \frac{32}{9}\zeta_3 - \frac{160}{27}\zeta_2 \Big) L_{fr} + \Big(\frac{220}{9} - \frac{64}{27}\zeta_3 \\
& - \frac{608}{27}\zeta_2 \Big) L_{qr} \Big\} + C_F^2 n_f \Big\{ -\frac{421}{3} - \frac{608}{9}\zeta_5 + \frac{9448}{27}\zeta_3 + \frac{9064}{27}\zeta_2 - \frac{256}{3}\zeta_2\zeta_3 \\
& - \frac{36208}{135}\zeta_2^2 + \Big(-92 + 32\zeta_3 + 48\zeta_2 \Big) L_{qr}^2 + \Big(-\frac{275}{3} + \frac{256}{3}\zeta_3 + 40\zeta_2 \\
& + \frac{272}{5}\zeta_2^2 \Big) L_{fr} + \Big(20 - 32\zeta_3 - 48\zeta_2 \Big) L_{fr}^2 + \Big(230 - \frac{496}{3}\zeta_3 - 272\zeta_2 + \frac{464}{5}\zeta_2^2 \Big) L_{qr} \\
& + \Big(-12 \Big) L_{qr} L_{fr}^2 + \Big(-12 \Big) L_{qr}^2 L_{fr} + \Big(12 \Big) L_{fr}^3 + \Big(12 \Big) L_{qr}^3 + \Big(72 \Big) L_{qr} L_{fr} \Big\} \\
& + C_F^3 \Big\{ -\frac{5599}{6} + 1328\zeta_5 - 460\zeta_3 + 32\zeta_3^2 + \frac{2936}{3}\zeta_2 - 400\zeta_2\zeta_3 - \frac{5972}{5}\zeta_2^2 \\
& + \frac{169504}{315}\zeta_2^3 + \Big(-\frac{1495}{2} + 480\zeta_5 + 992\zeta_3 + 720\zeta_2 - 704\zeta_2\zeta_3 - \frac{1968}{5}\zeta_2^2 \Big) L_{fr} \\
& + \Big(-270 + 288\zeta_3 + 144\zeta_2 \Big) L_{fr}^2 + \Big(-270 + 288\zeta_3 + 144\zeta_2 \Big) L_{qr}^2 + \Big(540 \\
& - 576\zeta_3 - 288\zeta_2 \Big) L_{qr} L_{fr} + \Big(\frac{1495}{2} - 480\zeta_5 - 992\zeta_3 - 720\zeta_2 + 704\zeta_2\zeta_3 \\
& + \frac{1968}{5}\zeta_2^2 \Big) L_{qr} + \Big(-108 \Big) L_{qr}^2 L_{fr} + \Big(-36 \Big) L_{fr}^3 + \Big(36 \Big) L_{qr}^3 + \Big(108 \Big) L_{qr} L_{fr}^2 \Big\} \\
& + C_A C_F n_f \Big\{ \frac{110651}{243} - 8\zeta_5 - \frac{24512}{81}\zeta_3 - \frac{44540}{81}\zeta_2 + \frac{880}{9}\zeta_2\zeta_3 + \frac{1156}{135}\zeta_2^2 + \Big(\\
& - \frac{3052}{9} + \frac{3440}{27}\zeta_3 + \frac{7504}{27}\zeta_2 - \frac{344}{15}\zeta_2^2 \Big) L_{qr} + \Big(-40 - \frac{400}{9}\zeta_3 + \frac{2672}{27}\zeta_2 \\
& - \frac{8}{5}\zeta_2^2 \Big) L_{fr} + \Big(-\frac{146}{9} + 16\zeta_3 - \frac{352}{9}\zeta_2 \Big) L_{fr}^2 + \Big(-\frac{88}{9} \Big) L_{qr}^3 + \Big(\frac{88}{9} \Big) L_{fr}^3 \\
& + \Big(\frac{850}{9} - 16\zeta_3 - \frac{352}{9}\zeta_2 \Big) L_{qr}^2 \Big\} + C_A C_F^2 \Big\{ \frac{74321}{36} - \frac{5512}{9}\zeta_5 - \frac{51508}{27}\zeta_3 + \frac{592}{3}\zeta_3^2 \\
& - \frac{66544}{27}\zeta_2 + \frac{3680}{3}\zeta_2\zeta_3 + \frac{258304}{135}\zeta_2^2 - \frac{123632}{315}\zeta_2^3 + \Big(-\frac{3439}{2} + 240\zeta_5 + \frac{5368}{3}\zeta_3 \\
& + 1552\zeta_2 - 352\zeta_2\zeta_3 - \frac{2912}{5}\zeta_2^2 \Big) L_{qr} + \Big(-420 + 288\zeta_3 \Big) L_{qr} L_{fr} + \Big(-131 \\
& + 32\zeta_3 + 264\zeta_2 \Big) L_{fr}^2 + \Big(551 - 320\zeta_3 - 264\zeta_2 \Big) L_{qr}^2 + \Big(\frac{2348}{3} - 240\zeta_5 - \frac{4048}{3}\zeta_3 \\
& - 100\zeta_2 + 352\zeta_2\zeta_3 - \frac{1136}{5}\zeta_2^2 \Big) L_{fr} + \Big(-66 \Big) L_{fr}^3 + \Big(-66 \Big) L_{qr}^3 + \Big(66 \Big) L_{qr} L_{fr}^2 \\
& + \Big(66 \Big) L_{qr}^2 L_{fr} \Big\} + C_A^2 C_F \Big\{ -\frac{1505881}{972} - 204\zeta_5 + \frac{139345}{81}\zeta_3 - \frac{400}{3}\zeta_3^2 \\
& + \frac{130295}{81}\zeta_2 - \frac{7228}{9}\zeta_2\zeta_3 - \frac{23357}{135}\zeta_2^2 + \frac{7088}{63}\zeta_2^3 + \Big(-\frac{2429}{9} + 88\zeta_3 + \frac{968}{9}\zeta_2 \Big) L_{qr}^2 \\
& + \Big(-\frac{242}{9} \Big) L_{fr}^3 + \Big(\frac{242}{9} \Big) L_{qr}^3 + \Big(\frac{493}{9} - 88\zeta_3 + \frac{968}{9}\zeta_2 \Big) L_{fr}^2 + \Big(\frac{1657}{18} - 80\zeta_5 \\
& + \frac{3104}{9}\zeta_3 - \frac{8992}{27}\zeta_2 + 4\zeta_2^2 \Big) L_{fr} + \Big(\frac{3082}{3} + 80\zeta_5 - \frac{22600}{27}\zeta_3 - \frac{20720}{27}\zeta_2 \\
& + \frac{1964}{15}\zeta_2^2 \Big) L_{qr} \Big\} + N_4 n_{fv} C_F \Big\{ 8 - \frac{160}{3}\zeta_5 + \frac{28}{3}\zeta_3 + 20\zeta_2 - \frac{4}{5}\zeta_2^2 \Big\} .
\end{aligned} \tag{B.3}
$$

Here $N_4 = (n_c^2 - 4)/n_c$ and n_{fv} is proportional to the charge weighted sum of quark flavors [292].

The process-independent universal resum exponent defined in Eq. (2.107) which are used for DY-type processes are given as,

$$g_1^q = \left[\frac{A_1^q}{\beta_0}\left\{2 - 2\,\ln(1-\omega) + 2\,\ln(1-\omega)\,\omega^{-1}\right\}\right], \tag{B.4}$$

$$g_2^q = \left[\frac{D_1^q}{\beta_0}\left\{\frac{1}{2}\,\ln(1-\omega)\right\} + \frac{A_2^q}{\beta_0^2}\left\{-\ln(1-\omega) - \omega\right\} + \frac{A_1^q}{\beta_0}\left\{\left(\ln(1-\omega) + \frac{1}{2}\,\ln(1-\omega)^2 \right.\right.\right.$$
$$\left.\left.\left. + \,\omega\right)\left(\frac{\beta_1}{\beta_0^2}\right) + \left(\omega\right) L_{fr} + \left(\ln(1-\omega)\right) L_{qr}\right\}\right], \tag{B.5}$$

$$g_3^q = \left[\frac{A_3^q}{\beta_0^2}\left\{-\frac{\omega}{(1-\omega)} + \omega\right\} + \frac{A_2^q}{\beta_0}\left\{\left(2\,\frac{\omega}{(1-\omega)}\right) L_{qr} + \left(3\,\frac{\omega}{(1-\omega)} + 2\,\frac{\ln(1-\omega)}{(1-\omega)}\right.\right.\right.$$
$$\left.\left. - \,\omega\right)\left(\frac{\beta_1}{\beta_0^2}\right) + \left(-2\,\omega\right) L_{fr}\right\} + A_1^q\left\{-4\,\zeta_2\,\frac{\omega}{(1-\omega)} + \left(-\frac{\ln(1-\omega)^2}{(1-\omega)}\right.\right.$$
$$\left. - \frac{\omega}{(1-\omega)} - 2\,\frac{\ln(1-\omega)}{(1-\omega)} + 2\,\ln(1-\omega) + \omega\right)\left(\frac{\beta_1}{\beta_0^2}\right)^2 + \left(-\frac{\omega}{(1-\omega)}\right) L_{qr}^2 + \left(\right.$$
$$\left. - \frac{\omega}{(1-\omega)} - 2\,\ln(1-\omega) - \omega\right)\left(\frac{\beta_2}{\beta_0^3}\right) + \left(\left(-2\,\frac{\omega}{(1-\omega)}\right.\right.$$
$$\left.\left.\left. - \,2\,\frac{\ln(1-\omega)}{(1-\omega)}\right)\left(\frac{\beta_1}{\beta_0^2}\right)\right) L_{qr} + \left(\omega\right) L_{fr}^2\right\} + \frac{D_2^q}{\beta_0}\left\{\frac{\omega}{(1-\omega)}\right\} + D_1^q\left\{\left(\right.\right.$$
$$\left.\left.\left. - \frac{\omega}{(1-\omega)}\right) L_{qr} + \left(-\frac{\omega}{(1-\omega)} - \frac{\ln(1-\omega)}{(1-\omega)}\right)\left(\frac{\beta_1}{\beta_0^2}\right)\right\}\right], \tag{B.6}$$

$$
\begin{aligned}
g_4^q = \bigg[& \frac{A_4^q}{\beta_0^2} \bigg\{ \frac{1}{6}\, \frac{\omega(2-\omega)}{(1-\omega)^2} - \frac{1}{3}\, \omega \bigg\} + \frac{A_3^q}{\beta_0} \bigg\{ \bigg(- \frac{1}{2}\, \frac{\omega(2-\omega)}{(1-\omega)^2} \bigg)\, L_{qr} + \bigg(- \frac{5}{12}\, \frac{\omega(2-\omega)}{(1-\omega)^2} \\
& - \frac{1}{2}\, \frac{\ln(1-\omega)}{(1-\omega)^2} + \frac{1}{3}\, \omega \bigg) \bigg(\frac{\beta_1}{\beta_0^2} \bigg) + \bigg(\omega \bigg)\, L_{fr} \bigg\} + A_2^q \bigg\{ 2\, \zeta_2\, \frac{\omega(2-\omega)}{(1-\omega)^2} \\
& + \bigg(\frac{1}{2}\, \frac{\ln(1-\omega)^2}{(1-\omega)^2} - \frac{1}{12}\, \frac{\omega^2}{(1-\omega)^2} + \frac{5}{6}\, \frac{\omega}{(1-\omega)} + \frac{1}{2}\, \frac{\ln(1-\omega)}{(1-\omega)^2} - \frac{1}{3}\, \omega \bigg) \bigg(\frac{\beta_1}{\beta_0^2} \bigg)^2 \\
& + \bigg(\frac{1}{2}\, \frac{\omega(2-\omega)}{(1-\omega)^2} \bigg)\, L_{qr}^2 + \bigg(\frac{1}{3}\, \frac{\omega^2}{(1-\omega)^2} - \frac{1}{3}\, \frac{\omega}{(1-\omega)} + \frac{1}{3}\, \omega \bigg) \bigg(\frac{\beta_2}{\beta_0^3} \bigg) + \bigg(- \omega \bigg)\, L_{fr}^2 \\
& + \bigg(\bigg(\frac{1}{2}\, \frac{\omega(2-\omega)}{(1-\omega)^2} + \frac{\ln(1-\omega)}{(1-\omega)^2} \bigg) \bigg(\frac{\beta_1}{\beta_0^2} \bigg) \bigg)\, L_{qr} \bigg\} + \beta_0 A_1^q \bigg\{ \frac{8}{3}\, \zeta_3\, \frac{\omega(2-\omega)}{(1-\omega)^2} + \bigg(\\
& - \frac{1}{6}\, \frac{\ln(1-\omega)^3}{(1-\omega)^2} + \frac{1}{3}\, \frac{\omega^2}{(1-\omega)^2} - \frac{1}{3}\, \frac{\omega}{(1-\omega)} + \frac{1}{2}\, \frac{\ln(1-\omega)}{(1-\omega)^2} - \frac{\ln(1-\omega)}{(1-\omega)} \\
& + \frac{1}{2}\, \ln(1-\omega) + \frac{1}{3}\, \omega \bigg) \bigg(\frac{\beta_1}{\beta_0^2} \bigg)^3 + \bigg(- \frac{1}{6}\, \frac{\omega(2-\omega)}{(1-\omega)^2} \bigg)\, L_{qr}^3 + \bigg(\frac{1}{12}\, \frac{\omega(2-\omega)}{(1-\omega)^2} \\
& + \frac{1}{2}\, \ln(1-\omega) + \frac{1}{3}\, \omega \bigg) \bigg(\frac{\beta_3}{\beta_0^4} \bigg) + \bigg(- \frac{5}{12}\, \frac{\omega^2}{(1-\omega)^2} + \frac{1}{6}\, \frac{\omega}{(1-\omega)} - \frac{1}{2}\, \frac{\ln(1-\omega)}{(1-\omega)^2} \\
& + \frac{\ln(1-\omega)}{(1-\omega)} - \ln(1-\omega) - \frac{2}{3}\, \omega \bigg) \frac{\beta_1 \beta_2}{\beta_0^5} + \bigg(\frac{1}{3}\, \omega \bigg)\, L_{fr}^3 + \bigg(- 2\, \zeta_2\, \frac{\omega(2-\omega)}{(1-\omega)^2} + \bigg(\\
& - \frac{1}{2}\, \frac{\ln(1-\omega)^2}{(1-\omega)^2} + \frac{1}{2}\, \frac{\omega^2}{(1-\omega)^2} \bigg) \bigg(\frac{\beta_1}{\beta_0^2} \bigg)^2 + \bigg(- \frac{1}{2}\, \frac{\omega^2}{(1-\omega)^2} \bigg) \bigg(\frac{\beta_2}{\beta_0^3} \bigg) \bigg)\, L_{qr} + \bigg(\\
& - 2\, \zeta_2\, \frac{\ln(1-\omega)}{(1-\omega)^2} \bigg) \bigg(\frac{\beta_1}{\beta_0^2} \bigg) + \bigg(\bigg(- \frac{1}{2}\, \frac{\ln(1-\omega)}{(1-\omega)^2} \bigg) \bigg(\frac{\beta_1}{\beta_0^2} \bigg) \bigg)\, L_{qr}^2 + \bigg(\bigg(\\
& - \frac{1}{2}\, \omega \bigg) \bigg(\frac{\beta_1}{\beta_0^2} \bigg) \bigg)\, L_{fr}^2 \bigg\} + \frac{D_3^q}{\beta_0} \bigg\{ - \frac{1}{4}\, \frac{\omega(2-\omega)}{(1-\omega)^2} \bigg\} + D_2^q \bigg\{ \bigg(\frac{1}{4}\, \frac{\omega(2-\omega)}{(1-\omega)^2} \\
& + \frac{1}{2}\, \frac{\ln(1-\omega)}{(1-\omega)^2} \bigg) \bigg(\frac{\beta_1}{\beta_0^2} \bigg) + \bigg(\frac{1}{2}\, \frac{\omega(2-\omega)}{(1-\omega)^2} \bigg)\, L_{qr} \bigg\} + \beta_0 D_1^q \bigg\{ - \zeta_2\, \frac{\omega(2-\omega)}{(1-\omega)^2} + \bigg(\\
& - \frac{1}{4}\, \frac{\ln(1-\omega)^2}{(1-\omega)^2} + \frac{1}{4}\, \frac{\omega^2}{(1-\omega)^2} \bigg) \bigg(\frac{\beta_1}{\beta_0^2} \bigg)^2 + \bigg(- \frac{1}{4}\, \frac{\omega(2-\omega)}{(1-\omega)^2} \bigg)\, L_{qr}^2 + \bigg(\\
& - \frac{1}{4}\, \frac{\omega^2}{(1-\omega)^2} \bigg) \bigg(\frac{\beta_2}{\beta_0^3} \bigg) + \bigg(\bigg(- \frac{1}{2}\, \frac{\ln(1-\omega)}{(1-\omega)^2} \bigg) \bigg(\frac{\beta_1}{\beta_0^2} \bigg) \bigg)\, L_{qr} \bigg\} \bigg]. \qquad \text{(B.7)}
\end{aligned}
$$

Here A_i^q are the universal cusp anomalous dimensions for DY-type ($I = q$), D_i^q are the threshold noncusp anomalous dimensions for DY-type, and $\omega = 2 a_s \beta_0 \ln \overline{N}$. Note that all the perturbative quantities are expanded in powers of a_s.

B.2 Anomalous Dimensions

The cusp anomalous dimensions A_i^q are given as (with the recently known four-loops results [452–454]) ,

$$A_1^q = C_F\Big\{4\Big\}, \tag{B.8}$$

$$A_2^q = C_F\Big\{n_f\Big(-\frac{40}{9}\Big) + C_A\Big(\frac{268}{9} - 8\zeta_2\Big)\Big\}, \tag{B.9}$$

$$\begin{aligned} A_3^q = C_F\Big\{&{n_f}^2\Big(-\frac{16}{27}\Big) + C_F n_f\Big(-\frac{110}{3} + 32\zeta_3\Big) + C_A n_f\Big(-\frac{836}{27} - \frac{112}{3}\zeta_3 + \frac{160}{9}\zeta_2\Big) \\ &+ C_A^2\Big(\frac{490}{3} + \frac{88}{3}\zeta_3 - \frac{1072}{9}\zeta_2 + \frac{176}{5}\zeta_2^2\Big)\Big\}, \end{aligned} \tag{B.10}$$

$$\begin{aligned} A_4^q = C_F\Big\{&{n_f}^3\Big(-\frac{32}{81} + \frac{64}{27}\zeta_3\Big) + C_F {n_f}^2\Big(\frac{2392}{81} - \frac{640}{9}\zeta_3 + \frac{64}{5}\zeta_2^2\Big) + C_F^2 n_f\Big(\frac{572}{9} - 320\zeta_5 \\ &+ \frac{592}{3}\zeta_3\Big) + C_A {n_f}^2\Big(\frac{923}{81} + \frac{2240}{27}\zeta_3 - \frac{608}{81}\zeta_2 - \frac{224}{15}\zeta_2^2\Big) + C_A C_F n_f\Big(-\frac{34066}{81} \\ &+ 160\zeta_5 + \frac{3712}{9}\zeta_3 + \frac{440}{3}\zeta_2 - 128\zeta_2\zeta_3 - \frac{352}{5}\zeta_2^2\Big) + C_A^2 n_f\Big(-\frac{24137}{81} + \frac{2096}{9}\zeta_5 \\ &- \frac{23104}{27}\zeta_3 + \frac{20320}{81}\zeta_2 + \frac{448}{3}\zeta_2\zeta_3 - \frac{352}{15}\zeta_2^2\Big) + C_A^3\Big(\frac{84278}{81} - \frac{3608}{9}\zeta_5 + \frac{20944}{27}\zeta_3 \\ &- 16\zeta_3^2 - \frac{88400}{81}\zeta_2 - \frac{352}{3}\zeta_2\zeta_3 + \frac{3608}{5}\zeta_2^2 - \frac{20032}{105}\zeta_2^3\Big)\Big\} + \frac{d_R^{abcd}d_A^{abcd}}{N_R}\Big(\frac{3520}{3}\zeta_5 \\ &+ \frac{128}{3}\zeta_3 - 384\zeta_3^2 - 128\zeta_2 - \frac{7936}{35}\zeta_2^3\Big) + n_f\frac{d_R^{abcd}d_F^{abcd}}{N_R}\Big(-\frac{1280}{3}\zeta_5 - \frac{256}{3}\zeta_3 \\ &+ 256\zeta_2\Big). \end{aligned} \tag{B.11}$$

The quartic casimirs are given as

$$\frac{d_A^{abcd}d_A^{abcd}}{N_A} = \frac{n_c^2(n_c^2+36)}{24}, \frac{d_A^{abcd}d_F^{abcd}}{N_A} = \frac{n_c(n_c^2+6)}{48}, \tag{B.12}$$

$$\frac{d_F^{abcd}d_A^{abcd}}{N_F} = \frac{(n_c^2-1)(n_c^2+6)}{48}, \frac{d_F^{abcd}d_F^{abcd}}{N_F} = \frac{(n_c^2-1)(n_c^4-6n_c^2+18)}{96n_c^3}, \tag{B.13}$$

with $N_A = n_c^2 - 1$ and $N_F = n_c$ where $n_c = 3$ for QCD. The coefficients D_i^q are given as,

$$D_1^q = C_F \Big\{ 0 \Big\}, \tag{B.14}$$

$$D_2^q = C_F \Big\{ n_f \Big(\frac{224}{27} - \frac{32}{3}\zeta_2 \Big) + C_A \Big(-\frac{1616}{27} + 56\zeta_3 + \frac{176}{3}\zeta_2 \Big) \Big\}, \tag{B.15}$$

$$\begin{aligned} D_3^q = C_F \Big\{ & {n_f}^2 \Big(-\frac{3712}{729} + \frac{320}{27}\zeta_3 + \frac{640}{27}\zeta_2 \Big) + C_F n_f \Big(\frac{3422}{27} - \frac{608}{9}\zeta_3 - 32\zeta_2 - \frac{64}{5}\zeta_2^2 \Big) \\ & + C_A n_f \Big(\frac{125252}{729} - \frac{2480}{9}\zeta_3 - \frac{29392}{81}\zeta_2 + \frac{736}{15}\zeta_2^2 \Big) + C_A^2 \Big(-\frac{594058}{729} - 384\zeta_5 \\ & + \frac{40144}{27}\zeta_3 + \frac{98224}{81}\zeta_2 - \frac{352}{3}\zeta_2\zeta_3 - \frac{2992}{15}\zeta_2^2 \Big) \Big\}. \end{aligned} \tag{B.16}$$

Appendix C

Resummation coefficients for ZZ productions

C.1 Resummation coefficients

The process-dependent $\overline{g}_0^q$ coefficients for ZZ production, defined in Eq. (2.106) are given as (defining $L_{qr} = \ln\left(Q^2/\mu_R^2\right), L_{fr} = \ln\left(\mu_F^2/\mu_R^2\right)$),

$$\overline{g}_0^{q,(1)} = 2\mathcal{K}_{(0,1)} + 2C_F\Big\{ - 3L_{fr} + L_{qr}^2 + \zeta_2\Big\}, \tag{C.1}$$

$$\begin{aligned}\overline{g}_0^{q,(2)} &= \mathcal{K}_{(1,1)} + 2\mathcal{K}_{(0,2)} + C_F n_f\Big\{ - \frac{328}{21} + \frac{2}{3}L_{fr} + \frac{112}{27}L_{qr} - \frac{20}{9}L_{qr}^2 - \frac{10}{9}\zeta_2 + \frac{16}{3}L_{fr}\zeta_2 \\ &- \frac{4}{3}L_{qr}\zeta_2 + \frac{32}{3}\zeta_3\Big\} + C_F^2\Big\{ - 3L_{fr} + 18L_{fr}^2 - 12L_{fr}L_{qr}^2 + 2L_{qr}^4 + 12L_{fr}\zeta_2 \\ &+ 4L_{qr}^2\zeta_2 + 2{\zeta_2}^2 - 48L_{fr}\zeta_3\Big\} + C_F\Big\{ + 3\beta_0 L_{fr}^2 - \frac{2}{3}\beta_0 L_{qr}^3 - 12L_{fr}\mathcal{K}_{(0,1)} \\ &+ 4L_{qr}^2\mathcal{K}_{(0,1)} - 6b\beta_0\zeta_2 - 2\beta_0 L_{qr}\zeta_2 + 4\mathcal{K}_{(0,1)}\zeta_2 + \frac{32}{3}\beta_0\zeta_3\Big\} + C_F C_A\Big\{ + \frac{2428}{81} \\ &- \frac{17}{3}L_{fr} - \frac{808}{27}L_{qr} + \frac{134}{9}L_{qr}^2 + \frac{67}{9}\zeta_2 - \frac{88}{3}L_{fr}\zeta_2 + \frac{22}{3}L_{qr}\zeta_2 - 4L_{qr}^2\zeta_2 - 12{\zeta_2}^2 \\ &- \frac{176}{3}\zeta_3 + 24L_{fr}\zeta_3 + 28L_{qr}\zeta_3\Big\}\end{aligned} \tag{C.2}$$

Here, we define

$$\mathcal{K}_{(m,n)} = \frac{\mathcal{M}^{\text{fin}}_{(m,n)}}{\mathcal{M}_{(0,0)}} \tag{C.3}$$

where,

$$\mathcal{M}^{\text{fin}}_{(m,n)} \equiv \langle \mathcal{M}_m | \mathcal{M}_n \rangle \tag{C.4}$$

and $|\mathcal{M}_n\rangle$ represents the UV-renormalized, IR-finite virtual amplitude at the n-th order in a_s, as given in Eq. (C3) of Ref. [277]. The one loop virtual contribution for Z-boson pair production is,

$$\mathcal{M}_{(0,1)} = a_s(\mu_R^2)\frac{\Gamma(1-\epsilon)}{\Gamma(1-2\epsilon)}(4\pi)^\epsilon\left(\frac{\mu_R^2}{s}\right)^\epsilon C_F\left[-4\left\{\frac{1}{\epsilon^2}+\frac{3}{2\epsilon}\right\}\mathcal{M}_{(0,0)}+\mathcal{M}^f_{(0,1)}\right]. \tag{C.5}$$

here,

$$\begin{aligned}
\mathcal{M}^f_{(0,1)} = B_f\mathrm{N}(c_v^4+6c_v^2c_a^2+c_a^4)\left(\frac{4}{t^2u^2}\right)\Big[&2\zeta_2\big(-20m_z^2tu(t+u)-4m_z^4(t^2-8tu+u^2)\\
&+tu(5t^2+4tu+5u^2)+\frac{tu}{\kappa s(4m_z^2-s)^2}\big(-32m_z^6tu-64m_z^8(t+u)\\
&+8m_z^2tu(t+u)^2-(t+u)^3(3t^2+4tu+3u^2)\\
&+m_z^4(22t^3+82t^2u+82tu^2+22u^3)\big)\big)+\ln\left(\frac{s}{m_z^2}\right)\frac{1}{(4m_z^2-s)^2}\big(\\
&8m_z^2t^2u^2(t+u)+12m_z^8(t^2-8tu+u^2)-tu(t+u)^2(3t^2+4tu+3u^2)\\
&+4m_z^6(3t^3-5t^2u-5tu^2+3u^3)\\
&+m_z^4(3t^4+14t^3u+78t^2u^2+14tu^3+3u^4)\big)\\
&+\frac{tu}{\kappa s(4m_z^2-s)^2}\big(\ln(x)+4\mathrm{Li}_2(-x)\big)\big(-32m_z^6tu-64m_z^8(t+u)\\
&+8m_z^2tu(t+u)^2-(t+u)^3(3t^2+4tu+3u^2)\\
&+m_z^4(22t^3+82t^2u+82tu^2+22u^3)\big)+\frac{1}{(t-m_z^2)(u-m_z^2)(4m_z^2-s)}\big(\\
&18m_z^{10}(t^2-8tu+u^2)+m_z^8(-9t^3+131t^2u+131tu^2-9u^3)\\
&-7t^2u^2(t^3+t^2u+tu^2+u^3)-4m_z^4tu(4t^3+23t^2u+23tu^2+4u^3)\\
&+m_z^6(-9t^4+14t^3u-66t^2u^2)+14tu^3-9u^4)\\
&+m_z^2tu(9t^4+32t^3u+82t^2u^2+32tu^3+9u^4)+\ln\left(\frac{-t}{m_z^2}\right)\frac{u}{(t-m_z^2)^2}\big(\\
&3m_z^8(-4t+u)+6m_z^6t(2t+u)-2m_z^2t^2u(4t+u)+3t^3u(2t+3u)\\
&+m_z^4t(-2t^2+tu-3u^2)\big)+\left(2\ln\left(\frac{-t}{m_z^2}\right)\ln\left(\frac{t-m_z^2}{m_z^2s}\right)+4\mathrm{Li}_2\left(\frac{t}{m_z^2}\right)\right.\\
&\left.-\ln^2\left(\frac{-t}{m_z^2}\right)\right)u\big(m_z^4(8t-2u)-4m_z^2t(2t+u)+t(2t^2+2tu+u^2)\big)\\
&+\ln\left(\frac{-u}{m_z^2}\right)\frac{t}{(u-m_z^2)^2}\big(3m_z^8(-4u+t)+6m_z^6u(2u+t)-2m_z^2u^2t(4u+t)\\
&+3u^3t(2u+3t)+m_z^4u(-2u^2+tu-3t^2)\big)+\left(2\ln\left(\frac{-u}{m_z^2}\right)\ln\left(\frac{u-m_z^2}{m_z^2s}\right)\right.\\
&\left.+4\mathrm{Li}_2\left(\frac{u}{m_z^2}\right)-\ln^2\left(\frac{-u}{m_z^2}\right)\right)t\big(m_z^4(8u-2t)-4m_z^2u(2u+t)\\
&+u(2u^2+2tu+t^2)\big)\Big].
\end{aligned}$$

$$x=\frac{1-\kappa}{1+\kappa};\quad \kappa=\sqrt{1-4\frac{m_z^2}{s}} \tag{C.6}$$

Appendix D

Polylogs and Operator Renormalization constants

D.1 GPLs and HPLs

We recall here that the GPLs are defined as iterated integrals over the rational functions as,

$$G(l_1, l_2, ..., l_n; x) = \int_0^x \frac{dt}{t - l_1} \, G(l_2, ..., l_n; t), \tag{D.1}$$

$$G(\underbrace{0, 0, .., 0}_{n}; x) = \frac{1}{n!} \ln^n(x), \;\; G(x) = 1; \tag{D.2}$$

The definitions of the one and 2d-HPL for weight (n) one are:

$$\begin{aligned} H(1;y) &= -\ln(1-y) \,, \\ H(0;y) &= \ln y \,, \\ H(-1;y) &= \ln(1+y) \\ H(1-z;y) &= -\ln\left(1 - \frac{y}{1-z}\right) \,, \\ H(z;y) &= \ln\left(\frac{y+z}{z}\right) . \end{aligned} \tag{D.3}$$

and the rational fractions for 1d-HPL

$$f(1;y) = \frac{1}{1-y} \,, f(0;y) = \frac{1}{y} \,, f(-1;y) = \frac{1}{1+y} \,, \tag{D.4}$$

For 2d-HPL, the rational fraction in terms of y, z

$$f(1-z;y) = \;\; \frac{1}{1-y-z} \;, \;\; f(z;y) = \;\; \frac{1}{y+z} \;, \tag{D.5}$$

such that

$$\frac{\partial}{\partial y} H(a;y) = f(a;y), \quad \text{with} \quad a = +1, 0, -1, 1-z, z. \tag{D.6}$$

For $n > 1$:

$$H(0,\ldots,0;y) = \frac{1}{n!}\ln^n y\,, \tag{D.7}$$

$$H(a,\vec{b};y) = \int_0^y dt f(a;t)H(\vec{b};t)\,, \tag{D.8}$$

which satisfies the equation

$$\frac{\partial}{\partial y}H(a,\vec{b};y) = f(a;y)H(\vec{b};y)\,. \tag{D.9}$$

D.2 Operator Renormalization constants

The operator renormalization constant that given in Eq. (6.26) and Eq. (6.27) are

$$Z_{GG} = 1 + a_s\left[\frac{1}{\epsilon}\left\{\frac{22}{3}C_A - \frac{4}{3}n_f\right\}\right] + a_s^2\left[\frac{1}{\epsilon^2}\left\{\frac{484}{9}C_A^2 - \frac{176}{9}C_A n_f + \frac{16}{9}n_f^2\right\} + \frac{1}{\epsilon}\left\{\frac{34}{3}C_A^2 - \frac{10}{3}C_A n_f - 2C_F n_f\right\}\right] \tag{D.10}$$

$$Z_{GJ} = a_s\left[-\frac{24}{\epsilon}C_F\right] + a_s^2\left[\frac{1}{\epsilon^2}\left\{-176C_AC_F + 32C_Fn_f\right\} + \frac{1}{\epsilon}\left\{-\frac{284}{3}C_AC_F + \frac{8}{3}C_Fn_f + 84C_F^2\right\}\right] \tag{D.11}$$

$$Z_{JJ} = 1 + a_s\left[-4C_F\right] + a_s^2\left[\frac{1}{\epsilon}\left\{\frac{44}{3}C_AC_F - \frac{10}{3}C_Fn_f\right\} - \frac{107}{9}C_AC_F + \frac{31}{18}C_Fn_f + 22C_F^2\right] \tag{D.12}$$

Bibliography

[1] CMS collaboration, A. M. Sirunyan et al., *Measurement of the differential Drell-Yan cross section in proton-proton collisions at $\sqrt{s}$ = 13 TeV*, *JHEP* **12** (2019) 059 [1812.10529].

[2] CMS collaboration, A. Tumasyan et al., *Measurement of simplified template cross sections of the Higgs boson produced in association with W or Z bosons in the $H{\to}bb^{-}$ decay channel in proton-proton collisions at $s{=}13$ TeV*, *Phys. Rev. D* **109** (2024) 092011 [2312.07562].

[3] ATLAS collaboration, G. Aad et al., *Measurements of WH and ZH production in the $H \to b\bar{b}$ decay channel in pp collisions at 13 TeV with the ATLAS detector*, *Eur. Phys. J. C* **81** (2021) 178 [2007.02873].

[4] ATLAS collaboration, G. Aad et al., *Measurement of ZZ production cross-sections in the four-lepton final state in pp collisions at $s{=}13.6$TeV with the ATLAS experiment*, *Phys. Lett. B* **855** (2024) 138764 [2311.09715].

[5] S. L. Glashow, *Partial Symmetries of Weak Interactions*, *Nucl. Phys.* **22** (1961) 579.

[6] S. Weinberg, *A Model of Leptons*, *Phys. Rev. Lett.* **19** (1967) 1264.

[7] A. Salam, *Weak and Electromagnetic Interactions*, *Conf. Proc. C* **680519** (1968) 367.

[8] F. Englert and R. Brout, *Broken Symmetry and the Mass of Gauge Vector Mesons*, *Phys. Rev. Lett.* **13** (1964) 321.

[9] P. W. Higgs, *Broken symmetries, massless particles and gauge fields*, *Phys. Lett.* **12** (1964) 132.

[10] P. W. Higgs, *Broken Symmetries and the Masses of Gauge Bosons*, *Phys. Rev. Lett.* **13** (1964) 508.

[11] G. S. Guralnik, C. R. Hagen and T. W. B. Kibble, *Global Conservation Laws and Massless Particles*, *Phys. Rev. Lett.* **13** (1964) 585.

[12] P. W. Higgs, *Spontaneous Symmetry Breakdown without Massless Bosons*, *Phys. Rev.* **145** (1966) 1156.

[13] J. Beacham et al., *Physics Beyond Colliders at CERN: Beyond the Standard Model Working Group Report*, *J. Phys. G* **47** (2020) 010501 [1901.09966].

[14] Z. Liu and L.-T. Wang, *Physics at Future Colliders: the Interplay Between Energy and Luminosity*, in *Snowmass 2021*, 4, 2022, 2205.00031.

[15] P. Bambade et al., *The International Linear Collider: A Global Project*, 1903.01629.

[16] LCC Physics Working Group collaboration, K. Fujii et al., *Tests of the Standard Model at the International Linear Collider*, 1908.11299.

[17] FCC collaboration, A. Abada et al., *FCC-ee: The Lepton Collider: Future Circular Collider Conceptual Design Report Volume 2*, *Eur. Phys. J. ST* **228** (2019) 261.

[18] Gargamelle Neutrino collaboration, F. J. Hasert et al., *Observation of Neutrino Like Interactions Without Muon Or Electron in the Gargamelle Neutrino Experiment*, *Phys. Lett. B* **46** (1973) 138.

[19] UA1 collaboration, G. Arnison et al., *Experimental Observation of Isolated Large Transverse Energy Electrons with Associated Missing Energy at* $\sqrt{s} = 540$ *GeV*, *Phys. Lett. B* **122** (1983) 103.

[20] UA2 collaboration, M. Banner et al., *Observation of Single Isolated Electrons of High Transverse Momentum in Events with Missing Transverse Energy at the CERN anti-p p Collider*, *Phys. Lett. B* **122** (1983) 476.

[21] SLAC-SP-017 collaboration, J. E. Augustin et al., *Discovery of a Narrow Resonance in* e^+e^- *Annihilation*, *Phys. Rev. Lett.* **33** (1974) 1406.

[22] E598 collaboration, J. J. Aubert et al., *Experimental Observation of a Heavy Particle J*, *Phys. Rev. Lett.* **33** (1974) 1404.

[23] E288 collaboration, S. W. Herb et al., *Observation of a Dimuon Resonance at 9.5-GeV in 400-GeV Proton-Nucleus Collisions*, *Phys. Rev. Lett.* **39** (1977) 252.

[24] E288 collaboration, W. R. Innes et al., *Observation of Structure in the* Υ *Region*, *Phys. Rev. Lett.* **39** (1977) 1240.

[25] CDF collaboration, F. Abe et al., *Observation of top quark production in* $\bar{p}p$ *collisions*, *Phys. Rev. Lett.* **74** (1995) 2626 [hep-ex/9503002].

[26] D0 collaboration, S. Abachi et al., *Observation of the top quark*, *Phys. Rev. Lett.* **74** (1995) 2632 [hep-ex/9503003].

[27] ATLAS collaboration, G. Aad et al., *Observation of a new particle in the search for the Standard Model Higgs boson with the ATLAS detector at the LHC*, *Phys. Lett. B* **716** (2012) 1 [1207.7214].

[28] CMS collaboration, S. Chatrchyan et al., *Observation of a New Boson at a Mass of 125 GeV with the CMS Experiment at the LHC*, *Phys. Lett. B* **716** (2012) 30 [1207.7235].

[29] UA1 collaboration, C. Albajar et al., *Intermediate Vector Boson Cross-Sections at the CERN Super Proton Synchrotron Collider and the Number of Neutrino Types*, *Phys. Lett. B* **198** (1987) 271.

[30] UA2 collaboration, R. Ansari et al., *Measurement of W and Z Production Properties at the CERN anti-p p Collider*, *Phys. Lett. B* **194** (1987) 158.

[31] G. Altarelli, R. K. Ellis and G. Martinelli, *Leptoproduction and Drell-Yan Processes Beyond the Leading Approximation in Chromodynamics*, *Nucl. Phys. B* **143** (1978) 521.

[32] G. Altarelli, R. K. Ellis and G. Martinelli, *Large Perturbative Corrections to the Drell-Yan Process in QCD*, *Nucl. Phys. B* **157** (1979) 461.

[33] J. Kubar-Andre and F. E. Paige, *Gluon Corrections to the Drell-Yan Model*, *Phys. Rev. D* **19** (1979) 221.

[34] G. Altarelli, R. K. Ellis, M. Greco and G. Martinelli, *Vector Boson Production at Colliders: A Theoretical Reappraisal*, *Nucl. Phys. B* **246** (1984) 12.

[35] G. Altarelli, R. K. Ellis and G. Martinelli, *Vector Boson Production at Present and Future Colliders*, *Z. Phys. C* **27** (1985) 617.

[36] B. Humpert and W. L. van Neerven, *Infrared and Mass Regularization in Af Field Theories 2. QCD*, *Nucl. Phys. B* **184** (1981) 225.

[37] G. Parisi, *Summing Large Perturbative Corrections in QCD*, *Phys. Lett. B* **90** (1980) 295.

[38] LEP Working Group for Higgs boson searches, ALEPH, DELPHI, L3, OPAL collaboration, R. Barate et al., *Search for the standard model Higgs boson at LEP*, *Phys. Lett. B* **565** (2003) 61 [hep-ex/0306033].

[39] CDF, D0 collaboration, T. Aaltonen et al., *Combination of Tevatron Searches for the Standard Model Higgs Boson in the W^+W^- Decay Mode*, *Phys. Rev. Lett.* **104** (2010) 061802 [1001.4162].

[40] ALEPH, CDF, D0, DELPHI, L3, OPAL, SLD, LEP Electroweak Working Group, Tevatron Electroweak Working Group, SLD Electroweak, Heavy Flavour Groups collaboration, *Precision Electroweak Measurements and Constraints on the Standard Model*, 1012.2367.

[41] T. Matsuura and W. L. van Neerven, *Second Order Logarithmic Corrections to the Drell-Yan Cross-section*, *Z. Phys. C* **38** (1988) 623.

[42] T. Matsuura, S. C. van der Marck and W. L. van Neerven, *The Calculation of the Second Order Soft and Virtual Contributions to the Drell-Yan Cross-Section*, *Nucl. Phys. B* **319** (1989) 570.

[43] R. Hamberg, W. L. van Neerven and T. Matsuura, *A complete calculation of the order $\alpha - s^2$ correction to the Drell-Yan K factor*, *Nucl. Phys. B* **359** (1991) 343.

[44] E. B. Zijlstra and W. L. van Neerven, *Order alpha-s**2 QCD corrections to the deep inelastic proton structure functions F2 and F(L)*, *Nucl. Phys. B* **383** (1992) 525.

[45] H. M. Georgi, S. L. Glashow, M. E. Machacek and D. V. Nanopoulos, *Higgs Bosons from Two Gluon Annihilation in Proton Proton Collisions*, *Phys. Rev. Lett.* **40** (1978) 692.

[46] A. Djouadi, M. Spira and P. M. Zerwas, *Production of Higgs bosons in proton colliders: QCD corrections*, *Phys. Lett. B* **264** (1991) 440.

[47] S. Dawson, *Radiative corrections to Higgs boson production*, *Nucl. Phys. B* **359** (1991) 283.

[48] M. Spira, A. Djouadi, D. Graudenz and P. M. Zerwas, *Higgs boson production at the LHC*, *Nucl. Phys. B* **453** (1995) 17 [hep-ph/9504378].

[49] S. Catani, D. de Florian and M. Grazzini, *Higgs production in hadron collisions: Soft and virtual QCD corrections at NNLO*, *JHEP* **05** (2001) 025 [hep-ph/0102227].

[50] R. V. Harlander and W. B. Kilgore, *Soft and virtual corrections to proton proton —> H + x at NNLO*, *Phys. Rev. D* **64** (2001) 013015 [hep-ph/0102241].

[51] R. V. Harlander and W. B. Kilgore, *Next-to-next-to-leading order Higgs production at hadron colliders*, *Phys. Rev. Lett.* **88** (2002) 201801 [hep-ph/0201206].

[52] C. Anastasiou and K. Melnikov, *Higgs boson production at hadron colliders in NNLO QCD*, *Nucl. Phys. B* **646** (2002) 220 [hep-ph/0207004].

[53] V. Ravindran, J. Smith and W. L. van Neerven, *NNLO corrections to the total cross-section for Higgs boson production in hadron hadron collisions*, *Nucl. Phys. B* **665** (2003) 325 [hep-ph/0302135].

[54] P. Nason, S. Dawson and R. K. Ellis, *The Total Cross-Section for the Production of Heavy Quarks in Hadronic Collisions*, *Nucl. Phys. B* **303** (1988) 607.

[55] W. Beenakker, W. L. van Neerven, R. Meng, G. A. Schuler and J. Smith, *QCD corrections to heavy quark production in hadron hadron collisions*, *Nucl. Phys. B* **351** (1991) 507.

[56] P. Nason, S. Dawson and R. K. Ellis, *The One Particle Inclusive Differential Cross-Section for Heavy Quark Production in Hadronic Collisions*, *Nucl. Phys. B* **327** (1989) 49.

[57] S. Catani, S. Devoto, M. Grazzini, S. Kallweit, J. Mazzitelli and H. Sargsyan, *Top-quark pair hadroproduction at next-to-next-to-leading order in QCD*, *Phys. Rev. D* **99** (2019) 051501 [1901.04005].

[58] M. Czakon and A. Mitov, *NNLO corrections to top-pair production at hadron colliders: the all-fermionic scattering channels*, *JHEP* **12** (2012) 054 [1207.0236].

[59] M. Czakon and A. Mitov, *NNLO corrections to top pair production at hadron colliders: the quark-gluon reaction*, *JHEP* **01** (2013) 080 [1210.6832].

[60] S. D. Ellis, Z. Kunszt and D. E. Soper, *Two jet production in hadron collisions at order alpha-s**3 in QCD*, *Phys. Rev. Lett.* **69** (1992) 1496.

[61] W. T. Giele, E. W. N. Glover and D. A. Kosower, *The Two-Jet Differential Cross Section at $\mathcal{O}(\alpha_s^3)$ in Hadron Collisions*, *Phys. Rev. Lett.* **73** (1994) 2019 [hep-ph/9403347].

[62] S. Dittmaier, A. Huss and C. Speckner, *Weak radiative corrections to dijet production at hadron colliders*, *JHEP* **11** (2012) 095 [1210.0438].

[63] J. Currie, A. Gehrmann-De Ridder, T. Gehrmann, E. W. N. Glover, A. Huss and J. Pires, *Precise predictions for dijet production at the LHC*, *Phys. Rev. Lett.* **119** (2017) 152001 [1705.10271].

[64] M. Becchetti, R. Bonciani, L. Cieri, F. Coro and F. Ripani, *Full top-quark mass dependence in diphoton production at NNLO in QCD*, *Phys. Lett. B* **848** (2024) 138362 [2308.10885].

[65] T. Gehrmann, M. Grazzini, S. Kallweit, P. Maierhöfer, A. von Manteuffel, S. Pozzorini et al., *W^+W^- Production at Hadron Colliders in Next to Next to Leading Order QCD*, *Phys. Rev. Lett.* **113** (2014) 212001 [1408.5243].

[66] M. Grazzini, S. Kallweit and D. Rathlev, *$W\gamma$ and $Z\gamma$ production at the LHC in NNLO QCD*, *JHEP* **07** (2015) 085 [1504.01330].

[67] S. Kallweit and M. Wiesemann, *ZZ production at the LHC: NNLO predictions for $2\ell2\nu$ and 4ℓ signatures*, *Phys. Lett. B* **786** (2018) 382 [1806.05941].

[68] S. Kallweit, V. Sotnikov and M. Wiesemann, *Triphoton production at hadron colliders in NNLO QCD*, *Phys. Lett. B* **812** (2021) 136013 [2010.04681].

[69] C. Anastasiou, C. Duhr, F. Dulat, F. Herzog and B. Mistlberger, *Higgs Boson Gluon-Fusion Production in QCD at Three Loops*, *Phys. Rev. Lett.* **114** (2015) 212001 [1503.06056].

[70] B. Mistlberger, *Higgs boson production at hadron colliders at N^3LO in QCD*, *JHEP* **05** (2018) 028 [1802.00833].

[71] C. Duhr and B. Mistlberger, *Lepton-pair production at hadron colliders at N^3LO in QCD*, *JHEP* **03** (2022) 116 [2111.10379].

[72] C. Duhr, F. Dulat and B. Mistlberger, *Charged current Drell-Yan production at N^3LO*, *JHEP* **11** (2020) 143 [2007.13313].

[73] J. Baglio, C. Duhr, B. Mistlberger and R. Szafron, *Inclusive production cross sections at N^3LO*, *JHEP* **12** (2022) 066 [2209.06138].

[74] *Search for resonances decaying to photon pairs in 3.2 fb^{-1} of pp collisions at $\sqrt{s}$ = 13 TeV with the ATLAS detector*, .

[75] CMS collaboration, *Search for new physics in high mass diphoton events in proton-proton collisions at 13TeV*, .

[76] J. H. Christenson, G. S. Hicks, L. M. Lederman, P. J. Limon, B. G. Pope and E. Zavattini, *Observation of massive muon pairs in hadron collisions*, *Phys. Rev. Lett.* **25** (1970) 1523.

[77] S. Catani, D. de Florian, M. Grazzini and P. Nason, *Soft gluon resummation for Higgs boson production at hadron colliders*, *JHEP* **07** (2003) 028 [hep-ph/0306211].

[78] S. Moch and A. Vogt, *Higher-order soft corrections to lepton pair and Higgs boson production*, *Phys. Lett. B* **631** (2005) 48 [hep-ph/0508265].

[79] E. Laenen and L. Magnea, *Threshold resummation for electroweak annihilation from DIS data*, *Phys. Lett. B* **632** (2006) 270 [hep-ph/0508284].

[80] A. Idilbi, X.-d. Ji, J.-P. Ma and F. Yuan, *Threshold resummation for Higgs production in effective field theory*, *Phys. Rev. D* **73** (2006) 077501 [hep-ph/0509294].

[81] V. Ravindran, *On Sudakov and soft resummations in QCD*, *Nucl. Phys. B* **746** (2006) 58 [hep-ph/0512249].

[82] V. Ravindran, *Higher-order threshold effects to inclusive processes in QCD*, *Nucl. Phys. B* **752** (2006) 173 [hep-ph/0603041].

[83] V. Ahrens, T. Becher, M. Neubert and L. L. Yang, *Renormalization-Group Improved Prediction for Higgs Production at Hadron Colliders*, *Eur. Phys. J. C* **62** (2009) 333 [0809.4283].

[84] D. de Florian and M. Grazzini, *Higgs production through gluon fusion: Updated cross sections at the Tevatron and the LHC*, *Phys. Lett. B* **674** (2009) 291 [0901.2427].

[85] C. Anastasiou, C. Duhr, F. Dulat, E. Furlan, T. Gehrmann, F. Herzog et al., *Higgs boson gluon–fusion production at threshold in N^3LO QCD*, *Phys. Lett. B* **737** (2014) 325 [1403.4616].

[86] Y. Li, A. von Manteuffel, R. M. Schabinger and H. X. Zhu, *N^3LO Higgs boson and Drell-Yan production at threshold: The one-loop two-emission contribution*, *Phys. Rev. D* **90** (2014) 053006 [1404.5839].

[87] C. Anastasiou, C. Duhr, F. Dulat, E. Furlan, T. Gehrmann, F. Herzog et al., *Higgs Boson GluonFfusion Production Beyond Threshold in N^3LO QCD*, *JHEP* **03** (2015) 091 [1411.3584].

[88] D. de Florian, J. Mazzitelli, S. Moch and A. Vogt, *Approximate N^3LO Higgs-boson production cross section using physical-kernel constraints*, *JHEP* **10** (2014) 176 [1408.6277].

[89] T. Schmidt and M. Spira, *Higgs Boson Production via Gluon Fusion: Soft-Gluon Resummation including Mass Effects*, *Phys. Rev. D* **93** (2016) 014022 [1509.00195].

[90] R. V. Harlander and W. B. Kilgore, *Higgs boson production in bottom quark fusion at next-to-next-to leading order*, *Phys. Rev. D* **68** (2003) 013001 [hep-ph/0304035].

[91] C. Duhr, F. Dulat and B. Mistlberger, *Higgs Boson Production in Bottom-Quark Fusion to Third Order in the Strong Coupling*, *Phys. Rev. Lett.* **125** (2020) 051804 [1904.09990].

[92] LHC Higgs Cross Section Working Group collaboration, S. Dittmaier et al., *Handbook of LHC Higgs Cross Sections: 1. Inclusive Observables*, 1101.0593.

[93] M. Carena, S. Heinemeyer, C. E. M. Wagner and G. Weiglein, *Suggestions for improved benchmark scenarios for Higgs boson searches at LEP-2*, in *Workshop on New Theoretical Developments for Higgs Physics at LEP-2*, 12, 1999, hep-ph/9912223.

[94] CMS collaboration, A. M. Sirunyan et al., *Observation of the Higgs boson decay to a pair of τ leptons with the CMS detector*, *Phys. Lett. B* **779** (2018) 283 [1708.00373].

[95] ATLAS collaboration, M. Aaboud et al., *Cross-section measurements of the Higgs boson decaying into a pair of τ-leptons in proton-proton collisions at $\sqrt{s} = 13$ TeV with the ATLAS detector*, *Phys. Rev. D* **99** (2019) 072001 [1811.08856].

[96] D. Dicus, T. Stelzer, Z. Sullivan and S. Willenbrock, *Higgs boson production in association with bottom quarks at next-to-leading order*, *Phys. Rev. D* **59** (1999) 094016 [hep-ph/9811492].

[97] S. Dawson, C. B. Jackson, L. H. Orr, L. Reina and D. Wackeroth, *Theoretical progress for the associated production of a Higgs boson with heavy quarks at hadron colliders*, *Eur. Phys. J. C* **33** (2004) S451 [hep-ph/0311216].

[98] J. M. Campbell, S. Dawson, S. Dittmaier, C. Jackson, M. Kramer, F. Maltoni et al., *Higgs boson production in association with bottom quarks*, in *3rd Les Houches Workshop on Physics at TeV Colliders*, 5, 2004, hep-ph/0405302.

[99] F. Maltoni, Z. Sullivan and S. Willenbrock, *Higgs-Boson Production via Bottom-Quark Fusion*, *Phys. Rev. D* **67** (2003) 093005 [hep-ph/0301033].

[100] R. Harlander, M. Kramer and M. Schumacher, *Bottom-quark associated Higgs-boson production: reconciling the four- and five-flavour scheme approach*, 1112.3478.

[101] R. V. Harlander, A. Tripathi and M. Wiesemann, *Higgs production in bottom quark annihilation: Transverse momentum distribution at NNLO+NNLL*, *Phys. Rev. D* **90** (2014) 015017 [1403.7196].

[102] CMS collaboration, A. M. Sirunyan et al., *Observation of Higgs boson decay to bottom quarks*, *Phys. Rev. Lett.* **121** (2018) 121801 [1808.08242].

[103] ATLAS collaboration, M. Aaboud et al., *Observation of $H \to b\bar{b}$ decays and VH production with the ATLAS detector*, *Phys. Lett. B* **786** (2018) 59 [1808.08238].

[104] T. Han and S. Willenbrock, *QCD correction to the $pp \to WH$ and ZH total cross-sections*, *Phys. Lett. B* **273** (1991) 167.

[105] J. Ohnemus and W. J. Stirling, *Order alpha-s corrections to the differential cross-section for the W H intermediate mass Higgs signal*, *Phys. Rev. D* **47** (1993) 2722.

[106] O. Brein, M. Ciccolini, S. Dittmaier, A. Djouadi, R. Harlander and M. Kramer, *Precision calculations for associated WH and ZH production at hadron colliders*, in *3rd Les Houches Workshop on Physics at TeV Colliders*, 2, 2004, hep-ph/0402003.

[107] G. Ferrera, M. Grazzini and F. Tramontano, *Associated WH production at hadron colliders: a fully exclusive QCD calculation at NNLO*, *Phys. Rev. Lett.* **107** (2011) 152003 [1107.1164].

[108] O. Brein, R. V. Harlander and T. J. E. Zirke, *vh@nnlo - Higgs Strahlung at hadron colliders*, *Comput. Phys. Commun.* **184** (2013) 998 [1210.5347].

[109] G. Ferrera, M. Grazzini and F. Tramontano, *Associated ZH production at hadron colliders: the fully differential NNLO QCD calculation*, *Phys. Lett. B* **740** (2015) 51 [1407.4747].

[110] R. V. Harlander, J. Klappert, S. Liebler and L. Simon, *vh@nnlo-v2: New physics in Higgs Strahlung*, *JHEP* **05** (2018) 089 [1802.04817].

[111] M. L. Ciccolini, S. Dittmaier and M. Kramer, *Electroweak radiative corrections to associated WH and ZH production at hadron colliders*, *Phys. Rev. D* **68** (2003) 073003 [hep-ph/0306234].

[112] A. Denner, S. Dittmaier, S. Kallweit and A. Muck, *Electroweak corrections to Higgs-strahlung off W/Z bosons at the Tevatron and the LHC with HAWK*, *JHEP* **03** (2012) 075 [1112.5142].

[113] S. Dawson, T. Han, W. K. Lai, A. K. Leibovich and I. Lewis, *Resummation Effects in Vector-Boson and Higgs Associated Production*, *Phys. Rev. D* **86** (2012) 074007 [1207.4207].

[114] M. C. Kumar, M. K. Mandal and V. Ravindran, *Associated production of Higgs boson with vector boson at threshold N^3LO in QCD*, *JHEP* **03** (2015) 037 [1412.3357].

[115] D. A. Dicus and C. Kao, *Higgs Boson - Z^0 Production From Gluon Fusion*, *Phys. Rev. D* **38** (1988) 1008.

[116] B. A. Kniehl, *Associated Production of Higgs and Z Bosons From Gluon Fusion in Hadron Collisions*, *Phys. Rev. D* **42** (1990) 2253.

[117] B. A. Kniehl, *On the Decay Mode $Z \to H\, gg$*, *Phys. Rev. D* **42** (1990) 3100.

[118] B. A. Kniehl and C. P. Palisoc, *Associated production of Z and neutral Higgs bosons at the CERN Large Hadron Collider*, *Phys. Rev. D* **85** (2012) 075027 [1112.1575].

[119] L. Altenkamp, S. Dittmaier, R. V. Harlander, H. Rzehak and T. J. E. Zirke, *Gluon-induced Higgs-strahlung at next-to-leading order QCD*, *JHEP* **02** (2013) 078 [1211.5015].

[120] A. Hasselhuhn, T. Luthe and M. Steinhauser, *On top quark mass effects to $gg \to ZH$ at NLO*, *JHEP* **01** (2017) 073 [1611.05881].

[121] L. Chen, G. Heinrich, S. P. Jones, M. Kerner, J. Klappert and J. Schlenk, *ZH production in gluon fusion: two-loop amplitudes with full top quark mass dependence*, *JHEP* **03** (2021) 125 [2011.12325].

[122] L. Alasfar, G. Degrassi, P. P. Giardino, R. Gröber and M. Vitti, *Virtual corrections to $gg \to ZH$ via a transverse momentum expansion*, *JHEP* **05** (2021) 168 [2103.06225].

[123] G. Wang, X. Xu, Y. Xu and L. L. Yang, *Next-to-leading order corrections for $gg \to ZH$ with top quark mass dependence*, *Phys. Lett. B* **829** (2022) 137087 [2107.08206].

[124] L. Bellafronte, G. Degrassi, P. P. Giardino, R. Groeber and M. Vitti, *Gluon fusion production at NLO: merging the transverse momentum and the high-energy expansions*, *JHEP* **07** (2022) 069 [2202.12157].

[125] L. Chen, J. Davies, G. Heinrich, S. P. Jones, M. Kerner, G. Mishima et al., *ZH production in gluon fusion at NLO in QCD*, *JHEP* **08** (2022) 056 [2204.05225].

[126] G. Degrassi, R. Gröber, M. Vitti and X. Zhao, *On the NLO QCD corrections to gluon-initiated ZH production*, *JHEP* **08** (2022) 009 [2205.02769].

[127] R. V. Harlander, A. Kulesza, V. Theeuwes and T. Zirke, *Soft gluon resummation for gluon-induced Higgs Strahlung*, *JHEP* **11** (2014) 082 [1410.0217].

[128] CDF collaboration, T. Aaltonen et al., *First Measurement of ZZ Production in panti-p Collisions at $\sqrt{s}$ = 1.96-TeV*, *Phys. Rev. Lett.* **100** (2008) 201801 [0801.4806].

[129] D0 collaboration, V. M. Abazov et al., *Observation of ZZ production in $p\bar{p}$ collisions at $\sqrt{s}$ = 1.96-TeV*, *Phys. Rev. Lett.* **101** (2008) 171803 [0808.0703].

[130] ATLAS collaboration, G. Aad et al., *Measurement of ZZ production in pp collisions at $\sqrt{s} = 7$ TeV and limits on anomalous ZZZ and $ZZ\gamma$ couplings with the ATLAS detector*, *JHEP* **03** (2013) 128 [1211.6096].

[131] CMS collaboration, S. Chatrchyan et al., *Measurement of the ZZ Production Cross Section and Search for Anomalous Couplings in 2 l2l ' Final States in pp Collisions at $\sqrt{s} = 7$ TeV*, *JHEP* **01** (2013) 063 [1211.4890].

[132] F. Cascioli, T. Gehrmann, M. Grazzini, S. Kallweit, P. Maierhöfer, A. von Manteuffel et al., *ZZ production at hadron colliders in NNLO QCD*, *Phys. Lett. B* **735** (2014) 311 [1405.2219].

[133] M. Grazzini, S. Kallweit and D. Rathlev, *ZZ production at the LHC: fiducial cross sections and distributions in NNLO QCD*, *Phys. Lett. B* **750** (2015) 407 [1507.06257].

[134] Y. Wang, C. S. Li, Z. L. Liu and D. Y. Shao, *Threshold resummation for $W^{\pm}Z$ and ZZ pair production at the LHC*, *Phys. Rev. D* **90** (2014) 034008 [1406.1417].

[135] ATLAS collaboration, G. Aad et al., *Evidence for the spin-0 nature of the Higgs boson using ATLAS data*, *Phys. Lett. B* **726** (2013) 120 [1307.1432].

[136] CMS collaboration, V. Khachatryan et al., *Constraints on the spin-parity and anomalous HVV couplings of the Higgs boson in proton collisions at 7 and 8 TeV*, *Phys. Rev. D* **92** (2015) 012004 [1411.3441].

[137] ATLAS collaboration, M. Aaboud et al., *Search for squarks and gluinos in final states with hadronically decaying τ-leptons, jets, and missing transverse momentum using pp collisions at $\sqrt{s}$ = 13 TeV with the ATLAS detector*, *Phys. Rev. D* **99** (2019) 012009 [1808.06358].

[138] ATLAS collaboration, G. Aad et al., *Search for heavy Higgs bosons decaying into two tau leptons with the ATLAS detector using pp collisions at $\sqrt{s} = 13$ TeV*, *Phys. Rev. Lett.* **125** (2020) 051801 [2002.12223].

[139] P. Fayet, *Supergauge Invariant Extension of the Higgs Mechanism and a Model for the electron and Its Neutrino*, *Nucl. Phys. B* **90** (1975) 104.

[140] P. Fayet, *Spontaneously Broken Supersymmetric Theories of Weak, Electromagnetic and Strong Interactions*, *Phys. Lett. B* **69** (1977) 489.

[141] S. Dimopoulos and H. Georgi, *Softly Broken Supersymmetry and SU(5)*, *Nucl. Phys. B* **193** (1981) 150.

[142] N. Sakai, *Naturalness in Supersymmetric Guts*, *Z. Phys. C* **11** (1981) 153.

[143] K. Inoue, A. Kakuto, H. Komatsu and S. Takeshita, *Aspects of Grand Unified Models with Softly Broken Supersymmetry*, *Prog. Theor. Phys.* **68** (1982) 927.

[144] K. Inoue, A. Kakuto, H. Komatsu and S. Takeshita, *Low-Energy Parameters and Particle Masses in a Supersymmetric Grand Unified Model*, *Prog. Theor. Phys.* **67** (1982) 1889.

[145] K. Inoue, A. Kakuto, H. Komatsu and S. Takeshita, *Renormalization of Supersymmetry Breaking Parameters Revisited*, *Prog. Theor. Phys.* **71** (1984) 413.

[146] H. E. Haber and G. L. Kane, *The Search for Supersymmetry: Probing Physics Beyond the Standard Model*, *Phys. Rept.* **117** (1985) 75.

[147] G. Branco, P. Ferreira, L. Lavoura, M. Rebelo, M. Sher and J. P. Silva, *Theory and phenomenology of two-Higgs-doublet models*, *Phys. Rept.* **516** (2012) 1 [1106.0034].

[148] R. P. Kauffman and W. Schaffer, *QCD corrections to production of Higgs pseudoscalars*, *Phys. Rev. D* **49** (1994) 551 [hep-ph/9305279].

[149] M. Spira, A. Djouadi, D. Graudenz and P. M. Zerwas, *SUSY Higgs production at proton colliders*, *Phys. Lett. B* **318** (1993) 347.

[150] R. V. Harlander and M. Steinhauser, *Hadronic Higgs production and decay in supersymmetry at next-to-leading order*, *Phys. Lett. B* **574** (2003) 258 [hep-ph/0307346].

[151] R. Harlander, *Supersymmetric Higgs production at the Large Hadron Collider*, *Eur. Phys. J. C* **33** (2004) S454 [hep-ph/0311005].

[152] R. V. Harlander and W. B. Kilgore, *Production of a pseudoscalar Higgs boson at hadron colliders at next-to-next-to leading order*, *JHEP* **10** (2002) 017 [hep-ph/0208096].

[153] C. Anastasiou and K. Melnikov, *Pseudoscalar Higgs boson production at hadron colliders in NNLO QCD*, *Phys. Rev. D* **67** (2003) 037501 [hep-ph/0208115].

[154] S. Catani, D. de Florian and M. Grazzini, *Direct Higgs production and jet veto at the Tevatron and the LHC in NNLO QCD*, *JHEP* **01** (2002) 015 [hep-ph/0111164].

[155] C. F. Berger, C. Marcantonini, I. W. Stewart, F. J. Tackmann and W. J. Waalewijn, *Higgs Production with a Central Jet Veto at NNLL+NNLO*, *JHEP* **04** (2011) 092 [1012.4480].

[156] X. Chen, J. Cruz-Martinez, T. Gehrmann, E. W. N. Glover and M. Jaquier, *NNLO QCD corrections to Higgs boson production at large transverse momentum*, *JHEP* **10** (2016) 066 [1607.08817].

[157] R. Boughezal, F. Caola, K. Melnikov, F. Petriello and M. Schulze, *Higgs boson production in association with a jet at next-to-next-to-leading order in perturbative QCD*, *JHEP* **06** (2013) 072 [1302.6216].

[158] X. Chen, T. Gehrmann, E. W. N. Glover and M. Jaquier, *Precise QCD predictions for the production of Higgs + jet final states*, *Phys. Lett. B* **740** (2015) 147 [1408.5325].

[159] R. Boughezal, F. Caola, K. Melnikov, F. Petriello and M. Schulze, *Higgs boson production in association with a jet at next-to-next-to-leading order*, *Phys. Rev. Lett.* **115** (2015) 082003 [1504.07922].

[160] R. Boughezal, C. Focke, W. Giele, X. Liu and F. Petriello, *Higgs boson production in association with a jet at NNLO using jettiness subtraction*, *Phys. Lett. B* **748** (2015) 5 [1505.03893].

[161] F. Caola, K. Melnikov and M. Schulze, *Fiducial cross sections for Higgs boson production in association with a jet at next-to-next-to-leading order in QCD*, *Phys. Rev. D* **92** (2015) 074032 [1508.02684].

[162] L. J. Dixon, E. W. N. Glover and V. V. Khoze, *MHV rules for Higgs plus multi-gluon amplitudes*, *JHEP* **12** (2004) 015 [hep-th/0411092].

[163] S. D. Badger, E. W. N. Glover and V. V. Khoze, *MHV rules for Higgs plus multi-parton amplitudes*, *JHEP* **03** (2005) 023 [hep-th/0412275].

[164] S. D. Badger and E. W. N. Glover, *One-loop helicity amplitudes for H —> gluons: The All-minus configuration*, *Nucl. Phys. B Proc. Suppl.* **160** (2006) 71 [hep-ph/0607139].

[165] L. J. Dixon and Y. Sofianatos, *Analytic one-loop amplitudes for a Higgs boson plus four partons*, *JHEP* **08** (2009) 058 [0906.0008].

[166] S. Badger, E. W. Nigel Glover, P. Mastrolia and C. Williams, *One-loop Higgs plus four gluon amplitudes: Full analytic results*, *JHEP* **01** (2010) 036 [0909.4475].

[167] S. Badger, J. M. Campbell, R. K. Ellis and C. Williams, *Analytic results for the one-loop NMHV Hqqgg amplitude*, *JHEP* **12** (2009) 035 [0910.4481].

[168] T. Gehrmann, T. Lübbert and L. L. Yang, *Transverse parton distribution functions at next-to-next-to-leading order: The quark-to-quark case*, *Phys. Rev. Lett.* **109** (2012) 242003 [1209.0682].

[169] J. F. Gunion, H. E. Haber, G. L. Kane and S. Dawson, *The Higgs Hunter's Guide*, vol. 80. 2000, 10.1201/9780429496448.

[170] CMS collaboration, A. M. Sirunyan et al., *Search for additional neutral MSSM Higgs bosons in the $\tau\tau$ final state in proton-proton collisions at $\sqrt{s} = 13$ TeV*, *JHEP* **09** (2018) 007 [1803.06553].

[171] D. Graudenz, M. Spira and P. M. Zerwas, *QCD corrections to Higgs boson production at proton proton colliders*, *Phys. Rev. Lett.* **70** (1993) 1372.

[172] B. Field, J. Smith, M. E. Tejeda-Yeomans and W. L. van Neerven, *NLO corrections to differential cross-sections for pseudoscalar Higgs boson production*, *Phys. Lett. B* **551** (2003) 137 [hep-ph/0210369].

[173] W. Bernreuther, P. Gonzalez and M. Wiebusch, *Pseudoscalar Higgs Bosons at the LHC: Production and Decays into Electroweak Gauge Bosons Revisited*, *Eur. Phys. J. C* **69** (2010) 31 [1003.5585].

[174] P. Banerjee, P. K. Dhani and V. Ravindran, *Two loop QCD corrections for the process Pseudo-scalar Higgs $\rightarrow$ 3 partons*, *JHEP* **10** (2017) 067 [1708.02387].

[175] Y. Kim and C. Williams, *Pseudoscalar Higgs plus jet production at Next-to-Next-to-Leading Order in QCD*, *JHEP* **08** (2024) 042 [2405.02210].

[176] S. A. Larin and J. A. M. Vermaseren, *The Three loop QCD Beta function and anomalous dimensions*, *Phys. Lett. B* **303** (1993) 334 [hep-ph/9302208].

[177] K. G. Chetyrkin, B. A. Kniehl, M. Steinhauser and W. A. Bardeen, *Effective QCD interactions of CP odd Higgs bosons at three loops*, *Nucl. Phys.* **B535** (1998) 3 [hep-ph/9807241].

[178] A. A H, P. Mukherjee and V. Ravindran, *Next to soft corrections to Drell-Yan and Higgs boson productions*, *Phys. Rev. D* **105** (2022) 094035 [2006.06726].

[179] A. A H, P. Mukherjee, V. Ravindran, A. Sankar and S. Tiwari, *Next-to-soft corrections for Drell-Yan and Higgs boson rapidity distributions beyond N^3LO*, *Phys. Rev. D* **103** (2021) L111502 [2010.00079].

[180] S. Moch, J. A. M. Vermaseren and A. Vogt, *Higher-order corrections in threshold resummation*, *Nucl. Phys. B* **726** (2005) 317 [hep-ph/0506288].

[181] G. Das, C. Dey, M. C. Kumar and K. Samanta, *Threshold enhanced cross sections for colorless productions*, *Phys. Rev. D* **107** (2023) 034038 [2210.17534].

[182] G. Das, C. Dey, M. C. Kumar and K. Samanta, *Soft gluon resummation for gluon fusion ZH production*, 2501.10330.

[183] P. Banerjee, C. Dey, M. C. Kumar and V. Pandey, *Threshold resummation for Z-boson pair production at NNLO+NNLL*, 2409.16375.

[184] P. Banerjee, C. Dey, M. C. Kumar and V. Ravindran, *Pseudoscalar Higgs boson decay to three parton amplitudes at NNLO to higher orders in the dimensional regulator*, *Phys. Rev. D* **111** (2025) 054037 [2411.17611].

[185] P. Nogueira, *Automatic Feynman Graph Generation*, *J. Comput. Phys.* **105** (1993) 279.

[186] J. A. M. Vermaseren, *New features of FORM*, math-ph/0010025.

[187] B. Ruijl, T. Ueda and J. A. M. Vermaseren, *FORM version 4.2*, 1707.06453.

[188] R. N. Lee, *Presenting LiteRed: a tool for the Loop InTEgrals REDuction*, 1212.2685.

[189] A. von Manteuffel and C. Studerus, *Reduze 2 - Distributed Feynman Integral Reduction*, 1201.4330.

[190] G. 't Hooft and M. J. G. Veltman, *Regularization and Renormalization of Gauge Fields*, *Nucl. Phys.* **B44** (1972) 189.

[191] W. A. Bardeen, A. J. Buras, D. W. Duke and T. Muta, *Deep Inelastic Scattering Beyond the Leading Order in Asymptotically Free Gauge Theories*, *Phys. Rev. D* **18** (1978) 3998.

[192] D. J. Gross and F. Wilczek, *Ultraviolet Behavior of Nonabelian Gauge Theories*, *Phys. Rev. Lett.* **30** (1973) 1343.

[193] H. D. Politzer, *Reliable Perturbative Results for Strong Interactions?*, *Phys. Rev. Lett.* **30** (1973) 1346.

[194] W. E. Caswell, *Asymptotic Behavior of Nonabelian Gauge Theories to Two Loop Order*, *Phys. Rev. Lett.* **33** (1974) 244.

[195] D. R. T. Jones, *Two Loop Diagrams in Yang-Mills Theory*, *Nucl. Phys. B* **75** (1974) 531.

[196] E. Egorian and O. V. Tarasov, *Two Loop Renormalization of the QCD in an Arbitrary Gauge*, *Teor. Mat. Fiz.* **41** (1979) 26.

[197] O. V. Tarasov, A. A. Vladimirov and A. Yu. Zharkov, *The Gell-Mann-Low Function of QCD in the Three Loop Approximation*, *Phys. Lett.* **B93** (1980) 429.

[198] T. van Ritbergen, J. A. M. Vermaseren and S. A. Larin, *The Four loop beta function in quantum chromodynamics*, *Phys. Lett. B* **400** (1997) 379 [hep-ph/9701390].

[199] Particle Data Group collaboration, R. L. Workman et al., *Review of Particle Physics*, *Prog. Theor. Exp. Phys.* **2022** (2022) 083C01.

[200] T. Kinoshita, *Mass singularities of Feynman amplitudes*, *J. Math. Phys.* **3** (1962) 650.

[201] T. D. Lee and M. Nauenberg, *Degenerate Systems and Mass Singularities*, *Phys. Rev.* **133** (1964) B1549.

[202] G. Altarelli and G. Parisi, *Asymptotic Freedom in Parton Language*, *Nucl. Phys. B* **126** (1977) 298.

[203] K. G. Chetyrkin, B. A. Kniehl and M. Steinhauser, *Decoupling relations to O (alpha-s**3) and their connection to low-energy theorems*, *Nucl. Phys. B* **510** (1998) 61 [hep-ph/9708255].

[204] V. V. Sudakov, *Vertex parts at very high-energies in quantum electrodynamics*, *Sov. Phys. JETP* **3** (1956) 65.

[205] A. H. Mueller, *On the Asymptotic Behavior of the Sudakov Form-factor*, *Phys. Rev. D* **20** (1979) 2037.

[206] J. C. Collins, *Algorithm to Compute Corrections to the Sudakov Form-factor*, *Phys. Rev. D* **22** (1980) 1478.

[207] A. Sen, *Asymptotic Behavior of the Sudakov Form-Factor in QCD*, *Phys. Rev. D* **24** (1981) 3281.

[208] S. Moch, J. A. M. Vermaseren and A. Vogt, *The Quark form-factor at higher orders*, *JHEP* **08** (2005) 049 [hep-ph/0507039].

[209] S. Moch, J. A. M. Vermaseren and A. Vogt, *Three-loop results for quark and gluon form-factors*, *Phys. Lett. B* **625** (2005) 245 [hep-ph/0508055].

[210] S. Moch, J. A. M. Vermaseren and A. Vogt, *The Three loop splitting functions in QCD: The Nonsinglet case*, *Nucl. Phys. B* **688** (2004) 101 [hep-ph/0403192].

[211] A. Vogt, S. Moch and J. A. M. Vermaseren, *The Three-loop splitting functions in QCD: The Singlet case*, *Nucl. Phys. B* **691** (2004) 129 [hep-ph/0404111].

[212] V. Ravindran, J. Smith and W. L. van Neerven, *Two-loop corrections to Higgs boson production*, *Nucl. Phys. B* **704** (2005) 332 [hep-ph/0408315].

[213] C. Duhr, F. Dulat and B. Mistlberger, *Drell-Yan Cross Section to Third Order in the Strong Coupling Constant*, *Phys. Rev. Lett.* **125** (2020) 172001 [2001.07717].

[214] A. A H, *Radiative Corrections and Resummation Effects to Higgs Physics in QCD*, Ph.D. thesis, HBNI, Mumbai, 2021.

[215] M. Bonvini, S. Forte, M. Ghezzi and G. Ridolfi, *Threshold Resummation in SCET vs. Perturbative QCD: An Analytic Comparison*, *Nucl. Phys. B* **861** (2012) 337 [1201.6364].

[216] G. Sterman and M. Zeng, *Quantifying Comparisons of Threshold Resummations*, *JHEP* **05** (2014) 132 [1312.5397].

[217] T. Becher, A. Broggio and A. Ferroglia, *Introduction to Soft-Collinear Effective Theory*, vol. 896. Springer, 2015, 10.1007/978-3-319-14848-9, [1410.1892].

[218] M. Bonvini, *Resummation of soft and hard gluon radiation in perturbative QCD*, Ph.D. thesis, Genoa U., 2012. 1212.0480.

[219] G. F. Sterman, *Summation of Large Corrections to Short Distance Hadronic Cross-Sections*, *Nucl. Phys. B* **281** (1987) 310.

[220] S. Catani and L. Trentadue, *Resummation of the QCD Perturbative Series for Hard Processes*, *Nucl. Phys. B* **327** (1989) 323.

[221] A. A H, P. Mukherjee, V. Ravindran, A. Sankar and S. Tiwari, *Next-to SV resummed Drell–Yan cross section beyond leading-logarithm*, *Eur. Phys. J. C* **82** (2022) 234 [2107.09717].

[222] A. A H, P. Mukherjee, V. Ravindran, A. Sankar and S. Tiwari, *Resummed Higgs boson cross section at next-to SV to* $\mathrm{NNLO} + \overline{\mathrm{NNLL}}$, *Eur. Phys. J. C* **82** (2022) 774 [2109.12657].

[223] M. van Beekveld, E. Laenen, J. Sinninghe Damsté and L. Vernazza, *Next-to-leading power threshold corrections for finite order and resummed colour-singlet cross sections*, *JHEP* **05** (2021) 114 [2101.07270].

[224] M. van Beekveld, L. Vernazza and C. D. White, *Threshold resummation of new partonic channels at next-to-leading power*, *JHEP* **12** (2021) 087 [2109.09752].

[225] S. Catani, M. L. Mangano, P. Nason and L. Trentadue, *The Resummation of soft gluons in hadronic collisions*, *Nucl. Phys. B* **478** (1996) 273 [hep-ph/9604351].

[226] A. Vogt, *Efficient evolution of unpolarized and polarized parton distributions with QCD-PEGASUS*, *Comput. Phys. Commun.* **170** (2005) 65 [hep-ph/0408244].

[227] G. Heinrich, *Collider Physics at the Precision Frontier*, *Phys. Rept.* **922** (2021) 1 [2009.00516].

[228] S. D. Drell and T.-M. Yan, *Massive lepton-pair production in hadron-hadron collisions at high energies*, *Phys. Rev. Lett.* **25** (1970) 316.

[229] J. Abad and B. Humpert, *Perturbative QCD Corrections in ep Scattering*, *Phys. Lett. B* **77** (1978) 105.

[230] K. Harada, T. Kaneko and N. Sakai, *Hadronic Lepton Pair Production Beyond the Leading Order in Perturbative QCD*, *Nucl. Phys. B* **155** (1979) 169.

[231] B. Humpert and W. L. Van Neerven, *AMBIGUITIES IN THE INFRARED REGULARIZATION OF QCD*, *Phys. Lett. B* **84** (1979) 327.

[232] J. Kubar, M. Le Bellac, J. L. Meunier and G. Plaut, *QCD Corrections to the Drell-Yan Mechanism and the Pion Structure Function*, *Nucl. Phys. B* **175** (1980) 251.

[233] P. Mathews, V. Ravindran, K. Sridhar and W. L. van Neerven, *Next-to-leading order QCD corrections to the Drell-Yan cross section in models of TeV-scale gravity*, *Nucl. Phys. B* **713** (2005) 333 [hep-ph/0411018].

[234] T. Ahmed, P. Banerjee, P. K. Dhani, M. C. Kumar, P. Mathews, N. Rana et al., *NNLO QCD corrections to the Drell–Yan cross section in models of TeV-scale gravity*, *Eur. Phys. J. C* **77** (2017) 22 [1606.08454].

[235] P. Banerjee, P. K. Dhani, M. C. Kumar, P. Mathews and V. Ravindran, *NNLO QCD corrections to production of a spin-2 particle with nonuniversal couplings in the Drell-Yan process*, *Phys. Rev. D* **97** (2018) 094028 [1710.04184].

[236] F. A. Dreyer and A. Karlberg, *Vector-Boson Fusion Higgs Production at Three Loops in QCD*, *Phys. Rev. Lett.* **117** (2016) 072001 [1606.00840].

[237] L.-B. Chen, H. T. Li, H.-S. Shao and J. Wang, *The gluon-fusion production of Higgs boson pair: N^3LO QCD corrections and top-quark mass effects*, *JHEP* **03** (2020) 072 [1912.13001].

[238] F. A. Dreyer and A. Karlberg, *Vector-Boson Fusion Higgs Pair Production at N^3LO*, *Phys. Rev. D* **98** (2018) 114016 [1811.07906].

[239] M. Bonvini, S. Marzani, C. Muselli and L. Rottoli, *On the Higgs cross section at N^3LO+N^3LL and its uncertainty*, *JHEP* **08** (2016) 105 [1603.08000].

[240] R. V. Harlander, S. Liebler and H. Mantler, *SusHi Bento: Beyond NNLO and the heavy-top limit*, *Comput. Phys. Commun.* **212** (2017) 239 [1605.03190].

[241] F. Dulat, A. Lazopoulos and B. Mistlberger, *iHixs 2 — Inclusive Higgs cross sections*, *Comput. Phys. Commun.* **233** (2018) 243 [1802.00827].

[242] S. Dittmaier and M. Krämer, *Electroweak radiative corrections to W boson production at hadron colliders*, *Phys. Rev. D* **65** (2002) 073007 [hep-ph/0109062].

[243] U. Baur, O. Brein, W. Hollik, C. Schappacher and D. Wackeroth, *Electroweak radiative corrections to neutral current Drell-Yan processes at hadron colliders*, *Phys. Rev. D* **65** (2002) 033007 [hep-ph/0108274].

[244] U. Baur and D. Wackeroth, *Electroweak radiative corrections to $p\bar{p} \to W^{\pm} \to \ell^{\pm}\nu$ beyond the pole approximation*, *Phys. Rev. D* **70** (2004) 073015 [hep-ph/0405191].

[245] A. Arbuzov, D. Bardin, S. Bondarenko, P. Christova, L. Kalinovskaya, G. Nanava et al., *One-loop corrections to the Drell-Yan process in SANC. I. The Charged current case*, *Eur. Phys. J. C* **46** (2006) 407 [hep-ph/0506110].

[246] C. M. Carloni Calame, G. Montagna, O. Nicrosini and A. Vicini, *Precision electroweak calculation of the charged current Drell-Yan process*, *JHEP* **12** (2006) 016 [hep-ph/0609170].

[247] V. A. Zykunov, *Weak radiative corrections to Drell-Yan process for large invariant mass of di-lepton pair*, *Phys. Rev. D* **75** (2007) 073019 [hep-ph/0509315].

[248] C. M. Carloni Calame, G. Montagna, O. Nicrosini and A. Vicini, *Precision electroweak calculation of the production of a high transverse-momentum lepton pair at hadron colliders*, *JHEP* **10** (2007) 109 [0710.1722].

[249] A. Arbuzov, D. Bardin, S. Bondarenko, P. Christova, L. Kalinovskaya, G. Nanava et al., *One-loop corrections to the Drell–Yan process in SANC. (II). The Neutral current case*, *Eur. Phys. J. C* **54** (2008) 451 [0711.0625].

[250] S. Dittmaier and M. Huber, *Radiative corrections to the neutral-current Drell-Yan process in the Standard Model and its minimal supersymmetric extension*, *JHEP* **01** (2010) 060 [0911.2329].

[251] R. Bonciani, F. Buccioni, N. Rana and A. Vicini, *Next-to-Next-to-Leading Order Mixed QCD-Electroweak Corrections to on-Shell Z Production*, *Phys. Rev. Lett.* **125** (2020) 232004 [2007.06518].

[252] R. Bonciani, L. Buonocore, M. Grazzini, S. Kallweit, N. Rana, F. Tramontano et al., *Mixed Strong-Electroweak Corrections to the Drell-Yan Process*, *Phys. Rev. Lett.* **128** (2022) 012002 [2106.11953].

[253] R. Bonciani, F. Buccioni, N. Rana and A. Vicini, *On-shell Z boson production at hadron colliders through $\mathcal{O}(\alpha\alpha_S)$* , *JHEP* **02** (2022) 095 [2111.12694].

[254] T. Armadillo, R. Bonciani, S. Devoto, N. Rana and A. Vicini, *Two-loop mixed QCD-EW corrections to neutral current Drell-Yan*, *JHEP* **05** (2022) 072 [2201.01754].

[255] A. H. Ajjath, P. Banerjee, A. Chakraborty, P. K. Dhani, P. Mukherjee, N. Rana et al., *NNLO QCD$\oplus$QED corrections to Higgs production in bottom quark annihilation*, *Phys. Rev. D* **100** (2019) 114016 [1906.09028].

[256] T. Ahmed, N. Rana and V. Ravindran, *Higgs boson production through $b\bar{b}$ annihilation at threshold in N^3LO QCD*, *JHEP* **10** (2014) 139 [1408.0787].

[257] A. H. Ajjath, A. Chakraborty, G. Das, P. Mukherjee and V. Ravindran, *Resummed prediction for Higgs boson production through $b\bar{b}$ annihilation at N^3LL*, *JHEP* **11** (2019) 006 [1905.03771].

[258] T. Ahmed, M. Mahakhud, N. Rana and V. Ravindran, *Drell-Yan Production at Threshold to Third Order in QCD*, *Phys. Rev. Lett.* **113** (2014) 112002 [1404.0366].

[259] T. Ahmed, A. H. Ajjath, L. Chen, P. K. Dhani, P. Mukherjee and V. Ravindran, *Polarised Amplitudes and Soft-Virtual Cross Sections for* $b\bar{b} \to ZH$ *at NNLO in QCD*, *JHEP* **01** (2020) 030 [1910.06347].

[260] S. Catani, L. Cieri, D. de Florian, G. Ferrera and M. Grazzini, *Threshold resummation at* N^3LL *accuracy and soft-virtual cross sections at* N^3LO, *Nucl. Phys. B* **888** (2014) 75 [1405.4827].

[261] G. Das, S.-O. Moch and A. Vogt, *Soft corrections to inclusive DIS at four loops and beyond*, *PoS* **DIS2019** (2019) 010 [1908.03071].

[262] G. Das, S.-O. Moch and A. Vogt, *Soft corrections to inclusive deep-inelastic scattering at four loops and beyond*, *JHEP* **03** (2020) 116 [1912.12920].

[263] G. Das, S. Moch and A. Vogt, *Approximate four-loop QCD corrections to the Higgs-boson production cross section*, *Phys. Lett. B* **807** (2020) 135546 [2004.00563].

[264] H. Contopanagos, E. Laenen and G. F. Sterman, *Sudakov factorization and resummation*, *Nucl. Phys. B* **484** (1997) 303 [hep-ph/9604313].

[265] L. Magnea, *Analytic resummation for the quark form-factor in QCD*, *Nucl. Phys. B* **593** (2001) 269 [hep-ph/0006255].

[266] A. V. Manohar, *Deep inelastic scattering as* $x \longrightarrow 1$ *using soft collinear effective theory*, *Phys. Rev. D* **68** (2003) 114019 [hep-ph/0309176].

[267] T. O. Eynck, E. Laenen and L. Magnea, *Exponentiation of the Drell-Yan cross-section near partonic threshold in the DIS and MS-bar schemes*, *JHEP* **06** (2003) 057 [hep-ph/0305179].

[268] A. Idilbi, X.-d. Ji and F. Yuan, *Resummation of threshold logarithms in effective field theory for DIS, Drell-Yan and Higgs production*, *Nucl. Phys. B* **753** (2006) 42 [hep-ph/0605068].

[269] T. Becher, M. Neubert and B. D. Pecjak, *Factorization and Momentum-Space Resummation in Deep-Inelastic Scattering*, *JHEP* **01** (2007) 076 [hep-ph/0607228].

[270] D. de Florian and J. Mazzitelli, *A next-to-next-to-leading order calculation of soft-virtual cross sections*, *JHEP* **12** (2012) 088 [1209.0673].

[271] M. Bonvini and S. Marzani, *Resummed Higgs cross section at* N^3LL, *JHEP* **09** (2014) 007 [1405.3654].

[272] A. H. Ajjath, G. Das, M. C. Kumar, P. Mukherjee, V. Ravindran and K. Samanta, *Resummed Drell-Yan cross-section at* N^3LL, *JHEP* **10** (2020) 153 [2001.11377].

[273] A. H. Ajjath, P. Mukherjee, V. Ravindran, A. Sankar and S. Tiwari, *Resummed Higgs boson cross section at next-to SV to* $\mathrm{NNLO} + \overline{\mathrm{NNLL}}$, *Eur. Phys. J. C* **82** (2022) 774 [2109.12657].

[274] A. H. Ajjath, P. Mukherjee, V. Ravindran, A. Sankar and S. Tiwari, *Next-to SV resummed Drell–Yan cross section beyond leading-logarithm*, *Eur. Phys. J. C* **82** (2022) 234 [2107.09717].

[275] A. H. Ajjath and H.-S. Shao, *N^3LO+N^3LL QCD improved Higgs pair cross sections*, 2209.03914.

[276] M. Forslund and N. Kidonakis, *Resummation for $2 \to n$ processes in single-particle-inclusive kinematics*, *Phys. Rev. D* **102** (2020) 034006 [2003.09021].

[277] T. Ahmed, A. H. Ajjath, G. Das, P. Mukherjee, V. Ravindran and S. Tiwari, *Soft-virtual correction and threshold resummation for n-colorless particles to fourth order in QCD: Part I*, 2010.02979.

[278] T. Ahmed, M. Bonvini, M. C. Kumar, P. Mathews, N. Rana, V. Ravindran et al., *Pseudo-scalar Higgs boson production at $N^3\ LO_A + N^3\ LL'$*, *Eur. Phys. J. C* **76** (2016) 663 [1606.00837].

[279] D. de Florian and J. Zurita, *Soft-gluon resummation for pseudoscalar Higgs boson production at hadron colliders*, *Phys. Lett. B* **659** (2008) 813 [0711.1916].

[280] G. Das, M. C. Kumar and K. Samanta, *Resummed inclusive cross-section in ADD model at N^3LL*, *JHEP* **10** (2020) 161 [1912.13039].

[281] G. Das, M. C. Kumar and K. Samanta, *Resummed inclusive cross-section in Randall-Sundrum model at NNLO+NNLL*, *JHEP* **07** (2020) 040 [2004.03938].

[282] G. Das, M. C. Kumar and K. Samanta, *Precision QCD phenomenology of exotic spin-2 search at the LHC*, *JHEP* **04** (2021) 111 [2011.15121].

[283] W. Beenakker, S. Brensing, M. Kramer, A. Kulesza, E. Laenen and I. Niessen, *Soft-gluon resummation for squark and gluino hadroproduction*, *JHEP* **12** (2009) 041 [0909.4418].

[284] W. Beenakker, C. Borschensky, M. Krämer, A. Kulesza and E. Laenen, *NNLL-fast: predictions for coloured supersymmetric particle production at the LHC with threshold and Coulomb resummation*, *JHEP* **12** (2016) 133 [1607.07741].

[285] J. Fiaschi, B. Fuks, M. Klasen and A. Neuwirth, *Soft gluon resummation for associated squark-electroweakino production at the LHC*, *JHEP* **06** (2022) 130 [2202.13416].

[286] M. Krämer, A. Kulesza, A. Mück and R. Schürmann, *Threshold Resummation for Dark-Matter Production at the LHC*, *JHEP* **07** (2019) 064 [1903.06417].

[287] A. Bhattacharya, M. C. Kumar, P. Mathews and V. Ravindran, *Next-to-soft-virtual resummed prediction for pseudoscalar Higgs boson production at $NNLO+\overline{NNLL}$*, *Phys. Rev. D* **105** (2022) 116015 [2112.02341].

[288] M. Bonvini and L. Rottoli, *Three loop soft function for N^3LL' gluon fusion Higgs production in soft-collinear effective theory*, *Phys. Rev. D* **91** (2015) 051301 [1412.3791].

[289] M. Bonvini, S. Marzani, J. Rojo, L. Rottoli, M. Ubiali, R. D. Ball et al., *Parton distributions with threshold resummation*, *JHEP* **09** (2015) 191 [1507.01006].

[290] M. Bonvini and S. Marzani, *Four-loop splitting functions at small x*, *JHEP* **06** (2018) 145 [1805.06460].

[291] P. A. Baikov, K. G. Chetyrkin, A. V. Smirnov, V. A. Smirnov and M. Steinhauser, *Quark and gluon form factors to three loops*, *Phys. Rev. Lett.* **102** (2009) 212002 [0902.3519].

[292] T. Gehrmann, E. W. N. Glover, T. Huber, N. Ikizlerli and C. Studerus, *Calculation of the quark and gluon form factors to three loops in QCD*, *JHEP* **06** (2010) 094 [1004.3653].

[293] T. Gehrmann and D. Kara, *The $Hb\bar{b}$ form factor to three loops in QCD*, *JHEP* **09** (2014) 174 [1407.8114].

[294] A. Kulesza, G. F. Sterman and W. Vogelsang, *Joint resummation in electroweak boson production*, *Phys. Rev. D* **66** (2002) 014011 [hep-ph/0202251].

[295] L. A. Harland-Lang, A. D. Martin, P. Motylinski and R. S. Thorne, *Parton distributions in the LHC era: MMHT 2014 PDFs*, *Eur. Phys. J. C* **75** (2015) 204 [1412.3989].

[296] A. Buckley, J. Ferrando, S. Lloyd, K. Nordström, B. Page, M. Rüfenacht et al., *LHAPDF6: parton density access in the LHC precision era*, *Eur. Phys. J. C* **75** (2015) 132 [1412.7420].

[297] J. M. Campbell, R. K. Ellis and C. Williams, *Associated production of a Higgs boson at NNLO*, *JHEP* **06** (2016) 179 [1601.00658].

[298] R. Frederix, S. Frixione, V. Hirschi, D. Pagani, H. S. Shao and M. Zaro, *The automation of next-to-leading order electroweak calculations*, *JHEP* **07** (2018) 185 [1804.10017].

[299] J. Alwall, R. Frederix, S. Frixione, V. Hirschi, F. Maltoni, O. Mattelaer et al., *The automated computation of tree-level and next-to-leading order differential cross sections, and their matching to parton shower simulations*, *JHEP* **07** (2014) 079 [1405.0301].

[300] O. Brein, R. Harlander, M. Wiesemann and T. Zirke, *Top-Quark Mediated Effects in Hadronic Higgs-Strahlung*, *Eur. Phys. J. C* **72** (2012) 1868 [1111.0761].

[301] J. Davies, G. Mishima and M. Steinhauser, *Virtual corrections to $gg \to ZH$ in the high-energy and large-m_t limits*, *JHEP* **03** (2021) 034 [2011.12314].

[302] S. Alekhin, J. Blümlein, S. Moch and R. Placakyte, *Parton distribution functions, α_s, and heavy-quark masses for LHC Run II*, *Phys. Rev. D* **96** (2017) 014011 [1701.05838].

[303] T.-J. Hou et al., *Progress in the CTEQ-TEA NNLO global QCD analysis*, 1908.11394.

[304] R. D. Ball et al., *Parton distributions with LHC data*, *Nucl. Phys. B* **867** (2013) 244 [1207.1303].

[305] J. Butterworth et al., *PDF4LHC recommendations for LHC Run II*, *J. Phys. G* **43** (2016) 023001 [1510.03865].

[306] C. Englert, M. McCullough and M. Spannowsky, *Gluon-initiated associated production boosts Higgs physics*, *Phys. Rev. D* **89** (2014) 013013 [1310.4828].

[307] B. Hespel, F. Maltoni and E. Vryonidou, *Higgs and Z boson associated production via gluon fusion in the SM and the 2HDM*, *JHEP* **06** (2015) 065 [1503.01656].

[308] D. Goncalves, F. Krauss, S. Kuttimalai and P. Maierhöfer, *Higgs-Strahlung: Merging the NLO Drell-Yan and Loop-Induced 0+1 jet Multiplicities*, *Phys. Rev. D* **92** (2015) 073006 [1509.01597].

[309] ATLAS collaboration, M. Aaboud et al., *Measurement of VH,* $\mathrm{H} \to \mathrm{b\bar{b}}$ *production as a function of the vector-boson transverse momentum in 13 TeV pp collisions with the ATLAS detector*, *JHEP* **05** (2019) 141 [1903.04618].

[310] ATLAS collaboration, G. Aad et al., *Measurement of the associated production of a Higgs boson decaying into b-quarks with a vector boson at high transverse momentum in pp collisions at* $\sqrt{s} = 13$ *TeV with the ATLAS detector*, *Phys. Lett. B* **816** (2021) 136204 [2008.02508].

[311] CMS collaboration, *Combined Higgs boson production and decay measurements with up to 137 fb*$^{-1}$ *of proton-proton collision data at* $\sqrt{s} = 13$ *TeV*, .

[312] ATLAS collaboration, *Combination of measurements of Higgs boson production in association with a W or Z boson in the* $b\bar{b}$ *decay channel with the ATLAS experiment at* $\sqrt{s} = 13$ *TeV*, .

[313] CMS collaboration, V. Chekhovsky et al., *Constraints on standard model effective field theory for a Higgs boson produced in association with W or Z bosons in the* $H \to \mathrm{b\bar{b}}$ *decay channel in proton-proton collisions at* $\sqrt{s} = 13$ *TeV*, 2411.16907.

[314] CMS collaboration, A. Hayrapetyan et al., *Study of WH production through vector boson scattering and extraction of the relative sign of the W and Z couplings to the Higgs boson in proton-proton collisions at* $\sqrt{s} = 13$ *TeV*, 2405.16566.

[315] CMS collaboration, A. Hayrapetyan et al., *Search for ZZ and ZH production in the* $b\bar{b}b\bar{b}$ *final state using proton-proton collisions at* $\sqrt{s} = 13$ *TeV*, *Eur. Phys. J. C* **84** (2024) 712 [2403.20241].

[316] CMS collaboration, A. Hayrapetyan et al., *Search for Higgs boson pair production with one associated vector boson in proton-proton collisions at* $\sqrt{s} = 13$ *TeV*, *JHEP* **10** (2024) 061 [2404.08462].

[317] ATLAS collaboration, G. Aad et al., *Measurements of* WH *and* ZH *production with Higgs boson decays into bottom quarks and direct constraints on the charm Yukawa coupling in* 13 TeV *pp collisions with the ATLAS detector*, 2410.19611.

[318] O. Brein, A. Djouadi and R. Harlander, *NNLO QCD corrections to the Higgs-strahlung processes at hadron colliders*, *Phys. Lett. B* **579** (2004) 149 [hep-ph/0307206].

[319] G. Ferrera, G. Somogyi and F. Tramontano, *Associated production of a Higgs boson decaying into bottom quarks at the LHC in full NNLO QCD*, *Phys. Lett. B* **780** (2018) 346 [1705.10304].

[320] L. D. Landau, *On the angular momentum of a system of two photons*, *Dokl. Akad. Nauk SSSR* **60** (1948) 207.

[321] C.-N. Yang, *Selection Rules for the Dematerialization of a Particle Into Two Photons*, *Phys. Rev.* **77** (1950) 242.

[322] S. Catani and L. Trentadue, *Comment on QCD exponentiation at large x*, *Nucl. Phys. B* **353** (1991) 183.

[323] T. Ahmed, G. Das, M. C. Kumar, N. Rana and V. Ravindran, *RG improved Higgs boson production to N^3LO in QCD*, 1505.07422.

[324] A. A H, A. Chakraborty, G. Das, P. Mukherjee and V. Ravindran, *Resummed prediction for Higgs boson production through $b\overline{b}$ annihilation at N^3LL*, *JHEP* **11** (2019) 006 [1905.03771].

[325] A. A H, G. Das, M. C. Kumar, P. Mukherjee, V. Ravindran and K. Samanta, *Resummed Drell-Yan cross-section at N^3LL*, *JHEP* **10** (2020) 153 [2001.11377].

[326] S. Moch and A. Vogt, *On non-singlet physical evolution kernels and large-x coefficient functions in perturbative QCD*, *JHEP* **11** (2009) 099 [0909.2124].

[327] G. Soar, S. Moch, J. A. M. Vermaseren and A. Vogt, *On Higgs-exchange DIS, physical evolution kernels and fourth-order splitting functions at large x*, *Nucl. Phys. B* **832** (2010) 152 [0912.0369].

[328] D. Bonocore, E. Laenen, L. Magnea, S. Melville, L. Vernazza and C. D. White, *A factorization approach to next-to-leading-power threshold logarithms*, *JHEP* **06** (2015) 008 [1503.05156].

[329] V. Del Duca, E. Laenen, L. Magnea, L. Vernazza and C. D. White, *Universality of next-to-leading power threshold effects for colourless final states in hadronic collisions*, *JHEP* **11** (2017) 057 [1706.04018].

[330] N. Bahjat-Abbas, D. Bonocore, J. Sinninghe Damsté, E. Laenen, L. Magnea, L. Vernazza et al., *Diagrammatic resummation of leading-logarithmic threshold effects at next-to-leading power*, *JHEP* **11** (2019) 002 [1905.13710].

[331] M. Beneke, A. Broggio, S. Jaskiewicz and L. Vernazza, *Threshold factorization of the Drell-Yan process at next-to-leading power*, *JHEP* **07** (2020) 078 [1912.01585].

[332] M. van Beekveld, W. Beenakker, R. Basu, E. Laenen, A. Misra and P. Motylinski, *Next-to-leading power threshold effects for resummed prompt photon production*, *Phys. Rev. D* **100** (2019) 056009 [1905.11771].

[333] A. A H, P. Mukherjee and V. Ravindran, *Going beyond soft plus virtual*, *Phys. Rev. D* **105** (2022) L091503 [2204.09012].

[334] PDF4LHC Working Group collaboration, R. D. Ball et al., *The PDF4LHC21 combination of global PDF fits for the LHC Run III*, *J. Phys. G* **49** (2022) 080501 [2203.05506].

[335] Particle Data Group collaboration, S. Navas et al., *Review of particle physics*, *Phys. Rev. D* **110** (2024) 030001.

[336] CMS collaboration, A. Tumasyan et al., *Measurements of the electroweak diboson production cross sections in proton-proton collisions at $\sqrt{s} = 5.02$ TeV using leptonic decays*, *Phys. Rev. Lett.* **127** (2021) 191801 [2107.01137].

[337] ATLAS collaboration, G. Aad et al., *Measurement of the ZZ production cross section and limits on anomalous neutral triple gauge couplings in proton-proton collisions at $\sqrt{s} = 7$ TeV with the ATLAS detector*, *Phys. Rev. Lett.* **108** (2012) 041804 [1110.5016].

[338] CMS collaboration, V. Khachatryan et al., *Measurements of the Z Z production cross sections in the 2l2ν channel in proton–proton collisions at $\sqrt{s} = 7$ and 8 TeV and combined constraints on triple gauge couplings*, *Eur. Phys. J. C* **75** (2015) 511 [1503.05467].

[339] CMS collaboration, S. Chatrchyan et al., *Measurement of W^+W^- and ZZ Production Cross Sections in pp Collisions at $\sqrt{s} = 8TeV$*, *Phys. Lett. B* **721** (2013) 190 [1301.4698].

[340] CMS collaboration, V. Khachatryan et al., *Measurement of the pp $\to$ ZZ Production Cross Section and Constraints on Anomalous Triple Gauge Couplings in Four-Lepton Final States at $\sqrt{s} = 8$ TeV*, *Phys. Lett. B* **740** (2015) 250 [1406.0113].

[341] ATLAS collaboration, G. Aad et al., *Measurements of four-lepton production in pp collisions at $\sqrt{s} = 8$ TeV with the ATLAS detector*, *Phys. Lett. B* **753** (2016) 552 [1509.07844].

[342] ATLAS collaboration, M. Aaboud et al., *Measurement of the ZZ production cross section in proton-proton collisions at $\sqrt{s} = 8$ TeV using the $ZZ \to \ell^-\ell^+\ell'^-\ell'^+$ and $ZZ \to \ell^-\ell^+\nu\bar{\nu}$ channels with the ATLAS detector*, *JHEP* **01** (2017) 099 [1610.07585].

[343] CMS collaboration, A. M. Sirunyan et al., *Measurement of differential cross sections for Z boson pair production in association with jets at $\sqrt{s} = 8$ and 13 TeV*, *Phys. Lett. B* **789** (2019) 19 [1806.11073].

[344] CMS collaboration, V. Khachatryan et al., *Measurement of the ZZ production cross section and $Z \to \ell^+\ell^-\ell'^+\ell'^-$ branching fraction in pp collisions at $\sqrt{s}$=13 TeV*, *Phys. Lett. B* **763** (2016) 280 [1607.08834].

[345] ATLAS collaboration, M. Aaboud et al., *$ZZ \to \ell^+\ell^-\ell'^+\ell'^-$ cross-section measurements and search for anomalous triple gauge couplings in 13 TeV pp collisions with the ATLAS detector*, *Phys. Rev. D* **97** (2018) 032005 [1709.07703].

[346] CMS collaboration, A. M. Sirunyan et al., *Measurements of the pp $\to$ ZZ production cross section and the Z $\to 4\ell$ branching fraction, and constraints on anomalous triple gauge couplings at $\sqrt{s} = 13$ TeV*, *Eur. Phys. J. C* **78** (2018) 165 [1709.08601].

[347] ATLAS collaboration, M. Aaboud et al., *Measurement of ZZ production in the $\ell\ell\nu\nu$ final state with the ATLAS detector in pp collisions at $\sqrt{s} = 13$ TeV*, *JHEP* **10** (2019) 127 [1905.07163].

[348] CMS collaboration, A. M. Sirunyan et al., *Measurements of* pp $\rightarrow$ ZZ *production cross sections and constraints on anomalous triple gauge couplings at* $\sqrt{s} = 13$ *TeV*, *Eur. Phys. J. C* **81** (2021) 200 [2009.01186].

[349] ATLAS collaboration, G. Aad et al., *Measurement of zz production cross-sections in the four-lepton final state in pp collisions at s=13.6tev with the atlas experiment*, *Physics Letters B* **855** (2024) 138764.

[350] J. Ohnemus and J. F. Owens, *Order-α_s calculation of hadronic zz production*, *Phys. Rev. D* **43** (1991) 3626.

[351] B. Mele, P. Nason and G. Ridolfi, *QCD radiative corrections to Z boson pair production in hadronic collisions*, *Nucl. Phys. B* **357** (1991) 409.

[352] C. Zecher, T. Matsuura and J. J. van der Bij, *Leptonic signals from off-shell Z boson pairs at hadron colliders*, *Z. Phys. C* **64** (1994) 219 [hep-ph/9404295].

[353] J. Ohnemus, *Hadronic ZZ, W^-W^+, and $W^\pm Z$ production with QCD corrections and leptonic decays*, *Phys. Rev. D* **50** (1994) 1931 [hep-ph/9403331].

[354] J. M. Campbell and R. K. Ellis, *An Update on vector boson pair production at hadron colliders*, *Phys. Rev. D* **60** (1999) 113006 [hep-ph/9905386].

[355] L. J. Dixon, Z. Kunszt and A. Signer, *Helicity amplitudes for O(alpha-s) production of W^+W^-, $W^\pm Z$, ZZ, $W^\pm\gamma$, or $Z\gamma$ pairs at hadron colliders*, *Nucl. Phys. B* **531** (1998) 3 [hep-ph/9803250].

[356] J. M. Campbell, R. K. Ellis and C. Williams, *Vector Boson Pair Production at the LHC*, *JHEP* **07** (2011) 018 [1105.0020].

[357] T. Melia, P. Nason, R. Rontsch and G. Zanderighi, *W+W-, WZ and ZZ production in the POWHEG BOX*, *JHEP* **11** (2011) 078 [1107.5051].

[358] P. Nason and G. Zanderighi, *W^+W^- , WZ and ZZ production in the POWHEG-BOX-V2*, *Eur. Phys. J. C* **74** (2014) 2702 [1311.1365].

[359] R. Frederix, S. Frixione, V. Hirschi, F. Maltoni, R. Pittau and P. Torrielli, *Four-lepton production at hadron colliders: aMC@NLO predictions with theoretical uncertainties*, *JHEP* **02** (2012) 099 [1110.4738].

[360] N. Agarwal, V. Ravindran, V. K. Tiwari and A. Tripathi, *Z boson pair production at the LHC to O(alpha(s)) in TeV scale gravity models*, *Nucl. Phys. B* **830** (2010) 248 [0909.2651].

[361] T. Binoth, T. Gleisberg, S. Karg, N. Kauer and G. Sanguinetti, *NLO QCD corrections to ZZ+ jet production at hadron colliders*, *Phys. Lett. B* **683** (2010) 154 [0911.3181].

[362] F. Campanario, M. Kerner, L. D. Ninh and D. Zeppenfeld, *Next-to-leading order QCD corrections to ZZ production in association with two jets*, *JHEP* **07** (2014) 148 [1405.3972].

[363] T. Gehrmann, A. von Manteuffel and L. Tancredi, *The two-loop helicity amplitudes for $q\bar{q}' \rightarrow V_1V_2 \rightarrow 4$ leptons*, *JHEP* **09** (2015) 128 [1503.04812].

[364] G. Heinrich, S. Jahn, S. P. Jones, M. Kerner and J. Pires, *NNLO predictions for Z-boson pair production at the LHC*, *JHEP* **03** (2018) 142 [1710.06294].

[365] M. Grazzini, S. Kallweit, D. Rathlev and M. Wiesemann, *$W^{\pm}Z$ production at the LHC: fiducial cross sections and distributions in NNLO QCD*, *JHEP* **05** (2017) 139 [1703.09065].

[366] G. Das, C. Dey, M. C. Kumar and K. Samanta, *Precision Studies for Higgs-Strahlung Process at Hadron Collider*, *Springer Proc. Phys.* **304** (2024) 245.

[367] F. Dulat, B. Mistlberger and A. Pelloni, *Differential Higgs production at N^3LO beyond threshold*, *JHEP* **01** (2018) 145 [1710.03016].

[368] T. Ahmed, M. C. Kumar, P. Mathews, N. Rana and V. Ravindran, *Pseudo-scalar Higgs boson production at threshold N^3 LO and N^3 LL QCD*, *Eur. Phys. J. C* **76** (2016) 355 [1510.02235].

[369] G. Das and A. Sankar, *Next-to-soft threshold effects on Higgs boson production via bottom quark annihilation*, 2409.01553.

[370] P. Banerjee, G. Das, P. K. Dhani and V. Ravindran, *Threshold resummation of the rapidity distribution for Drell-Yan production at NNLO+NNLL*, *Phys. Rev. D* **98** (2018) 054018 [1805.01186].

[371] G. Das, *$Z, W^{\pm}$ rapidity distributions at NNLL and beyond*, 2303.16578.

[372] T. Ahmed, A. A H, P. Mukherjee, V. Ravindran and A. Sankar, *Rapidity distribution at soft-virtual and beyond for n-colorless particles to N^4LO in QCD*, *Eur. Phys. J. C* **81** (2021) 943 [2010.02980].

[373] A. A H, P. Mukherjee, V. Ravindran, A. Sankar and S. Tiwari, *Next-to-soft-virtual resummed rapidity distribution for the Drell-Yan process to NNLO+$\overline{\text{NNLL}}$*, *Phys. Rev. D* **106** (2022) 034005 [2112.14094].

[374] V. Ravindran, A. Sankar and S. Tiwari, *Rapidity distribution of pseudoscalar Higgs boson to NNLOA+$\overline{\text{NNLL}}$*, *Phys. Rev. D* **110** (2024) 016019 [2309.14833].

[375] T. Ahmed, M. K. Mandal, N. Rana and V. Ravindran, *Rapidity Distributions in Drell-Yan and Higgs Productions at Threshold to Third Order in QCD*, *Phys. Rev. Lett.* **113** (2014) 212003 [1404.6504].

[376] P. Banerjee, G. Das, P. K. Dhani and V. Ravindran, *Threshold resummation of the rapidity distribution for Higgs production at NNLO+NNLL*, *Phys. Rev. D* **97** (2018) 054024 [1708.05706].

[377] V. Ravindran, A. Sankar and S. Tiwari, *Resummed next-to-soft corrections to rapidity distribution of Higgs boson to NNLO+$\overline{\text{NNLL}}$*, *Phys. Rev. D* **108** (2023) 014012 [2205.11560].

[378] G. Das, *Higgs boson rapidity distribution in bottom annihilation at NNLL and beyond*, *Phys. Rev. D* **108** (2023) 094028 [2306.04561].

[379] M. Grazzini, S. Kallweit, D. Rathlev and M. Wiesemann, *Transverse-momentum resummation for vector-boson pair production at NNLL+NNLO*, *JHEP* **08** (2015) 154 [1507.02565].

[380] J. M. Campbell, R. K. Ellis, T. Neumann and S. Seth, *Transverse momentum resummation at N^3LL+NNLO for diboson processes*, *JHEP* **03** (2023) 080 [2210.10724].

[381] L. Buonocore, G. Koole, D. Lombardi, L. Rottoli, M. Wiesemann and G. Zanderighi, *ZZ production at nNNLO+PS with MiNNLO$_{PS}$*, *JHEP* **01** (2022) 072 [2108.05337].

[382] T. Binoth, N. Kauer and P. Mertsch, *Gluon-induced QCD corrections to pp —> ZZ —> l anti-l l-prime anti-l-prime*, in *16th International Workshop on Deep Inelastic Scattering and Related Subjects*, p. 142, 7, 2008, 0807.0024, DOI.

[383] F. Caola, K. Melnikov, R. Röntsch and L. Tancredi, *QCD corrections to ZZ production in gluon fusion at the LHC*, *Phys. Rev. D* **92** (2015) 094028 [1509.06734].

[384] M. Grazzini, S. Kallweit, M. Wiesemann and J. Y. Yook, *ZZ production at the LHC: NLO QCD corrections to the loop-induced gluon fusion channel*, *JHEP* **03** (2019) 070 [1811.09593].

[385] M. Grazzini, S. Kallweit, M. Wiesemann and J. Y. Yook, *Four lepton production in gluon fusion: Off-shell Higgs effects in NLO QCD*, *Phys. Lett. B* **819** (2021) 136465 [2102.08344].

[386] B. Agarwal, S. Jones, M. Kerner and A. von Manteuffel, *Complete NLO QCD Corrections to ZZ Production in Gluon Fusion*, 2404.05684.

[387] S. Alioli, F. Caola, G. Luisoni and R. Röntsch, *ZZ production in gluon fusion at NLO matched to parton-shower*, *Phys. Rev. D* **95** (2017) 034042 [1609.09719].

[388] A. Bierweiler, T. Kasprzik and J. H. Kühn, *Vector-boson pair production at the LHC to $\mathcal{O}(\alpha^3)$ accuracy*, *JHEP* **12** (2013) 071 [1305.5402].

[389] M. Grazzini, S. Kallweit, J. M. Lindert, S. Pozzorini and M. Wiesemann, *NNLO QCD + NLO EW with Matrix+OpenLoops: precise predictions for vector-boson pair production*, *JHEP* **02** (2020) 087 [1912.00068].

[390] A. Denner and G. Pelliccioli, *NLO EW and QCD corrections to polarized ZZ production in the four-charged-lepton channel at the LHC*, *JHEP* **10** (2021) 097 [2107.06579].

[391] FCC collaboration, A. Abada et al., *FCC-hh: The Hadron Collider: Future Circular Collider Conceptual Design Report Volume 3*, *Eur. Phys. J. ST* **228** (2019) 755.

[392] S. A. Larin, *Theoretical aspects of quantum field theory*, *Journal of Theoretical Physics* **27** (1993) 123.

[393] J. Blümlein, P. Marquard, C. Schneider and K. Schönwald, *The three-loop unpolarized and polarized non-singlet anomalous dimensions from off shell operator matrix elements*, *Nucl. Phys. B* **971** (2021) 115542 [2107.06267].

[394] A. A H and H.-S. Shao, *N^3LO+N^3LL QCD improved Higgs pair cross sections*, *JHEP* **02** (2023) 067 [2209.03914].

[395] S. Catani, *The singular behaviour of qcd amplitudes at two-loop order*, *Physics Letters B* **427** (1998) 161–171.

[396] L. Naterop, A. Signer and Y. Ulrich, *handyG —Rapid numerical evaluation of generalised polylogarithms in Fortran*, *Comput. Phys. Commun.* **253** (2020) 107165 [1909.01656].

[397] M. Grazzini, S. Kallweit and M. Wiesemann, *Fully differential NNLO computations with MATRIX*, *Eur. Phys. J. C* **78** (2018) 537 [1711.06631].

[398] A. Denner, S. Dittmaier and L. Hofer, *Collier: a fortran-based Complex One-Loop LIbrary in Extended Regularizations*, *Comput. Phys. Commun.* **212** (2017) 220 [1604.06792].

[399] F. Cascioli, P. Maierhofer and S. Pozzorini, *Scattering Amplitudes with Open Loops*, *Phys. Rev. Lett.* **108** (2012) 111601 [1111.5206].

[400] F. Buccioni, J.-N. Lang, J. M. Lindert, P. Maierh"ofer, S. Pozzorini, H. Zhang et al., *OpenLoops 2*, *Eur. Phys. J. C* **79** (2019) 866 [1907.13071].

[401] F. Buccioni, S. Pozzorini and M. Zoller, *On-the-fly reduction of open loops*, *Eur. Phys. J. C* **78** (2018) 70 [1710.11452].

[402] S. Bailey, T. Cridge, L. A. Harland-Lang, A. D. Martin and R. S. Thorne, *Parton distributions from LHC, HERA, Tevatron and fixed target data: MSHT20 PDFs*, *Eur. Phys. J. C* **81** (2021) 341 [2012.04684].

[403] J. Alwall, M. Herquet, F. Maltoni, O. Mattelaer and T. Stelzer, *Madgraph 5: going beyond*, *Journal of High Energy Physics* **2011** (2011) .

[404] ATLAS collaboration, G. Aad et al., *Higgs boson production cross-section measurements and their EFT interpretation in the 4ℓ decay channel at $\sqrt{s}$ =13 TeV with the ATLAS detector*, *Eur. Phys. J. C* **80** (2020) 957 [2004.03447].

[405] CMS collaboration, A. M. Sirunyan et al., *Measurements of $\mathrm{t\bar{t}}H$ Production and the CP Structure of the Yukawa Interaction between the Higgs Boson and Top Quark in the Diphoton Decay Channel*, *Phys. Rev. Lett.* **125** (2020) 061801 [2003.10866].

[406] CMS collaboration, A. Tumasyan et al., *Analysis of the CP structure of the Yukawa coupling between the Higgs boson and τ leptons in proton-proton collisions at $\sqrt{s}$ = 13 TeV*, *JHEP* **06** (2022) 012 [2110.04836].

[407] P. W. Higgs, *Broken symmetries and the masses of gauge bosons*, *Phys. Rev. Lett.* **13** (1964) 508.

[408] D. L. Rainwater and D. Zeppenfeld, *Searching for $H \to \gamma\gamma$ in weak boson fusion at the LHC*, *JHEP* **12** (1997) 005 [hep-ph/9712271].

[409] D. L. Rainwater, D. Zeppenfeld and K. Hagiwara, *Searching for $H \to \tau^+\tau^-$ in weak boson fusion at the CERN LHC*, *Phys. Rev. D* **59** (1998) 014037 [hep-ph/9808468].

[410] S. Catani, S. Devoto, M. Grazzini, S. Kallweit, J. Mazzitelli and C. Savoini, *Higgs Boson Production in Association with a Top-Antitop Quark Pair in Next-to-Next-to-Leading Order QCD*, *Phys. Rev. Lett.* **130** (2023) 111902 [2210.07846].

[411] B. Agarwal, G. Heinrich, S. P. Jones, M. Kerner, S. Y. Klein, J. Lang et al., *Two-loop amplitudes for $t\bar{t}H$ production: the quark-initiated N_f-part*, *JHEP* **05** (2024) 013 [2402.03301].

[412] D. de Florian, M. Grazzini and Z. Kunszt, *Higgs production with large transverse momentum in hadronic collisions at next-to-leading order*, *Phys. Rev. Lett.* **82** (1999) 5209 [hep-ph/9902483].

[413] V. Ravindran, J. Smith and W. L. Van Neerven, *Next-to-leading order QCD corrections to differential distributions of Higgs boson production in hadron hadron collisions*, *Nucl. Phys. B* **634** (2002) 247 [hep-ph/0201114].

[414] M. Kramer, E. Laenen and M. Spira, *Soft gluon radiation in Higgs boson production at the LHC*, *Nucl. Phys. B* **511** (1998) 523 [hep-ph/9611272].

[415] M. Czakon, R. V. Harlander, J. Klappert and M. Niggetiedt, *Exact Top-Quark Mass Dependence in Hadronic Higgs Production*, *Phys. Rev. Lett.* **127** (2021) 162002 [2105.04436].

[416] C. Anastasiou, C. Duhr, F. Dulat, E. Furlan, T. Gehrmann, F. Herzog et al., *High precision determination of the gluon fusion Higgs boson cross-section at the LHC*, *JHEP* **05** (2016) 058 [1602.00695].

[417] X. Chen, T. Gehrmann, E. W. N. Glover, A. Huss, B. Mistlberger and A. Pelloni, *Fully Differential Higgs Boson Production to Third Order in QCD*, *Phys. Rev. Lett.* **127** (2021) 072002 [2102.07607].

[418] K. D. Lane, *An Introduction to technicolor*, in *Theoretical Advanced Study Institute (TASI 93) in Elementary Particle Physics: The Building Blocks of Creation - From Microfermius to Megaparsecs*, 6, 1993, hep-ph/9401324, DOI.

[419] N. Arkani-Hamed, S. Dimopoulos and G. R. Dvali, *The Hierarchy problem and new dimensions at a millimeter*, *Phys. Lett. B* **429** (1998) 263 [hep-ph/9803315].

[420] L. Randall and R. Sundrum, *A Large mass hierarchy from a small extra dimension*, *Phys. Rev. Lett.* **83** (1999) 3370 [hep-ph/9905221].

[421] M. Drees, R. Godbole and P. Roy, *Theory and Phenomenology of SParticles: an Account of Four-Dimensional N=1 Supersymmetry in High Energy Physics*. 2004, 10.1142/4001.

[422] P. Fayet, *Supersymmetry and Weak, Electromagnetic and Strong Interactions*, *Phys. Lett. B* **64** (1976) 159.

[423] T. Ahmed, V. Ravindran, A. Sankar and S. Tiwari, *Two-loop amplitudes for di-Higgs and di-pseudo-Higgs productions through quark annihilation in QCD*, *JHEP* **01** (2022) 189 [2110.11476].

[424] A. Bhattacharya, M. Mahakhud, P. Mathews and V. Ravindran, *Two loop QCD amplitudes for di-pseudo scalar production in gluon fusion*, *JHEP* **02** (2020) 121 [1909.08993].

[425] G. Bozzi, S. Catani, D. de Florian and M. Grazzini, *Transverse-momentum resummation and the spectrum of the Higgs boson at the LHC*, *Nucl. Phys. B* **737** (2006) 73 [hep-ph/0508068].

[426] N. Agarwal, P. Banerjee, G. Das, P. K. Dhani, A. Mukhopadhyay, V. Ravindran et al., *Resummed transverse momentum distribution of pseudo-scalar Higgs boson at NNLO$_A$+NNLL*, *JHEP* **12** (2018) 105 [1805.12553].

[427] J. M. Campbell, R. K. Ellis and S. Seth, *H + 1 jet production revisited*, *JHEP* **10** (2019) 136 [1906.01020].

[428] T. Gehrmann, P. Jakubčík, C. C. Mella, N. Syrrakos and L. Tancredi, *Two-loop helicity amplitudes for H+jet production to higher orders in the dimensional regulator*, *JHEP* **04** (2023) 016 [2301.10849].

[429] S. Catani, *The Singular behavior of QCD amplitudes at two loop order*, *Phys. Lett. B* **427** (1998) 161 [hep-ph/9802439].

[430] S. L. Adler and W. A. Bardeen, *Absence of higher order corrections in the anomalous axial vector divergence equation*, *Phys. Rev.* **182** (1969) 1517.

[431] C. Studerus, *Reduze-Feynman Integral Reduction in C++*, *Comput. Phys. Commun.* **181** (2010) 1293 [0912.2546].

[432] T. Gehrmann and E. Remiddi, *Two loop master integrals for gamma* –> 3 jets: The Nonplanar topologies*, *Nucl. Phys. B* **601** (2001) 287 [hep-ph/0101124].

[433] T. Gehrmann and E. Remiddi, *Two loop master integrals for gamma* —> 3 jets: The Planar topologies*, *Nucl. Phys. B* **601** (2001) 248 [hep-ph/0008287].

[434] J. Klappert, F. Lange, P. Maierhöfer and J. Usovitsch, *Integral reduction with Kira 2.0 and finite field methods*, *Comput. Phys. Commun.* **266** (2021) 108024 [2008.06494].

[435] S. Laporta, *High-precision calculation of multiloop Feynman integrals by difference equations*, *Int. J. Mod. Phys. A* **15** (2000) 5087 [hep-ph/0102033].

[436] F. V. Tkachov, *A Theorem on Analytical Calculability of Four Loop Renormalization Group Functions*, *Phys. Lett.* **B100** (1981) 65.

[437] K. G. Chetyrkin and F. V. Tkachov, *Integration by Parts: The Algorithm to Calculate beta Functions in 4 Loops*, *Nucl. Phys.* **B192** (1981) 159.

[438] T. Gehrmann and E. Remiddi, *Differential equations for two loop four point functions*, *Nucl. Phys.* **B580** (2000) 485 [hep-ph/9912329].

[439] M. Heller and A. von Manteuffel, *MultivariateApart: Generalized partial fractions*, *Comput. Phys. Commun.* **271** (2022) 108174 [2101.08283].

[440] T. L. Trueman, *Chiral Symmetry in Perturbative QCD*, *Phys. Lett. B* **88** (1979) 331.

[441] M. F. Zoller, *OPE of the pseudoscalar gluonium correlator in massless QCD to three-loop order*, *JHEP* **07** (2013) 040 [1304.2232].

[442] T. Ahmed, T. Gehrmann, P. Mathews, N. Rana and V. Ravindran, *Pseudo-scalar Form Factors at Three Loops in QCD*, *JHEP* **11** (2015) 169 [1510.01715].

[443] G. F. Sterman and M. E. Tejeda-Yeomans, *Multiloop amplitudes and resummation*, *Phys. Lett.* **B552** (2003) 48 [hep-ph/0210130].

[444] T. Becher and M. Neubert, *Infrared singularities of scattering amplitudes in perturbative QCD*, *Phys. Rev. Lett.* **102** (2009) 162001 [0901.0722].

[445] I. A. Korchemskaya and G. P. Korchemsky, *On lightlike Wilson loops*, *Phys. Lett. B* **287** (1992) 169.

[446] G. P. Korchemsky and A. V. Radyushkin, *Renormalization of the Wilson Loops Beyond the Leading Order*, *Nucl. Phys. B* **283** (1987) 342.

[447] C. Duhr and F. Dulat, *PolyLogTools — polylogs for the masses*, *JHEP* **08** (2019) 135 [1904.07279].

[448] J. Kuipers, T. Ueda and J. A. M. Vermaseren, *Code Optimization in FORM*, *Comput. Phys. Commun.* **189** (2015) 1 [1310.7007].

[449] J. Kuipers, A. Plaat, J. A. M. Vermaseren and H. J. van den Herik, *Improving multivariate Horner schemes with Monte Carlo tree search*, *Comput. Phys. Commun.* **184** (2013) 2391 [1207.7079].

[450] M. Tentyukov and J. A. M. Vermaseren, *The Multithreaded version of FORM*, *Comput. Phys. Commun.* **181** (2010) 1419 [hep-ph/0702279].

[451] P. Banerjee, C. Dey, M. C. Kumar and V. Ravindran, "Supplemental material for: Pseudoscalar higgs boson decay to three parton amplitudes at nnlo to higher orders in the dimensional regulator." http://link.aps.org/supplemental/10.1103/PhysRevD.111.054037, 2025.

[452] J. M. Henn, G. P. Korchemsky and B. Mistlberger, *The full four-loop cusp anomalous dimension in $\mathcal{N} = 4$ super Yang-Mills and QCD*, *JHEP* **04** (2020) 018 [1911.10174].

[453] T. Huber, A. von Manteuffel, E. Panzer, R. M. Schabinger and G. Yang, *The four-loop cusp anomalous dimension from the $N = 4$ Sudakov form factor*, *Phys. Lett. B* **807** (2020) 135543 [1912.13459].

[454] A. von Manteuffel, E. Panzer and R. M. Schabinger, *Cusp and collinear anomalous dimensions in four-loop QCD from form factors*, *Phys. Rev. Lett.* **124** (2020) 162001 [2002.04617].

List of Publications

Publications included in the Thesis

International Journals

1. *Threshold enhanced cross-sections for colorless productions.*

   Goutam Das, **Chinmoy Dey**, M.C. Kumar, Kajal Samanta

   Published in: Phys.Rev.D 107 (2023) 3, 034038, arXiv: 2210.17534 [hep-ph].

2. *Pseudo-scalar Higgs decay to three parton amplitudes at NNLO to higher orders in dimensional regulator.*

   Pulak Banerjee , **Chinmoy Dey**, M.C. Kumar, V. Ravindran

   Published in: Phys.Rev.D 111 (2025) 5, 054037, arXiv: 2411.17611 [hep-ph].

3. *Threshold resummation for Z-boson pair production at NNLO+NNLL.*

   Pulak Banerjee, **Chinmoy Dey**, M.C. Kumar, Vaibhav Pandey

   arXiv: 2409.16375 [hep-ph]. **(In communication)**

4. *Soft gluon resummation for gluon fusion ZH production.*

   Goutam Das, **Chinmoy Dey**, M.C. Kumar, Kajal Samanta

   arXiv: 2401.10330 [hep-ph]. **(In communication)**

Conferences Proceeding

1. *Precision Studies for Higgs-Strahlung Process at Hadron Collider.*

   Goutam Das, **Chinmoy Dey**, M.C. Kumar, Kajal Samanta

   Published in: Springer Proc.Phys. 304 (2024) 245-249 , Contribution to: 25th DAE-BRNS High Energy Physics Symposium, 245-249.

2. *Threshold resummation for Z-boson pair production.*

   Pulak Banerjee, **Chinmoy Dey**, M.C. Kumar, Vaibhav Pandey.Published in: Acta Phys.Polon.Supp. 18 (2025) 1, 1 , Contribution to: Diffraction and Low-x 2024, 1.

Publications not included in the Thesis

International Journals

1. *Next to Soft Threshold Resummation for VH Production*

   Arunima Bhattacharya, **Chinmoy Dey**, M.C. Kumar, Vaibhav Pandey, arXiv: 2502.20331 [hep-ph]. **(In communication)**

Talk/Poster presented at Conferences/School/Academic visits

1. **Title**: *Threshold resummation for Drell-Yan like processes at N^3LL.* **(Oral)**

   Advancements in Methods for Precision Studies 2024, 29*th* September 2024,

   Indian Institute of Science Education and Research, Mohali, India.

2. **Title**: *Threshold resummation for Drell-Yan like processes at N3LL.* **(Oral)**

   Academic Visit at University of Hamburg, 16*th* June 2024,

   University of Hamburg, Hamburg, Germany.

3. **Title**: *Threshold resummation for Drell-Yan like processes at N3LL.* **(Poster)**

   MCnet Summer School 2024, 10*th* June 2024,

   CERN, Geneva, Switzerland.

4. **Title**: *Threshold enhanced cross sections for colorless productions.* **(Oral)**

   Advanced School & Workshop on Multiloop Scattering Amplitudes 2024, 19*th* January 2024,

   National Institute of Science Education and Research, Bhubaneswar, India.

5. **Title**: *Threshold resummation for colour singlet productions.* **(Oral)**
   Summer School on Particle Physics 2023, 22*th* June 2023,
   International Centre for Theoretical Physics, Trieste, Italy.

6. **Title**: *Threshold resummation for Higgs-Strahlung process at hadron collider.* **(Oral)**
   International Meeting on High Energy Physics 2023, 21*st* February 2023,
   Institute of Physics, Bhubaneswar, India.

7. **Title**: *Precision studies for Higgs-Strahlung process at hadron collider.* **(Oral)**
   XXV DAE-BRNS High Energy Physics Symposium 2022, 12*th* December 2022,
   Indian Institute of Science Education and Research, Mohali, India.

Conferences and School attended

1. **Summer School on Particle Physics 2021:** I have attended ICTP "**Summer School on Particle Physics**" online from 31st May 2021 to 11th June 2021.

2. **MCnet-CTEQ Summer School 2021:** I have also participated "**MCnet-CTEQ Summer School 2021 VIRTUAL**" from 5th Sep 2021 to 16th Sep 2021.

3. **Data and Machine Learning at the Large Hadron Collider:** I have also participated in "**Data and Machine Learning at the Large Hadron Collider**" from 22nd to 28th August 2022 at IIT Hyderabad, India.

4. **Recent Advances in Perturbative Quantum Chromodynamics:** I have also participated GIAN course in "**Recent Advances in Perturbative Quantum Chromodynamics (pQCD)**" from 2nd to 9th November 2022 at University of Mumbai, India.

5. **XXV DAE-BRNS High Energy Physics Symposium:** I have also participated and gave an oral presentaion in "**XXV DAE-BRNS High Energy**

Physics Symposium" from 12th to 16th December 2022 at IISER Mohali, India.

6. **International Meeting on High Energy Physics 2023:** I have also participated and gave a talk in "**International Meeting on High Energy Physics 2023**" from 16th to 22nd February 2023 at Institute of Physics, India.

7. **Summer School on Particle Physics 2023:** I have paricipated and gave a presentation in the "**Summer School on Particle Physics**" from 19th June 2023 to 30th June 2023 at ICTP, Trieste, Italy.

8. **Advanced School & Workshop on Multiloop Scattering Amplitudes 2024:** I have paricipated and gave a presentation in the "**Advanced School & Workshop on Multiloop Scattering Amplitudes**" from 15th January 2024 to 19th January 2024 at NISER, Bhubaneswar, India.

9. **MCnet Summer School 2024:** I have paricipated and gave a poster presentation in the "**MCnet Summer School**" from 10th June 2024 to 14th June 2024 at CERN, Geneva, Switzerland.

10. **Advancements in Methods for Precision Studies (AMPS) 2024:** I have paricipated and gave a presentation in the "**Advancements in Methods for Precision Studies**" from 28th September 2024 to 30th September 2024 at IISER, Mohali, India.